UNIVERSITY OF SOUTHAMPTON

FACULTY OF ENGINEERING, SCIENCE & MATHEMATICS

School of Ocean and Earth Science

Rifted margin formation in the northwest Indian ocean: the extensional and magmatic history of the Laxmi Ridge continental margin.

by

Christine Irene Lane

This dissertation is submitted for the degree of Doctor of Philosophy

September 2006

UNIVERSITY OF SOUTHAMPTON
ABSTRACT
FACULTY OF ENGINEERING, SCIENCE & MATHEMATICS
SCHOOL OF OCEAN AND EARTH SCIENCES
Doctor of Philosophy
Rifted margin formation in the northwest Indian ocean: the extensional
and magmatic history of the Laxmi Ridge continental margin
by Christine Irene Lane

The phase of rifting between India and the Seychelles that ultimately led
to continental breakup began 61 M.y. ago, and is inferred by previous plate
reconstructions to have been rapid. A geophysical survey was undertaken over
the resulting rifted margins to determine the crustal architecture and syn-rift
magmatism resulting from this rapid extension. An added control on the
morphology of the margins may be thermal: final breakup occurred shortly
after the end of the Deccan phase of magmatism on the Indian subcontinent.

Continental breakup formed a conjugate margin pair: the Seychelles Bank and
Laxmi Ridge. This thesis focuses on geophysical data collected over the Laxmi
Ridge margin. A 480 km wide-angle velocity model is presented, along with
coincident normal-incidence reflection data, gravity and magnetic modelling.
The wide-angle model is broadly divided into four areas of crustal provenance:
the southern-most crust is Chron 27 oceanic crust, which is around 5 km thick
and reaches velocities of 7.4 km s^{-1} at its base. Laxmi Ridge is adjacent to this
crust, and is a 130 km wide, 9 km thick section of thinned continental crust.
It is underlain by 11 km of high velocity material, whose P-wave velocities
reach 7.70 km s^{-1} at the base. Laxmi Ridge abuts against Gop Rift, which is
a 55 km wide basin with crust up to 13 km thick. North of Gop Rift is the
continental rise of India, which is interpreted as stretched continental crust
based on its P-wave velocites and low remanent magnetisation.

Despite predictions that rapid extension should lead to increased magmatic
upwelling and therefore significant amounts of melting, the Laxmi Ridge mar-
gin has features usually diagnostic of amagmatic rifted margins, including thin
(5 km) first-formed oceanic crust south of Laxmi Ridge and weak seaward-
dipping reflectors at the ocean-continent boundary. However, thick oceanic
crust is observed in Gop Rift, an isolated asymmetric basin landward of Laxmi
Ridge. Gop Rift is flanked by two $\sim$ 100 km wide, almost 13 km thick bodies
in the deep crust, whose P-wave velocities reach 7.70 km s^{-1}. These bodies are
interpreted to be magmatic underplate associated with rifting over a thermal
anomaly.

This apparent disparity between magmatic and amagmatic features on the
same margin is solved if the magmatic features are attributed to a prior phase
of spreading in Gop Rift, most likely Chron 29 in age, with the magmatic
material supplied by enhanced melting over the Deccan plume. This spreading
ceased once the thermal anomaly cooled. The final breakup of India and the
Seychelles then occurred within the weakened underplated lithosphere, and
was relatively amagmatic despite the rapid extension. This could be due to
overcooling of the upwelling magma by conductive cooling against the thick
Indian lithosphere.

Graduate School of the National Oceanography Centre, Southampton

This PhD dissertation by

Christine Irene Lane

has been produced under the supervision of the following persons:

Supervisor

Prof. Tim A. Minshull

Supervisor

Dr. Jenny Collier

Chair of Advisory Panel

Prof. Martin Sinha

Member of Advisory Panel

Prof. Andrew Roberts

To know is not to pull apart nor to explain. It is to attain vision. But in order to see, we must first participate, and it is a hard apprenticeship.

Antoine de Saint-Exupéry, Flight to Arras (Pilote de guerre) 1942

Acknowledgements

List of abbreviations

AGC	Automatic Gain Control
CD144	*Charles Darwin* Cruise 144
CDP	Common Depth Point
CMP	Common Mid-Point
CTB	Cretaceous- Tertiary Boundary
D-GPS	Differential Global Positioning System
HVSCB	High velocity sub-crustal body
IGRF	International Geomagnetic Reference Field
LG	Levelling Geophone
LIP	Large Igneous Province
LMO	Linear Move-Out
MBS	Marine Broadband Seismocorder
MCS	Multichannel Seismic Reflection
MLS	Marine Longtime Seismocorder
Moho	Mohorovičić discontinuity
NERC	Natural Environment Research Council
NGDC	National Geophysical Data Centre
NMO	Normal Move-Out
OBS/H	Ocean Bottom Seismometer/ Hydrophone
OCB	Ocean-Continent boundary
PSDM	Pre-Stack Depth Migration
RMS	Root-Mean-Square
SDR	Seaward-dipping reflector
SEGY	Society of Exploration Geophysicists digital recording standard Y
SVP	Sound-Velocity Profile
TAR	True Amplitude Recovery
TWT	Two-Way Time
V_P	P-wave velocity
XBT	Expendable Bathy-Thermograph

Contents

List of Figures

List of Tables

1 ‖ Introduction

The surface of the earth is made up of rigid lithospheric plates, which consist of an upper layer called the crust and a lower layer of lithospheric mantle. The crust can be up to 60 km thick in old cratons. The crust is divided into a brittle, strong upper layer and a ductile, weak lower layer. Similarly, the lithospheric mantle consists of a strong upper layer and an underlying warm layer that deforms plastically (Fig. 1.1). The plates are in motion, and it is this motion that generates much of the Earth's volcanism and tectonism. The rigidity of the plates means that most of the volcanism and tectonism occurs at the boundaries of the plates. Plate boundaries can be either divergent, where new oceanic crust forms by the pulling apart of continental plates (e.g., the Mid-Atlantic Ridge); convergent, where colliding material is subducted into the mantle (e.g., the Japan Trench), obducted onto the crust or buckled to form mountain ranges; or transform, where two plates slide past one another (e.g., the San Andreas Fault).

This thesis is concerned with the nature of continental margin formation at the Laxmi Ridge rifted (i.e., divergent) margin. This introductory chapter is intended to summarise the current state of knowledge about the tectonic and magmatic processes that control and result from continental rupture, and the previous research undertaken over the Laxmi Ridge rifted margin.

1.1 Rifted continental margins

Rifted continental margins form when continental crust is placed under extensional stress either due to passive far-field stresses in the tectonic plate (McKenzie, 1978; McKenzie and Bickle, 1988) or due to active uplift from a thermal anomaly at the base of the lithosphere (Bott and Kusznir, 1979; Dewey and Burke, 1975). If the extension is sufficiently rapid or continues for a sufficient period of time, the crust may rupture. Upwelling asthenosphere crosses the mantle solidus and produces melt by adiabatic decompression. This melt freezes in place to accrete new oceanic crust by the coalescence of intrusions progressively emplaced toward the axis of the rifting (Whitmarsh et al., 2001b). This process forms a new ocean basin bounded by a conjugate pair of rifted continental margins.

Based on extensive work in the Northern Atlantic, rifted continental margins have traditionally been classified as 'non-volcanic' or 'volcanic' end members (White, 1992), with volcanic margins formed by rifting over a thermal anomaly (White and McKenzie, 1989). However, this classification does not reflect the range of magmatic styles that

1

$$\sigma_1 - \sigma_3$$
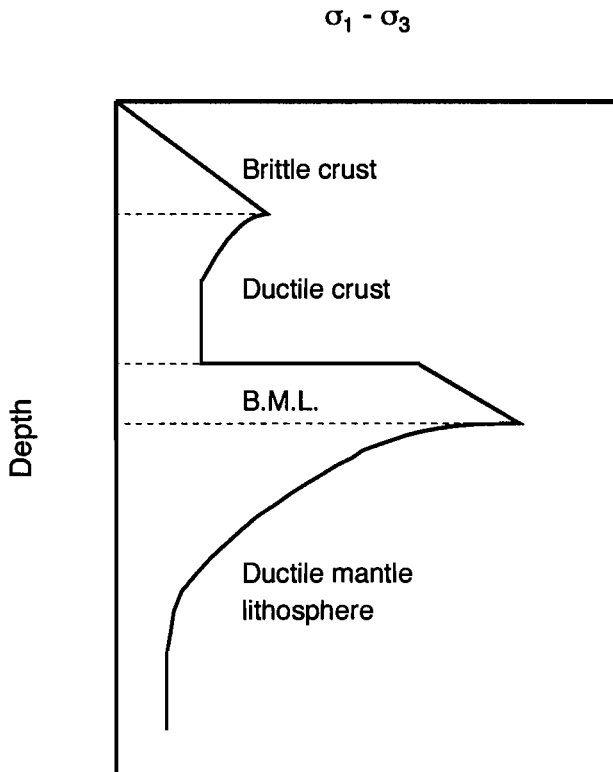
Figure 1.1: Relative yield strength of continental lithosphere: Parts of the lithosphere in brittle regimes will deform by brittle failure if their yield strength is exceeded. This manifests in the upper crust by normal faulting. The ductile regions of the lithosphere deform by plastic flow. Strain less than the yield strength will lead to elastic deformation in both the brittle and ductile regimes. BML is the brittle mantle lithosphere. Variations in strength are due to the geothermal gradient and changes in mineralogy. This strength profile is questioned by several authors, e.g., Jackson (2002) uses accurate earthquake locations to show that the earthquakes, and therefore brittle strength of the lithosphere, originate in the crust, which implies that the mantle is weak. After Molnar (1988).

exist in nature (Mutter, 1993). Both volcanic and non-volcanic margins are observed on North Atlantic margins, with volcanic margins generally occurring at latitudes higher than 50°N. These volcanic margins are interpreted as being associated with the Iceland hotspot.

The observation of 'volcanic' features (seaward dipping reflectors (SDRs) and magmatic underplating of the extended continental crust) on margins that do not have an associated mantle thermal anomaly (e.g., the East Coast USA, Kelemen and Holbrook, 1995), has led some authors to question the validity of a simple division of rifted margins into non-volcanic caused by continental extension and volcanic caused by rifting over a mantle hotspot (Mutter, 1993; Holbrook and Keleman, 1993). An alternative theory invokes small-scale convection caused by abrupt thinning of the lithosphere (Mutter et al., 1988; Keen et al., 1994).

1.1.1 Observations at volcanic margins

A margin is classified as volcanic if arcuate SDRs are observed at the ocean-continent boundary (OCB). These were first identified by Hinz (1981) on several margins, and drilling of the SDR sequence off the Vøring margin (Viereck et al., 1989) revealed sub-aerially extruded basalts with a continental affinity, intercalated with sediments. This volcano-stratigraphy represents an early form of seafloor spreading (Planke and Eldholm, 1994). Hinz (1981) describes wedge-shaped sets of SDRs on the Vøring margin, 20 to 60 km wide and with a maximum thickness of 5 km. Individual reflectors have a divergent morphology.

SDRs have seismic velocities similar to oceanic layer 2 (Minshull, 1993). It has been proposed that they form either by extrusion just prior to breakup, and so lie on extended continental crust (Hinz, 1981), or by a process of sub-aerial spreading (Sellevoll and Mokhtari, 1988; Mutter et al., 1982; Hopper et al., 2003) prior to subsidence and submarine spreading. Barton and White (1997) observe seaward dipping reflectors at Edoras Bank, both on the thinned continental crust and overlying the first-formed oceanic crust. On some margins of the Atlantic and Western Australia, two sets of SDRs are observed parallelling the margin and separated by a basement high. The landward set is termed 'inner SDRs' and the seaward set 'outer SDRs'. The two sets may represent a change from sub-aerial to shallow submarine extrusion (Planke et al., 2000). Inner and outer SDRs are observed on the Southeastern US margin by Oh et al. (1995). Landward sets are generally concave downward, wedge-shaped, internally divergent, 30-40 km wide and up to 10 km thick. The wedges dip at 30° and have P-wave velocities (V_P) of 6.5 km s^{-1}. No basal layer separates the SDR packages from underlying high velocity material at the base of the crust. The seaward sets are 25-30 km wide and dip at 15°.

Volcanic margins often have a body of high velocity ($V_P = 7.2$ km s^{-1} - 7.6 km s^{-1} (Eldholm and Grue, 1994)) material beneath the extended continental lithosphere and first formed oceanic crust. Funk et al. (2001) identify a 15 to 20 km thick wedge of high velocity lower crust beneath the Labrador margin, which has velocities of 7.1 to 7.4 km s^{-1} in an upper layer and 7.6 to 7.8 km s^{-1} in a lower layer. These high velocity bodies are magmatic underplate emplaced at the base of the crust during rifting. Thermal subsidence beneath the Rockall-Faeroe-Shetland region of the North Sea is less than expected for the age of the region. This was interpreted by Clift and Turner (1998) as being due to low density magmatic underplate buoying up the crust.

The first-formed oceanic crust on a volcanic margin can have a thickness up to 3 times greater than that of normal oceanic crust (Holbrook et al., 2001). Initial oceanic crust formed by the Greenland-Iceland Ridge is 30 km thick within 500 km of the hotspot track and 18 km thick between 500 and 1100 km from the hotspot.

1.1.2 Observations at amagmatic margins

Non-volcanic, or 'magma-poor' (Whitmarsh et al., 2001a) margins are characterised by thinning of the continental crust over a region up to 250 km wide by amagmatic extension on a series of rotated fault blocks. These fault blocks have been imaged by reflection seismology (e.g., the Galicia Bank margin, Whitmarsh et al., 1996), and the crust may be as little as 5 km thick (Horsefield et al., 1993). Velocities from wide angle seismic profiles show little or no evidence for the presence of either intrusive or extrusive high velocity magmatic material (White, 1992).

A broad transition zone of anomalous velocity crust may separate the thinned continental crust from oceanic crust (Chian and Louden, 1995). This transition zone is generally characterised by anomalously high velocities at acoustic basement and a low topographic expression (Reid, 1994; Sibuet et al., 1995; Dean et al., 2000; Whitmarsh and Wallace, 2001; Bullock and Minshull, 2005). The transition zone may have magnetic anomalies that cannot be modelled as seafloor spreading anomalies, and a high velocity gradient in the upper part of the anomalous body (Dean et al., 2000). The transition zone is believed to be serpentinised mantle based on the recovery of peridotites off the Iberia margin (Recq et al., 1996; Whitmarsh and Wallace, 2001) and the diagnostic Poisson's ratio of the 120 km wide transition zone at the Goban Spur margin (Bullock and Minshull, 2005). Similar transitional, high velocity regions have been alternatively interpreted as thinned continental crust (e.g., the Galicia Bank margin, Sibuet et al., 1995), and oceanic crust formed by ultra-slow spreading (e.g., the Newfoundland margin, Reid, 1994). Gravity and velocity modelling show that the transition zone on the Newfoundland margin is 50 km wide, and consists of less than 2 km thickness of 6.5 km s^{-1} magmatic crust underlain by 7.2 to 7.6 km s^{-1} material that is interpreted as exhumed serpentinised mantle. The margins of the Labrador Sea also have a transition zone consisting of less than 2 km of low velocity upper crust underlain by a 6.4 to 7.7 km s^{-1} anomalous layer that may be serpentinite. The transition zone on the Labrador Sea margins is asymmetric: 140 km wide on the Labrador margin and 70 km on the Greenland margin. Initial seafloor spreading in the Labrador Sea was very slow, around 1 mm yr^{-1}, and the crust was very thin, but normal oceanic crustal thicknesses are soon reached (Chian and Louden, 1995). Serpentinite on the Goban Spur margin underlies sediments, showing that the mantle was completely unroofed and no new magmatic crust was generated (Bullock and Minshull, 2005).

Tilted fault blocks on the Galicia margin are underlain by a low-angle reflector (the S reflector), which is not cross-cut by those faults (Hoffman and Reston, 1992). Hoffman and Reston (1992) interpret this reflector as a zone of major detachment in the crust that may occur at the boundary between brittle and ductile crust. However, at the

Biscay margin the S reflector is observed at different levels in the crust; where the crust is thin it coincides with the Moho (Bullock, 2004). Low-angle reflectors (Section 1.2.1) are a common feature of non-volcanic rifted margins (Le Pichon and Barbier, 1987; Chian et al., 1995; Reston, 1996). There is some debate as to whether normal faults can be active below 30° (Jackson, 1987; Rietbrock et al., 1996; Abers, 2001). Jackson (1987) shows that it is geometrically unlikely that faults can be active at angles less than 30°, but Rietbrock et al. (1996) present fault plane solutions for 8 microearthquakes in Corinth that show active normal faulting at dips of 12 to 20°.

1.2 The nature of the continental crust and its response to extension

Continental crust is highly variable in its thickness and velocity structure because it may have survived repeated tectonic events and had its structure modified by intrusions, faulting and erosion. A global average thickness of 39.2 km is observed (Christensen and Mooney, 1995), and velocities at the base of the crust can be 6.7 km s^{-1} or greater, depending on whether or not magmatic material has been added.

1.2.1 Factors that affect continental breakup

Strain regime

When continental lithosphere is placed under strain it can either rupture by brittle failure or deform in an elastic or plastic manner. The nature of the lithosphere's response to strain is controlled by temperature and composition, which determine the yield strength of the rocks; if the strain exceeds the yield strength brittle failure or permanent ductile deformation occurs, depending on the temperature and composition of the rock. If the yield strength exceeds the strain applied, the lithosphere will deform elastically (Fig. 1.1).

Conjugate margins are hypothesised to break apart under pure shear, simple shear or a combination of these two end-members (Fig. 1.2). Homogeneous pure shear stretching of the lithosphere would lead to symmetrical margins, with oceanward-dipping normal fault blocks in the brittle upper crust, and ductile necking in the weaker lower lithosphere (McKenzie, 1978). The geometry that would be formed by this process is observed in the North Sea, where the post-rift thermal subsidence is symmetrical (White and McKenzie, 1989). The pure shear model predicts homogeneous stretching at all depths within the lithosphere, yet the lithosphere exhibits a depth-dependant rheology due to changes in mineralogy, water content and the thermal regime with depth (Kusznir and Park, 1987; Watts, 2001; Davis and Kusznir, 2003, Fig. 1.1).

If breakup occurs by simple shear, the lithosphere is cut by a low angle fault (Wernicke, 1981), leading to asymmetric margins. Perez-Gussinye and Reston (2001) suggest lithospheric scale rifting by simple shear could be initiated by stretching old, cold orogenic and cratonic crust: strain hardening would then cause the whole crust to deform by brittle failure, leading to exhumation and serpentinisation of the mantle. The S reflector observed at the Biscay and Galicia Bank margins (Section 1.1.2, Le Pichon and Barbier, 1987; Reston, 1996) was interpreted as a detachment fault by Reston (1996) because listric normal faults are observed to sole out onto it. This low angle detachment may provide a mechanism for mantle unroofing at amagmatic margins. However, this simple shear mechanism predicts detachment along a very low angle fault, and whether detachment faults can be seismically active at less than 30° is a matter of debate (Jackson, 1987; Rietbrock et al., 1996; Abers, 2001). McNeill et al. (2005) found that, despite the presence of a low angle reflector, all the extension in the Gulf of Corinth is accommodated by continental normal faulting. Such features often mark the base of brittle deformation in the upper crust. Simple shear predicts significantly less magmatism on breakup than pure shear, which does not match the observations of magmatism at rifted margins (Latin and White, 1990).

Composite shearing of the lithosphere (e.g., Lister et al., 1986; Lister and Davis, 1989) allows the upper crust to be extended asymmetrically by simple shear, and the ductile lithosphere to deform by pure shear within shear zones. This mechanism avoids the kinematic problem of having a low angle fault cut the whole lithosphere. Rifting between the conjugate Galicia Bank and Flemish Cap margins was asymmetric (Hopper et al., 2004), but there is no seismic evidence for the melt distribution between the upper and lower plates being significantly different, which would be expected if the crust was rifted by bulk simple shear. Asymmetric (i.e., simple shear), low angle faults are restricted to the upper crust at Galicia Bank and there is no evidence of lithosphere-scale faulting, implying a composite shear regime (Whitmarsh et al., 1996).

The exhumation of mantle peridotites observed at magma-poor margins was modelled by Brun and Beslier (1996) as being due to heterogeneous stretching of the lithosphere. Strength variations in the lithosphere cause asymmetrical shear zones to develop within the weak lower crust and mantle. The differential stretching that occurs can allow mantle rocks to rise to the surface. The modelling technique used by Brun and Beslier (1996) does not allow the mechanical properties of the lithosphere to evolve as it is strained, but strain-dependant modification of the rheology of the lithosphere could be an important control on rifted margin geometry (Bassi, 1995). This is discussed in the following section.
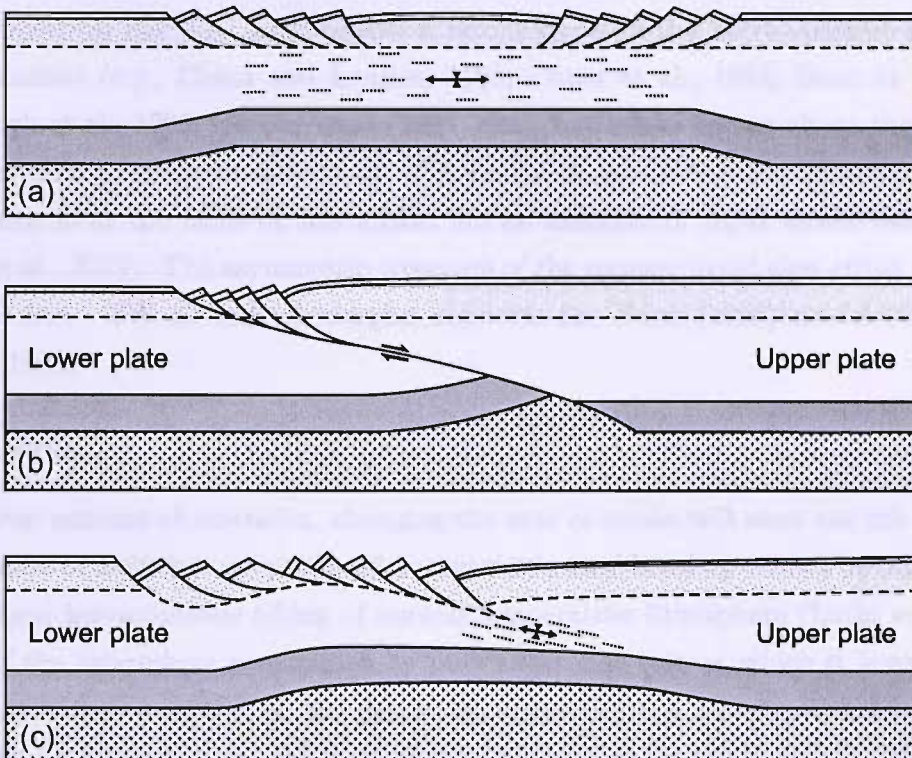
Figure 1.2: Modes of continental extension: *a)* Pure shear: homogeneous extension at all depths is compensated for by brittle faulting in the upper crust and ductile flow beneath the brittle-ductile boundary (dashed line), which may coincide with the 400°C isotherm (Watts, 2001). Continental margins and subsidence are both symmetrical. *b)* Simple shear: lithospheric-scale simple shear accommodated by a low angle fault that cuts the whole lithosphere. Subsidence and margins would be asymmetric. *c)* Composite shear: Simple shear occurs in the brittle upper crust with pure shear in the ductile lithosphere. This model is preferred to the simple shear model as it does not require a lithospheric scale low angle fault. From Dean (1999) after Lister et al. (1986) and Lister and Davis (1989).

Strain rate

As the crust is strained, changes in the temperature profile may modify its rheology, for example cooling at low extension rates may strengthen the lithosphere and limit rifting (England, 1983). Numerical modelling by Bassi (1995) suggests that if the continental crust is strained slowly, the lithosphere may undergo a modification of its rheology in the form of strain hardening. If this occurs, the locus of maximum stress will migrate from the axis of symmetry of the rift to a weaker, necked region at the edge of the strained crust. If breakup occurs in a necked region, the result will be asymmetric margins. This asymmetric shear will only arise if the lithosphere is weak and viscous, i.e., thin (90 km) and warm (675°C - 770°C at the Moho.), otherwise the strain hardening will result in strengthening that prevents strain migration. If the lithosphere is strained quickly, then strain hardening does not occur and breakup takes place at the axis of symmetry to

give symmetrical margins. Low extension rate margins in the north Atlantic have been widely studied (e.g., Chian and Louden, 1995; Chian et al., 1995; Dean et al., 2000; Whitmarsh et al., 1996; Hopper et al., 2004, etc.), but less is known about the effects of rapidly straining the continental crust. The Laxmi Ridge - Seychelles Plateau conjugate pair, which form the focus of this thesis, are an example of rapid strain rate margins (Royer et al., 2002). The asymmetric structure of the reconstructed slow-rifted conjugate Labrador Sea - SW Greenland margins supports the Bassi (1995) model (Chian and Louden, 1995).

Rift duration

For a given amount of extension, changing the rate of strain will alter the rift duration. The volumes of melt that are produced during continental breakup cannot be explained by simple shear instantaneous rifting of normal temperature lithosphere (Latin and White, 1990). If the lithosphere is extended by pure shear, the rate at which it is extended is potentially a major control on the degree of magmatism: A rift duration of 15 Myr is sufficient to reduce melt generation to zero by conductive cooling if the mantle potential temperature is not anomalous. This mechanism could explain the suppression of melting and the exhumation of mantle material at amagmatic margins (Bown and White, 1995), and matches observations of melt volumes and rift durations at the Iberia margin (Minshull et al., 2001). Harry and Bowling (1999) model the effect of strain rate on strain localisation in the mantle as an alternative to a conductive cooling mechanism. If the crust is homogeneous and the strain rate is greater than 15mm Myr^{-1}, melting should be inhibited until 2 Ma prior to breakup, the point at which strain in the mantle is sufficiently localised to cause melting. However, this model does not match observations at the Iberia margin (Minshull et al., 2001).

Rift geometry

The geometry of the rifting crust may have an influence on mantle upwelling and therefore melt volumes generated. If the transition between continent and oceanic crust occurs in a narrow zone, then the cold lithosphere beneath the continental margin is adjacent to the hot, upwelling mantle beneath the incipient rift. This lateral temperature gradient can set up a convection cell, which would bring more deep, hot, mantle material to shallow depths than passive upwelling alone, and therefore generate more melt. Margins with a narrow transition zone should tend to exhibit more volcanism than those with a wide transition zone (Mutter et al., 1988). However, the width of the transition zone of non-volcanic rifted margins in the northern Atlantic varies from 50 km to greater than 120 km (Dean, 1999). The relative thickness of the brittle crust and ductile lithosphere may influence the

width of the rifted zone, as it controls the depth to which brittle deformation can occur. If the crust is relatively thin, narrow margins can form, with wider margins forming where the crust is thick (Hopper and Buck, 1996). Ghods (2002) argued that modelling the effects of small scale convection with a more realistic melting model and viscosity laws than those used by Mutter et al. (1988) does not produce sufficient magmatism to explain the formation of volcanic passive margins.

Pre-existing tectonic fabrics

Rifting of old cratonic crust can follow pre-existing weaknesses from earlier phases of rifting. This occurs at the western Indian continental margin, where continental breakup parallels the Precambrian Dharwar structural trend (Kolla and Coumes, 1990).

Mantle potential temperature

Rifting above hotter than normal mantle is expressed as excessive magmatism during breakup (White and McKenzie, 1989) and thick first-formed oceanic crust, e.g., at the Iceland margin (Dewey and Burke, 1975; Bott and Kusznir, 1979). Anomalously hot mantle is also inferred by negative velocity anomalies imaged by tomographic methods, e.g., beneath the Korean margin (Kim et al., 2003). Holbrook et al. (2001) attribute the volcanic character of the Southeast Greenland margin to a combination of a thermal anomaly of 100°C greater than normal mantle potential temperatures, and a process of active upwelling bringing hot asthenospheric mantle underneath the rift faster than extension-driven passive upwelling alone.

Melt generation occurs in the asthenospheric mantle by partial melting, with some mineral phases preferentially going into the melt depending on the temperature. High asthenospheric temperatures increase the melt fraction, which generates a magnesium-rich melt. This can lead to the accretion of magmatic material beneath the crust (underplate) with high P-wave velocities (Staples et al., 1997). These underplates are diagnostic of volcanic margins (Section 1.1.1).

Thermal anomalies influence rifting by weakening the lithosphere and adding tensional stress by uplift. Thermal and mechanical thinning of the lithosphere allows replacement of the lithosphere with lower density asthenosphere, which leads to progressive doming of the crust (Wilson, 1989, 1993; Bott, 1992). The presence of a thermal anomaly alone is not likely to cause rifting, since intra-ocean hotspots such as Hawaii are not associated with major extensional faulting (Burke and Whiteman, 1973), so a combination of thermal and tectonic factors must be considered responsible for the nature of rift-hotspot interactions.

Reston and Phipps Morgan (2004) hypothesise that the normal mantle potential temperature beneath continental crust is sufficiently low that significant melting will only

occur during rifting if a thermal anomaly is present beneath the rift, such as by bringing hot mantle material from greater depths.

1.3 The nature and provenance of oceanic crust

Oceanic crust is formed by adiabatic upwelling and subsequent decompression melting in response to extension of the lithosphere. The consistency in mode of formation means that the structure of oceanic crust is predictable if passive decompression melting is the major control. Seismic observations and geochemical predictions both support an average crustal thickness of around 6 km (White et al., 1992). The crust consists broadly of 2 layers: layer 2 is a 2-3 km upper layer underlain by a 3-5 km layer 3 (Raitt, 1963). A high velocity gradient (0.5-1.0 s^{-1}) is observed in layer 2, and a low velocity gradient (0.1-0.2 s^{-1}) is observed in layer 3 (Spudditch and Orcutt, 1980). The boundary between layer 2 and layer 3 occurs at around 6.5 km s^{-1} and the boundary between layer 3 and the mantle is a step up to around 8 km s^{-1} (Mutter and Mutter, 1993). Velocities in the oceanic mantle may be low close to the ridge axis; velocities of 7.5 km s^{-1} are observed close the the East Pacific Rise, increasing to 8.02 km s^{-1} after a few million years (Bibee and Shor, 1976; Grevemeyer et al., 1998). Layers 2 and 3 can be subdivided further: layer 2A is the low velocity upper portion of layer 2 that does not generate seismic first-arrivals because it is a thin layer with a velocity similar to that of the overlying sediments (Houtz and Ewing, 1976; Carlson, 1998). The seismic velocity of layer 2A increases rapidly in the first 10 Myr after formation, and this is interpreted as being due to hydrothermal infilling of the porosity (Grevemeyer and Weigel, 1996).

The nature of the layer 2/3 boundary has been attributed to both the mode of formation and varying porosity with depth. The formation model describes layer 2 as basalt dykes and layer 3 as intrusive gabbros (Cann, 1974). This model is supported by observations on the East Pacific Rise: on axis, the top of the magma chamber is at the same depth as the off-axis layer 2/3 boundary (Vera et al., 1990). However, the layer 2/3 boundary has also been interpreted as the limit of dyke brecciation in the Bay of Islands ophiolite (Salisbury and Christensen, 1978, Fig. 1.3), which implies that porosity is the major control on the velocity change. Refraction experiments and downhole logging at the Costa Rica Rift place the layer 2/3 boundary within the dyke section of the oceanic crust (Detrick et al., 1994). Wilson et al. (2006) directly sampled gabbros within seismic layer 2 by drilling 1.2 km into super-fast spreading Pacific crust. Direct sampling by drilling (Wilson et al., 2006) is the most reliable method of determining lithology, so it is fair to assume that the layer 2/3 boundary is a mechanical boundary rather than a lithological one. However, the fast-spreading Pacific crust may not be representative of other types of oceanic crust.
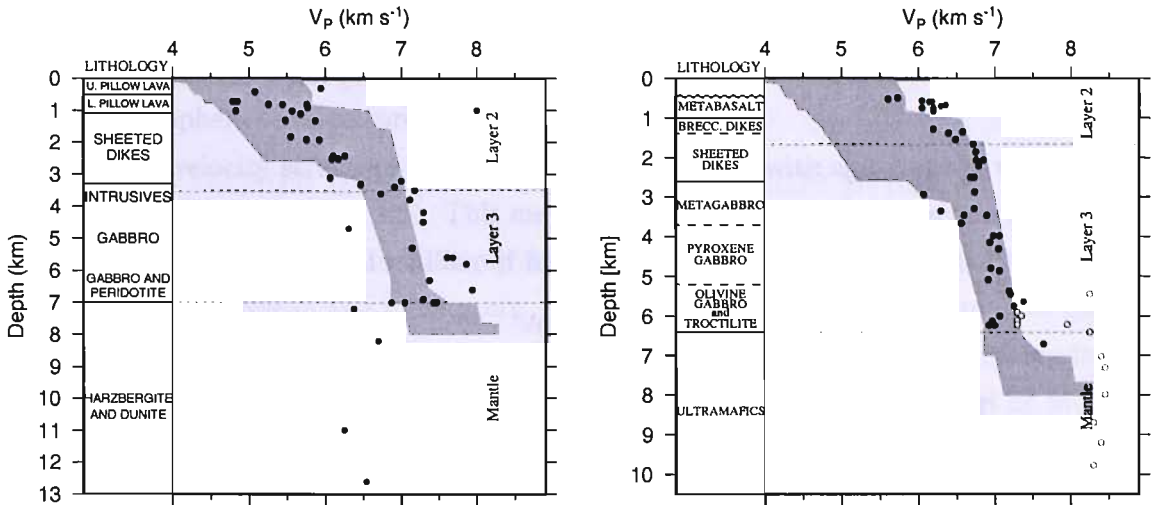
Figure 1.3: Oceanic velocity structure from ophiolites: *Left:* Interpreted velocity-depth profile through the Oman ophiolite. The range of observed velocities is much wider than those determined seismically for in-situ crust (shaded area; White, 1992), and mantle velocities are very low. After Christensen and Smewing (1981). *Right:* Interpreted velocity-depth profile through the Bay of Islands Ophiolite, Newfoundland; filled circles are direct measurements, open circles are estimated from the composition. The layer 2/3 boundary occurs within the dykes so is interpreted to be a porosity horizon rather than a lithological change. The profile shows a reasonable match for the velocity and velocity gradient of seismically determined in-situ crust (shaded area; White (1992)), especially in layer 3. After Salisbury and Christensen (1978). Redrawn from Bullock (2004).

The crust-mantle interface is the Mohorovičić discontinuity (Moho). The Moho is defined seismically as a jump in P-wave velocity from up to 7.8 km s^{-1} at the base of the crust to 8.0 - 8.4 km s^{-1} in the lithospheric mantle. Ophiolite studies suggest that this velocity jump is due to a pressure and temperature induced metamorphic phase change from granulite facies in the crust to eclogite in the mantle (Le Pichon et al., 1997).

Spreading rate can influence the thickness of the accreting oceanic crust. Slow spreading rates allow conductive cooling of the upwelling asthenosphere, which reduces the amount of melting that can take place (Reid and Jackson, 1981). The Southwest Indian Ridge is spreading at 15 mm yr^{-1} and accretes crust 4 km thick (Muller et al., 2000). Initial oceanic crust adjacent to a rifted margin can also be affected by conductive heat loss into the continental crust (Bown and White, 1995).

If upwelling material crosses the mantle solidus at a greater depth than normal (i.e., if there is a positive mantle thermal anomaly), melting starts at that depth. Alternatively, the solidus may be deflected shallower by hydration of the mantle, allowing melting to begin at shallower depths. In both cases, excess melting will lead to thicker than average oceanic crust. Oceanic crust formed at the present -day location of the Iceland hotspot is up to 40 km thick (Bjarnason et al., 1993; Staples et al., 1997; Darbyshire et al., 1998).

Velocity gradients in the crust are lower than normal and the velocities at the base of layer 3 are high. The high velocities could be due to high magnesium melt generated by high asthenosphere temperatures (Staples et al., 1997).

The bulk velocity structure of oceanic crust varies little with age, but the velocities in layer 2 tend to increase (Fig. 1.4). This may be a consequence of the reduction in porosity of the crust by hydrothermal infilling of fractures (Grevemeyer and Weigel, 1996).
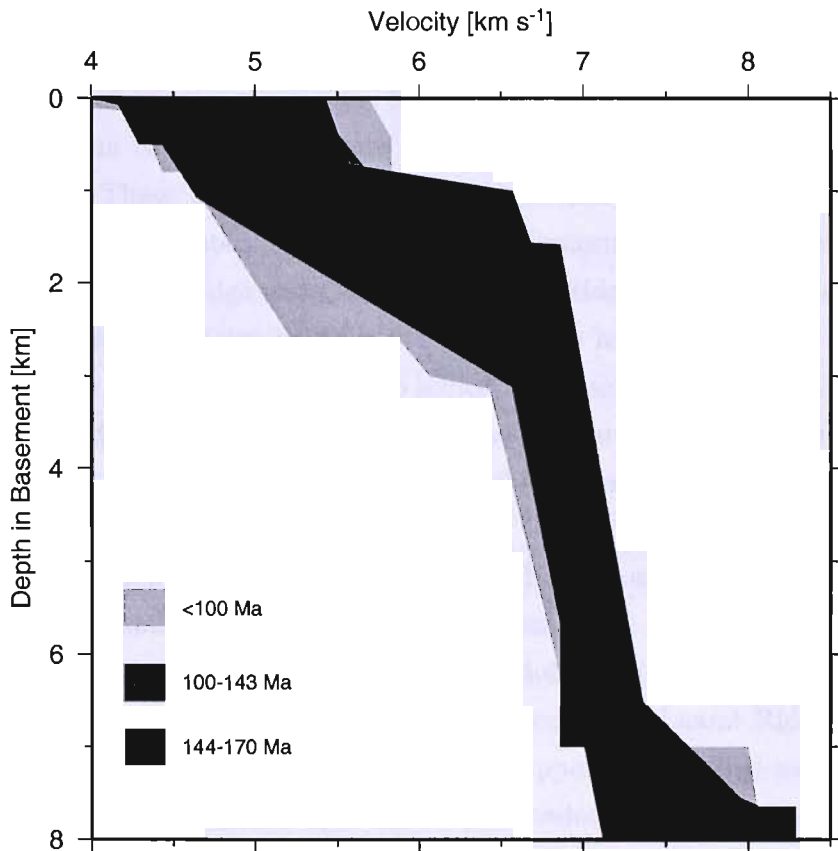
Figure 1.4: Variation of oceanic crustal velocities: Seismically determined bounds of normal Atlantic oceanic crust P-wave velocities are grouped by age. The velocities in layer 2 tend to increase due to a loss of porosity. After White (1992).

1.4 Tectonics of the NW Indian Ocean

The northwest Indian Ocean has a long and complicated history of continental extension, rift-hotspot interaction and continental collision. A map of the major tectonic features in the Indian Ocean is shown in Figure 1.5. The provenance of many of these features is still debated, and this debate will be outlined in this section. A simplified tectonic history of the region is given in Figure 1.6.

Laxmi Ridge was originally identified by Naini and Talwani (1977) when they noticed that a number of isolated basement highs between 15°N and 18°N off the west coast

of India were actually a continuous ridge structure. Laxmi Ridge is a basement high approximately 650 km off the west coast of India. It extends between 14°N and 19°N, and is around 100 km at its widest point. It trends NW-SE, approximately parallel with the shelf break of the continent, and bends east-west at its northern-most section (Miles and Roest, 1993). It has a negative free air gravity anomaly of 25 mgal, and a negative magnetic anomaly of the order of 100 nT. Previous seismic experiments over the northern section of Laxmi Ridge are shown in Figure 1.7.

Naini and Talwani (1982) determined the crustal structure beneath the NW Indian ocean with a seismic experiment using 67 sonobuoy refraction profiles. The seafloor to the west of India can be divided into the Eastern (Laxmi) Basin and the Western (Arabian) Basin. These basins are segregated by Laxmi Ridge to the north and the Chagos-Laccadive ridge system to the south. The Eastern Basin has a similar velocity structure to both Laxmi Ridge and Chagos-Laccadive Ridge (Naini and Talwani, 1982), and has linear magnetic anomalies that may be due to intrusions (Miles et al., 1998). The Western Basin has a velocity structure indicative of normal oceanic crust (Naini and Talwani, 1982) and well developed seafloor spreading marine magnetic anomalies from Chron 27 onwards (Miles et al., 1998). Some authors (Naini and Talwani, 1982; Miles and Roest, 1993; Chaubey et al., 2002a) interpret Chron 28 just off Laxmi Ridge, but Chron 28 is not seen on the conjugate Seychelles Bank margin so Miles et al. (1998) interpret the same anomaly as a magnetised basement spur. Laxmi Ridge was found to have a crustal thickness greater than 21 km; the Moho was not seen by the refraction experiments of Naini and Talwani (1982). Their models for Laxmi Ridge had a three layer velocity structure consisting of a 2.4 km thick upper layer with P-wave velocities of 5.3 km s^{-1}, a 4.5 km thick middle layer with P-wave velocities of 6.2 km s^{-1} and a lower layer with P-wave velocities of 7.2 km s^{-1}. The upper layer had a similar velocity structure to oceanic layer 2 and the Deccan basalts (Dube et al., 1973), so it was speculated that it may be an offshore continuation of the Deccan Traps. The average sediment thickness over Laxmi Ridge is 500m, and sediment velocities vary from 1.7 km s^{-1} to 3.9 km s^{-1}. The negative free-air gravity anomaly over Laxmi Ridge is unusual because aseismic ridges normally have positive free-air gravity anomalies due to isostatic compensation (e.g., the Shatsky Ridge, Den, 1969). The free-air gravity profile is more like those seen over the Rockall microcontinent (Scrutton, 1971).
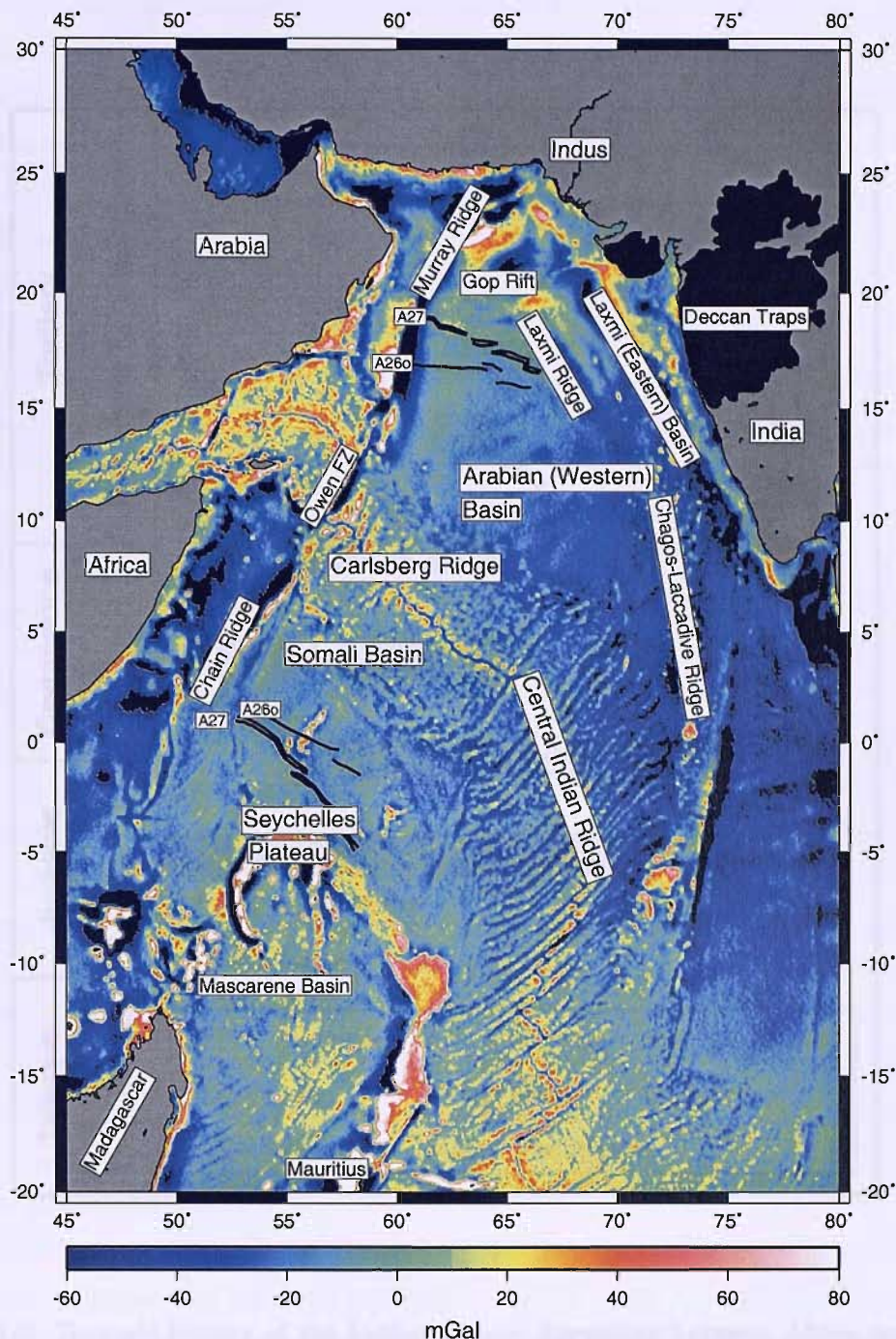
Figure 1.5: Tectonic map of the NW Indian Ocean: The Seychelles were separated from Madagascar by spreading in the Mascarene Basin prior to spreading between Laxmi Ridge and the Seychelles in the Arabian Basin. Magnetic anomaly picks from Miles et al. (1998) are shown seaward of the Seychelles and Laxmi Ridge. The Deccan Traps, a large igneous province (LIP) on continental India extruded around the Cretaceous-Tertiary boundary, is indicated in black. Background field is free-air gravity (Sandwell and Smith, 1997), which highlights features such as the gravity low over Laxmi Ridge and the offset of the mid-ocean ridges by fracture zones. Carlsberg Ridge and the Central Indian Ridge mark the boundary between the Somali (African) and Indian Plates.
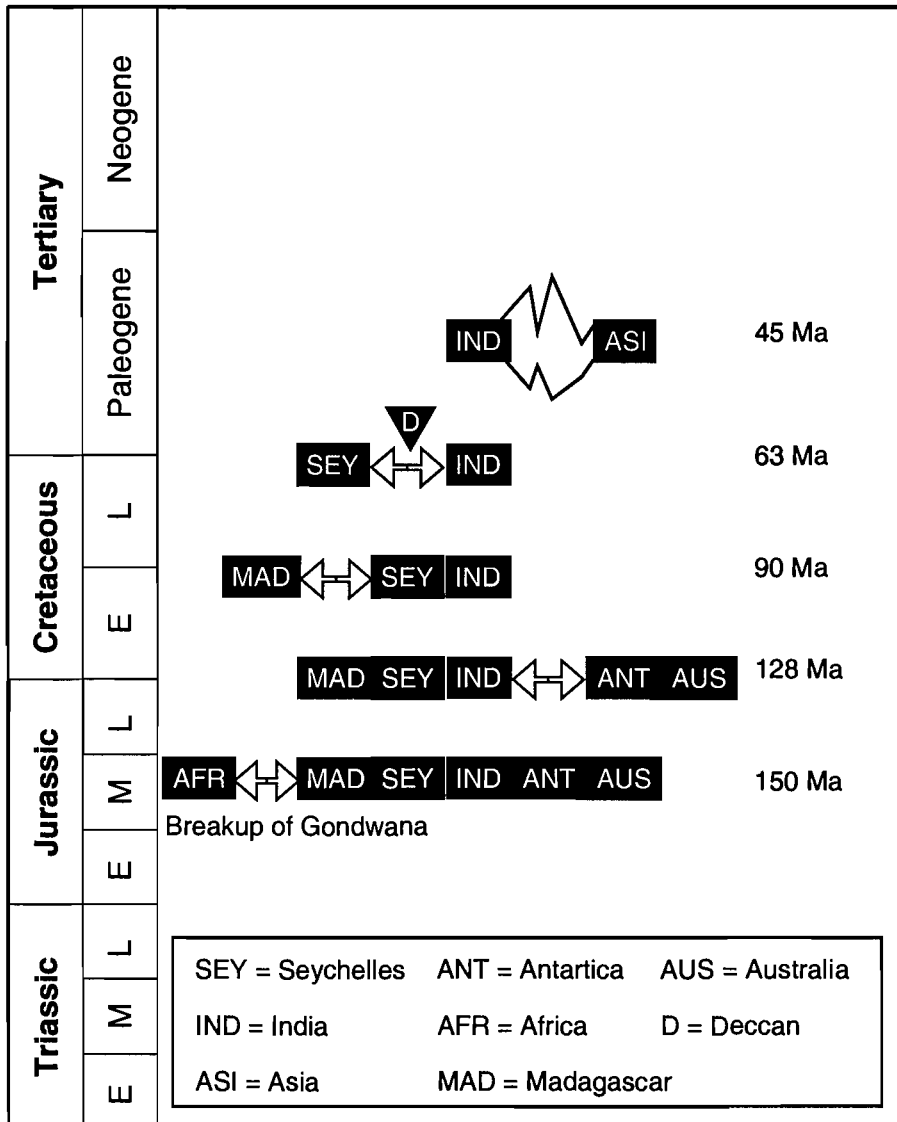
Figure 1.6: Tectonic history of the Indian Ocean: Spreading between Africa and Madagascar initiates the breakup of Gondwana in the middle Jurassic. Antarctic and Australia break off from India around 128 Ma. Spreading in the Mascarene Basin separates Madagascar and the Seychelles 90 Ma ago. Around the Cretaceous-Tertiary boundary, the spreading centre in the Indian Ocean jumps to the Arabian Basin, rifting India from the Seychelles. This occurs at approximately the same time as the extrusion of the Deccan Traps on continental India. Northward migration of the Indian and Somali plates cause India to collide with the Eurasian Plate, causing orogenesis and the slowing of accretion on the Carlsberg and Central Indian Ridges. Redrawn from Gombos et al. (1995); based on Norton and Sclater (1979).

Laxmi Ridge was interpreted as a continental sliver isolated by seafloor spreading based on an oceanic interpretation of the magnetic anomalies in the Eastern Basin (Bhattacharya et al., 1994). This is despite the 16 km thickness of crust beneath the Eastern Basin, and the velocities at the base of the crust reaching 7.19 km s^{-1} (Naini and Talwani, 1982), which are unusually high for normal oceanic crust (White, 1992). Spreading in the Eastern Basin would have predated the separation of Laxmi Ridge and the Seychelles (Bhattacharya et al., 1994). Bernard and Munschy (2000) predict synchronous opening in the Eastern Basin and extinction in the Mascarene Basin from plate reconstructions. Bhattacharya et al. (1994) suggest two possible time-frames for spreading in the Eastern Basin to match the observed magnetic anomalies. The earliest is spreading between Chrons 31 and 32 and requires spreading rates to vary between 2.6 and 40.3 mm yr^{-1}. The second involves spreading between Chrons 33 and 34 with rates varying between 4.0 and 9.0 mm yr^{-1}. Talwani and Reif (1998) support a Chron 33-34 phase of opening in the Eastern Basin, which makes the opening predate the Deccan hotspot (Section 1.4.1). Despite this, they attribute high velocities at the base of the crust beneath Laxmi Ridge to magmatic underplate, which would require some kind of thermal anomaly in the mantle. This problem could be solved by assuming a Chron 31-32 age for spreading in the Eastern Basin, which would require a highly variable spreading rate. More recent interpretation of the disputed magnetic anomalies showed that most of them can be tied to volcanic features observed on normal incidence reflection profiles (Krishna et al., 2006). The Eastern Basin is then interpreted as stretched, transitional crust (Miles and Roest, 1993; Chaubey et al., 2002b; Mishra et al., 2004; Krishna et al., 2006), attributing the magnetic anomalies to intrusions or volcanic basement features. The high velocities at the base of Laxmi Ridge are interpreted by Miles and Roest (1993) as magmatic underplate related to Deccan volcanism rather than extension. Gravity modelling indicates that underplate may also extend beneath the Eastern Basin (Mishra et al., 2004) and continental India (Negi et al., 1989).

Some authors interpret Laxmi Ridge as anomalously thick oceanic crust, thickened either by a compressional regime (Pandey et al., 1995), or by voluminous melt generated by the influence of the Deccan hotspot (Singh, 1999). Pandey et al. (1995) locate the OCB landward of both Laxmi Ridge and the Eastern Basin based on gravity modelling, explaining the thickened crust beneath Laxmi Ridge as being due to oceanic crust being squeezed between uplift from the Deccan hotspot and extension from the Carlsberg Ridge. Pandey et al. (1995) also attributes the Deccan Traps to a large bolide impact at the Cretaceous-Tertiary boundary (CTB). This interpretation seems extremely unlikely since the iridium layer associated with ejecta from the CTB bolide impact overlies three Deccan lava flows (Bhandari et al., 1995).

The Chagos-Laccadive Ridge has been interpreted as marking the OCB off western

India (Narain et al., 1968) and as a hotspot track linking the thermal anomaly responsible for the Deccan Traps and the thermal anomaly beneath Réunion (Francis and Shor, 1966; Whitmarsh, 1974). The sedimentation history over the Chagos-Laccadive Ridge suggests it was once closer to the India landmass than it is today (Whitmarsh, 1974). Kolla and Coumes (1990) interpret the northern part of the ridge that parallels the India continent as a continental sliver separated from India by rifted, transitional crust. A continental origin is reasonable as the Laccadives are 200-400 km off calculated plume tracks (White and McKenzie, 1989; Müller et al., 1993) and therefore unlikely to have been formed by plume related magmatism.

Laxmi Ridge, parts of the Chagos-Laccadive Ridge, Gop Rift and the Eastern Basin all parallel the Indian coast. The Precambrian Dharwar structural grain of continental India is also in this orientation, indicating that many of the structural features along the continental margin could be due to reactivation of Precambrian weaknesses in the crust (Kolla and Coumes, 1990). The Dharwar trend is one of three major structural trends cutting the Precambrian Indian shield, which resulted from 2 billion year old orogenesis (Gombos et al., 1995).

Plate reconstructions using magnetic lineations (seafloor spreading anomalies) and conjugate fracture zone crossings (Dyment, 1998; Royer et al., 2002) show that Laxmi Ridge is conjugate to the Seychelles Plateau. The Seychelles Plateau is a granitic micro-continent, separated from Madagascar by Cretaceous spreading in the Mascarene Basin (Gombos et al., 1995; Müller et al., 2001). Laxmi Ridge and the Seychelles Plateau were separated when the active spreading centre in the Mascarene Basin southwest of the Seychelles stepped northwest to the Arabian Basin, initiating spreading on the Carlsberg Ridge some time before Chron 27 (58 Ma) (Müller et al., 2001; Royer et al., 2002). This ridge jump may have been in response to thermal weakening of the lithosphere by the Deccan hotspot (Dyment, 1998). Opening of the Arabian Basin along the Carlsberg Ridge led to progressive extinction of spreading in the Mascarene Basin. This is because the low yield strength of mid-ocean ridges makes it difficult for extension to be accommodated on two ridges simultaneously (Bodine et al., 1981).

The initial rate of spreading on the Carlsberg Ridge was rapid, 118 mm yr^{-1} full spreading rate (Royer et al., 2002, Fig. 1.8), so it can be assumed that the rate of strain that the continental crust was placed under prior to rifting was also rapid. Spreading on Carlsberg Ridge was asymmetric, with more oceanic crust accreted to the Indian plate that the Somali plate: 544 km of oceanic crust has been generated in the East Somali Basin versus 760 km in the Arabian Basin (Miles et al., 1998; Royer et al., 2002). This asymmetry was largely due to variations in the direction of propagation of the Carlsberg Ridge. The ridge propagated to the east between Chrons 26n and 25n, then towards the west between Chrons 24n and 20n (Dyment, 1998; Chaubey et al., 2002a). Between
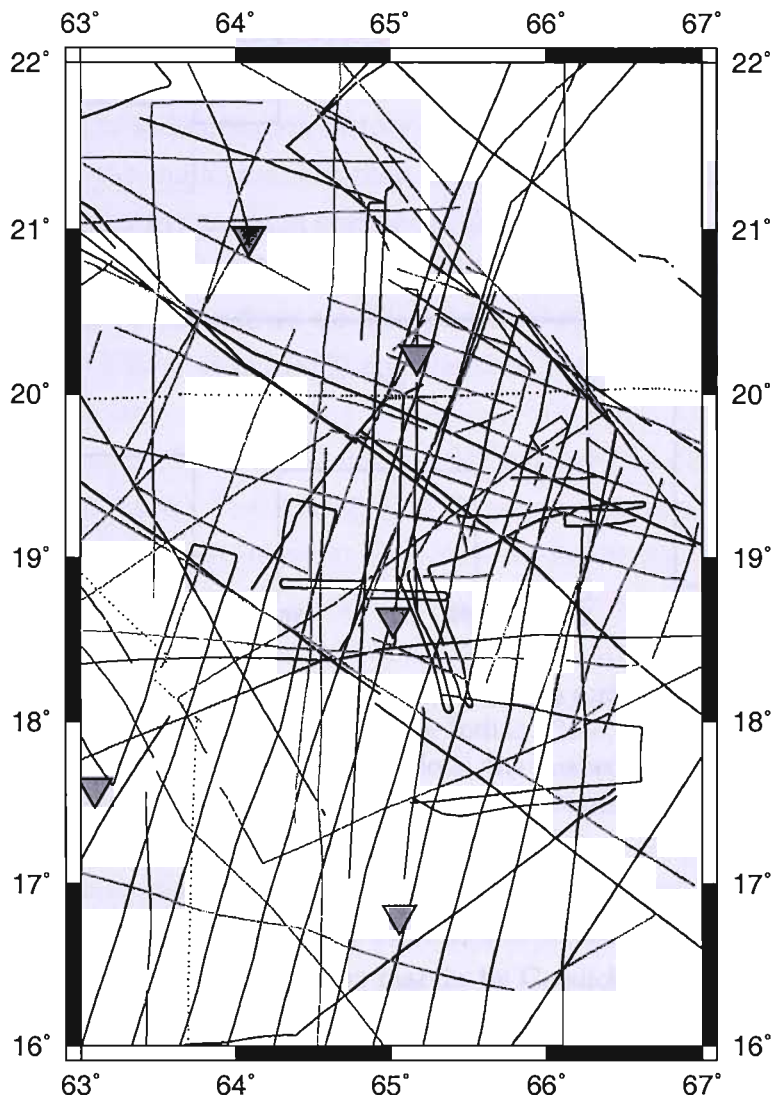
Figure 1.7: Data previously collected in this study area: Black lines indicate historical magnetic soundings; grey lines are single channel reflection seismic data (Miles et al., 1998; Malod et al., 1997); triangles are sonobuoys (Naini and Talwani, 1982).

Chrons 26 and 25, 65% of the crust formed at the Carlsberg Ridge accreted to the Somali Plate and between Chrons 24 and 20, 75% accreted to the Indian Plate. The ridge propagation may have occurred because the Deccan hotspot provided a thermal weakness in the lithosphere, which prevented the migration of the spreading centre away from the hotspot (Dyment, 1998). However, Royer et al. (2002) dispute this theory as it would involve the ridge moving first towards then away from the hotspot.

There is considerable debate in the literature about the nature of thermal anomalies in the mantle and whether mantle hotspots actually exist (e.g., Sheth, 1999). The debate is beyond the scope of this thesis: for the purpose of this work I accept there is a thermal anomaly in the mantle generating the voluminous lavas of the Deccan Traps, but make no assumptions about the cause of that thermal anomaly. Tentative evidence of synchronous
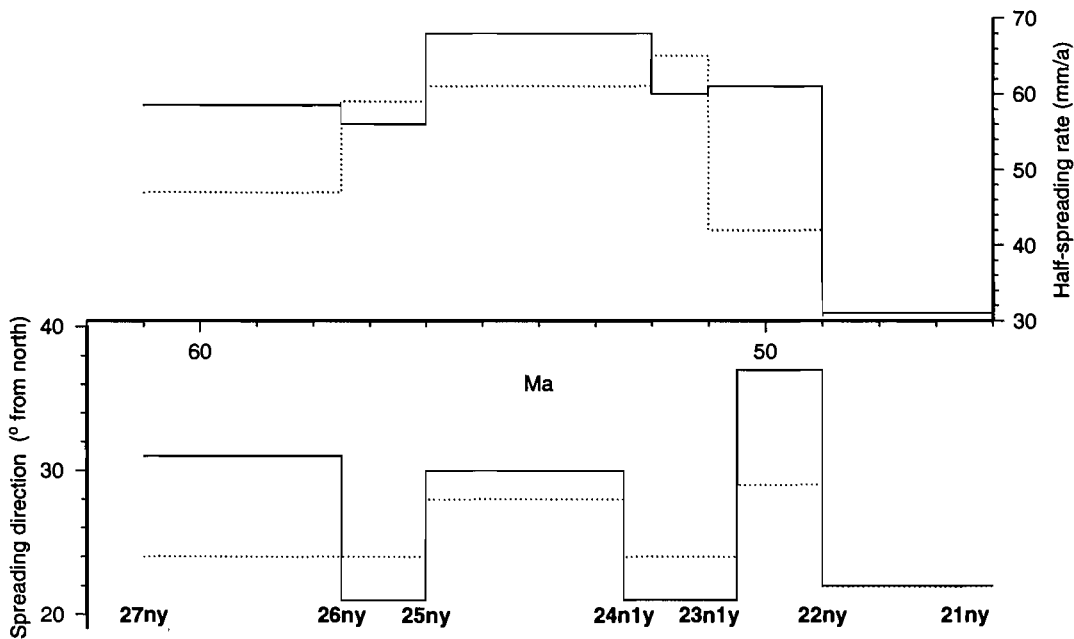
Figure 1.8: Spreading rates and directions between Indian and Somali Plates: *Top:* Half-spreading rate of the Somali Plate relative to the Indian Plate, mm y^{-1}. *Bottom:* Spreading direction in degrees from north. In both plots, the dashed line is a flow line at 56°E and the solid line is a flow line at 65°E. Symmetrical spreading was assumed. Redrawn from Royer et al. (2002).

rifting of Seychelles and Laxmi Ridge and the eruption of the Deccan Traps exists in the identification of SDRs at the Laxmi Ridge margin by Gaedicke et al. (2002a). The SDR package is 40 km long with single reflectors traceable for up to 17 km and dipping to the SE. Such SDRs are generally interpreted as evidence that there was a thermal anomaly in the mantle. However, the rapid extension of the crust could have been sufficient to increase upwelling and generate syn-rift magmatism (Bown and White, 1994). Deccan basalts are found on the Seychelloise island of Praslin (Devey and Stephens, 1991), suggesting that breakup either post-dates, or is synchronous with, the eruption of the Deccan Traps.

Gop Rift is a basement depression with a linear pattern of magnetic reversals and a small axial high (Palitana Ridge), between Laxmi Ridge and the continental shelf of India. The linear magnetic anomalies within Gop Rift may be early (prior to Chron 28) seafloor spreading anomalies (Malod et al., 1997). Gop Rift is laterally adjacent to the Eastern Basin, but appears to be a separate structure as it has a larger positive gravity anomaly than the Eastern Basin and higher amplitude magnetic anomalies. Spreading in Gop Rift may have been synchronous with spreading in the Mascarene Basin (Malod et al., 1997).

Part of the Arabian Basin is overlain by the Indus Fan, which consists of 5×10^6 km^3 of sediment eroded from the Indus suture zone and transported by the Indus River into the Indian Ocean. The proto-Indus Fan is at least 45 Ma old. Some of the oldest sediments

have been sampled over the Owen Ridge where uplift has made them more accessible (Clift et al., 2000). The Indus Fan is important as it places a huge load on the lithosphere, which must be isostatically compensated and may cause flexure of the underlying plate (Whiting et al., 1994).

Accretion on the Carlsberg Ridge was impeded around Chron 22 (49 Ma), when the Indian and Eurasian continental plates entered a compressional regime. This change reduced the spreading rate on the Carlsberg Ridge to 30 mm yr^{-1} half-rate (Royer et al., 2002) and forced a change in the spreading direction (Dyment, 1998; Royer et al., 2002). At Chron 18 (40 Ma), there is a contrast between the 600 km wide swathe of rough, slow-spreading young oceanic crust centred on the Ridge and smooth, fast spreading crust in the Arabian and East Somali Basins (Dyment, 1998). Oceanic crust continues to accrete today in the northwest Indian Ocean on the Carlsberg Ridge at 13 mm yr^{-1} half-rate (Ramana et al., 1993).

1.4.1 Age of the Deccan Traps

The Deccan Traps cover ~5x10^5 km^2 onshore. Depending on the duration of the eruption, eruption rates could have been as high as 8.2 km^3 Myr^{-1} (Coffin and Eldholm, 1993) The age of the Deccan Traps is important as it provides evidence for or against a Deccan thermal influence for the tectonic features in the Indian Ocean. However, there is considerable debate about the age and duration of the Deccan Traps, even amongst geochemists using the same technique. The resolving power of the most commonly used method, ^{40}Ar/^{39}Ar dating, has a resolution of around 0.9 Ma for rocks of this age (Sen et al., 2006). Pande (2002) reviews all available data and produces a histogram that suggests episodic eruptions between 69 and 63 Ma, with the most intense period of activity around 66.9 Ma+/−0.2 Ma (Chron 30). Some of the ages and durations proposed for the Deccan Traps are given in Table 1.1.

1.5 Thesis outline

This thesis uses geophysical data collected during the Natural Environment Research Council (NERC) cruise *Charles Darwin 144* (CD144). The purpose of the experiment was to examine the conjugate Laxmi Ridge- Seychelles Plateau rifted margins (Royer et al., 2002) and draw conclusions about the nature of the tectonic and magmatic processes that have led to the current day architecture of the margins. Sufficient data were collected to allow the construction of wide-angle velocity models of both margins, which would be futher constrained using seismic reflection data and gravity and magnetic anomaly measurements. These models would allow the determination of the crustal architecture

Age	Duration	Method	Author
65.4 Ma	1800 m in < 1 Ma	^{40}Ar/^{39}Ar	Hofmann et al. (2000)
66 Ma	1.4 Myr	^{40}Ar/^{39}Ar	Pande (2004)
	22,800 yr	Phenocryst residency	Sen et al. (2006)
65.5 Ma	< 1 Myr	^{40}Ar/^{39}Ar	Vandamme et al. (1991)
67.2 Ma (+/-6.6Ma)		Palaeomagnetic dating	Vandamme et al. (1991)
64.7 Ma	< 2 Myr	^{40}Ar/^{39}Ar Rajahmundry Traps, East India	Knight et al. (2003)
60.4 Ma	8 Myr	^{40}Ar/^{39}Ar	Sheth et al. (2001)
65.6 Ma	0.5 Ma	^{187}Re/^{187}Os and palaeomagnetism	Allégre et al. (1999)

Table 1.1: Compilation of ages for the Deccan Traps

and velocity structure over both margins. Reconstructing the two margins would allow inferences to be made about the nature of breakup (e.g., from the symmetry of the margins). This thesis is mainly concerned with the Laxmi Ridge margin.

Chapter 2 discusses data collected during the cruise *Charles Darwin 144*, and the acquisition and processing of these data. Refraction and wide-angle reflection data from ocean bottom seismometers (OBS), hydrophones (OBH) and disposable sonobuoys are presented, along with multi-channel seismic (MCS) reflection profiles, bathymetric data (echo-sounding and swath) and potential field measurements (free-air gravity and magnetic anomaly). Data quality and processing techniques are described. The data discussed in Chapter two are modelled or interpreted in later chapters.

Chapter 3 presents a wide-angle velocity model orthogonal to the Laxmi Ridge margin, which was generated from inversion and forward modelling of travel time picks from the OBS/H and sonobouys and refined with seafloor and top basement picks from the MCS profiles. A margin-parallel model, modified from the work of Evain (2004), is shown. The degree of constraint on the velocity models is discussed, and the provenance of key features is debated. The Laxmi Ridge velocity structure is compared to the structure of the conjugate Seychelles Bank margin (Collier, pers. comm.), and the magmatic and tectonic processes that led to the formation and present day morphology of both margins is discussed.

Chapter 4 deals with the modelling and interpretation of gravity and magnetic data. A predicted gravity profile over a density model derived from the wide-angle velocity model is generated. This profile varies from the observed gravity profile over the southern flank of Laxmi Ridge, and reasons for this are explored. Magnetic modelling is used to infer crustal provenance across the margin and, for the magmatic rocks, the age of accretion. A simple plate reconstruction is presented to help explain the history of spreading at the margin. Wider implications, such as the potential influence of the Deccan hotspot, are

discussed.

Chapter 5 presents MCS profiles, including ones coincident with the wide-angle model. The MCS profiles are used to determine the stratigraphy over the margin using information from previous studies. Information from the stratigraphy is used to provide evidence for the timing of tectonic events. Reflections from within the crust are examined to characterise the short wavelength structure of the crust, and therefore provide evidence for changes in crustal provenance. Where it is observed, the reflection Moho gives an estimate of crustal thickness, which is compared to thicknesses predicted by the wide-angle velocity model.

Chapter 6 gives a brief overview of the conclusions and discussions from the previous chapters. As well as summarising the major conclusions of this thesis, this chapter also discusses some of the wider implications of the work and makes suggestions for further research.

2

Data acquisition and processing

Geophysical data presented in this thesis were collected across the Laxmi Ridge and Seychelles Plateau conjugate rifted continental margins in the northwest Indian Ocean, during the NERC cruise CD144 (Collier, 2003, Fig. 2.1), between 13th January and 22nd February 2003. This chapter discusses the data collected over the Laxmi Ridge margin; the Seychelles dataset is generally comparable in terms of type of data collected and its quality.
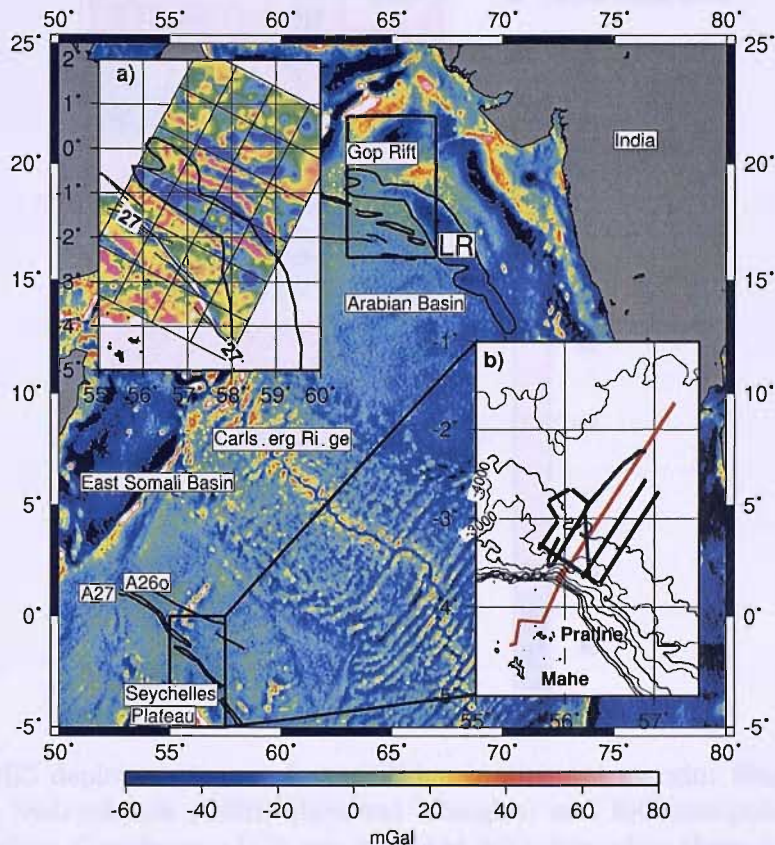
Figure 2.1: The CD144 study areas: Geophysical data were collected over the Laxmi Ridge (northern black box) and Seychelles Bank (southern black box) conjugate margins. Background field is free-air gravity (Smith and Sandwell, 1997). LR is Laxmi Ridge. *Inset (a)*: Laxmi Ridge (heavy line) rotated back to Chron 27 time; the Seychelles Plateau is fixed. The two margins are joined along Chron 27o picks (Miles et al., 1998), which are indicated for Laxmi Ridge and the Seychelles by solid and dotted lines respectively. The background field is free-air gravity. blues are negative anomaly values and reds are positive values. Laxmi Ridge is rotated by closing Carlsberg Ridge using the poles of Royer et al. (2002). *Inset (b)*: The Seychelles MCS (black) and ocean-bottom seismometer (OBS) (red) lines; contours are bathymetry plotted every 500 m. The Laxmi seismic experiment is shown separately in Figures 2.2 and 2.9.
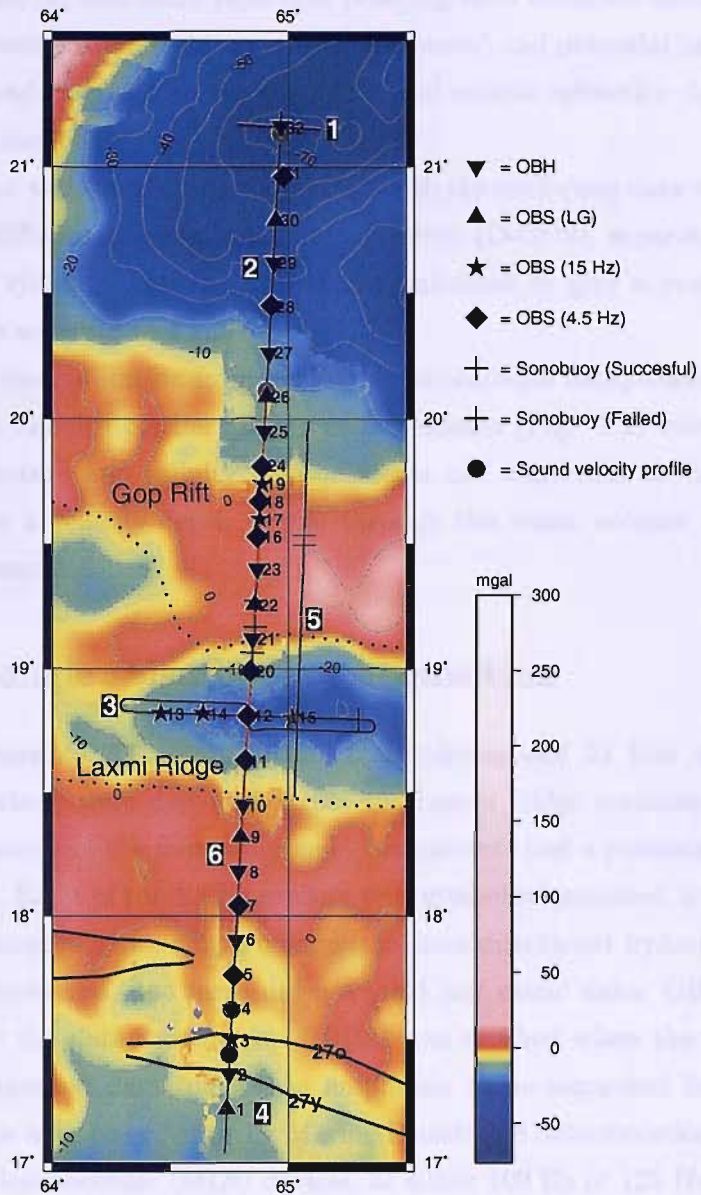
Figure 2.2: OBS deployments over Laxmi Ridge continental margin: Single component ocean-bottom hydrophones (OBH) (inverted triangles) and four component OBS were utilised. Levelling Geophones (LG) are indicated with triangles- these were gimballed-mounted. The indicated frequency value of the OBS refers to the resonant frequency of the receivers. The deployment position of XBTs, sound velocity probe measurements and sonobuoys are also indicated. Figures to the left of the OBS/H are the instrument deployment numbers. Large white numbers are MCS lines; shooting tracks are in black (lines 1-5) and red (line 6). Line 1 is a test line using only the two 1000 cu.in. single guns. Lines 2, 3 and 4 are coincident to the OBS acquisition, and were shot using the OBS array into an overly buoyant streamer. Line 5 and line 6 were shot using a balanced streamer and an airgun array optimised for deep reflection profiling. The background field is combined CD144 and satellite (Smith and Sandwell, 1997) gravity averaged onto a 0.5′ grid. Seafloor spreading anomalies 27 and 26 are marked (Malod et al., 1997), as is the outline of the gravity low associated with Laxmi Ridge (dashed line).

24

Data from OBS/H and MCS reflection profiling were collected across both margins, along with bathymetric data (echo-sounding and swath) and potential field measurements (free-air gravity and magnetic anomaly). Additional seismic refraction data were recorded using disposable sonobuoys.

The navigation and time stamps associated with the underway data were generated by a Trimble 4000 differential global positioning system (D-GPS), separate from the ship's main navigation system. This used up to five satellites to give a position accurate to 2-5 m and a time accurate to 1 s.

Temperature measurements from disposable expendable bathy-thermographs (XBT) and static sound velocity profiler (SVP) measurements (Fig. 2.2) were combined with historical temperature and salinity measurements and converted to velocities (Wilson, 1960) to produce a velocity-depth profile through the water column (Whitmarsh and Sansom, pers. comm.).

2.1 Wide-angle seismic data acquisition

Thirty-two instruments, 11 ocean bottom hydrophones and 21 four component ocean bottom seismometers, were deployed across the Laxmi Ridge continental margin. The geophone components of the four component instruments had a resonant frequency of either 4.5 or 15 Hz. Eight of the 4.5 Hz sensors were gimballed-mounted levelling geophones (LGs). All instruments had a single component, omnidirectional hydrophone. All 32 instruments were recovered, but three did not yield any useful data: OBH02 experienced a battery failure; the data recorder on OBH21 was crushed when the pressure housing failed; OBH25 returned data too low in amplitude to be separated from the recorded noise signal. Data were recorded using Marine Broadband Seismocorder (MBS) and Marine Long-Time Seismocorder (MLS) devices, at either 100 Hz or 125 Hz, onto removable flash cards with a capacity of 4 Gbyte (MBS) or 12 GByte (MLS). All the instruments had a free-running clock, which was calibrated to on-board time before deployment and after recovery. The drift of the internal clocks during the experiment was generally less than 30 ms. The corrected timing was combined with navigation and shot time data recorded onboard to split the continuous data from the instruments into *SEG-Y* record sections. These data were reduced at 6 km s^{-1} and cut down to 15 s long record sections.

The main (north-south) OBS line extended from the continental rise SW of India to 45 km south of Chron 27, the first undisputed seafloor spreading anomaly (Fig. 2.2).

Wide-angle seismic data were acquired using an airgun array optimised for low frequencies. This consisted of chambers hung from each of four 7 m beams; two 1000 cu.in. single guns were also used to boost energy at long offsets (Fig. 2.3). The source was designed to have peak frequencies in the range 5-10 Hz, which would propagate to large
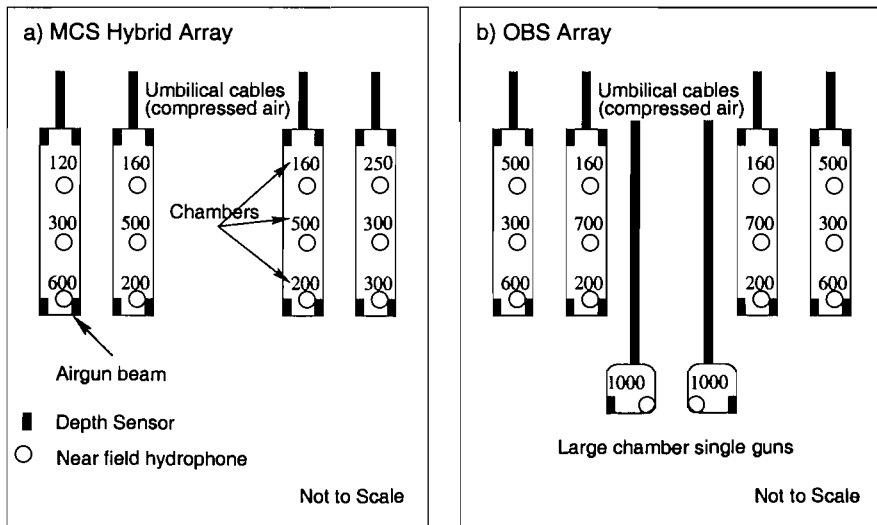
Figure 2.3: The airgun arrays: Chamber sizes are in cu.in. *a)* The MCS array, total size 3890 cu.in., pop rate 30 s. *b)* The OBS array, total size 6920 cu.in, pop rate 60 s. After Collier (2003).

offsets.

An important control on the frequency of the energy incident on the seabed is the tow depth of the array. This is because some energy from the airguns is reflected from the sea surface, and interacts with the main wave train to modify its frequency content. The intended tow depths of the OBS array was 18 m, but incorrect rope lengths were used to suspend the gun beams. This meant that the actual tow depth was ~ 13 m. The effects of this error are shown in Figure 2.4.

2.1.1 Processing

The wide-angle seismic data are generally of good quality; phases can be picked on data from twenty-six instruments on the main (north-south) line. Arrivals are seen out to a maximum of 100 km; noise from the previous shot obscures the data at ranges greater than this. The hydrophone components consistently show the best signal-to-noise ratio (Fig. 2.5). The vertical geophone component generally records strong arrivals, but the signal is usually more ringy than that recorded on the hydrophone, and this leads to overprinting of phases. Weak shear-wave arrivals are seen on the horizontal components.

Source to receiver offsets were calculated for each instrument based on its deployment position, using the reference ellipsoid *WGS-84*. This offset was written into the headers' of the wide angle data when the *SEG-Y* traces were generated. As the instrument sinks through the water column, it may be forced away from its deployment location by currents, making the calculated source to receiver offsets wrong. To correct for this, the instruments were relocated based on the shape and symmetry of the direct water wave when the
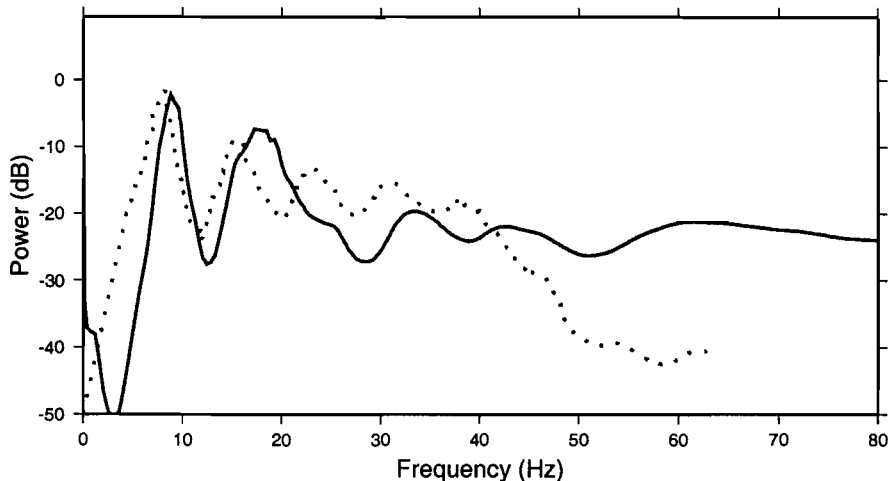
Figure 2.4: Effects of incorrect tow depth on source: Planned (solid line) and actual (dashed line) frequency content incident on the OBS/OBH. The peak energy is shifted to lower frequencies and the signature of the wave-train is altered by bubble-pulse interactions. The planned far field source is calculated from the interactions of recorded near-field gun signatures at the intended tow depth of the array (18 m), for an average source-receiver distance of 40 km. The actual source is from spectral analysis of the frequency content of OBS 01 at all offsets.

data are reduced at water velocities (Sansom, pers. comm.). This relocation used two-dimensional calculations, so any offline drift of the instrument is not corrected for.

In order to successfully pick and model arrivals observed in the wide-angle data, some pre-processing was necessary prior to picking. First, the traces were sorted according to offset rather than field file identification (FFID) number. The traces were weighted by offset to boost the amplitude of arrivals further from the instrument, and a bandpass filter was applied.

Filtering

Wide angle seismic data requires filtering in order to remove systematic noise, and increase the signal-to-noise ratio. A minimum phase filter was chosen, since travel time picking requires that the first energy of a phase is picked: if a zero phase filter were used, the onset of the phases would be shifted slightly earlier in time. Spectral analysis (Fig. 2.6) indicated that the frequency content of the useful signal was between 9 Hz and 35 Hz.

A trapezoidal filter which began to take effect at 7 Hz and 40 Hz and cut off completely at 0 Hz and 45 Hz seemed most appropriate based on spectral analysis. However, a harsher filter (2 Hz, 7 Hz, 15 Hz, 25 Hz) was found to be more useful, particularly in improving the clarity of phases at long offsets. The slope of the filter avoids introducing ringing into the signal. The effect of this filter on the frequency spectrum (Fig. 2.6) and data quality (Fig. 2.7) are shown .
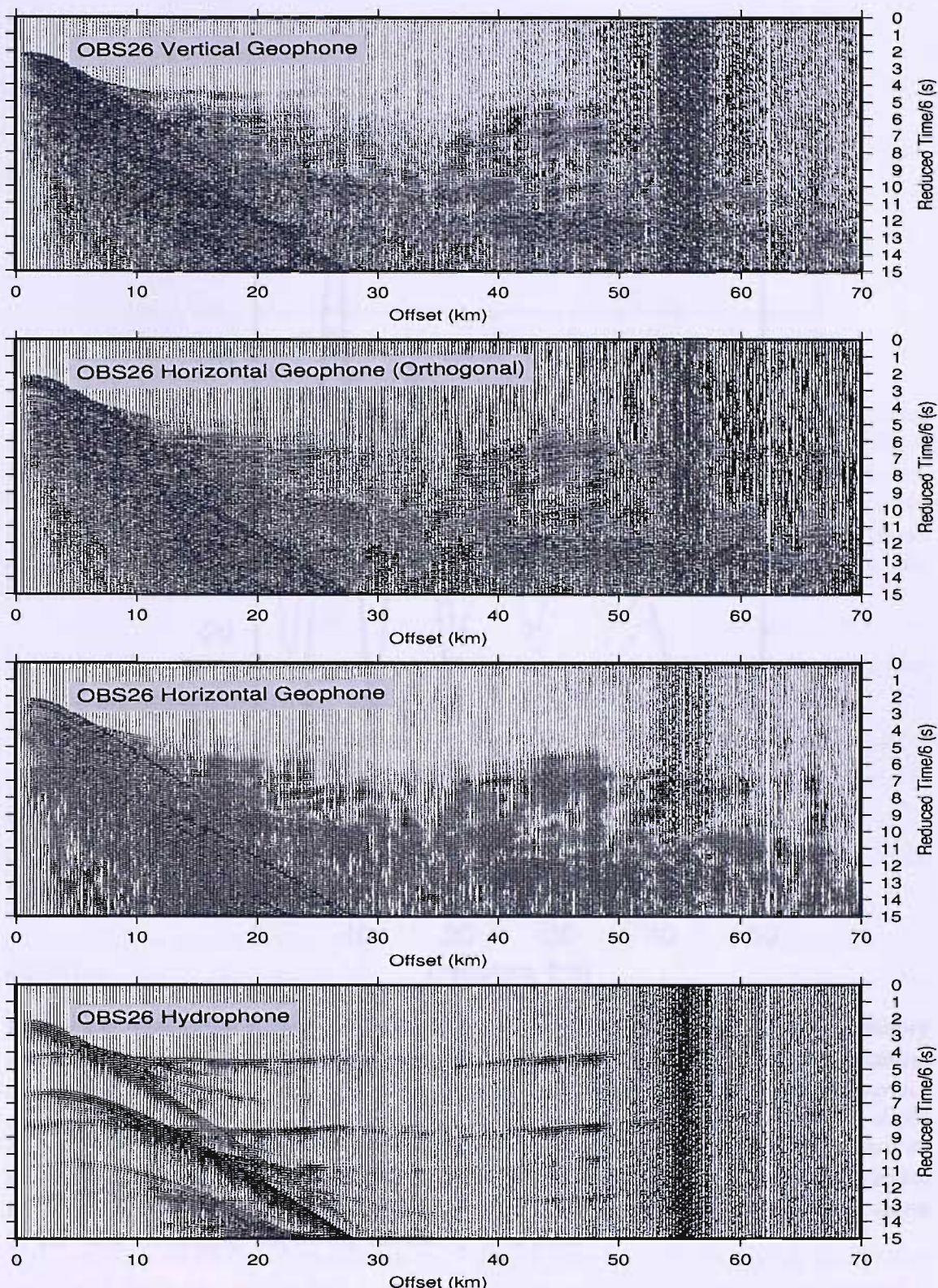
Figure 2.5: Example record sections for all components: The hydrophone record generally has higher signal-to-noise ratio and a less ringy character than the geophone records. The reduction velocity is 6 km s^{-1}
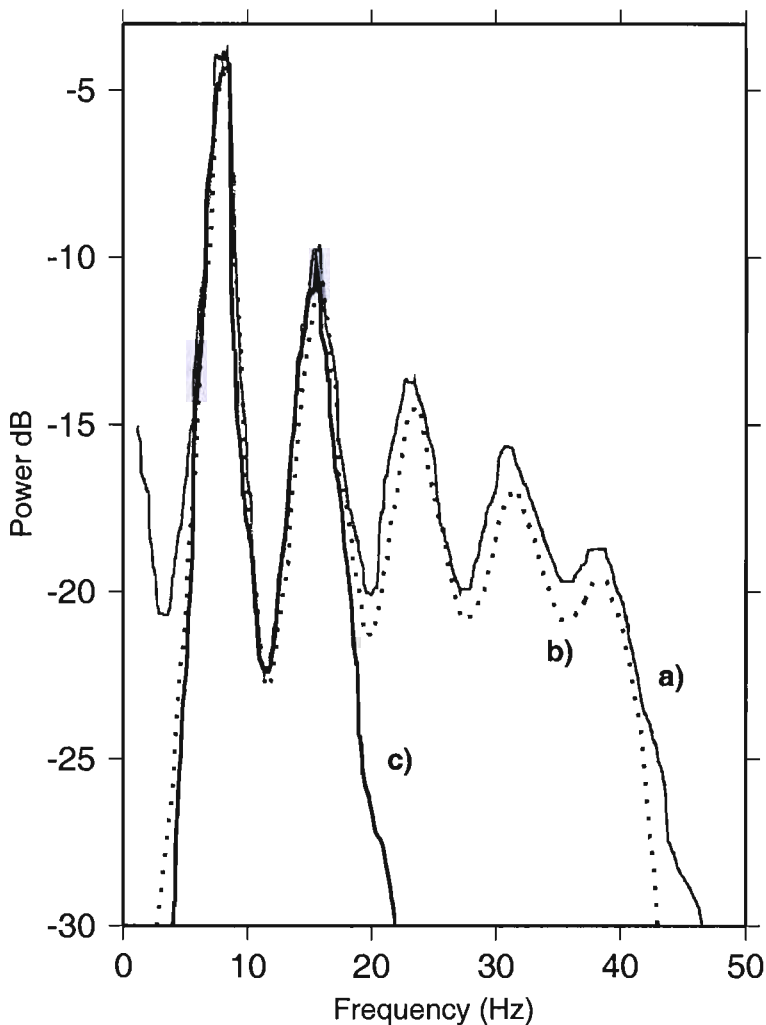
Figure 2.6: Frequency spectrum of wide-angle data: *a)* (Grey line) Unfiltered frequency spectrum of the hydrophone component of OBS 1, all traces. The oscillatory nature of the spectrum results from the interaction of the bubble pulse with the sea-surface reflection (i.e., the ghost effect). This is a consequence of the incorrect tow depth of the source (Section 2.1). *b)* (Dotted line) Frequency spectrum after applying a filter based on spectral analysis: water-borne noise at frequencies below about 5 Hz is successfully rolled off. *c)* (Black line) Ramping down the filter from 15 Hz to cutting all frequencies above 25 Hz removes ringing, improving the clarity of arrivals.
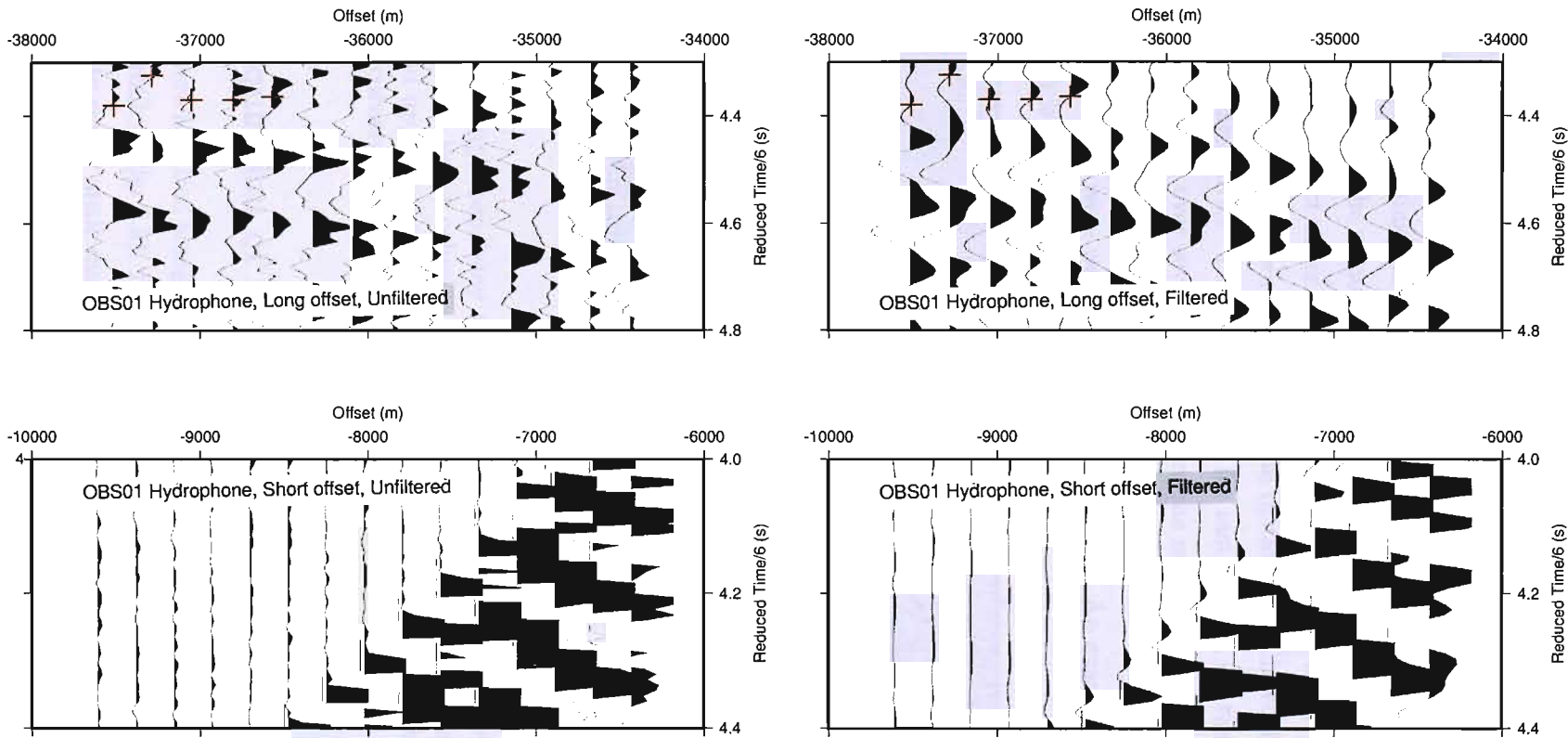
Figure 2.7: Effect of filtering on data quality: First arrival at short *(bottom)* and long *(top)* offsets, pre and post processing with 0-7 Hz, 15-25 Hz bandpass filter. Noise prior to the first arrival is subdued and the weak first arrival is enhanced at short offsets; at long offsets the signal is sharpened, making picking the first break (indicated by red crosses for the first few traces) easier. The reduction velocity is 6 km s^{-1}.

Sonobuoy processing

Eight disposable sonobuoys were deployed in this study area (Fig. 2.2). Of these, four returned useful data. Data were transmitted from the sonobuoys to an onboard VHF receiver, and were recorded onto the MCS logging system at a sample interval of 4 ms. The sonobuoys are free floating and therefore drift from their deployment position during their transmitting period. The amount of drift is calculated for each sonobuoy by measuring the arrival time of the direct water wave after each shot. Both the water velocity and distance the ship has moved are known, so any residual distance calculated from the arrival time must be instrument drift. The average drift for instruments on the main (north-south) OBS line was 1.9 km over several hours. Once the source-receiver offsets were corrected for drift, the data were processed using the same filter as that used for the OBS data, and individual traces were weighted according to offset. An example processed sonobuoy record section is shown in Figure 2.8.
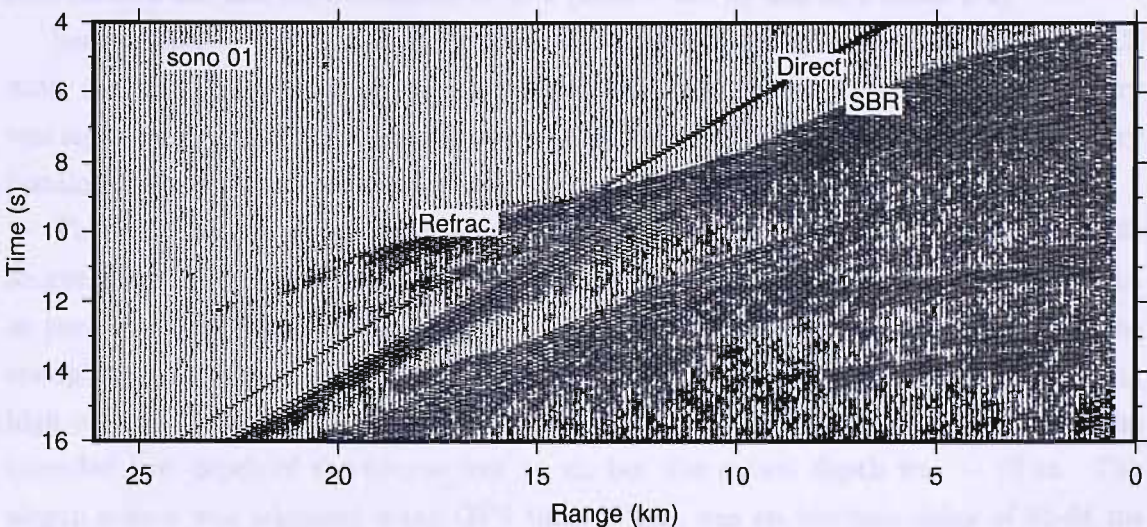
Figure 2.8: Example sonobuoy record section: Phases observed are: *Direct*, direct arrival through the water column; *SBR*, seabed reflection; *Refrac.*, refraction through the sediment and upper crust. Data are filtered using the bandpass filter designed for OBS processing (corners at 2 Hz, 7 Hz, 15 Hz and 25 Hz).

2.2   Acquisition of MCS data

MCS data were acquired along six lines over Laxmi Ridge, giving a total of around 900 km of seismic profiles (Fig. 2.9). Lines 5 and 6 are of good quality, while lines 2-4 are of poor quality due to errors made during acquisition (Section 2.3.6). Line 1 was a test line using two 1000 cu.in guns only, and was only processed to brute stack onboard.

Multichannel reflection data were recorded using a 96 channel, 2.4 km hydrophone streamer (Fig. 2.10). The geometry of the streamer and its relationship to the airgun array

is shown in Figure 2.11. The streamer was intended to be towed slightly deeper than the airguns to avoid noise generated by turbulence on firing, but it had been overfilled with oil after a recent refurbishment and was too buoyant. For the first half of the experiment, it was generally towed at 1 m - 7 m, with the front sections held deeper by the weight of the tow rope. Depth control birds, mounted on every active section, were unable to counteract the buoyancy of the streamer. Lines 1 to 4 were shot before this problem could be rectified. Lines 2, 4 and 3b are coincident with the OBS profiles, and were shot using the 6920 cu.in OBS array fired every 60 s. Lines 5 and 6 were shot after additional lead was added to the streamer, allowing it to reach $\sim$ 13 m depth. The source for these lines was a 3890 cu.in MCS array fired every 30 s. Line 6 was a partial re-shoot of the main OBS line (lines 2 and 4), and was shot south to north, the opposite direction to lines 2 and 4. Line 5 runs for approximately 150 km and is located around 20 km east of line 6, roughly parallelling line 6. Data were recorded onto 4 GByte DAT tapes with a sample interval of 4 ms, and record lengths of 30 s (lines 5 and 6) and 25 s (lines 1-4).

Source-receiver offsets were calculated as part of the onboard processing of the MCS data. A rough velocity model was constructed and the approximate experiment geometry was input to allow a brute stack of all lines to be made. Line 6 also had accurate geometry installed, allowing an intermediate stack to be made for this line (Collier, 2003).

The MCS airgun array was designed for higher resolution imaging than the OBS source. Gun sizes in this array were designed to give peak frequencies between 10-25 Hz, as part of a 3890 cu.in 'hybrid' array. This array was designed to have frequencies low enough to penetrate the large impedance contrast at top-basement, while still having high enough frequencies to give good vertical resolution in the shallow sediments. The intended tow depth of the source was 14 m, but the actual depth was $\sim$ 13 m. The airgun source was triggered using GPS time. There was an intrinsic delay of 62-64 ms between the nominal firing time and the airguns firing and this was corrected for in the MCS processing.
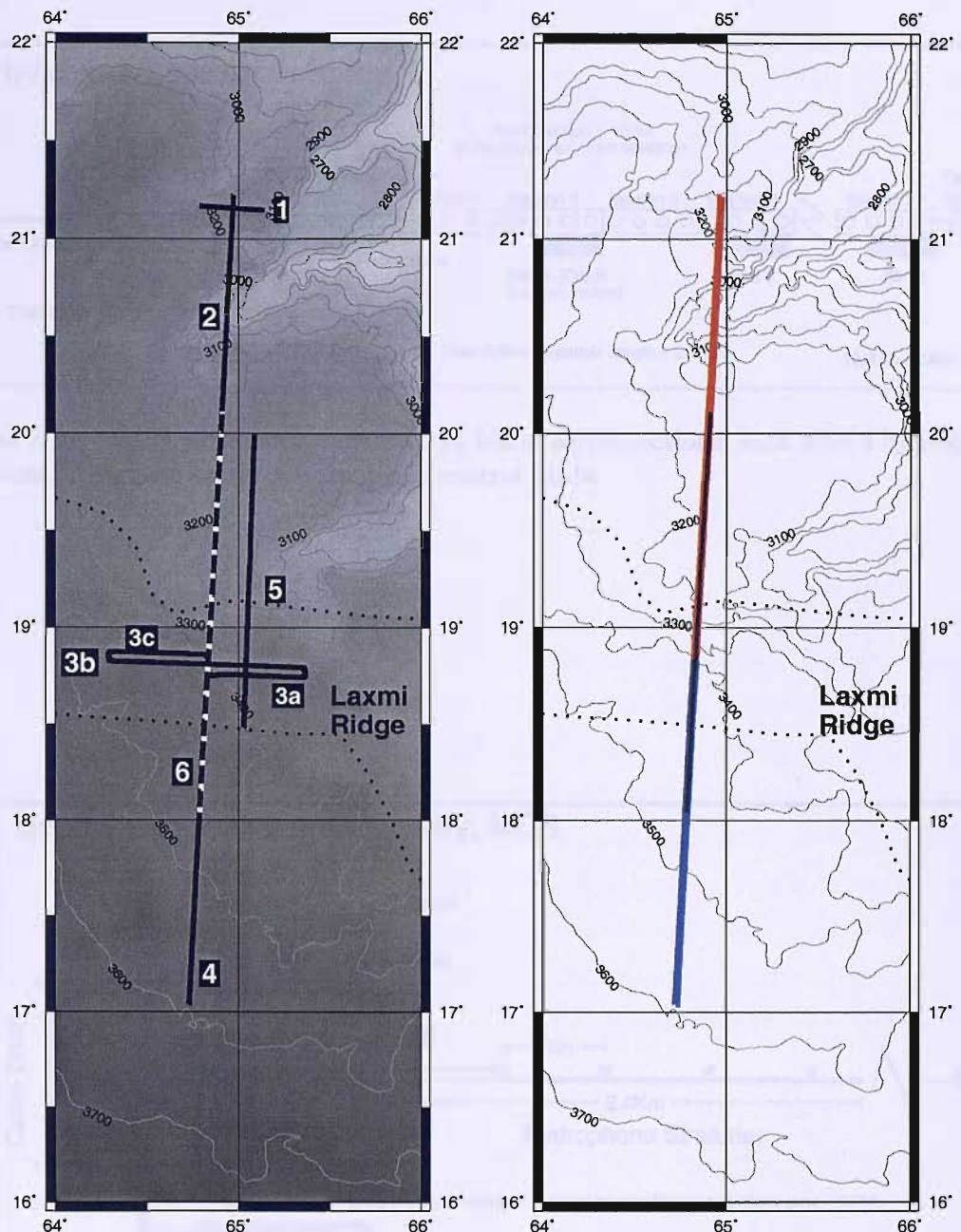
Figure 2.9: Left: Location of MCS lines. Line 1 was a test line shot with two 1000 cu. in. single guns. Lines 2-4 were shot using a source optimised for wide-angle data acquisition, while lines 5 and 6 were shot using a dedicated MCS source. Line 6 (white dashed line) is a partial re-shoot of lines 2 and 4, which are coincident with the north-south wide-angle line (Section 2.1). The dotted line marks the outline of Laxmi Ridge, identified from its gravity profile. The background field is combined historical and CD144 bathymetry, contours are in metres. Right: CD144-2 (red) CD144-4 (blue) and CD144-6 (black) are plotted to show the relationship between these lines.
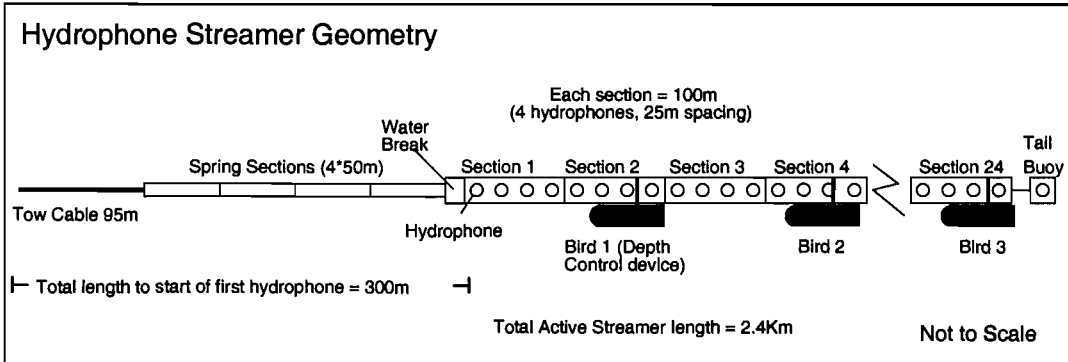
Figure 2.10: MCS hydrophone streamer: 24 100 m active sections, each with 4 hydrophone receivers. Alternate sections have depth control birds.
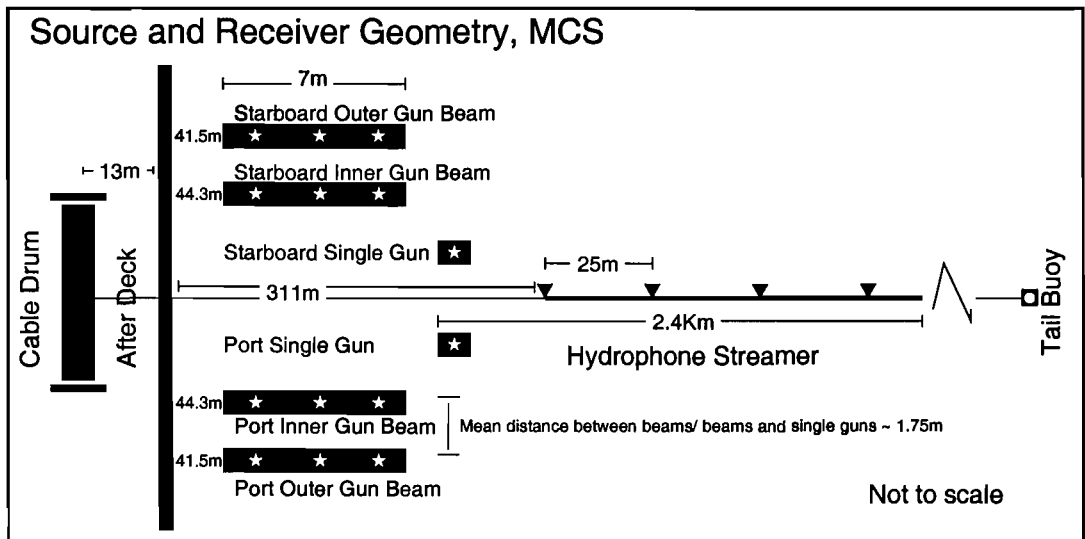
Figure 2.11: Streamer and airgun geometry: Black bars are airgun beams; stars are gun chambers. For chamber sizes, see Figure 2.3.

34
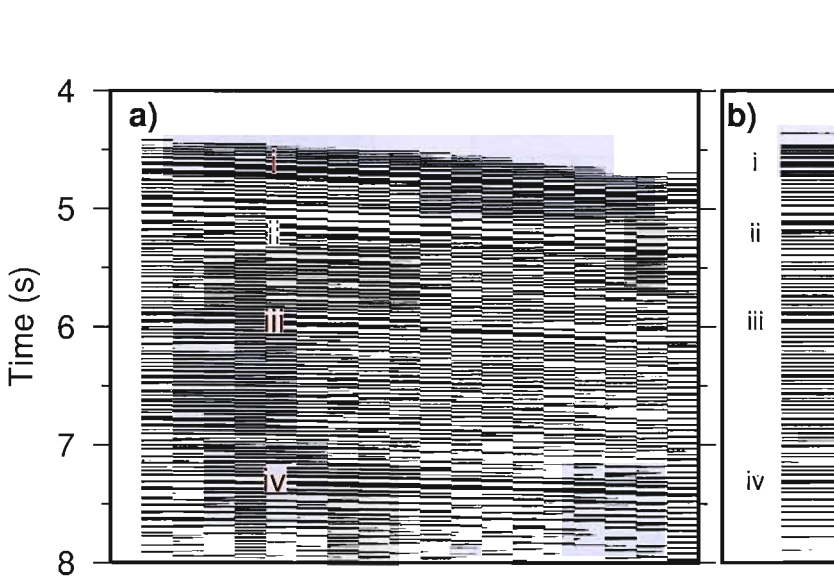
Figure 2.12: Actual CMP gather and stack: *a)* A CMP gather from line 6. Note the hyperbolic appearance of the reflections *i* to *iv*. *b)* The resulting CMP stack. The stacked reflections *i* to *iv* can be picked out easily and some of the background noise between these arrivals has stacked out.

2.3 Processing of MCS data

MCS acquisition involves recording multiple reflections from a common point on a horizon within the earth, and summing these reflections (stacking) to increase the signal-to-noise ratio of the data (Fig. 2.12). The number of traces stacked to make a single common mid-point (CMP) trace is known as the fold of the data. An image of the subsurface is generated by plotting CMP traces that record reflections from adjacent subsurface reflectors side by side. Normal incidence reflections are required in order to make this image. However, for practical reasons, reflections from varying angles of incidence are recorded. To correct the data back to normal incidence, a normal moveout (NMO) correction is applied. This uses a given velocity field and the known arrival offsets to correct for the hyperbolic increase in arrival times observed by recording signals from the same subsurface location at increasing incidences.

All processing of MCS data was done using Landmark's *ProMAX* package. Initial processing involved installing the correct geometry in the trace headers, including uploading shot positions from the on-board GPS receiver. A processing flow was then designed to produce the best stack possible, and to therefore maximise the signal-to-noise ratio of the data. The processing flow is described in detail for line 6; when the processing flow differs for other lines, this is described in the appropriate section. The processing flow is summarised in Figure 2.13.

2.3.1 Line 6 - Basic processing

The ship sailed at 4.5 Knots during acquisition and the shot interval was 30 s, giving a shot spacing of approximately 75 m. The spacing of hydrophones on the streamer was 25 m. A CMP spacing of 12.5 m and a 96 channel streamer gives an average fold of 16:
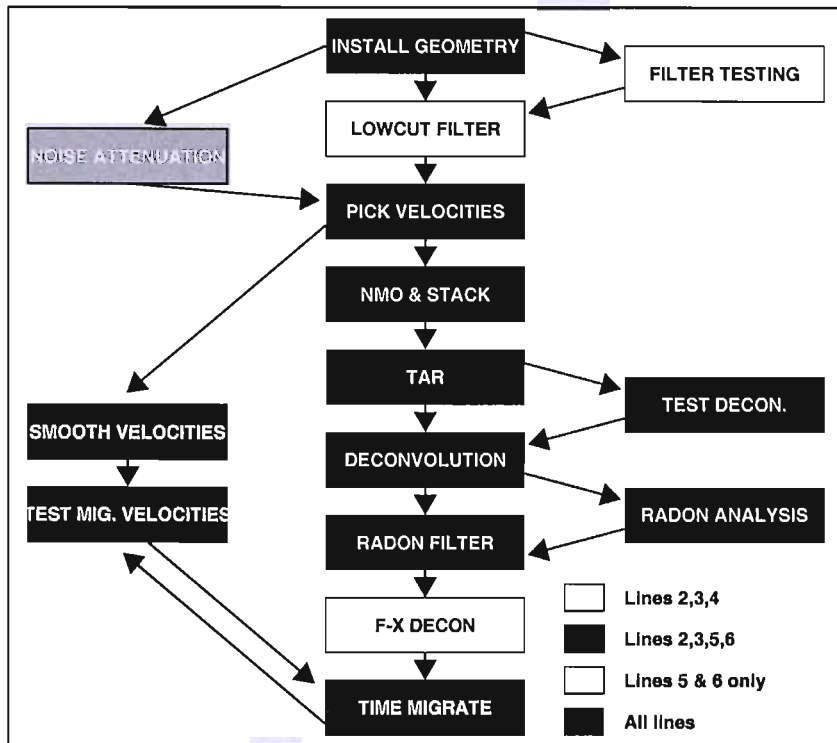
Figure 2.13: Summary of MCS processing flow: TAR is true amplitude recovery. Variations in processing steps are due to the variable quality of the data. Flow processes are shaded according to the lines that they apply to (see key). For a detailed description of the processing flow see text.

$$\text{Fold} = \frac{(\text{Number of channels} \cdot \text{receiver spacing})}{2 \cdot \text{shot spacing}} \tag{2.1}$$

A 63 ms static shift was applied to the data to correct for lag in the recorder startup time (Collier, 2003). Channels 64 and 82 were observed to be bad for all shots so were not included in the stack.

Different filter widths were tested; some examples are shown in Figure 2.14. A bandpass with corners at 4, 6, 40 and 45 Hz was found to be most effective at removing low frequency water-borne noise without degrading the wanted signal, or introducing ringing artifacts.

Stacking velocity analysis was performed every 500 CMPs (6.25 km) on supergathers of 15 CDPs. Supergathers were used to increase signal-to-noise ratio of the input data. Root mean square (RMS) automatic gain control (AGC) with a 500 ms moving window was applied to make picking low amplitude late arrivals (i.e., greater than 6 s) possible. Appropriate stacking velocities were chosen by picking the peak coherence between predicted hyperbolic trajectories of constant velocity and the semblance (similarity) of traces along that trajectory (Fig. 2.15). When a velocity successfully flattens and aligns arrivals on adjacent traces a peak is seen on the semblance plot. The correct velocity is that which
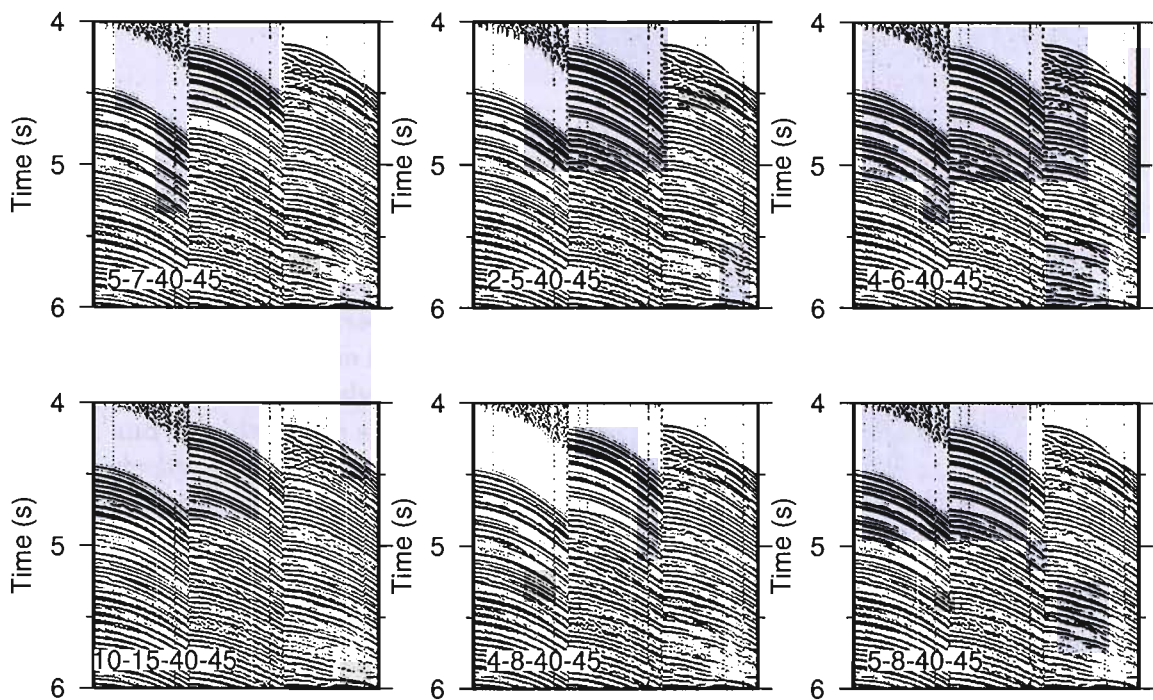
Figure 2.14: Testing of filter bounds: three shot gathers from line 6 with different bandpass filters applied. The labels give the filter corners; the inner two numbers are the frequencies at which the filter begins to reduce the amplitude of the data; the outer two numbers are the frequency at which the filter cuts off the data. The effect of the chosen filter, with corners at 4, 6, 40 and 45 Hz, is shown in the upper right panel. All these filters did a satisfactory job of reducing water-borne noise, but the chosen filter successfully removed noise without decreasing the amplitude of wanted arrivals. The filter with corners at 4-8-40-45 Hz reduces the amplitude of reflections deeper than around 4.7 s, while the 10-15-40-45 Hz filter reduces the amplitude of wanted arrivals at all times.

flattens a primary arrival when the NMO correction is applied at a given two-way time.

Velocities were picked down to a time of around 8.5 s, which is when the water bottom multiple arrives and obscures the primary reflections. Picked velocities were used to correct the CMP gathers for NMO, and the CMP gathers were then stacked. The picked velocities were also used to apply true amplitude recovery (TAR) to the dataset. This is a time-varying gain function applied to correct for amplitude loss due to spherical spreading of the wavefront as it travels through the earth. Spherical spreading is approximated as,

$$\frac{1}{\text{time} \cdot \text{vel}^2} \qquad (2.2)$$

with an optional dB s^{-1} scaling correction.

Parameter testing indicated that TAR with a gain correction of 2 dB s^{-1} was appropriate for this dataset. TAR was not applied at times greater than 8 s to avoid boosting the amplitude of the strong first multiple, which arrives between 8.5 s and 9.3 s (Fig. 2.16).

Figure 2.15: Semblance plot: The similarity (semblance) between predicted hyperbolic trajectories of constant velocity and the distribution of energy in the supergathers is plotted, to allow appropriate velocities to be selected for NMO correction. The orange line is a guide function based on previously picked velocities, and the black line shows the interval velocity in between semblance picks. The velocity scale is in m s^{-1}. When the peak semblance (red) is picked and the corresponding velocity applied, the hyperbolic reflectors are flattened *(right-hand panel)*. Note the muting of shallow reflectors at far-offsets - these traces are susceptible to distortion by stretching and so are muted out prior to stacking.
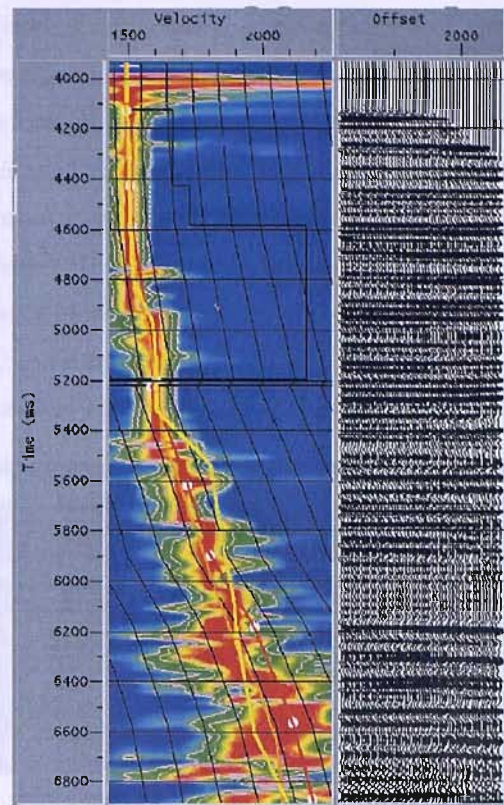
2.3.2   Post-stack deconvolution

The recorded seismogram is a convolution of the amplitude spectra of the input seismic wavelet, the earth's impulse response, and the frequency response of the recording hydrophones. The filtering effects of the earth act to attenuate the input wavelet, particularly at high frequencies. Reverberations of the wave-train within the earth also smear the signal, giving it a ringy nature, which can obscure closely spaced reflectors. Predictive deconvolution of the seismogram is a method of reducing this ringing to increase the vertical resolution (Yilmaz, 1987). The inverse of the seismic wavelet is calculated and
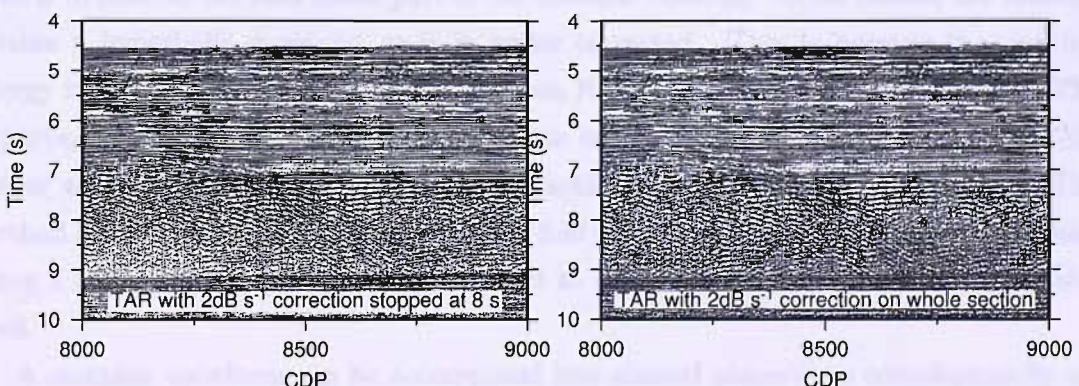
Figure 2.16: True amplitude recovery: True amplitude recovery is not applied later than 8 s, or it boosts the amplitude of the multiple that arrives at 9.2 s *(right)*.

used to filter the seismogram. This inverse filtering collapses the wavetrains to a series of simple wavelets that represent the impulse response of the earth.

Autocorrelation of the seismogram is performed by correlating the waveform with a shifted copy of itself. Autocorrelating this dataset showed that the primary wavelet was approximately 30 ms long, and a strong reverberation occurred at 100 ms (Fig. 2.17). A deconvolution operator was therefore designed with a 32 ms prediction distance. This avoids compressing the 30 ms primary phase, which would cause distortion of the wave shape and generate noise by whitening the frequency spectrum. Parameter testing indicated that a 240 ms minimum-phase operator was appropriate for this dataset.
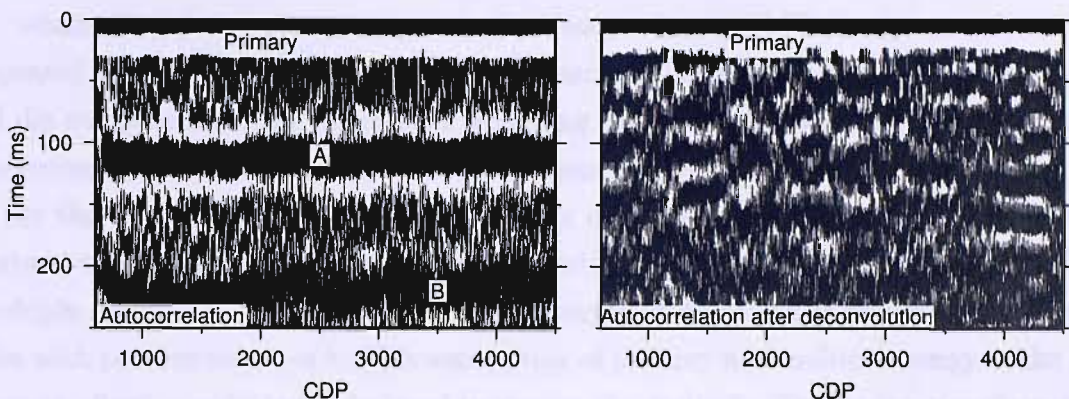
Figure 2.17: Autocorrelation of line 6: *Left:* In addition to the primary energy (labelled), strong ringing is seen in the recorded signal (events A and B). *Right:* After applying predictive deconvolution, the two ringing events are removed, so the vertical resolution of the reflection profile is improved.

2.3.3 Multiple attenuation

The first water-bottom multiple obscured any data arriving at around 8.5 s. To combat this, the multiple was muted at near-offsets, where it has a flat shape in a CMP gather. This is to prevent the near-offset part of the multiple stacking. At far offsets, the multiple retains a hyperbolic move-out as it is under corrected. This is because the multiple energy travels at water velocities, but has been NMO corrected at crustal velocities. This hyperbolic shape means the multiple reflection is not coherent across traces in the CMP gather so does not stack coherently, hence stacking attenuates the multiple energy. This method has the disadvantage of reducing the fold of the stack at depth. Further processing using a Radon demultiple filter was required to attenuate the multiple to an acceptable level.

A complex waveform can be decomposed into slanted plane-wave components by applying a linear moveout (LMO) through a coordinate transform from the travel time, offset *(t, x)* domain into the moveout, slowness *(τ, p)*. The transform is given by,

$$\tau = t - px \tag{2.3}$$

where τ is the time with linear moveout applied, t is two way travel time, x is offset and the slowness p is defined as the inverse of the horizontal phase velocity (Claerbout, 1978). Following the transform, events with the slope p are flat. Wave amplitudes are then summed along slanted paths over the offset axis,

$$S(p, \tau) = \sum_x p(x, \tau + px) \tag{2.4}$$

where $S(p,\tau)$ is a plane wave with slowness p. If this LMO transform and sum is repeated for a range of values of p, a slant stack gather is constructed, which contains all dip components of the input data. Following the mute, an inverse transform must be performed to return the stacks to the t,x domain (Thorson, 1978).

In the τ-p domain, primary reflections plot on or near the τ axis, because the NMO correction has been applied using a velocity field designed to flatten these arrivals. The multiple reflections, however, have a residual moveout due to their undercorrection, and plot with positive values of τ. This segregation of primary and multiple energy in the p-τ domain allows a mute to be designed to remove the multiple. The Radon transform tool (Forster and Mosher, 1992) in *ProMAX* was used to do this.

Removing the multiple allowed stacking velocities to be picked for events deeper than 8 s. This improved the resolution of deep crustal events: a reflection from the base of the crust is observed on some parts of the section (Fig. 2.18).

Prior to migration, the F-X deconvolution tool was used (Treitel, 1974), which uses a prediction filter in the frequency domain to reduce random noise. A Fourier transform is applied to transform the data into the frequency domain. Wanted signal can be described as the sum of sinusoidal components, and is therefore predictable along a given frequency slice. The F-X tool accepts this predictable component of the signal, and rejects random noise.
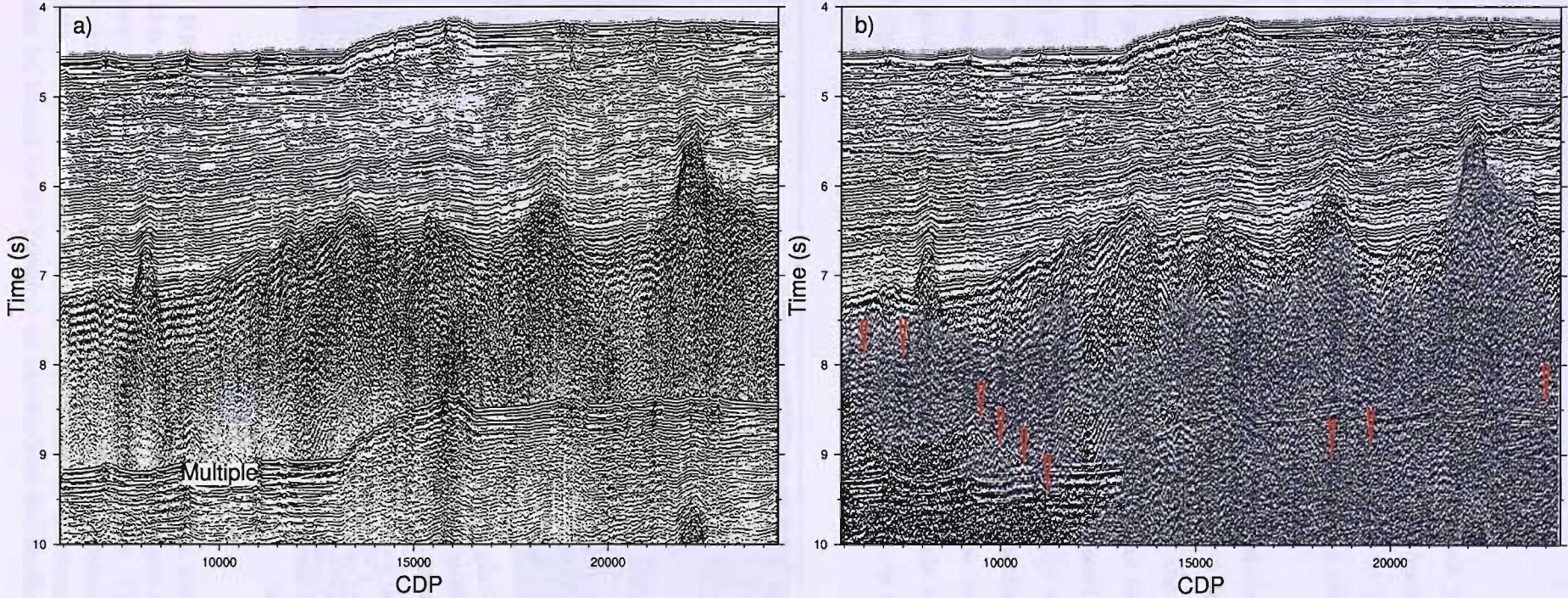
Figure 2.18: *Left:* Line 6 prior to application of Radon demultiple filter- the strong water bottom multiple obscures any weak, deep crustal reflections. *Right:* After applying the demultiple filter, picking stacking velocities later than 8 s and restacking the data, the multiple is attenuated and the reflection Moho is imaged in places (arrowed).

2.3.4 Migration

Common mid-points are sometimes referred to as common depth points (CDPs), but this nomenclature is only accurate if the subsurface reflectors are horizontal. A limitation of the CMP stacking method is that dipping reflectors may not be imaged in their correct lateral position in the seismic section. To correct for this, and to collapse diffracted energy from point scatterers in the earth, the stack is migrated.

Several migration types were tested; a Kirchhoff time migration was ultimately chosen (Fig. 2.19). This works by summing amplitudes along calculated diffraction curves within the section. The summed amplitude is placed at the apex of the curve in the migrated section. The method is appropriate for continuous reflectors as well as point diffractors, as any horizon can be considered as the sum of closely spaced point diffractors. In the resulting migrated section most diffractions are successfully collapsed and only the multiple is over migrated. A post-stack time migration was chosen as it produces a good migrated image without the same critical dependence on an accurate velocity field that pre-stack migration has. Velocity constraint from the wide-angle model (Section 3.4) was not included rigorously in the development of a migration velocity model as the smoothed stacking velocities produced a good final image.
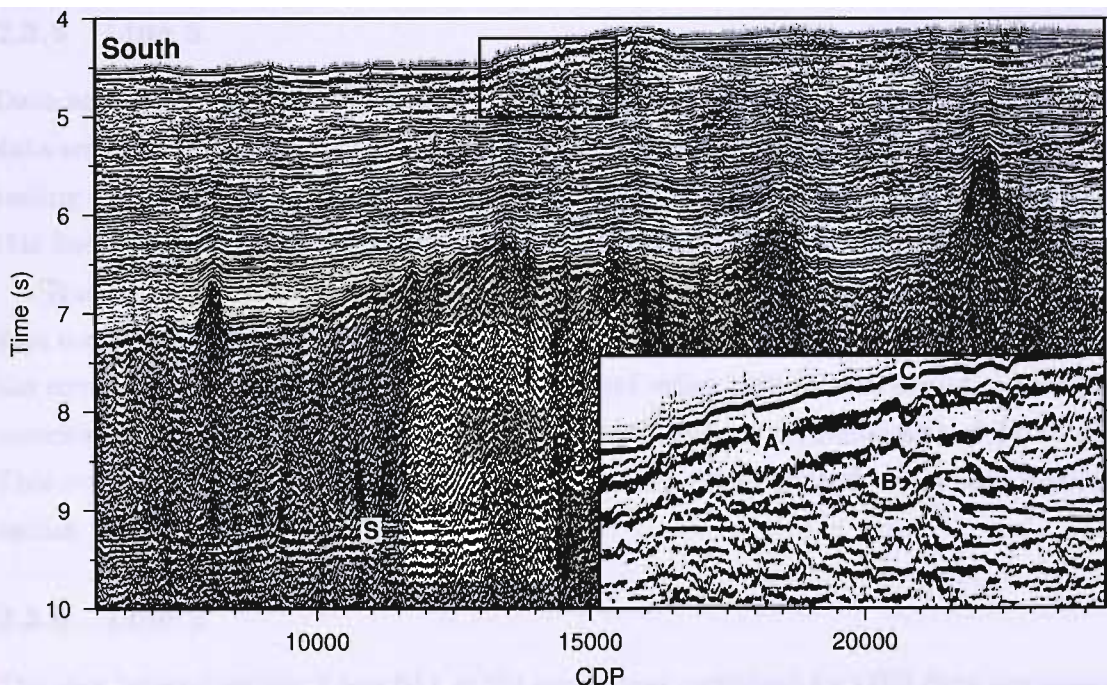
Figure 2.19: Kirchoff time migration of line 6: most diffractions are collapsed and dipping events should now be in their correct locations. S marks the apex of a 'smile'- an artifact caused by overmigration of the water-bottom multiple. *Inset:* The scrappy appearance of the upper sedimentary layers is due to the cross cutting relationships of channels in a complex deltaic system. Some channels (e.g A and B) are seen in cross-section view. Channel B can be traced to it's position on the modern day seafloor (C).

The migration requires a velocity field to remap dipping events to their correct subsurface position. The RMS stacking velocities were smoothed before being used in the migration algorithm to prevent artifacts being generated at sharp velocity steps. Testing indicated that 100% of the stacking velocities should be used in the sediments, with the velocities reduced to 90% at 8 s and 80% at 8.5 s. This was to combat the overmigration observed in the water bottom multiple. The basement multiple was muted out prior to migration as it generates severe overmigration artifacts (smiles). This is due to it having a mean velocity much lower than the basement structure that it overprints- the energy has travelled through the water column and sediments, but was migrated at crustal velocities.

Automatic gain control was applied after migration. AGC varies the gain of traces as a function of their RMS amplitude within a chosen time window. AGC can boost the amplitude of weak crustal reflections but it has the drawback that, in normalising trace amplitudes, it can reduce the amplitude of strong wanted signals. A variety of AGC window lengths were tested; this included using two different AGC operators: summing the output traces from a short gate (300 ms) to boost low amplitude signals, and a longer gate (3 s) to preserve the strong top basement reflection. A 1 s AGC operator was finally chosen as it provides a good compromise for the whole of the section.

2.3.5 Line 5

Data acquisition parameters for this line were comparable to line 6 (section 2.2), so the data are of good quality. The same processing flow was followed as designed for line 6, but testing indicated that some slightly different parameters were appropriate for processing this line. This is mainly due to the slightly shallower basement on this line.

True amplitude recovery was applied to correct for spherical spreading using a 2 db s^{-1} gain correction. This correction was stopped at 7.5 s to avoid boosting the amplitude of the strong first multiple. The stack was migrated using 100% of the smoothed stacking velocities down to 5.5 s then 90% down to 8.5 s, and 80% for the remainder of the section. This was to prevent the basement high at 6 s being overmigrated. The final migrated section is shown in Figure 2.20.

2.3.6 Line 2

The shot interval on line 2 was 60 s as the source was optimised for OBS data acquisition. This gives a shot spacing of approximately 150 m, which equates to an average fold of eight. Wave noise dominates this line, as part of the hydrophone streamer was on the sea surface during acquisition. The processing flow designed for line 6 was applied, with some changes made due to the poor quality of the data. Previous processing done on this line (Chand, pers. comm.) had incorrect geometry installed in the headers and therefore
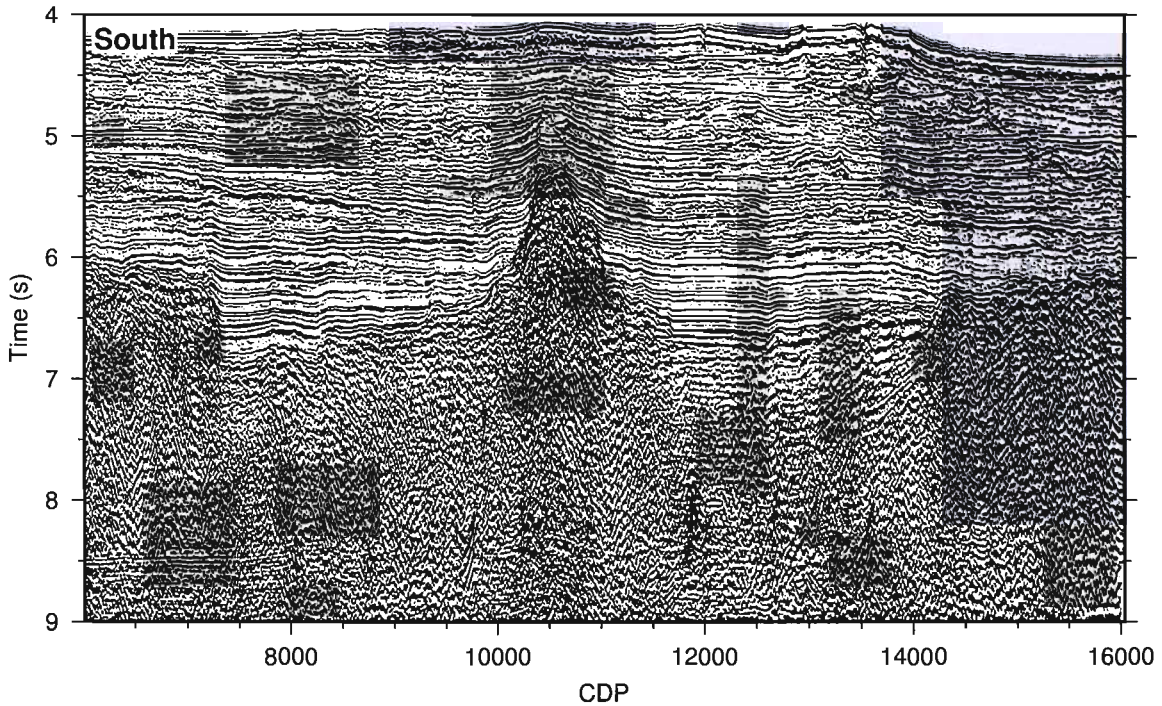
Figure 2.20: Kirchoff time migration of line 5: See text for details of processing.

could not be used. Chand developed a method for discarding channels with noise levels over a certain threshold. However, noisy channels are not discarded from the final stack in this work as the fold of the data is already low; instead, an effort was made to suppress noise by pre-processing and stacking the data.

In order to reduce the wave noise, some pre-processing of the data was necessary. A predictive F-X (noise) filter and a severe low-cut filter with a 15 Hz cut-off and a 20 Hz ramp were applied prior to velocity analysis. Velocities were picked every 500 CMPs. A Radon demultiple filter was also designed and applied to the data prior to picking. This reduced noise sufficiently to allow velocities to be picked down to around 12 s. The filter was applied to suppress the multiple in the final stack, but no structure can be imaged below 7.4 s due to the limitations of the data. A 500 ms AGC operator was applied to normalise amplitudes in the section. The water bottom multiple was not muted out, as the fold of this section is too low to justify the removal of traces and the subsequent reduction of fold. TAR was applied down 6 s, and a deconvolution operator with a 280 ms length and 54 ms prediction distance was used. Stacked sections were prepared both using all of the channels and excluding the noisiest channels for comparison (Fig. 2.21).

A Kirchhoff time migration was applied using 80% of the picked stacking velocities until 5.5 s, 60% down to 6.5 s and 50% to the bottom of the section. Figure 2.21 shows the effects of the noise reduction technique, and the migrated final section.

2.3.7 Line 4

Line 4 has similar noise problems to line 2, but the frequency content of the wanted signal is slightly different. A less severe low-cut filter, with a cut off at 5 Hz and a ramp at 12 Hz, was used to pre-process this line. Predictive noise removal in the frequency domain was also applied prior to velocity analysis. Deconvolution, TAR and Radon demultiple filtering were all tested and applied as described for line 2. An unmigrated section was chosen as the final stack for this line (Fig. 2.22). This is because the reflectors are flat, the structure is simple, and diffracted energy does not affect the quality of these data. In this case, the possibility of introducing of noise by overmigration outweighed the benefits of migration. Figure 2.23 shows the final stacks of lines 2 and 4 where they are coincident to line 6.

2.3.8 Line 3

Line three (Fig. 2.24) is divided into 3 parts: 3a runs east away from the main (OBS) line. 3b runs east-west and bisects the main line and 3c runs west-east to rejoin the main line. Line 3 was pre-processed with a low-cut filter with a cut-off at 5 Hz and a ramp to 12 Hz prior to picking velocities every 100 CMPs. After applying true amplitude recovery, Radon demultiple filtering and stacking, the stack was migrated. 100% of the smooth stacking velocities were used in the sediments, decreasing to 80% of the velocities in the basement.

2.4 Underway data

Bathymetry, free-air gravity and magnetic anomaly measurements were made for the duration of the cruise.

2.4.1 Free-air gravity

The gravity field was recorded using a LaCoste Romberg gravimeter, calibrated to base station ties made in Port Sultan Qaboos, Muscat and Victoria, Mahé. The drift between these ties was negligible. The Free-Air anomaly was extracted from the total field by applying the Eötvös (latitude) and elevation corrections during on-board processing. Anomalous data spikes were removed by hand. The internal RMS cross-over error for this data set is 3.91 mGal. A new map of the free-air anomaly in this study area has been compiled from CD144 and satellite gravity (Fig. 2.25). Within a 10 minute radius of the ship track CD144 gravity measurements were used, with satellite gravity (Smith and Sandwell, 1997) filling regions beyond this. The resulting combined data set was surfaced

and gridded. The difference between the satellite and shipboard gravity rarely exceeds the internal RMS cross-over error of the shipboard data (Fig 2.26).

2.4.2 Magnetic anomaly

The total magnetic field was sampled using a Varian V75 proton precession magnetometer. Data were corrected to the current international geomagnetic reference field (IGRF 2000) on board, but were not corrected for diurnal variation. A compilation of historic data from the National Geophysical Data Centre (NGDC) catalogue, previous *Charles Darwin* cruises (Miles et al., 1998), and French cruises (Malod et al., 1997) was made. Historic data were corrected to IGRF 2000 (Vermeesch, pers. comm.), and combined with the CD144 data, after removing bad datapoints from all datasets. The resulting combined dataset was averaged onto a 1 minute grid, and processed with a 5 km boxcar filter to remove short wavelength artifacts (Fig. 2.27). This was the smallest filter width that eliminated obvious artifacts. The RMS internal crossover error for the CD144 Laxmi Ridge dataset is 32.0 nT and the mean external crossover error with historical data is 87.2 nT. These values are comparable to the 28.7 nT internal crossover and 60.6 nT external crossover error for the CD144 Seychelles dataset (Sansom, pers. comm.). Crossover errors as large as 120.0 nT are observed on other cruises using similar acquisition techniques (Buchanan et al., 1996). The effect of the ship heading on the internal crossover error could be as large as 8.0 nT (Collier, 2003).

The Seychelles dataset was corrected for crossover errors and diurnal variation of the geomagnetic field, which reduced the internal crossover error to 17.2 nT and the crossover with historical datasets to 47.0 nT (Sansom, pers. comm.). These corrections have not been applied to the Laxmi Ridge dataset due to time constraints.

2.4.3 Bathymetry

Bathymetric data were collected using both a hull-mounted 10 kHz echo sounder, and a 10 kHz towed fish. The RMS cross-over error for the CD144 data was 10.37 m. These data have been combined with historical data, which has been hand-contoured (Fisher, pers. comm.), and then averaged onto a 0.5 minute grid to produce a new map of the regional bathymetry (Fig. 2.9).
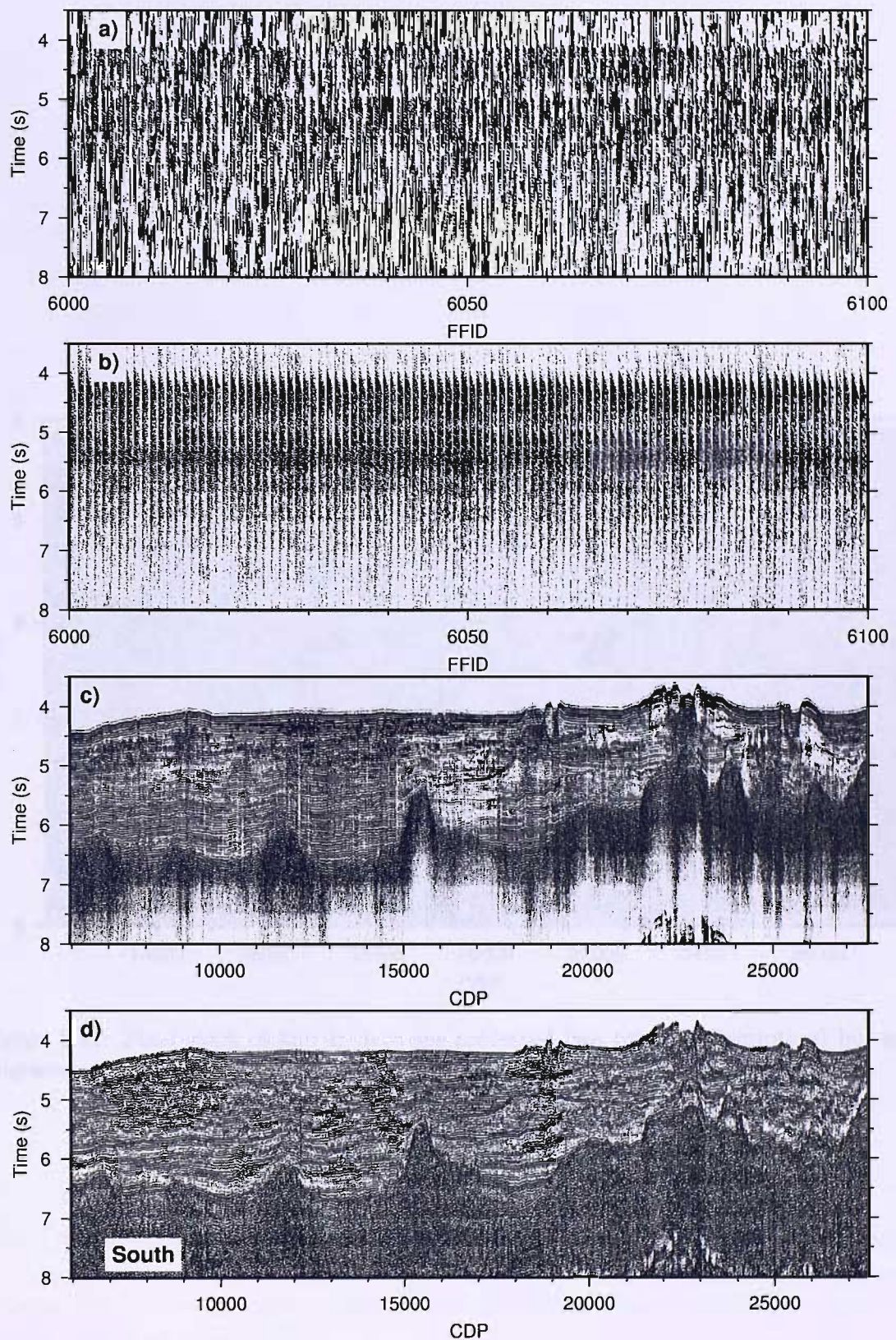
Figure 2.21: Kirchoff time migration of line 2: *a)* Unprocessed shot gathers are saturated with low frequency noise. *b)* Shot gathers after harsh filtering (see text). *c)* Stacked and migrated section including only the front half (channels 1-48) of the streamer. *d)* Stacked and migrated section including data from the whole streamer.
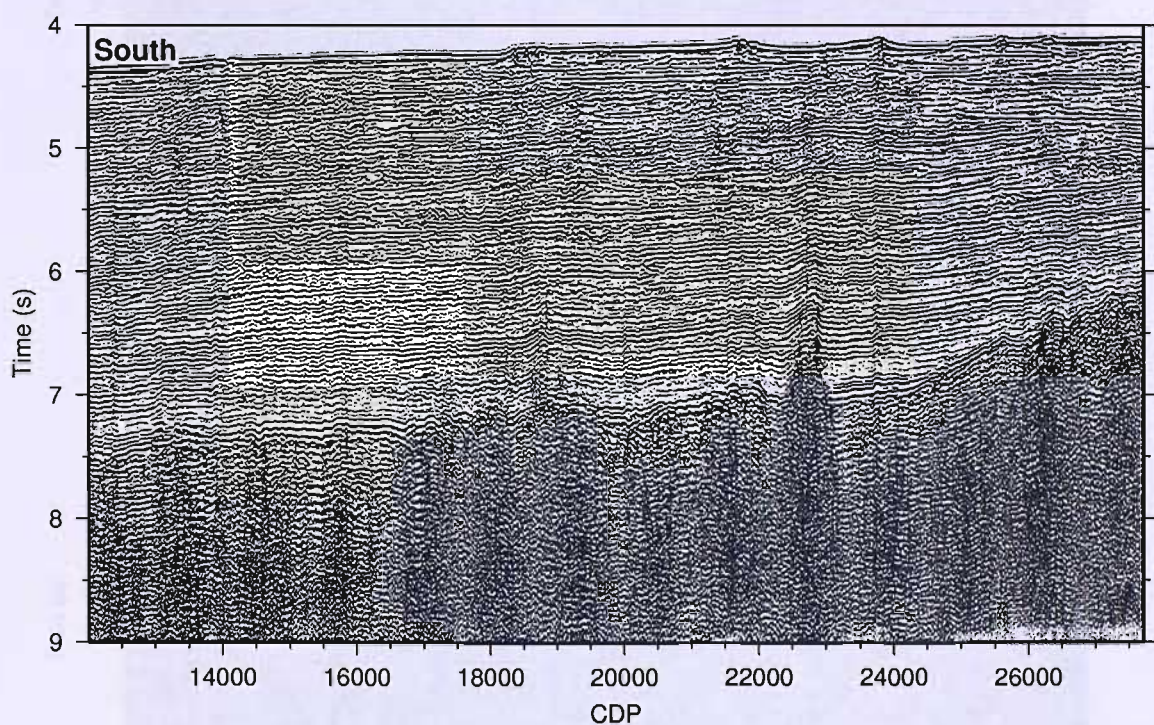
Figure 2.22: Final stack of line 4: data are processed (see text for description) but not migrated.
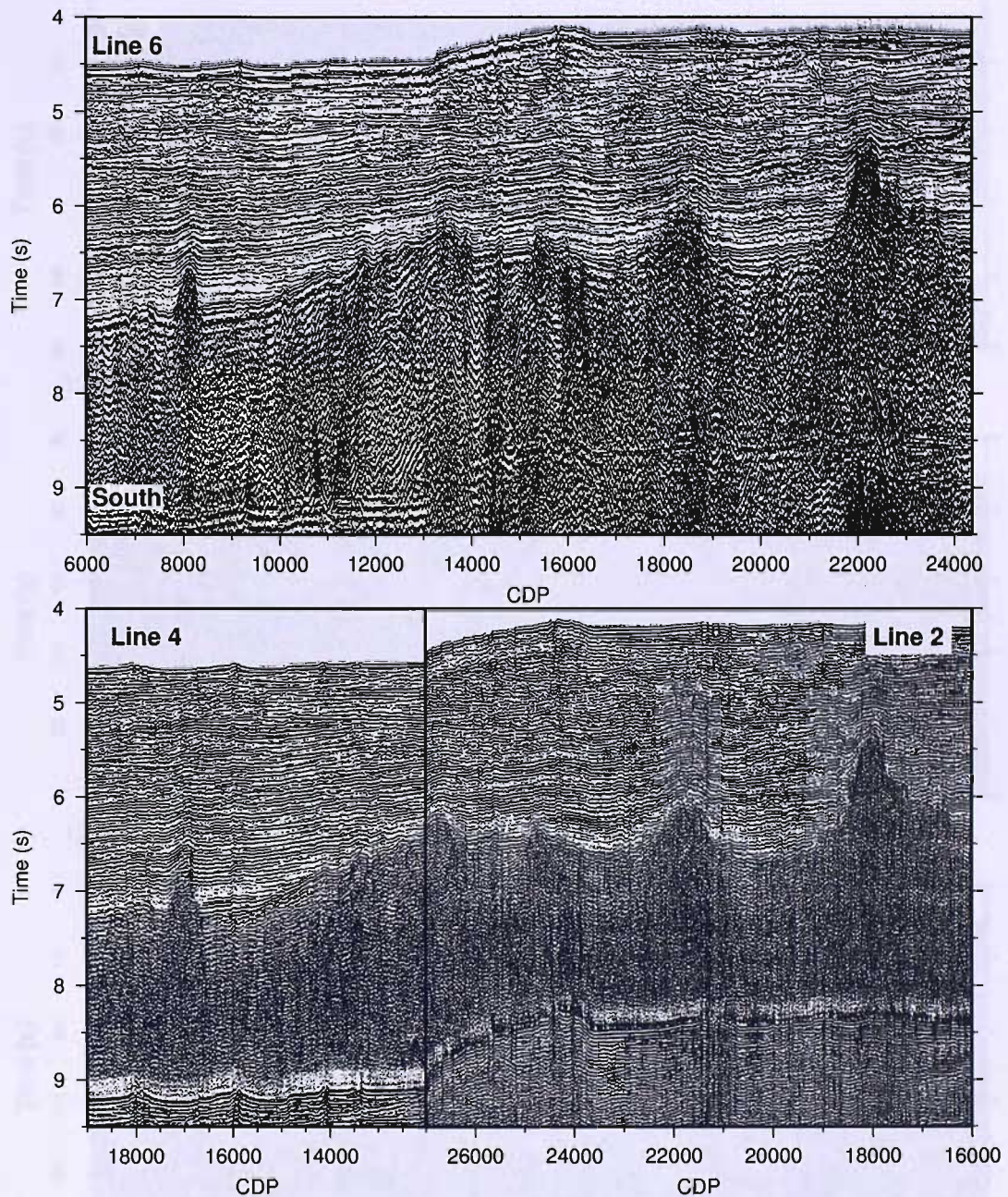
Figure 2.23: Comparison of coincident lines: Line 6 *top* is plotted with the coincident sections of lines 2 and 4 (bottom) for comparison. The sediments on all lines are well imaged, but basement is very poorly resolved on lines 2 and 4 due to the errors made during acquisition (Section 2.2).
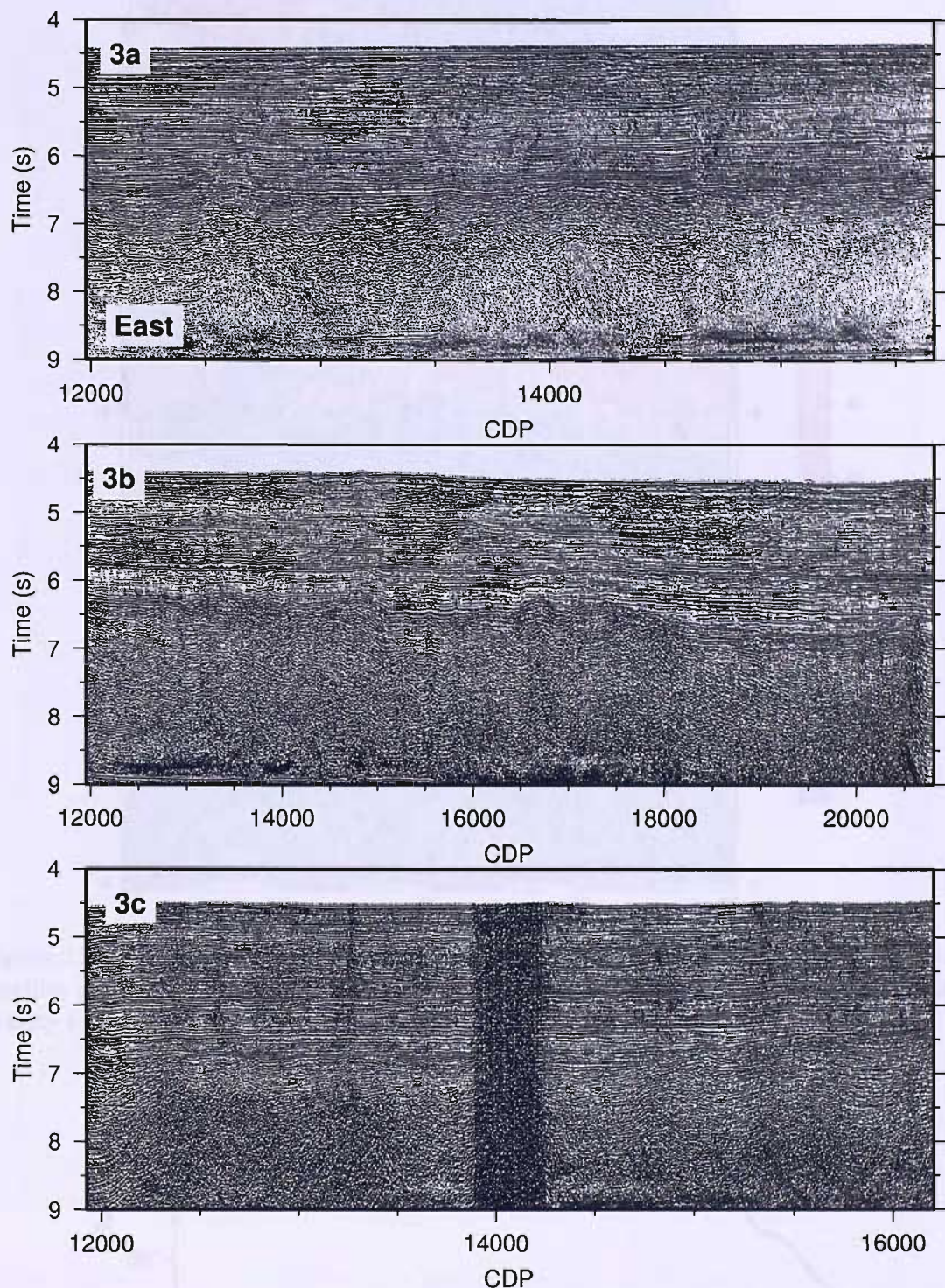
Figure 2.24: Final stack of line 3: data are processed and migrated.
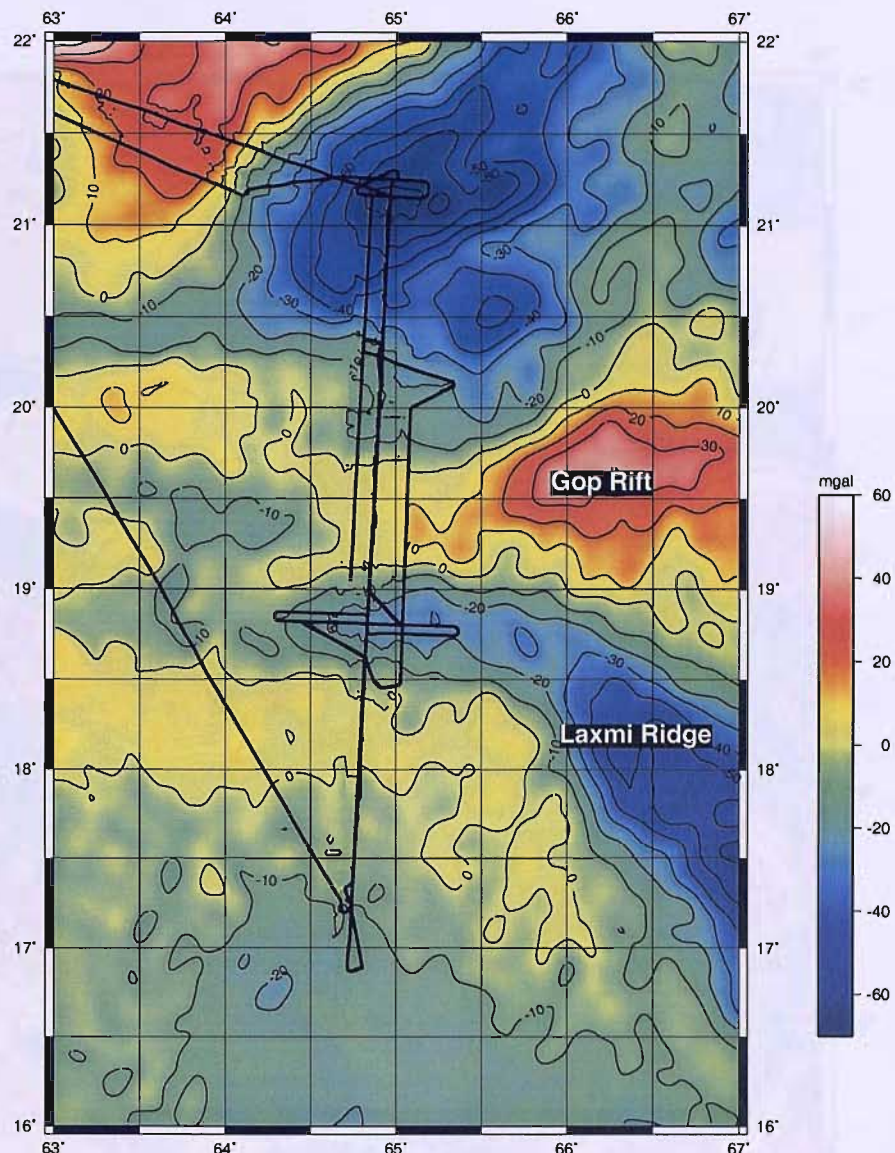
Figure 2.25: CD144 and satellite gravity: Shipboard gravity (black line) is combined with satellite gravity (Smith and Sandwell, 1997). Laxmi Ridge is identified as a prominent gravity low; Gop Rift has a positive gravity anomaly signature.
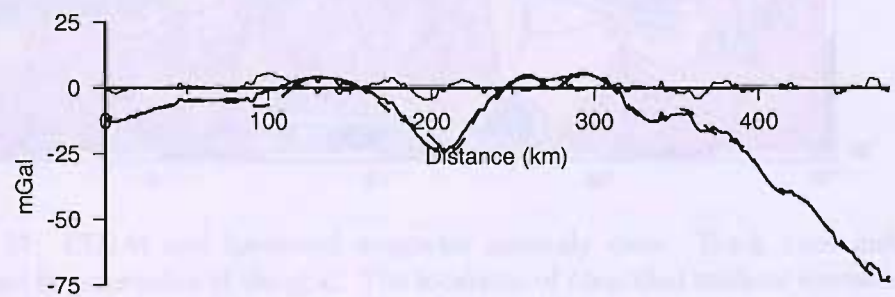
Figure 2.26: Comparison of CD144 and satellite gravity: The shipboard (solid line) and satellite gravity (dashed line) differ by a maximum of 5.5 mGal, RMS difference is 0.35 mGal. The difference between the two datasets is shown (grey line).

51
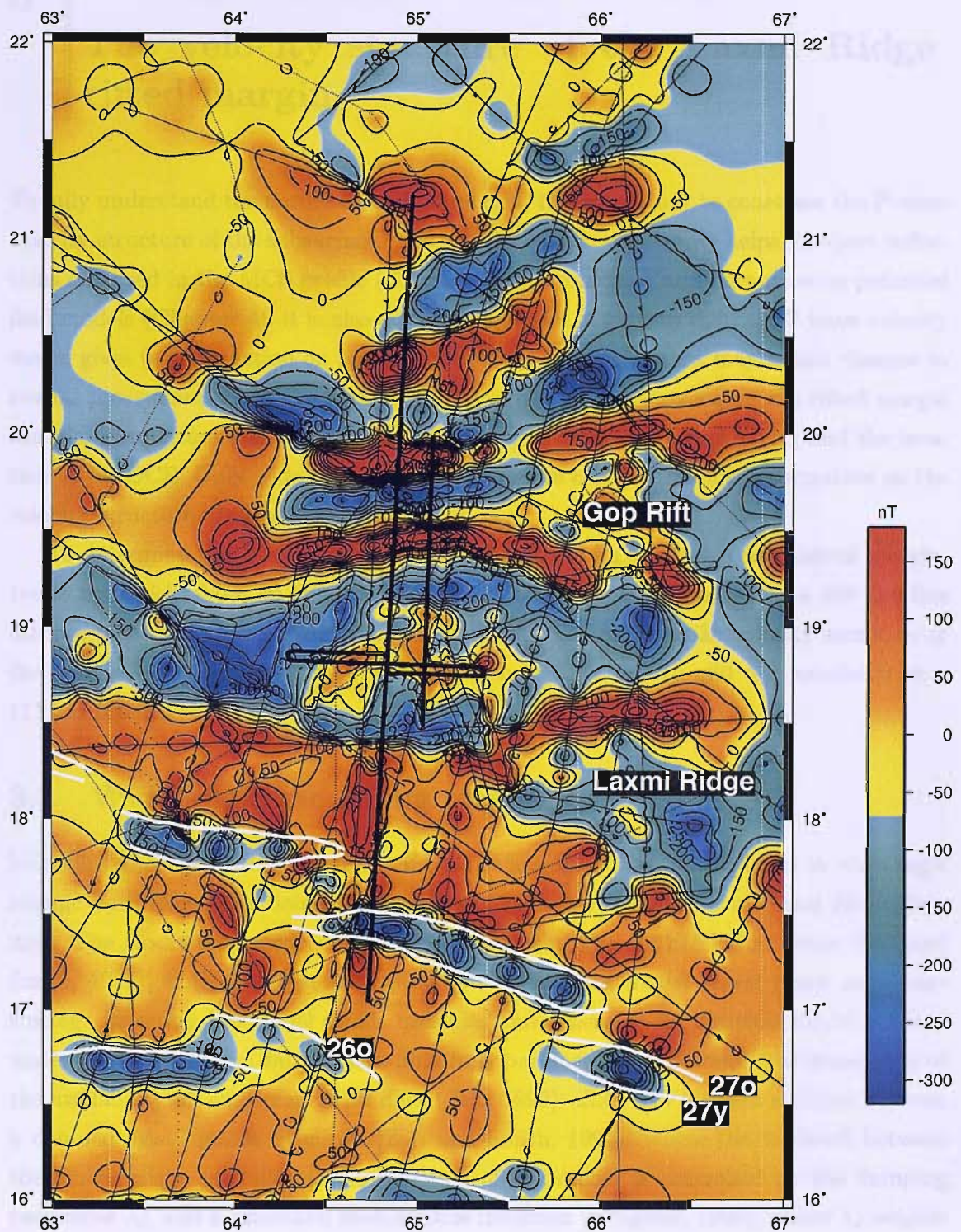
Figure 2.27: CD144 and historical magnetic anomaly data: Track lines indicate data points used in generation of the grid. The locations of identified seafloor spreading anomalies (Miles et al., 1998) are indicated by heavy white lines. Note the offset in the seafloor spreading anomalies: this is due to fracture zones. The linear anomalies observed in Gop Rift will be discussed in Section 4.2.2.

3

The velocity structure of the Laxmi Ridge rifted margin

To fully understand the nature of a rifted margin, it is important to constrain the P-wave velocity structure of the subsurface. The velocity structure not only helps interpret reflections observed in the MCS profile (Chapter 5) and construct and parameterise potential field models (Chapter 4), it is also an invaluable tool in its own right. A P-wave velocity model gives us information on bulk lateral velocity contrasts that may reflect changes in crustal provenance. Both the horizontal and vertical velocity structure of a rifted margin can place important constraints on rifting style, magmatism during rifting and the location of the OCB. Only wide-angle seismic techniques can give reliable information on the velocity structure of the deep subsurface.

To determine the P-wave velocity structure of the Laxmi Ridge continental margin, travel time picks from 26 OBS/H and 3 sonobuoys were modelled along a 480 km line orthogonal to the strike of the margin (Fig. 3.1). The along-strike velocity structure of the margin, discussed in Section 3.6, is constrained by 4 OBS and one sonobuoy on a 111 km profile.

3.1 Wide-angle modelling strategy

Modelling the observed travel times of both reflected and refracted phases in wide-angle seismic data allows the determination of sub-surface velocity structure and discontinuities. The model presented here was generated using the *RAYINVR* software (Zelt and Smith, 1992), both to invert data picks and to forward model travel times using ray-tracing. Inverting the model avoids user-bias and generates the simplest model without under or overfitting the data. A non-uniformly parameterised inversion was chosen due to the availability of coincident MCS data (Zelt, 1999). *RAYINVR* offers a choice between a damped least-squares inversion (Zelt and Smith, 1992), where the trade-off between the model misfit and allowed perturbation of the model is controlled by the damping parameter λ_d, and a smoothed least-squares inversion (Bruguier, 1996), where λ_s weights the trade off between misfit and model smoothness. The smoothed least squares algorithm was chosen, as the damped least squares routine can become unstable if there is a large lateral velocity gradient (Zelt and Smith, 1992). A limitation of the smoothed least-squares inversion is that it attempts to smooth the model horizontally. This is not appropriate for modelling across continental margins, where the velocity structure can
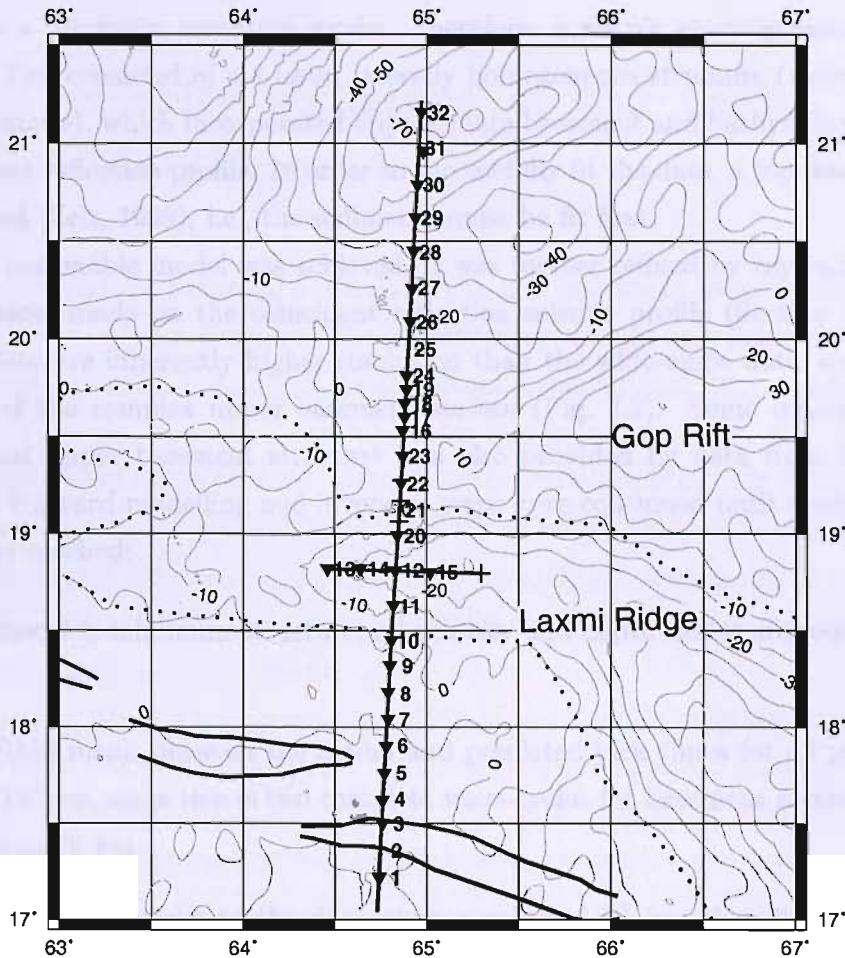
Figure 3.1: Location of wide-angle velocity models: the main (N-S) line is orthogonal to the Laxmi Ridge continental margin, and the velocity structure is constrained by 26 OBS/H (inverted triangles) and 3 sonobuoys (crosses). The along-strike (E-W) line is constrained by 4 OBS/H and one sonobuoy. The outline of Laxmi Ridge is marked with a dashed line. Background field is free air gravity in mGal. Heavy grey lines are the magnetic picks of Miles et al. (1998) for the old and young limits of Chron 27. OBS/H numbers with no associated symbol did not return useful data.

have significant lateral variations. To minimise this problem, groups of picks sampling the same part of the margin were inverted simultaneously. This method ensures that smoothing only occurs across parts of the model with a similar velocity structure. The modelling strategy involved inverting a model layer with a constant velocity gradient until a state of minimum misfit was achieved. The upper and lower velocities were then inverted separately. After the velocity was constrained, the horizon at the base of the layer would be adjusted by inverting wide-angle reflections from it, then a second iteration of velocity modelling was run. After each inversion step, the forward (ray tracing) step was run, both to apply the changes made by the inversion software and to check their effects.

Since any model fitting the data to a given misfit is non-unique, it is important

to generate a minimum structure model. therefore, a simple starting model was used (Fig. 3.2). This consisted of a 4 layer, laterally homogeneous structure (water, sediment, crust and mantle), which incorporated approximate basement and bathymetry picks from the coincident reflection profile. In order to successfully fit the data, a top-down approach must be used (Zelt, 1999), i.e., the sediments must be fit first.

Once a reasonable model was achieved, it was further refined by raytracing acoustic basement picks made on the coincident reflection seismic profile (Section 5.2.4). The reflection data are inherently higher resolution than the wide-angle data, so give better constraint of the complex upper basement surface (Fig. 3.2). Some constraint on the sediment and upper basement structure was also provided by data from 3 disposable sonobuoys. Forward modelling and inversion steps were continued until a set of stopping criteria were reached:

1. The model is minimum structure; all velocity and depth nodes are required by the data.

2. The RMS misfit between the actual and predicted pick times for all phases is less than 120 ms, since this is two complete wave-cycles for basement arrivals at ranges less than 70 km.

3. The fit of the model to the data gives a value of χ^2 less than 2, i.e., the misfit between the observed and predicted travel times is not statistically significant. χ^2 is defined as,

$$\chi^2 = \frac{1}{n-1} \sum_{i=1}^{n} \frac{(t_{icalc} - t_{iobs})^2}{unc_i^2} \qquad (3.1)$$

where the observed travel time (t_{iobs}) fits the predicted travel time (t_{icalc}) within an assigned uncertainty (unc_i) for the ith pick (Staples et al., 1997). A $\chi^2 > 2$ means the model fits the data poorly, while a $\chi^2 < 1$ indicates that the model is overfitting the data within the assigned uncertainty level. A χ^2 of 1 would be considered a statistically perfect fit to the data, but the desired fit is relaxed for this model due to the complexity of the margin. Decreasing the velocity or depth node spacing would reduce the value of χ^2 at the cost of reducing the model resolution, so it is an acceptable compromise to have a $\chi^2 > 1$ and a well resolved model (Zelt, 1999).

4. The model is geologically reasonable and does not contradict any other dataset in the same region.
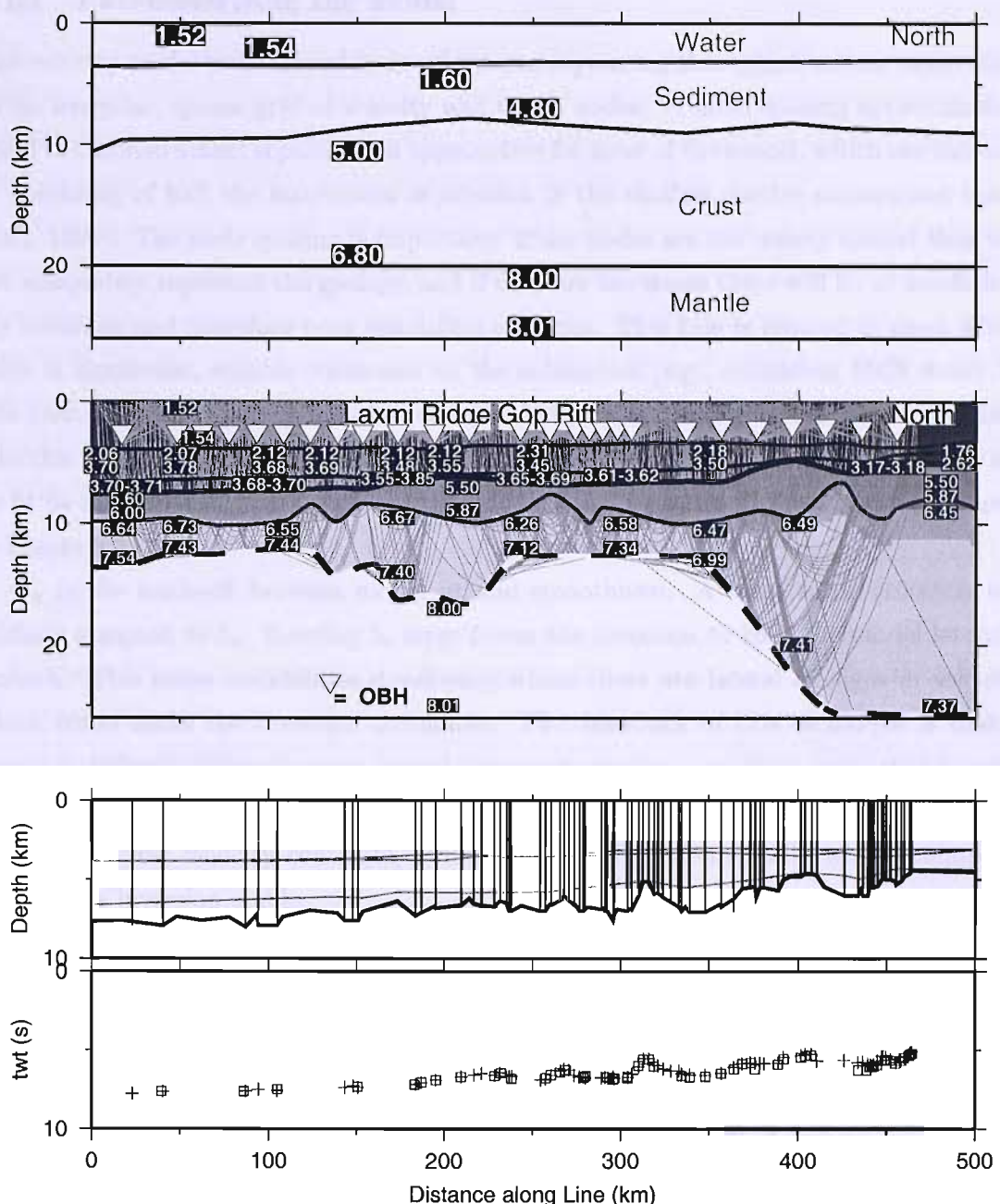
Figure 3.2: Building a velocity model: *Top:* starting velocity model, consisting of 4 layers with laterally homogeneous velocity structures. Velocity units are km s^{-1}. Known bathymetry and the approximate depth of the top basement reflector are inputted. *Middle:* After several iterations of inverting and forward modelling, an intermediate velocity model is constructed. Inverted triangles are OBS/H and black labels are velocity nodes, units are km s^{-1}. Raypaths through the model are shown in grey. *Bottom:* Top basement structure is refined using picks from the coincident reflection profile, MCS lines 2 and 4 (Sections 2.3.6 and 2.3.7). The top panel shows normal incidence ray paths (dark grey) from the streamer to the reflection point on the basement surface (black line). The bottom panel shows the fit of the picked travel times (crosses) to those predicted by the model (squares); the RMS residual is 102 ms and the χ^2 is 1.055.

3.1.1 Parameterising the model

The velocity model is developed by inversion and raytracing through structure constrained by an irregular, sparse grid of velocity and depth nodes. A node spacing approximately equal to the instrument separation is appropriate for most of the model, which can increase to a spacing of half the instrument separation in the shallow, better constrained layers (Zelt, 1999). The node spacing is important: if the nodes are too widely spaced they will not adequately represent the geology, and if they are too dense there will be to insufficient ray coverage and therefore poor resolution of nodes. This rule is relaxed in cases where there is significant, reliable constraint on the subsurface (e.g., coincident MCS data). In this case, the node spacing may be reduced. Velocity and depth nodes were introduced into the velocity model only where required by the data; i.e., where the data could not be fit by manipulating the simple starting model. The locations of these nodes are shown in Figure 3.3.

λ_s is the trade-off between model fit and smoothness. A large value (100000) was initially assigned to λ_s. Keeping λ_s large forces the inversion to keep the model laterally smooth. This stops instabilities developing where there are lateral changes in velocity, which could make the inversion unreliable. The drawback of this technique is that it makes it difficult to invert across lateral changes in geology and their associated velocity contrasts. In order to solve this problem, the value of λ_s was gradually reduced when modelling across velocity contrasts, reducing the misfit incrementally while attempting to keep the inversion stable.
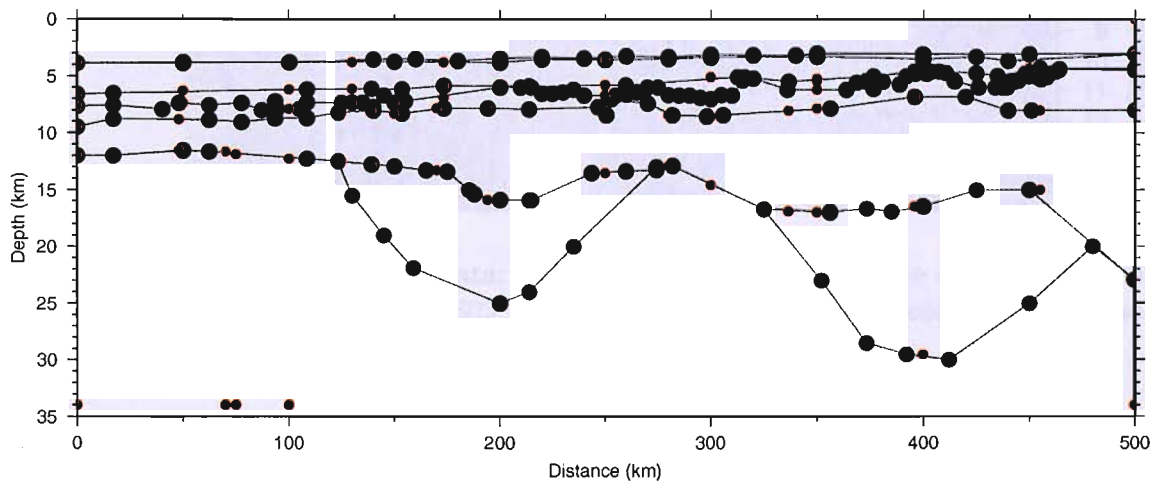
Figure 3.3: Depth and velocity nodes in the model: the location of depth nodes (black circles) and velocity nodes (red circles) in the velocity model are plotted. The model is minimum structure: nodes were added only where required by the data.

3.1.2 Phase picking

Phases identified in the wide-angle data (Fig. 3.4) were hand picked using the picking utility in *ProMAX*. The second zero crossing of a phase waveform was picked rather than the first arrival, as it is often easier to identify (Fig. 3.5). This was corrected for by subtracting half a cycle (30 ms) from the picked time. If picking this point was impractical because of interference from other phases, the next wave cycle was picked and an appropriate correction applied.

Picking was mostly done on the hydrophone component of the data, rather than the vertical geophone, as the signal-to-noise ratio is higher (Section 2.1.1). The exceptions were OBS28, where the vertical geophone was used and OBS18, where one of the horizontal components was used. In both cases, this was due to poor data quality on the other components. The instrument locations in model space and the ray coverage through the model is shown in Figure 3.6. All of the picks used in the wide-angle model, their fit to the model and the associated raypaths through the model are shown in Figures 3.7 to 3.20.
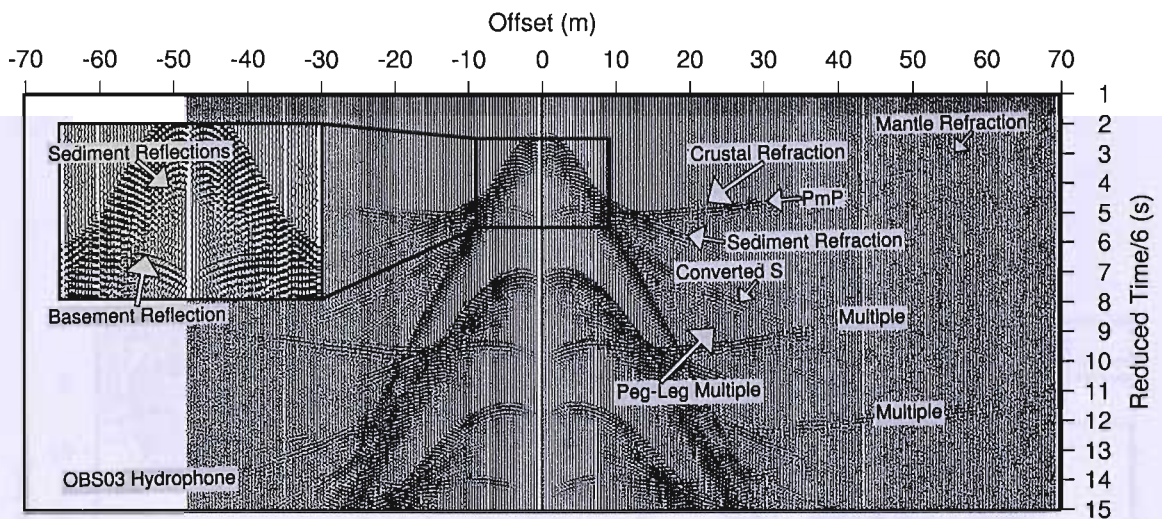
Figure 3.4: Phases in wide-angle data: Typical record section with the observed phases labelled. These data are from OBS03, which is from the southern (oceanic) end of the profile.
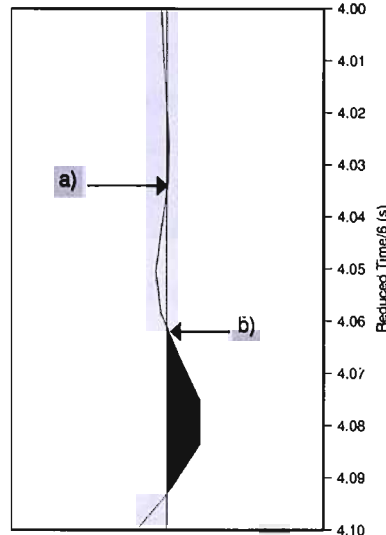
Figure 3.5: First break picking: The first arrival *a)* is the time when energy from a phase first arrives at the receiver. The second zero crossing, *b)* is generally picked and a half wavecycle (30 ms) correction applied to correct back to first arrival time. This is because the second zero crossing is often a stronger arrival and therefore easier to pick accurately. This is example is a refracted arrival from the upper basement recorded by OBS07.
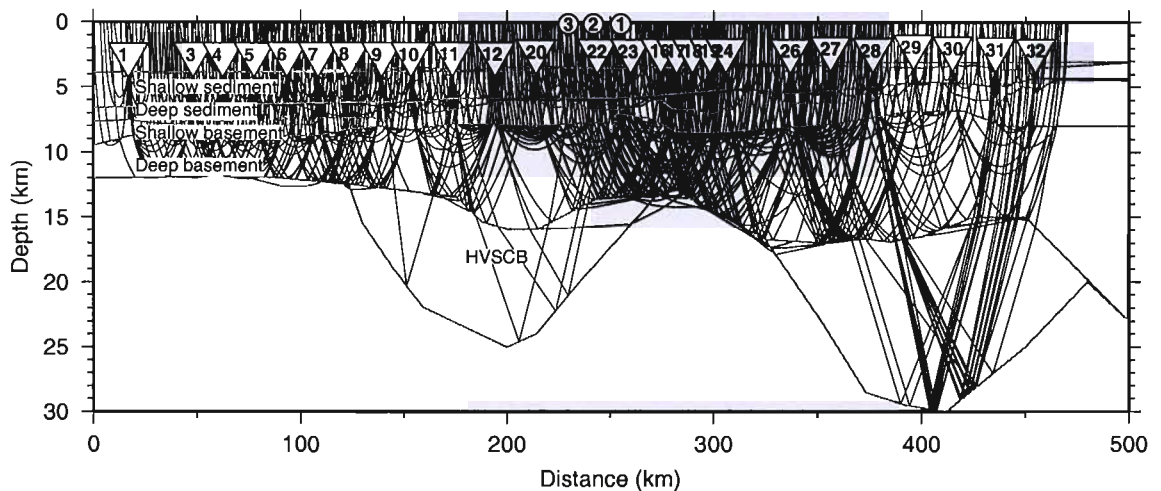
Figure 3.6: Instrument locations in model space: OBS/H are indicated by white inverted triangles; sonobuoys are indicated by circles. The numbers in the symbols are the deployment numbers for each instrument. Ray coverage through the final model is plotted to give and idea of the degree of constraint on the model; every 25th ray is plotted.
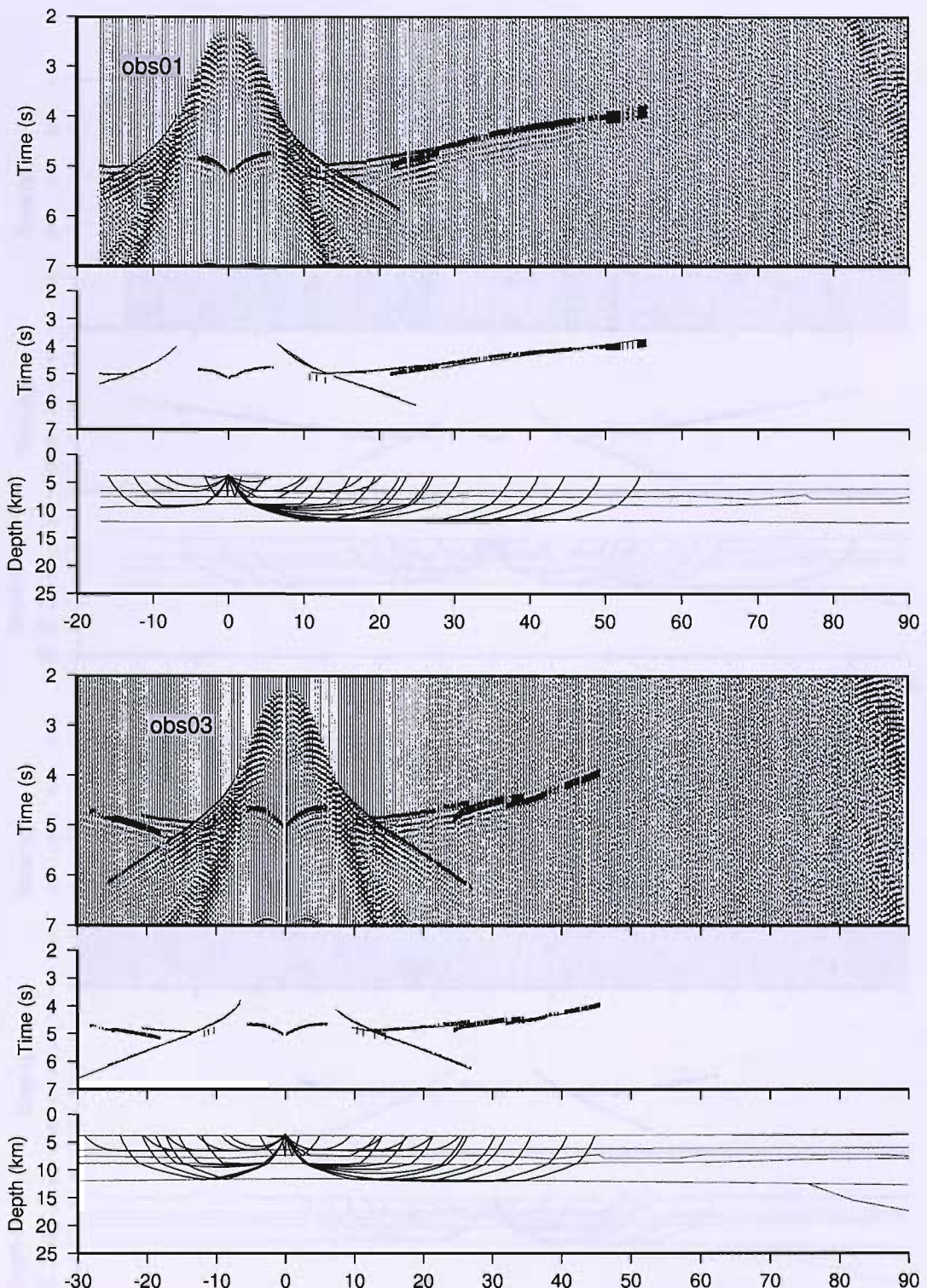
Figure 3.7: OBS/H data, travel-time fit and ray paths through model: *top:* OBS01 *bottom:* OBS03. In each figure, top plot is actual data; picks are overlain, bar size is proportional to pick uncertainty. Hydrophone component is shown unless otherwise stated; every third trace is plotted. Velocities are reduced at 6 km s^{-1}. Middle plot is picks (black bars) versus predicted arrival times from raytracing through the model (grey lines). Bottom plot shows raypaths through the model for every 25th pick.
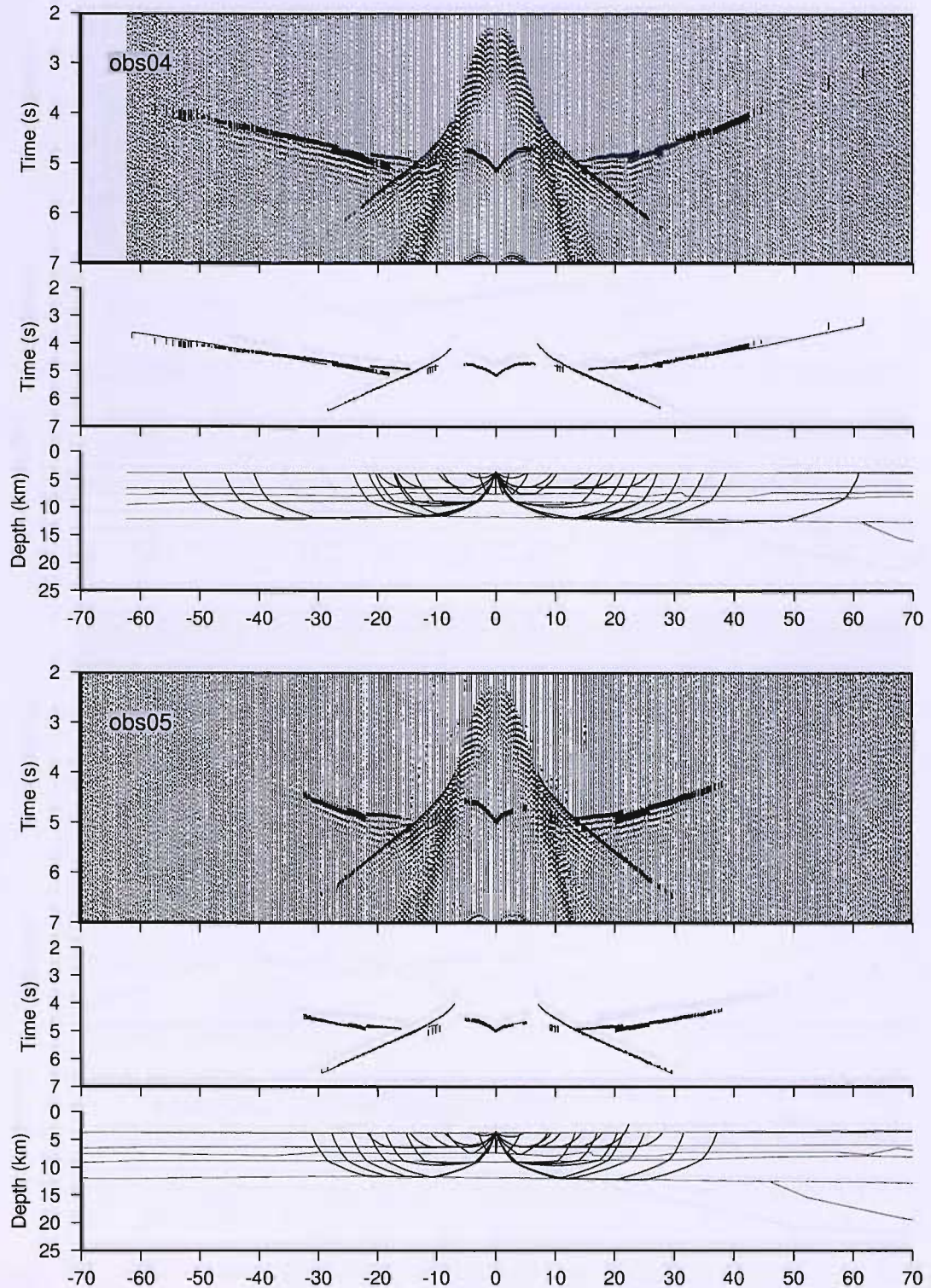
Figure 3.8: OBS/H data, travel-time fit and ray paths through model 2: *top:* OBH04 *bottom:* OBS05. Other details as Figure 3.7.
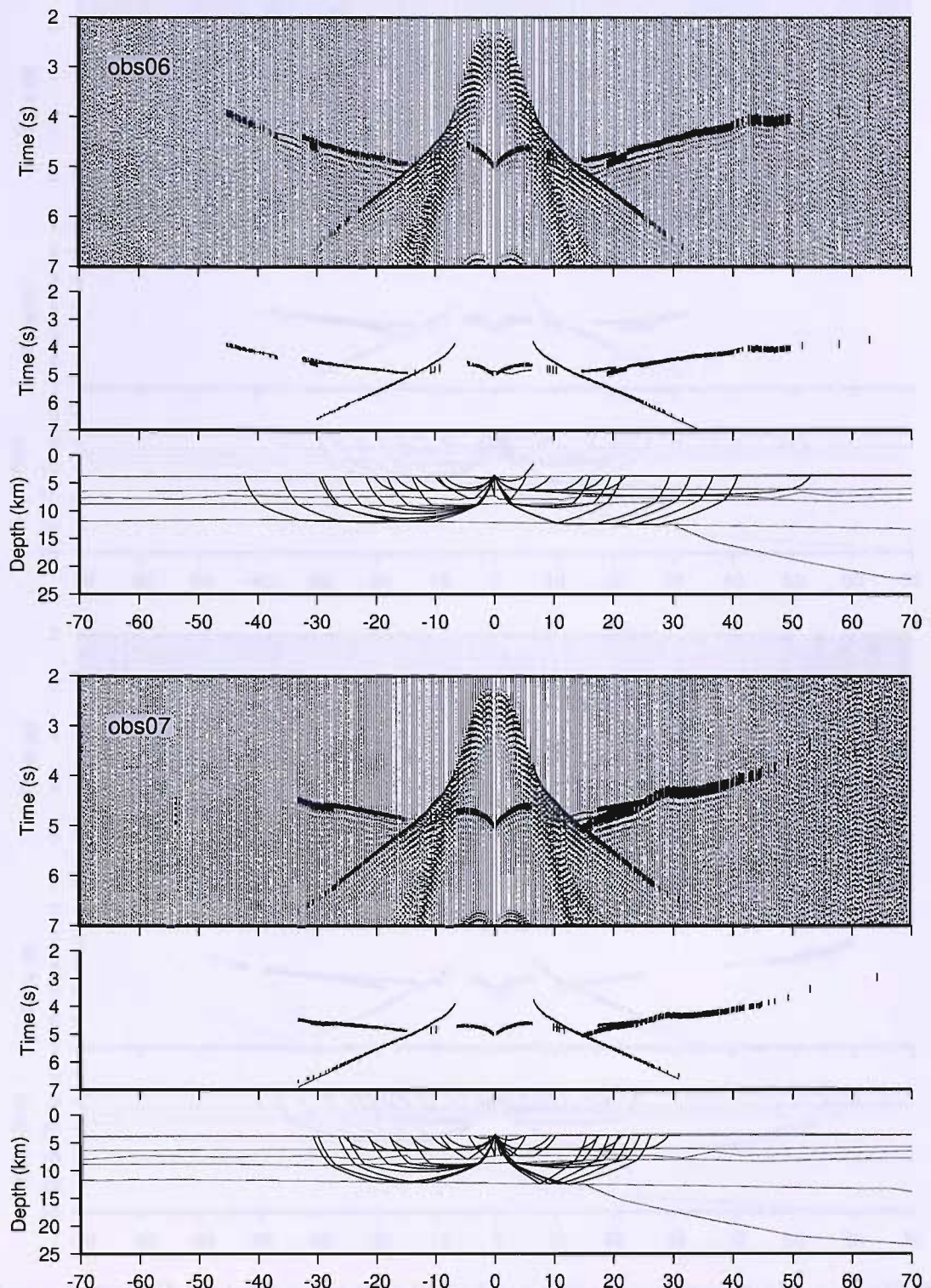
Figure 3.9: OBS/H data, travel-time fit and ray paths through model 3: *top:* OBH06 *bottom:* OBS07. Other details as Figure 3.7.
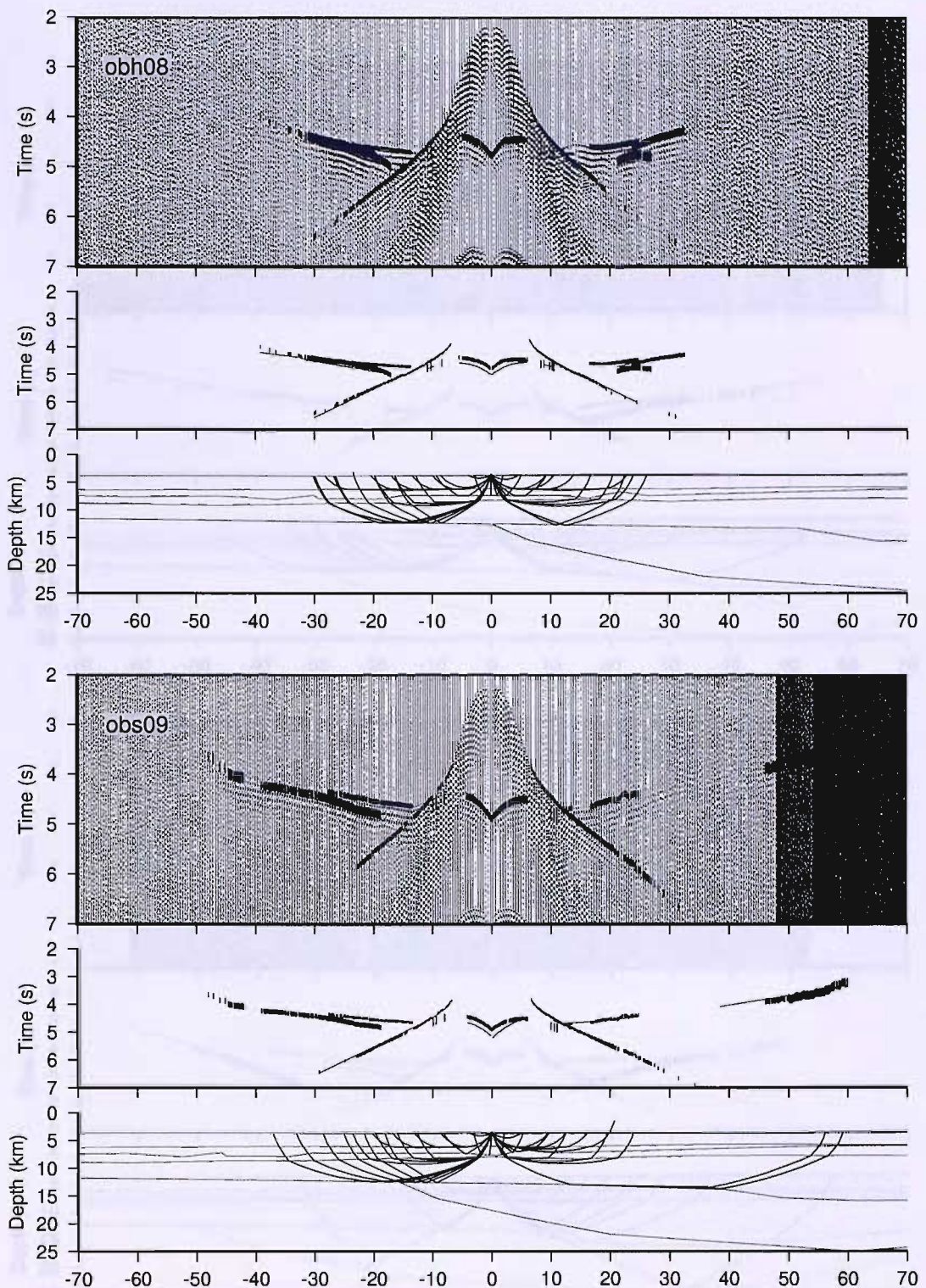
Figure 3.10: OBS/H data, travel-time fit and ray paths through model 4: *top:* OBH08 *bottom:* OBS09. Other details as Figure 3.7. The poor fit to the basement reflections is a consequence of the difficulty of picking wave cycles consistently between MCS and OBS/H data. MCS picks were preferentially fitted: arrivals are easier to pick on MCS data so these picks are considered more reliable.
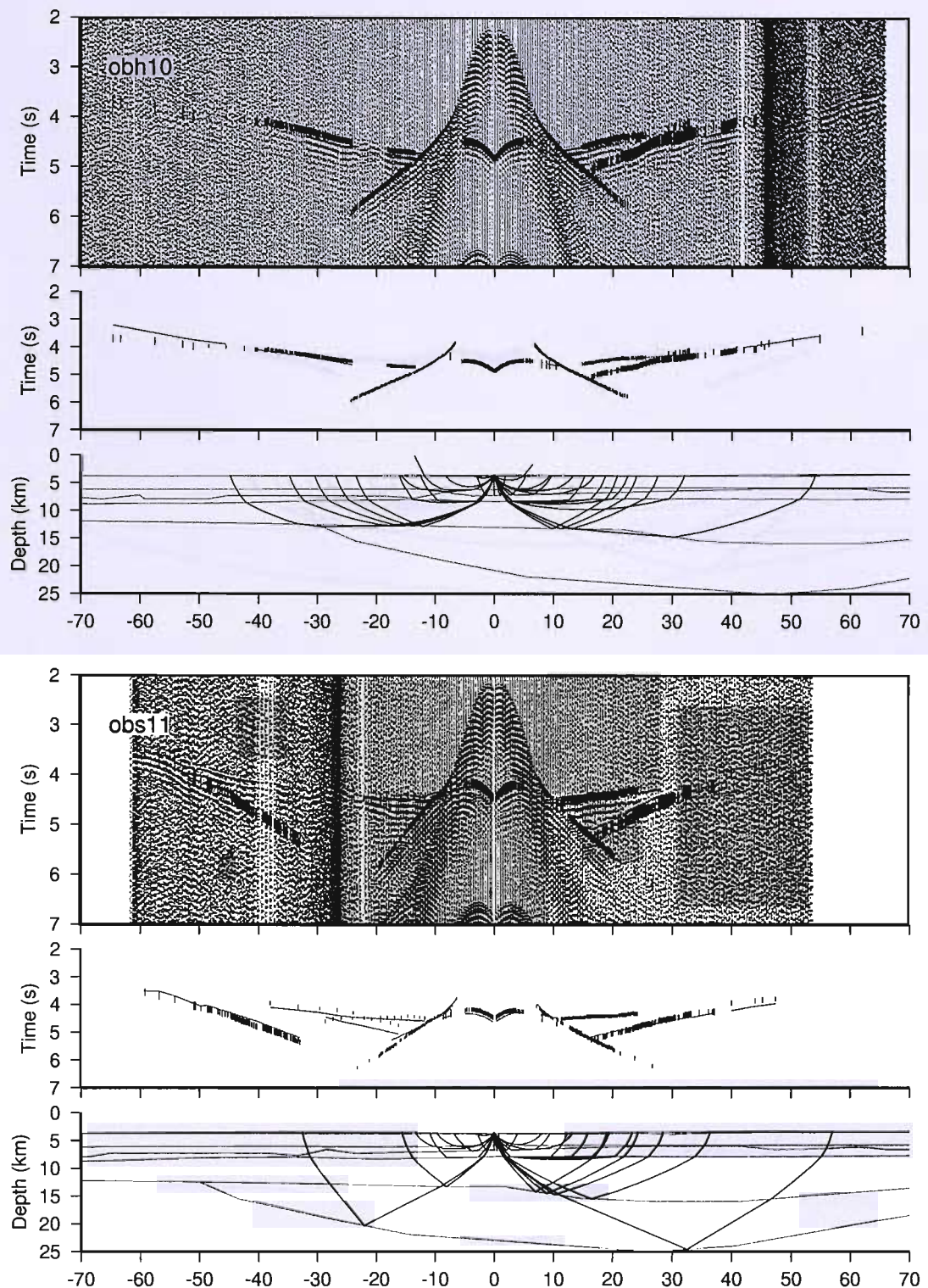
Figure 3.11: OBS/H data, travel-time fit and ray paths through model 5: *top:* OBH10 *bottom:* OBS11. Other details as Figure 3.7.
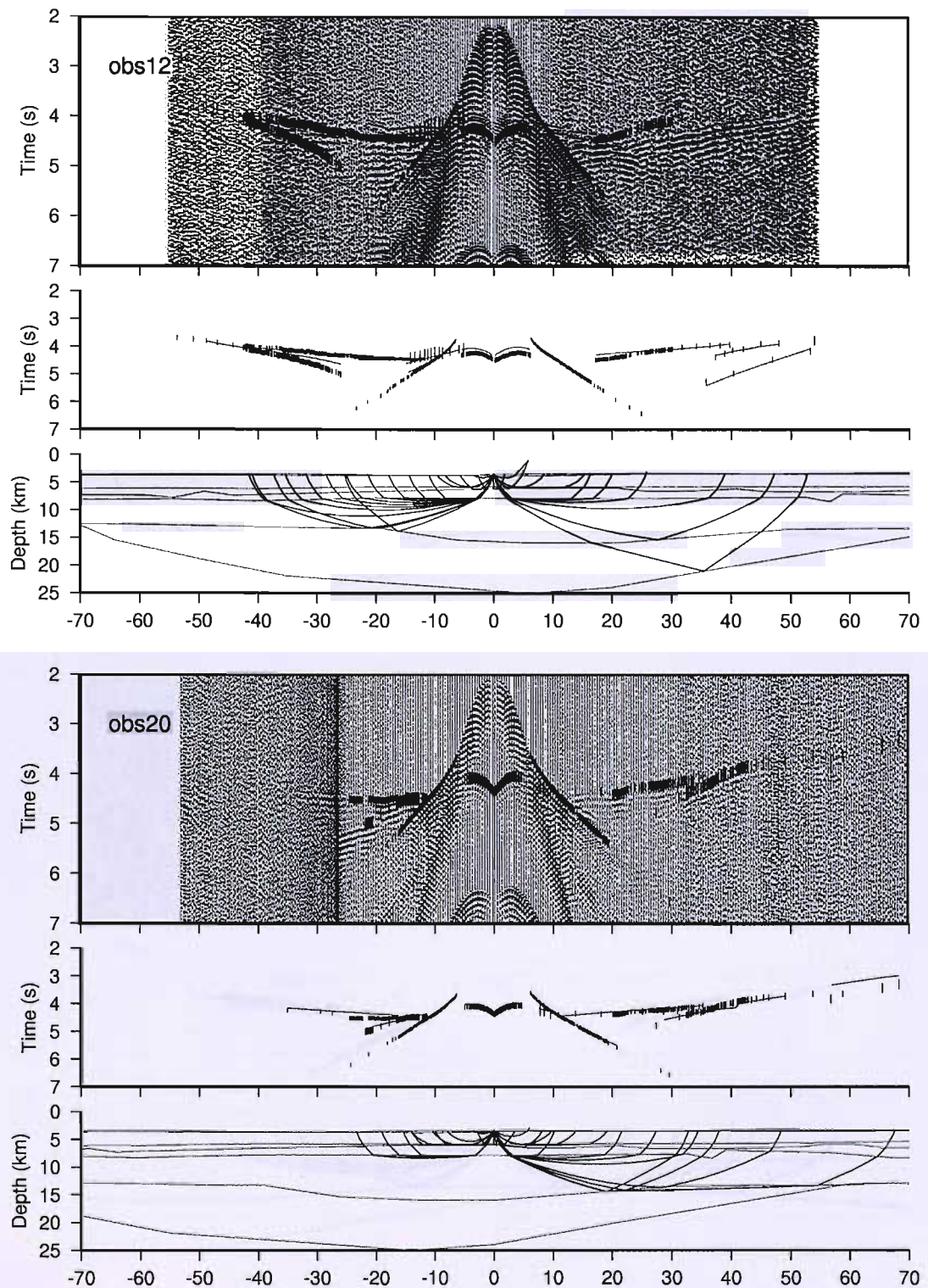
Figure 3.12: OBS/H data, travel-time fit and ray paths through model 6: *top:* OBS12 *bottom:* OBS20. Other details as Figure 3.7.
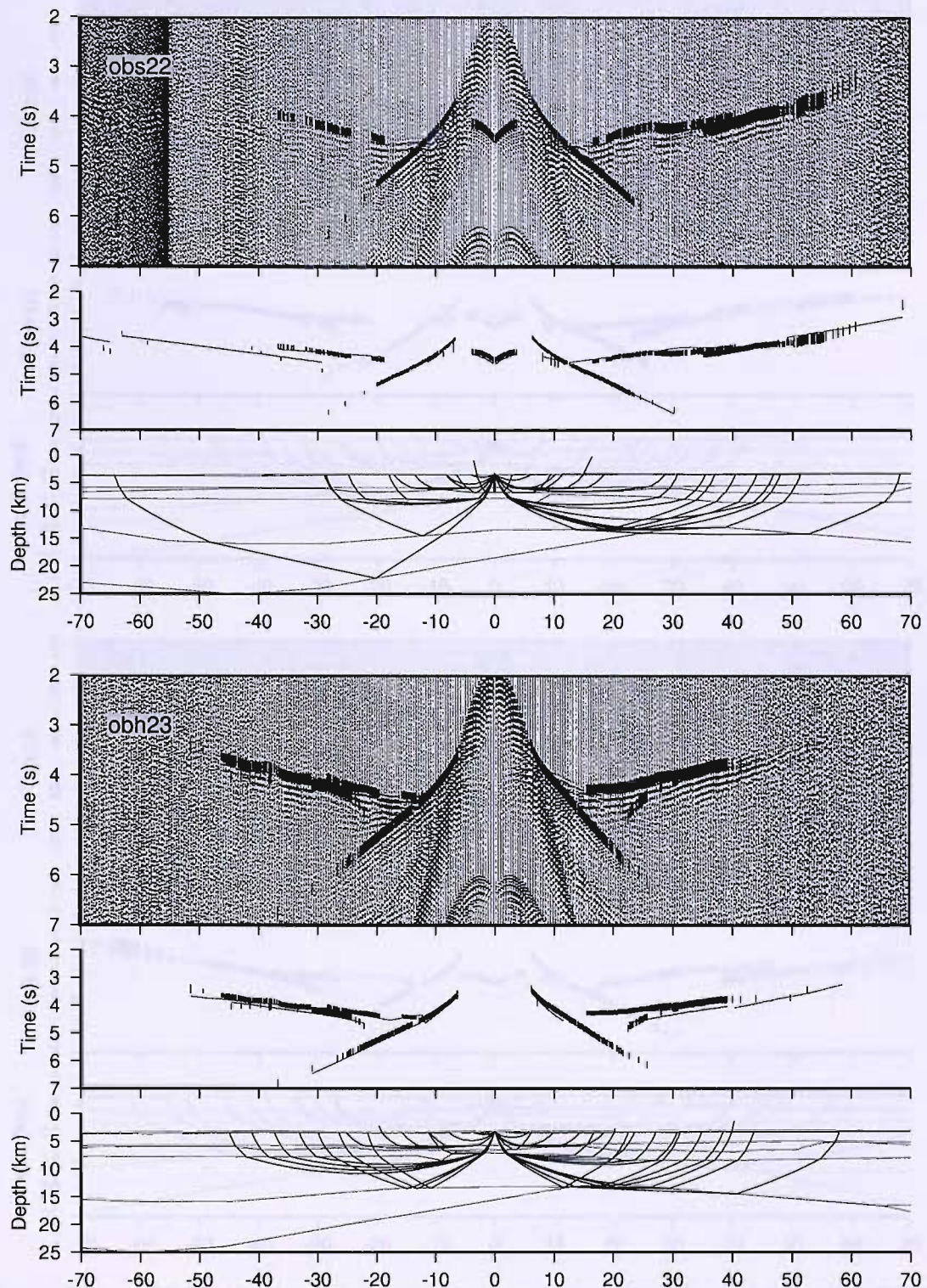
Figure 3.13: OBS/H data, travel-time fit and ray paths through model 7: *top:* OBS22 *bottom:* OBH23. Other details as Figure 3.7.
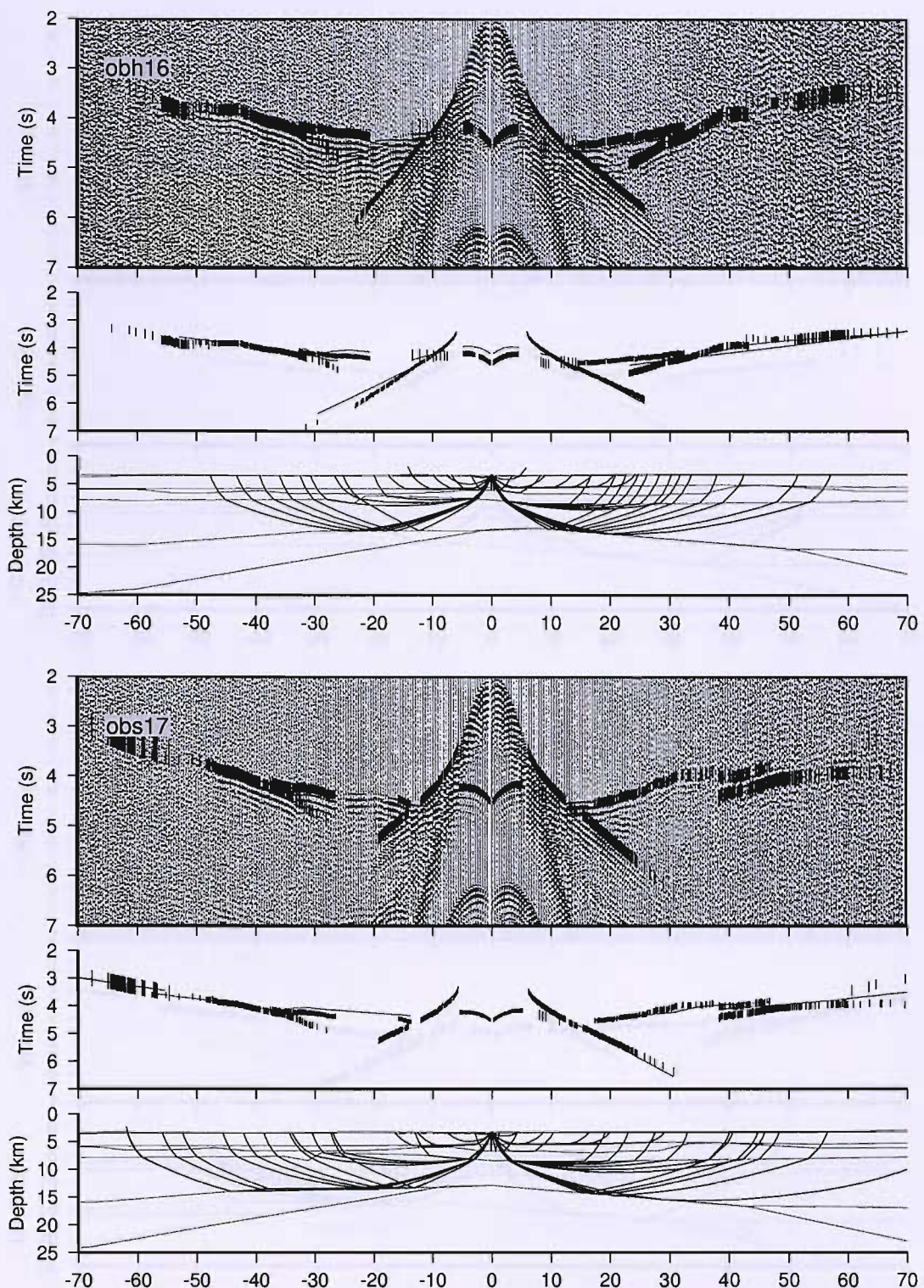
Figure 3.14: OBS/H data, travel-time fit and ray paths through model 8: *top:* OBS16 *bottom:* OBS17. Other details as Figure 3.7. The poor fit to the basement reflections is a consequence of the difficulty of picking wave cycles consistently between MCS and OBS/H data. MCS picks were preferentially fitted.
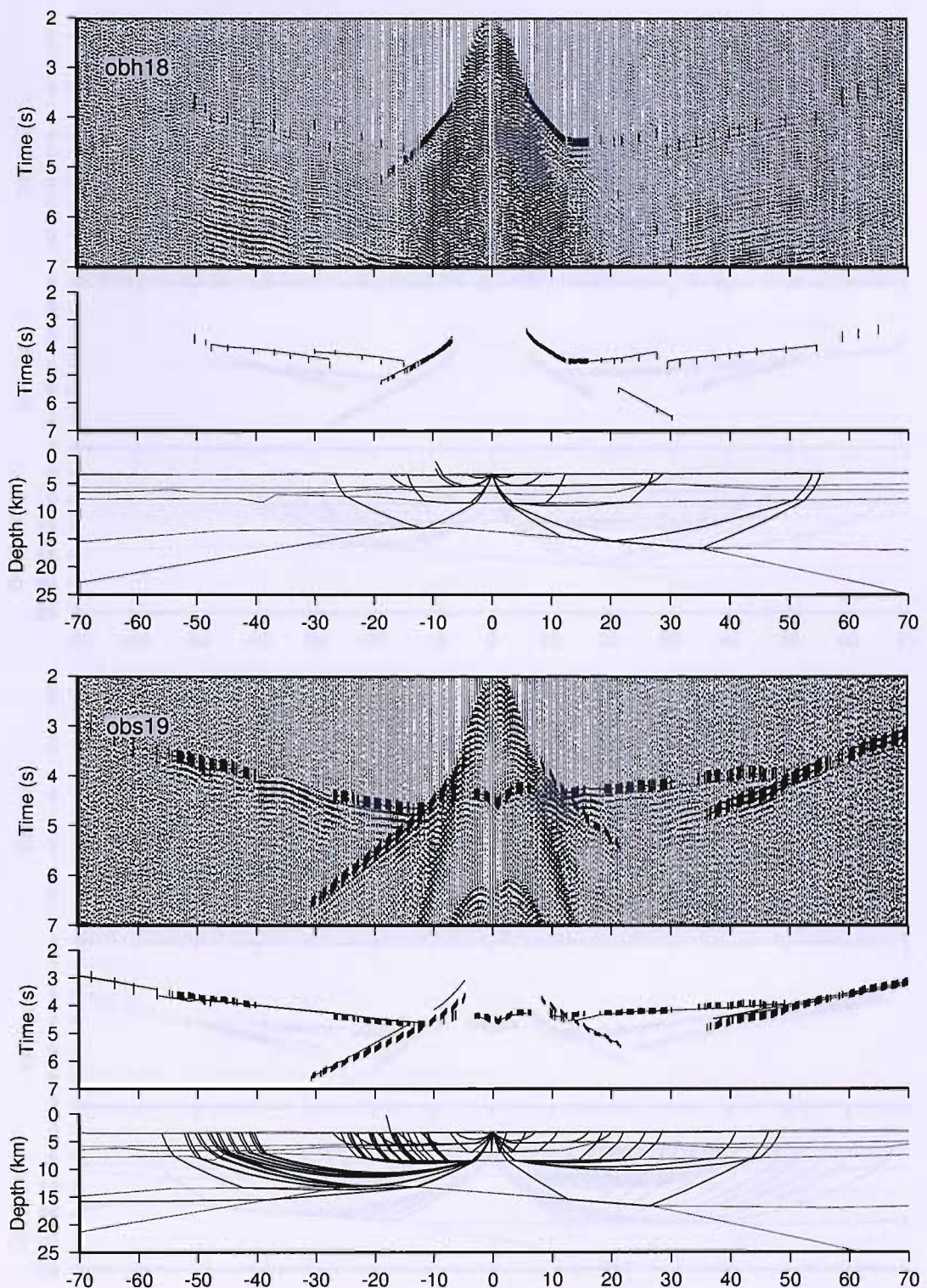
Figure 3.15: OBS/H data, travel-time fit and ray paths through model 9: *top:* OBS18, horizontal geophone (this was the only only component that returned data). *bottom:* OBS19. Other details as Figure 3.7.
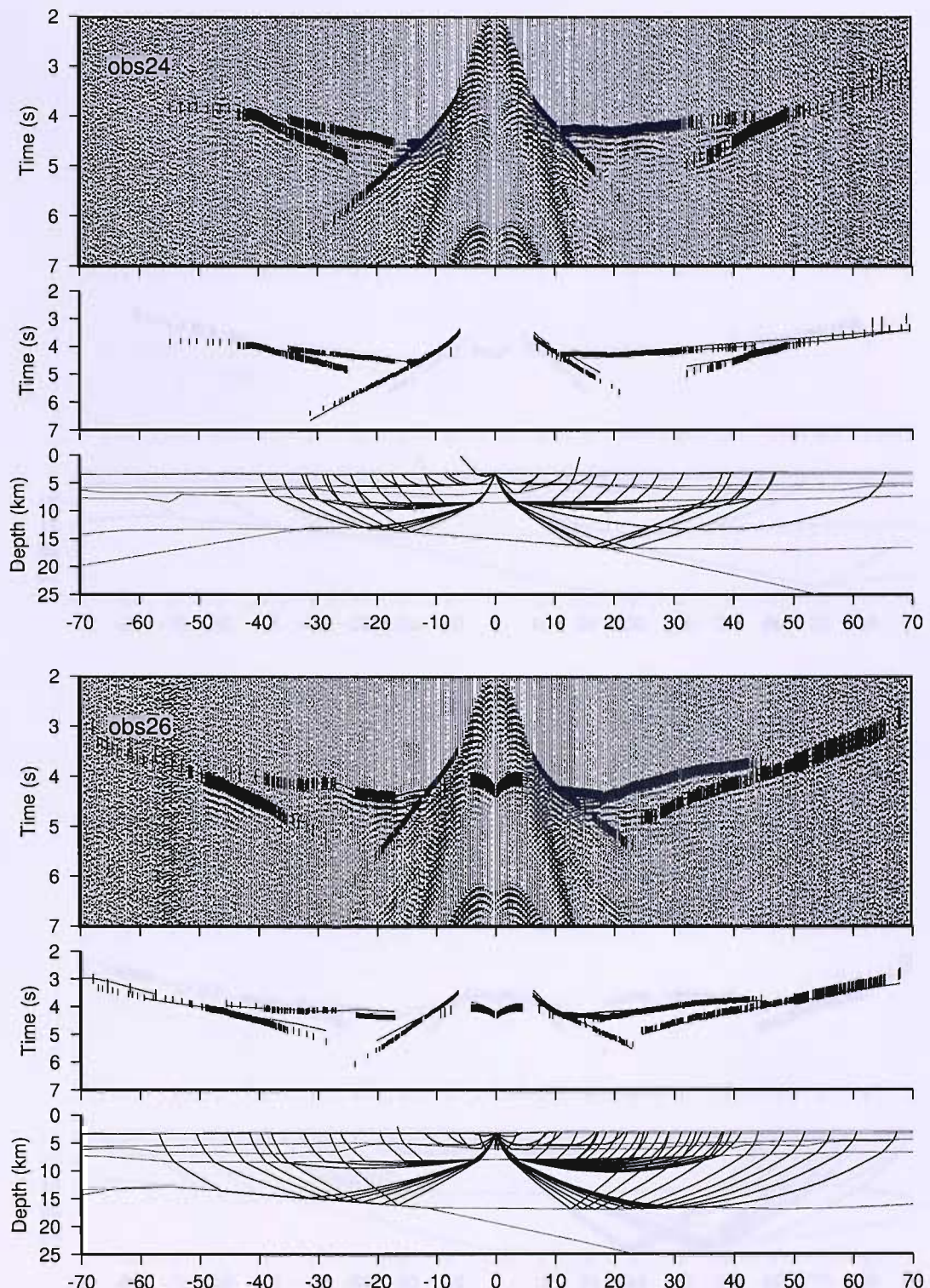
Figure 3.16: OBS/H data, travel-time fit and ray paths through model 10: *top:* OBS24 *bottom:* OBS26. Other details as Figure 3.7.
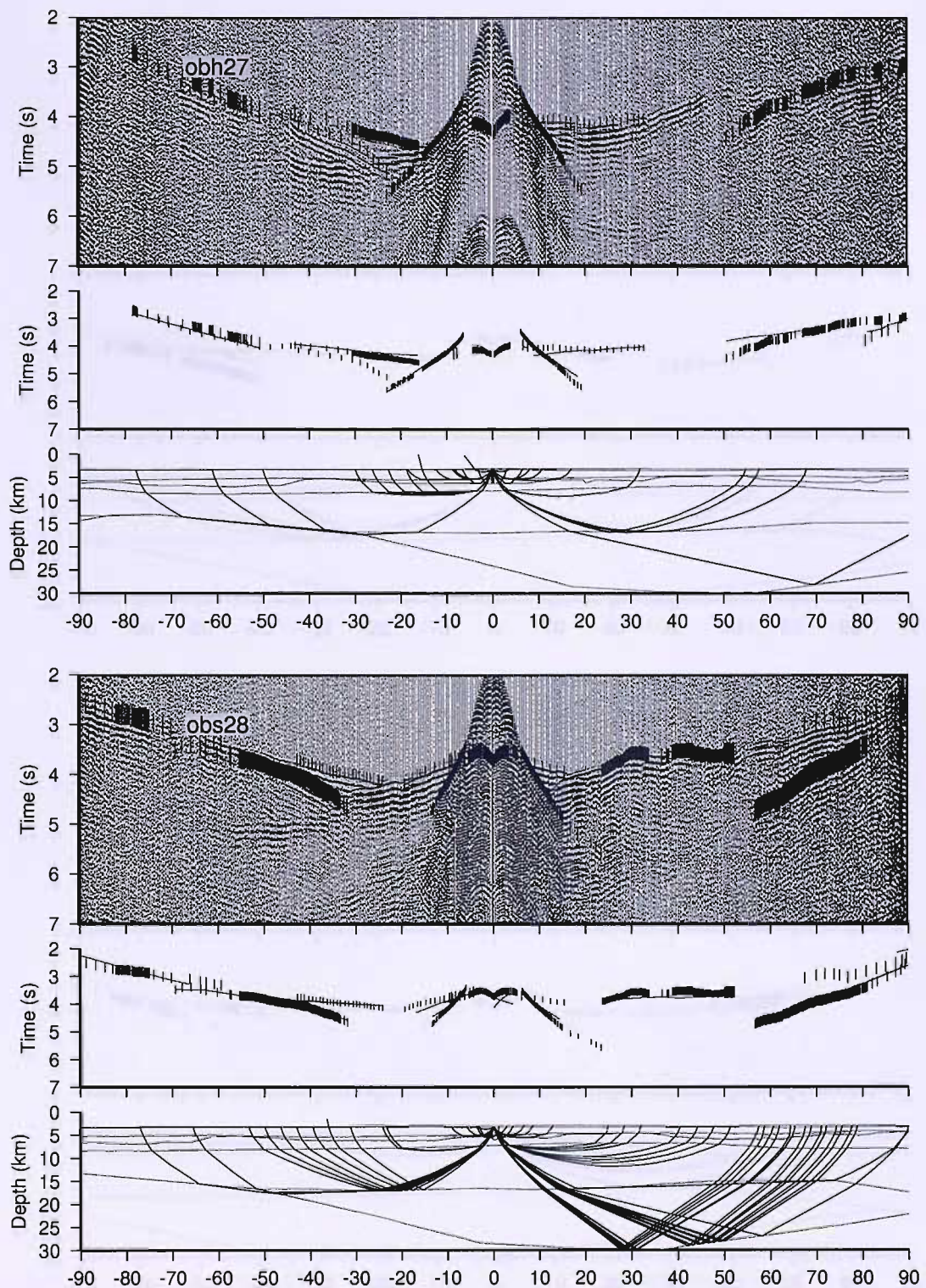
Figure 3.17: OBS/H data, travel-time fit and ray paths through model 11: *top:* OBH27 *bottom:* OBS28, vertical geophone. Other details as Figure 3.7.
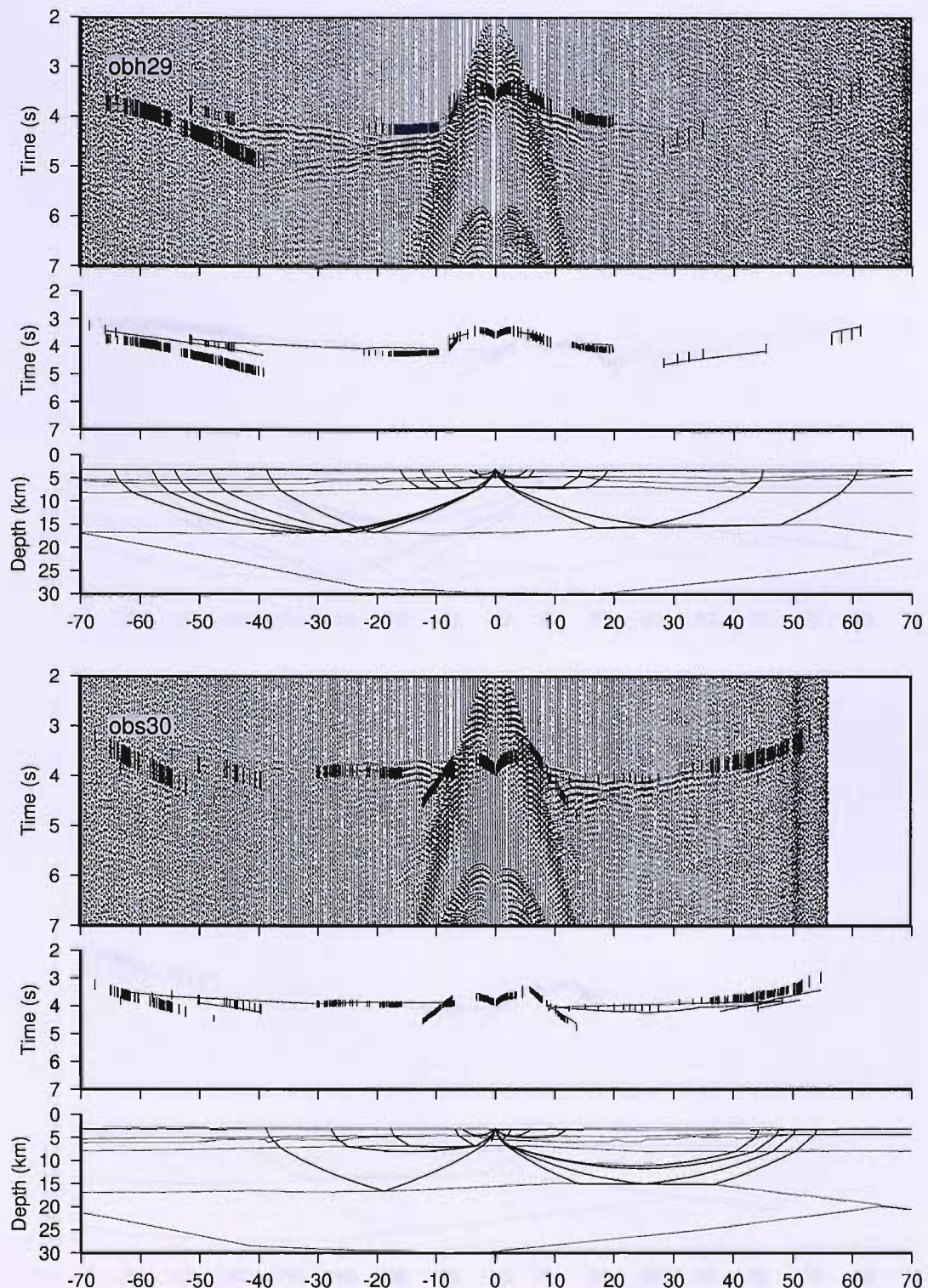
Figure 3.18: OBS/H data, travel-time fit and ray paths through model 12: *top:* OBH29, *bottom:* OBS30. Other details as Figure 3.7.
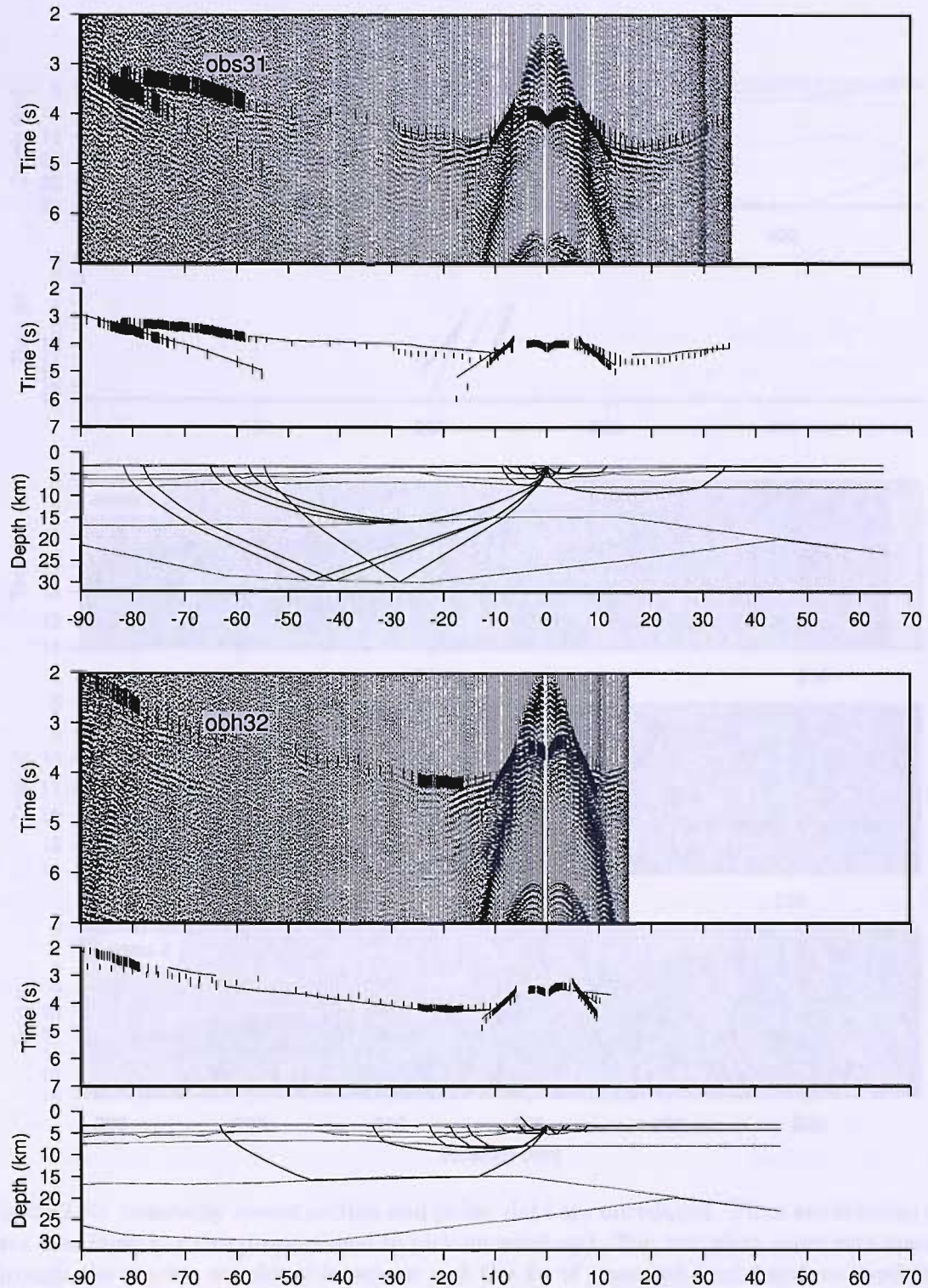
Figure 3.19: OBS/H data, travel-time fit and ray paths through model 13: *top:* OBS31 *bottom:* OBH32. Other details as Figure 3.7.
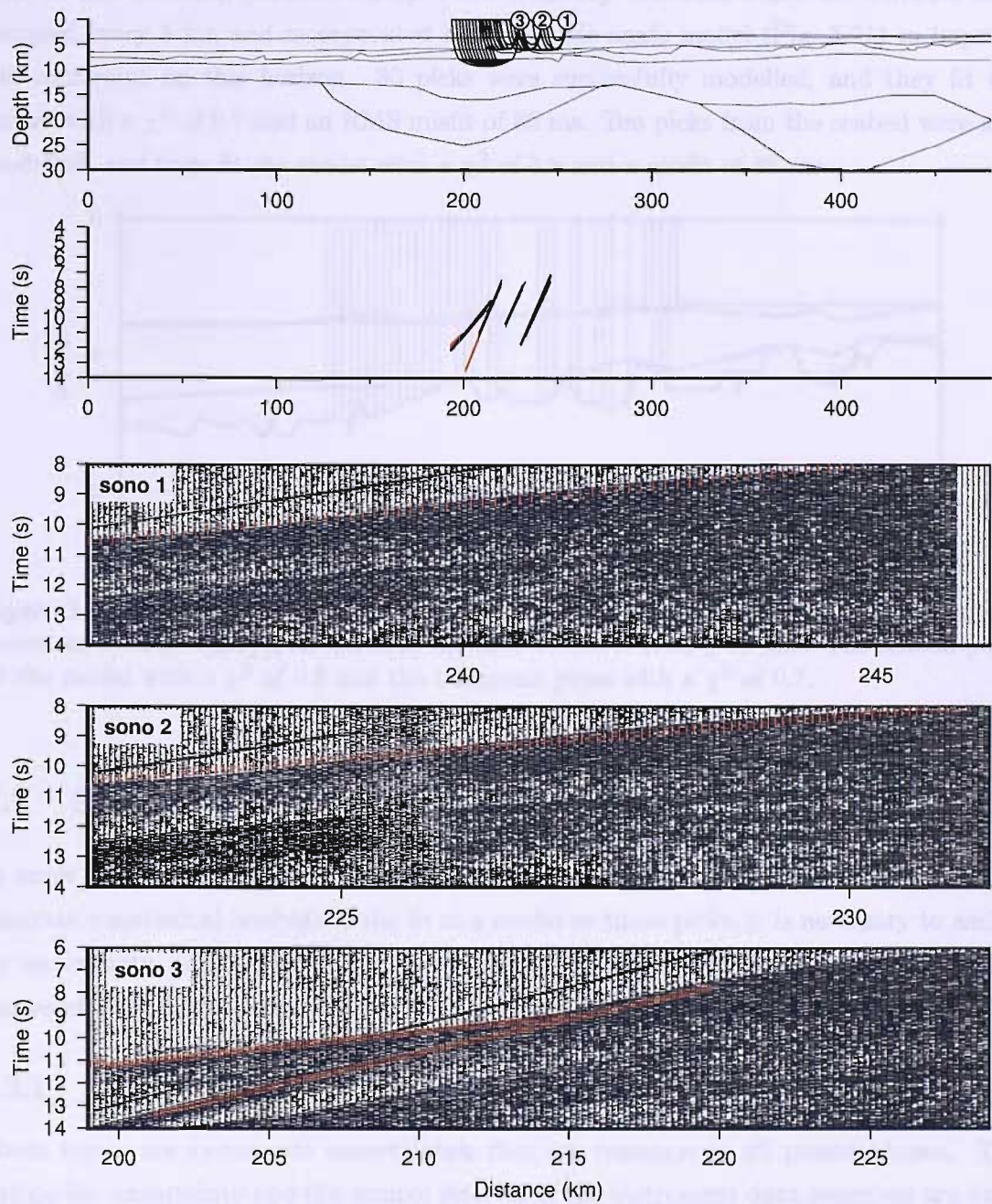
Figure 3.20: Sonobuoy record section and picks: data are unreduced. Picks are overlain on data (red bars; bar size proportional to pick uncertainty). Top two plots show rays traced through the model, sonobuoy locations and the fit of observed (red bars) to modelled (black lines) travel times.

3.1.3 Refining the model with MCS picks

A well defined, unequivocal reflection is seen from the top of acoustic basement on re-flection line CD144-6 (Section 5.2.2). Picks from top basement made on CD144-6 were sampled every 5 km and incorporated into the wide-angle model (Fig. 3.21) to improve the constraint on this horizon. 30 picks were successfully modelled, and they fit the model with a χ^2 of 0.7 and an RMS misfit of 80 ms. Ten picks from the seabed were also modelled, and they fit the model with a χ^2 of 0.9 and a misfit of 88 ms.
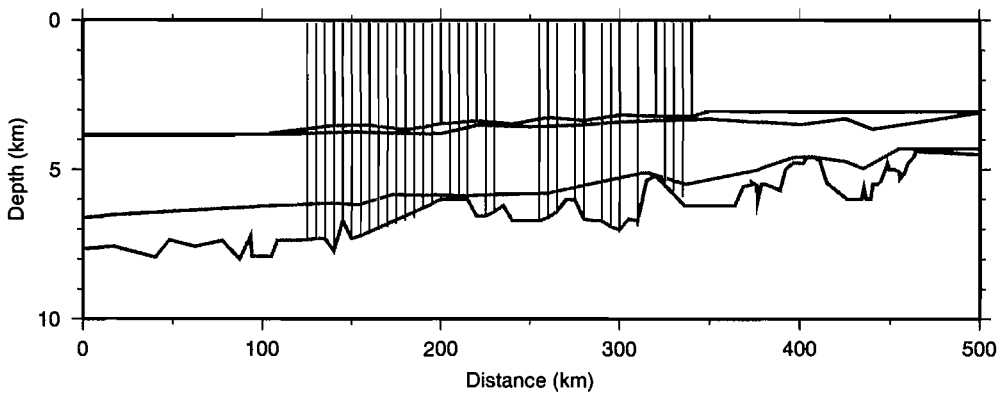
Figure 3.21: Modelling MCS picks: rays are traced down to the seabed (black) and top basement reflector (grey); all horizons are shown with a thick grey line. The seabed picks fit the model with a χ^2 of 0.9 and the basement picks with a χ^2 of 0.7.

3.2 Sources of uncertainty in the model

In order to weight travel time picks according to the level of confidence in them, and to generate a statistical analysis of the fit of a model to those picks, it is necessary to assign an uncertainty value to them. This uncertainty is decided by assessing the potential causes of error in the picked time.

3.2.1 Static errors

Static errors are systematic uncertainties that are common to all picked phases. The navigation uncertainty and the sample interval of the instrument data recorders are both static errors. The sample interval of the seismic data recorders is 10 ms, so a pick can be made to within 5 ms accuracy. The navigation error of the Trimble D-GPS system is of the order of 5 m. Raytracing showed that this gives a maximum travel time uncertainty through the water column of 3.03 ms at an offset of 100 km. Instrument relocation was done assuming a constant water velocity of 1.505 km s^{-1}. However, the actual velocity structure of the water column is more complex than this (Whitmarsh and Sansom, pers. comm; Collier (2003)). Ray tracing through both these velocity structures has shown that

this simplification introduces a 4 ms uncertainty. The total static uncertainty, determined by summing the squares of these individual errors, is therefore 7 ms.

3.2.2 Flat Earth approximation

Distances in the model will be underestimated, as the model space is treated as a 'flat earth', where the curvature of the earth is not taken into account. Arrivals are not seen in the data set at offsets greater than 100 km, and for an average crustal turning ray travelling this distance at 5 km s^{-1}, this simplification gives an error of the order of 1.5 ms. This error is insignificant compared to the picking uncertainties and so is not corrected for. The flat earth approximation is generally considered an important source of error for lines longer than 500 km (Zelt, 1999).

3.2.3 Off-line error

The off-line drift of the instruments is not known, but along line drift and perpendicular drift should be of the same orders of magnitude, and the average along line drift is $<$ 100 m (Sansom, pers. comm.). An off-line error of 100 m equates to a 1.1 ms difference in the arrival time of the direct water wave at the instrument, which is insignificant when compared with the picking uncertainties.

3.2.4 Picking error, assigned uncertainties and model fit

Table 3.1 summarises the picking uncertainties assigned to each phase. Arrivals seen over a large range of offsets have an offset-dependant component to their uncertainty in addition to the 7 ms static uncertainty discussed above. Phases seen over short ranges, or those that are hard to pick, have a single uncertainty value assigned to them. The uncertainty assignment scheme was chosen by a careful visual inspection of how waveforms vary with offset and arrival times, and how they interact with other phases.

The statistical fit of the preferred velocity model to the data is summarised in Tables 3.2 and 3.3.

3.3 Model resolution

An additional constraint on the validity of the velocity model is given by the diagonal of the resolution matrix. This is a statistical measure of how well constrained any given node is. A value of 1 indicates a properly resolved node, with a value less than one indicating spatial averaging of the true structure. In practise, a value of greater than 0.5 to 0.7 is considered optimal (Zelt, 1999). Resolution values are plotted for all velocity nodes in Figure 3.22. Most of the velocity nodes have resolution values between 0.5 and

Crustal Phases, picking uncertainty only	
Offset (km)	Uncertainty (ms)
<= 12.5	10
12.501 - 25.5	0.83*offset
25.501 - 45.5	1.00*offset
45.501 - 50.0	2.00*offset
> 50.0	100
Other Arrivals, total assigned uncertainties	
Phase	Assigned Uncertainty (ms)
Shallow sediment refraction	107
Deep sediment refraction	57
Near offset sediment reflection	57
Near offset basement reflection	37
Wide angle reflection	57
Upper basement refraction	157
High velocity lower crust reflection	157
High velocity lower crust refraction	157

Table 3.1: Uncertainties assigned to travel time picks: arrivals seen out to long ranges (top) are assigned an offset dependant uncertainty. Adding the 7 ms static uncertainty to the stated values gives the total uncertainty. Other phases (bottom), including those that are hard to pick, have a set value for their uncertainty, which includes the static component.

1, indicating that the model is generally very well resolved. The exception is the high velocity sub-crustal body (HVSCB). The HVSCB is poorly resolved because it is a deep body with limited ray coverage. Reducing the number of nodes constraining the HVSCB would increase the resolution value but would not be sufficient to describe the complexity of the bodies.

The diagonal of the resolution matrix are not plotted for depth nodes; depth nodes are inherently less well constrained as they represent a wide zone of seismic velocity contrast at a single vertical position.

3.4   The velocity structure

The final, margin-orthogonal velocity model across the Laxmi Ridge margin is presented in Figure 3.23. The model can be broadly divided into sediments, crust, HVSCB and mantle. The considerable lateral variation of the velocity structure, and its implications for crustal provenance are discussed in the following sections.

Instrument	n	RMS (ms)	χ^2
All	*16184*	*0.120*	*1.615*
01	596	0.073	1.410
03	761	0.087	2.590
04	800	0.075	1.771
05	619	0.037	0.572
06	659	0.064	1.196
07	621	0.061	0.871
08	614	0.108	2.513
09	669	0.083	1.363
10	535	0.065	0.826
11	458	0.111	2.178
12	566	0.123	2.325
20	456	0.094	1.295
22	632	0.097	0.964
23	702	0.154	2.071
16	837	0.140	2.157
17	818	0.136	1.371
18	137	0.090	1.189
19	1036	0.152	2.034
24	703	0.111	1.270
26	942	0.129	1.421
27	471	0.163	1.845
28	790	0.122	0.834
29	320	0.290	3.771
30	242	0.171	1.449
31	306	0.124	1.213
32	221	0.158	1.367
sonobuoy 1	460	0.130	0.677
sonobuoy 2	122	0.045	0.083
sonobuoy 3	96	0.185	1.387

Table 3.2: Model misfit by instrument: Instrument numbers refer to deployment locations (Fig. 3.1). n is the total number of picks modelled for the instrument; RMS is the Root Mean Square misfit of the pick times to the model; χ^2 is a measure of the statistical fit of the model to the data, with a χ^2 of 1 being optimal.

Phase	n	RMS (ms)	χ^2
All	*16184*	*0.120*	*1.615*
Shallow sediment refraction	1551	0.102	1.372
Deep sediment refraction	3224	0.095	1.286
W.A. reflection from basement surface	1461	0.133	2.651
Upper basement refraction	176	0.123	0.826
Deep basement refraction	4779	0.098	1.296
W.A reflection from top of HVSCB/ mantle	3054	0.151	1.506
Refraction within HVSCB	224	0.206	1.717
W.A. reflection from mantle HVSCB	364	0.116	0.727
Upper mantle refraction	1282	0.144	3.093

Table 3.3: Model misfit by phase: *W.A. reflection* is a wide-angle reflection observed on an OBS/H profile, as opposed to a normal incidence/ near-normal incidence reflection on an MCS profile. *HVSCB* is the high velocity sub-crustal body, an anomalous layer modelled at the base of the crust. n is the total number of picks modelled for the instrument; RMS is the Root Mean Square misfit of the pick times to the model; χ^2 is a measure of the statistical fit of the model to the data, with a χ^2 of 1 being optimal.
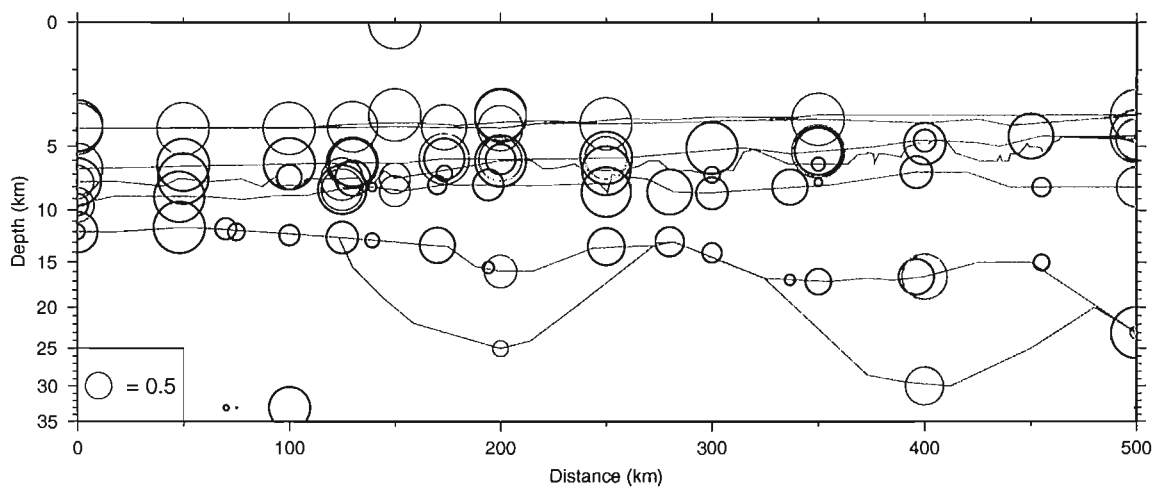
Figure 3.22: Resolution of velocity nodes: circles are centred on velocity nodes; circle size is proportional to the diagonal of the resolution matrix. Circles are coloured red then black for alternate layers. The largest circles represent a resolution of 1; the green circle in the key has a width of 0.5. The high values of the diagonal of the resolution matrix (generally > 0.5) show that the model is well constrained, with the exception of a few nodes in the HVSCB and mantle. This is due to the lower ray coverage through those parts of the model. Depth axis is non-linear to improve the clarity of the figure.
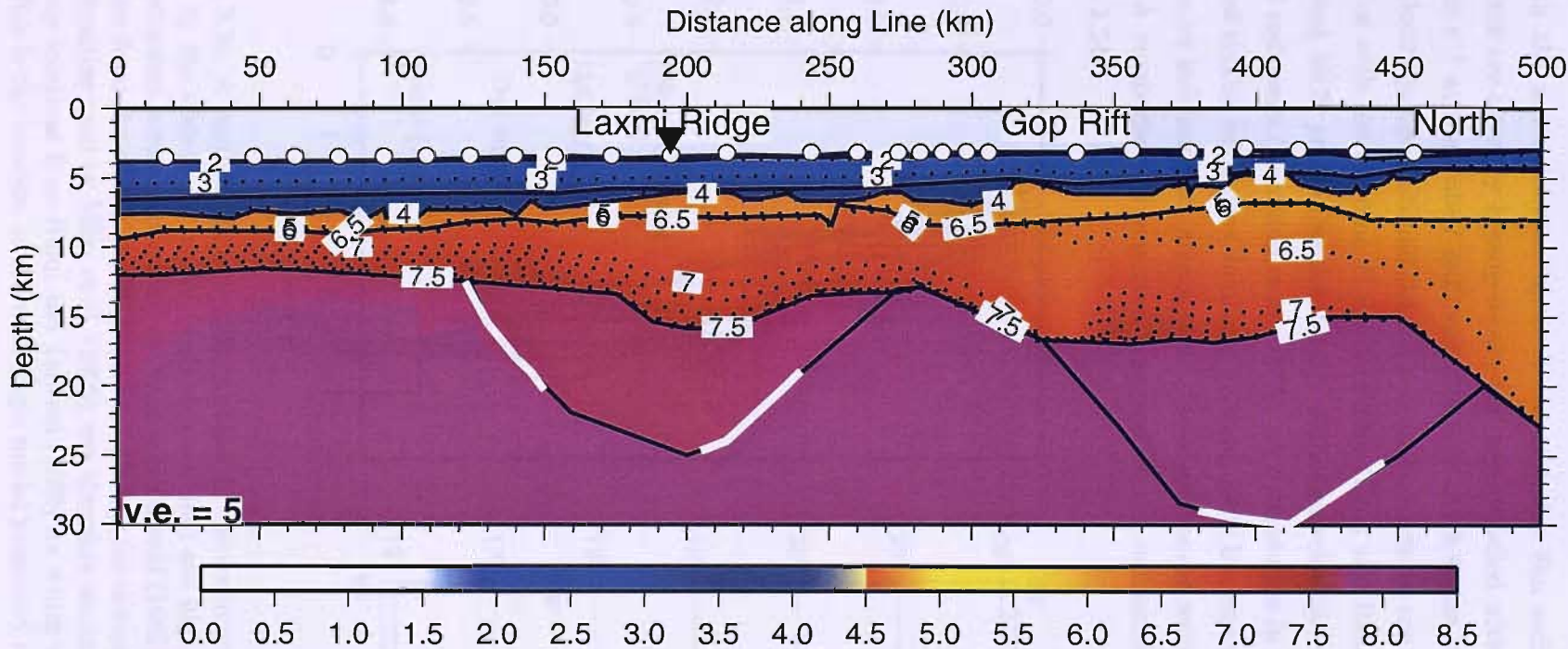
Figure 3.23: The wide-angle velocity model: sediments are coloured blue; basement orange; mantle and anomalously high velocity crust purple. Velocity scale is in km s⁻¹. OBS/H locations are shown by white circles and the crossing point with the margin-parallel line is shown by a black inverted triangle. The HVSCB at the northern end of the model has a velocity similar to that of the surrounding mantle, but clear wide-angle reflections are seen from its upper and lower surfaces. Where the base of the HVSCB is well constrained by wide-angle reflections, the horizon is drawn with a white line.

3.4.1 The sediments

Beneath the water column, up to 4 km of Indus Fan sediments are imaged. These sediments are laterally homogeneous, and are modelled with P-wave velocities between 1.58 km s^{-1} at the water/ sediment interface and 3.80 km s^{-1} at the base of the layer. The velocity jump of around 0.4 km s^{-1} at a horizon in the lower half of the sediments coincides with the Miocene U unconformity (Droz and Bellaiche, 1991) imaged on the coincident MCS profile (Section 5.1.3). Although velocities of 3.80 km s^{-1} are high for normal sediments (Hamilton et al., 1977), previous studies in this region using sonobuoys observed similar velocities (Naini and Talwani, 1982; Bachman and Hamilton, 1980). This may be an indication of intercalated lavas or carbonate sediments near the base of this unit. A comparison of velocities observed in the sediments in this region is given in Figure 3.24.
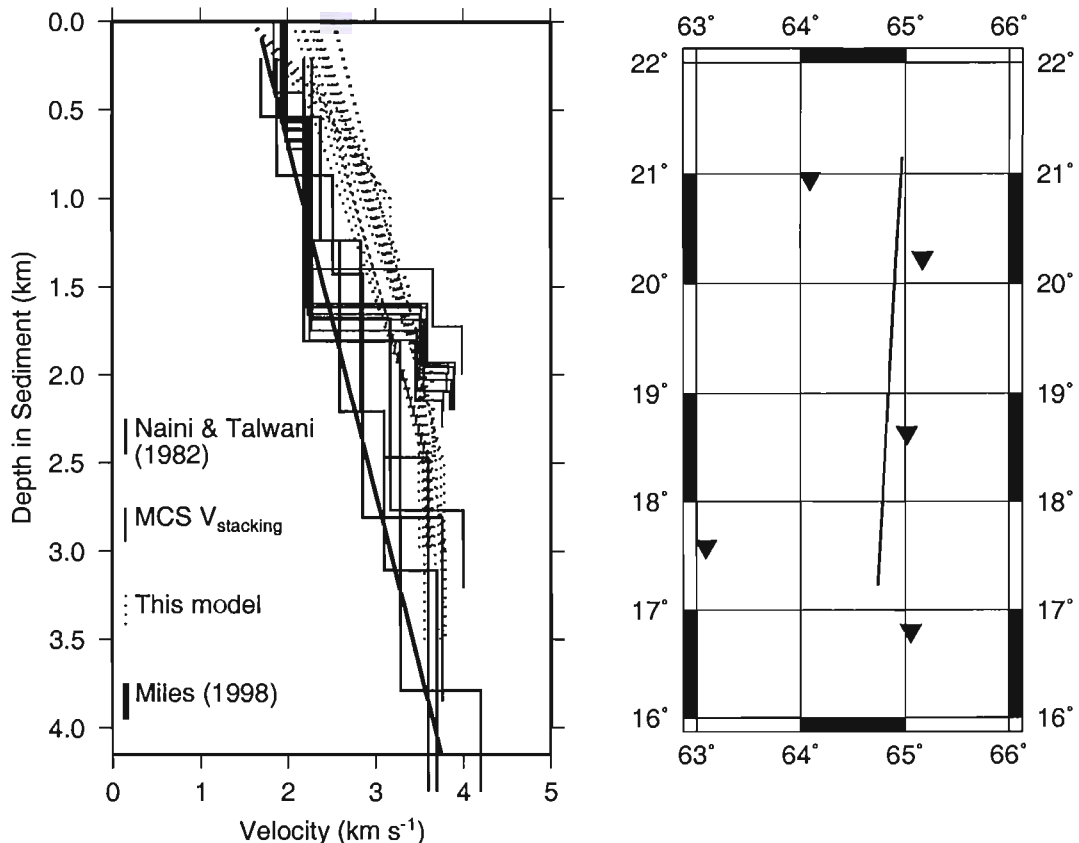
Figure 3.24: A comparison of velocity profiles in the sediments: sediment velocities predicted by the wide-angle model (dashed black line) are high, but high velocities in the deep sediments were also observed by Naini and Talwani (1982) using sonobuoys. Stacking velocities from the coincident MCS line are plotted for comparison (grey lines). The velocity function used by Miles et al. (1998) was therefore an underestimate. *Right:* map of sonobuoy locations from Naini and Talwani (1982) for which velocity profiles are plotted. Black line is the location of the wide-angle model presented in this chapter.

3.4.2 Oceanic crust

This section is concerned with the undisputed Chron 27 oceanic crust south of Laxmi Ridge. The ocean-continent boundary is considered to occur at the seamount 150 km along the profile based on changes in reflection characteristics (Section 5.2.2), magnetic properties (Sections 4.2.1 and 4.2.2) and basement topography at this point. There is a 10 km wide zone beneath the seamount where the HVSCB is modelled, even though this body is believed to pre-date the Chron 27 episode of seafloor spreading (Section 4.2.3). This is most likely due to an overestimation of the dimensions of the poorly constrained HVSCB, but it could alternatively be an indicator that the OCB is actually further seaward than predicted by magnetic modelling.

The Chron 27 oceanic crust is best modelled with an average thickness of 5 km, which is thin compared to the global average of 7 km (White et al., 1992). The Laxmi Ridge margin is interpreted as a volcanic margin due to the presence of seaward dipping reflectors (Section 5.3.2; Gaedicke et al., 2002a). However, volcanic margins generally have thicker than normal initial oceanic crust due to excess melting over a thermal anomaly (e.g., Edoras Bank, Hatton Bank and the Vøring margin, Morgan and Barton, 1990; Barton and White, 1995; Torne et al., 2003), but this does not seem to be the case here. This observation is discussed in Section 3.7.1.

The crust has a two layer structure. Velocities in the ~ 2 km thick upper layer (oceanic layer 2) range from 4.64 km s^{-1} to 4.67 km s^{-1}, and in the ~ 3 km thick lower layer (oceanic layer 3) from 6.74 s^{-1} to 7.44 s^{-1}. Generally, oceanic crust has a distinct velocity structure, with the decrease in porosity and seawater alteration with depth leading to a high velocity gradient in layer 2, and a velocity gradient of approximately 0.2 s^{-1} in layer 3 (Detrick et al., 1994). The Laxmi model has a significantly different velocity structure, with a low velocity gradient in layer 2 (0.02 s^{-1}) and a higher velocity gradient in layer 3, although layer 2 is not well constrained by our data. The velocity structure is compared to both normal and plume-influenced oceanic crust in Figure 3.25. The unusual layer 2 thickness could be due to rapid accretion of the oceanic crust (Royer et al., 2002); Houtz and Ewing (1976) describe fast-spreading Pacific oceanic crust as having a thin upper crust compared to slower spreading Atlantic sites, but the velocity values they modelled are not significantly different from those in the Atlantic. The high velocities in layer 2 could be a function of their age; extrapolation of age vs. velocity data from Houtz and Ewing (1976) predicts an upper crust velocity of 5 km s^{-1} for 60 Ma old crust.

Velocities in the oceanic mantle are 7.70 km s^{-1}. This is low for oceanic mantle, but still within the range of normal mantle velocities (White et al., 1992). Possible implications of the mantle velocity structure are discussed in Section 3.7.2.
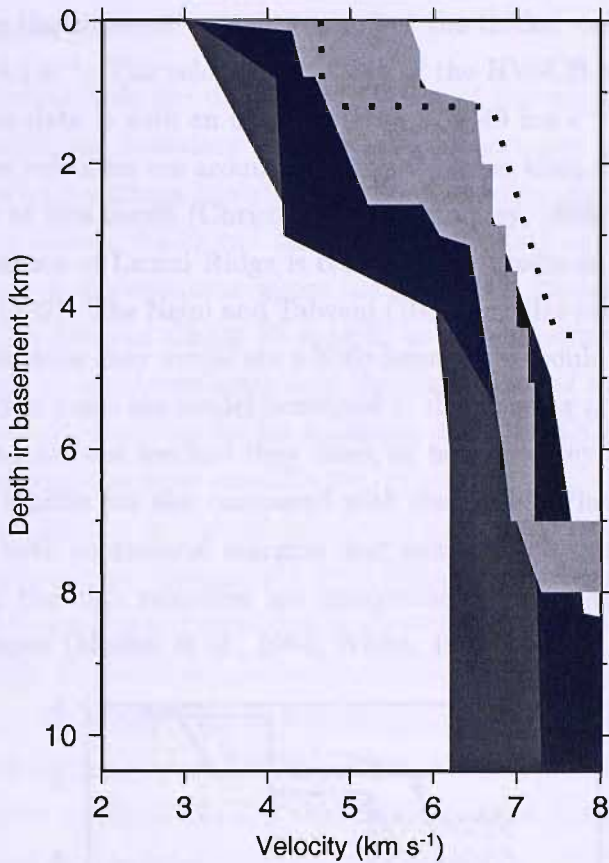
Figure 3.25: Comparison of oceanic crust types: Normal oceanic crust aged 0-100 Ma (light grey; White (1992)) has a high velocity gradient in layer 2 and a low velocity gradient in layer 3. In plume influenced oceanic crust (9-50 Ma black region; 51-56 Ma dark grey region), both layer 2 and 3 are thickened. Bounds are from White (1992). The average velocity structure of the Laxmi Ridge oceanic crust (dotted line) is anomalous, with a higher velocity gradient in layer 3 than layer 2. Mantle velocities are reached at around 5 km depth.

3.4.3 Laxmi Ridge

Despite the large variability in the velocity structure of continental crust, Laxmi Ridge is generally accepted to be of continental origin because of its low magnetisation and large (relative to oceanic crust) crustal thickness (e.g., Naini and Talwani, 1982; Miles et al., 1998; Talwani and Reif, 1998). The crust is thin compared to the global average of 39.2 km (Christensen and Mooney, 1995) for continental crust, which is evidence for tectonic thinning. Laxmi Ridge is modelled here as an 19 km thick, 3 layer structure: 1.9 km thick upper crust, 8 km thick lower crust and a 9 km thick high velocity sub-crustal body (HVSCB) that may be anomalously high velocity crust or anomalously low velocity mantle. Velocities in the upper crust vary from 4.65 km s^{-1} at the top basement surface to 4.69 km s^{-1} at the interface with the lower crust. The lower crustal velocities vary from 6.55 km s^{-1} to 7.32 km s^{-1} at the base of the layer. This is similar to the

82

velocities observed in the adjacent oceanic crust, but the thicker crust here gives a lower velocity gradient of 0.1 s^{-1}. The velocity structure of the HVSCB is poorly constrained, but the best fit to the data is with an upper velocity of 7.49 km s^{-1} and a lower velocity of 7.50 km s^{-1}. These velocities are around 0.5 km s^{-1} higher than the observed velocities for continental crust at this depth (Christensen and Mooney, 1995). In Figure 3.26, the average velocity structure of Laxmi Ridge is compared to previous models in this region (Naini and Talwani, 1982). The Naini and Talwani (1982) profiles predict the same crustal thickness, but the velocities they model are a little lower. This could be because the wide-angle techniques used to make the model presented in this chapter are more accurate than the unreversed slope-intercept method they used, or because they are only picking first arrivals. The Laxmi models are also compared with the Vøring Plateau and NW Rockall margins. These are both continental margins that exhibit high velocities at the base of crust. In both cases, the high velocities are interpreted as magmatic underplate caused by rifting over a hotspot (Mutter et al., 1984; White, 1992).
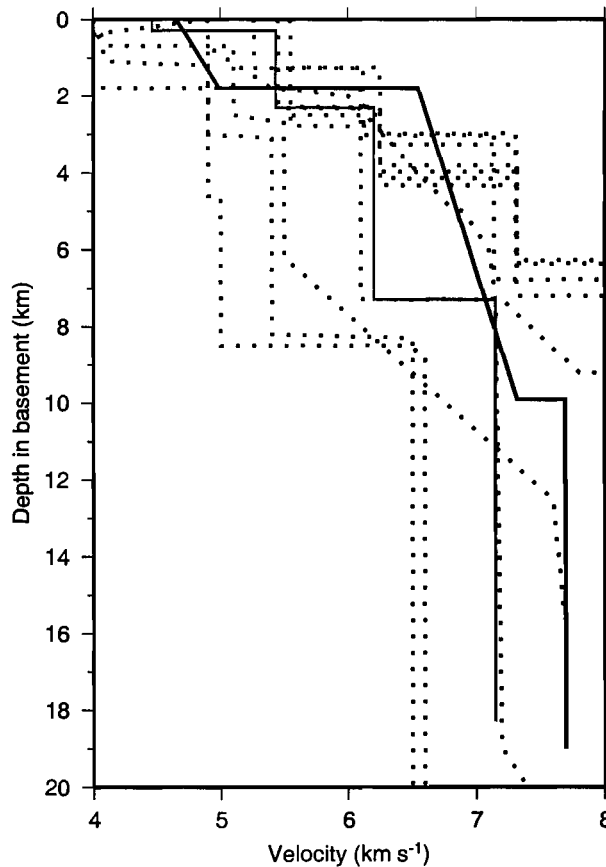
Figure 3.26: Velocity-depth profiles through Laxmi Ridge: an average velocity-depth profile from this work (black line) is compared to the velocity profile calculated by Naini and Talwani (1982) (grey line). The dotted lines are profiles from continental crust at volcanic margins: the Vøring Plateau, Hatton Bank and Moroccan margins (Mutter et al., 1984; Holik et al., 1992; White, 1992).

3.4.4 Gop Rift

Gop Rift is defined here as starting immediately north of Palitana Ridge, the seamount 275 km along the profile, and ending at around 380 km. Gop Rift was originally defined as starting south of Palitana Ridge, but magnetic modelling (Section 4.2.2) suggests a change in crustal type south of Palitana Ridge, so it is logical to move the boundaries so that they coincide with changes in provenance. Gop Rift was successfully modelled with a high remenant magnetisation (Section 4.2.2), which suggests that it is of oceanic origin. It has a similar velocity structure to the Chron 27 oceanic crust discussed earlier, except for beneath the seamount at 325 km. The seamount was hypothesised to coincide with the extinct spreading centre in Gop Rift (Section 5.3.3), so it is interesting that it has a distinct velocity structure.

The crustal thickness varies from 7 km in the south to 11 km in the north. The upper crust is $\sim$ 2 km thick, and has velocities of 4.70 km s^{-1} at its upper surface and 4.74 km s^{-1} at its base. The lower crust is more complex: velocities in the north increase from 6.64 km s^{-1} to 7.13 km s^{-1} with a velocity gradient of 0.11 s^{-1}; velocities in the south increase from 6.30 km s^{-1} to 7.40 km s^{-1} with a velocity gradient of 0.12 s^{-1}. The velocity gradient in northern Gop Rift decreases to 0.10 s^{-1} at 410 km, which is the approximate location of the OCB between spreading in Gop Rift and extended continental crust offshore India. Underneath the seamount that may be the extinct spreading centre, the velocities in the lower crust range from 6.41 km s^{-1} to 6.88 km s^{-1} and the velocity gradient is 0.05 s^{-1}.

Velocity-depth profiles through Gop Rift are compared with normal oceanic crust (White et al., 1992) and plume influenced oceanic crust (White, 1992) in Figure 3.27. The profile through northern Gop Rift matches the profile through Atlantic plume influenced oceanic crust well, while the profile through southern Gop Rift more closely matches normal oceanic crust. Depending on the width of the Deccan hotspot, it may have been off-axis relative to Gop Rift. The northern part of this basin would have been closer to the Deccan hotspot, which was active during accretion of this basin (Section 4.2.3), so the heat from the hotspot may have been driving increased melting north of the spreading centre. This is manifest by the larger crustal thickness in the northern side of the basin, and the observed asymmetry of the basin: there was around 100 km of horizontal accretion in the north and 60 km horizontal accretion in the south.

A velocity of 7.85 km s^{-1} is estimated for the upper mantle beneath Gop Rift, which is average for the section of the Laxmi Ridge margin modelled here.
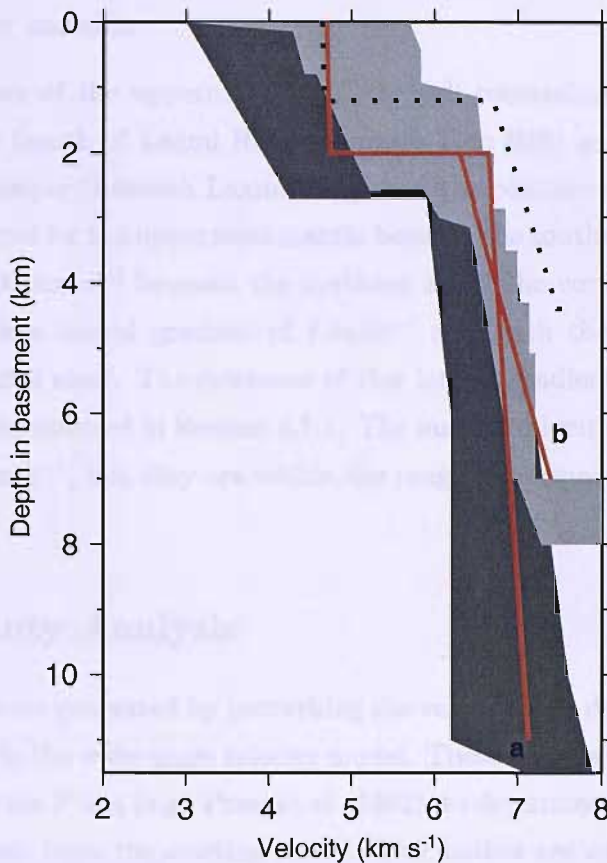
Figure 3.27: Velocity-depth profiles through Gop Rift: Red lines are profiles through Gop Rift. *a* is through northern Gop Rift and falls within the bounds of plume influenced Atlantic crust (dark grey; White (1992)). *b* is a profile through southern Gop Rift, and falls within the bounds of normal Atlantic oceanic crust aged 0-100 Ma (light grey; White (1992)). The average velocity structure of the Laxmi Ridge Chron 27 oceanic crust is plotted for comparison as a dotted line.

3.4.5   High velocity bodies in the deep crust

Two bodies of anomalous velocity are seen to be symmetrical about Gop Rift, beneath continental crust in Laxmi Ridge and the continental rise. Based on the velocity model only, it is unclear whether they represent anomalously high velocity crust or anomalously low velocity mantle. They are interpreted in Section 4.2.3 as magmatic material generated prior to extension in Gop Rift by melting associated with the Deccan hotspot. Their provenance is discussed further in Section 3.7.2.

The high velocity sub-crustal body beneath Laxmi Ridge is 9 km thick, 150 km wide and it's velocities increase from 7.49 km s^{-1} at the base of the crust to 7.50 km s^{-1} at the Moho (defined here as the base of the undisputed crust, so the top of the HVSCB), although this is poorly constrained. The HVSCB beneath the continental rise is 12 km thick, 150 km wide and has velocities of 7.40 km s^{-1} to 7.41 km s^{-1}.

3.4.6   The upper mantle

The velocity structure of the uppermost mantle is well constrained by our data where the Moho is shallow (south of Laxmi Ridge; beneath Gop Rift) and poorly constrained where the Moho is deeper (beneath Laxmi Ridge and the continental rise). Velocities of 7.70 km s^{-1} are inferred for the uppermost mantle beneath the southern end of the margin, with velocities of 8.00 km s^{-1} beneath the northern end. The vertical velocity gradient is 0.03 s^{-1}. There is a lateral gradient of 7.5x10^{-4} s^{-1}, with the velocities increasing towards the continental shelf. The existence of this lateral gradient is supported by the linear density gradient inferred in Section 4.1.1. The mantle velocities are generally lower than the typical 8 km s^{-1}, but they are within the range of normal mantle (White et al., 1992).

3.5   Uncertainty Analysis

Alternative models were generated by perturbing the velocity and depth nodes to test the degree of confidence in the wide-angle velocity model. These models were compared to the starting model using the F test (e.g., Press et al., 1992), to determine if the resulting model is statistically different from the starting model. The models are considered statistically different when the change in χ^2 is significant at the 95% confidence limit. Velocities were perturbed within each layer while keeping the velocity gradient constant, and horizons were perturbed by shifting every node defining that horizon by a constant amount. Rays were then traced through those parts of the model affected by the perturbation (i.e., the layer being perturbed, layers deeper than the layer being perturbed and the layer above if changing the depth nodes might alter its velocity gradient).

As is illustrated in Figure 3.28, velocities in the crust can be assigned an uncertainty of $+0.13/-0.03$ km s^{-1}. Velocities in the underplate have an uncertainty of $+0.22/-0.39$ km s^{-1}, which means they can be confidently described as being high for crustal rocks. Likewise, mantle velocities have an uncertainty of $+0.08/-0.04$ km s^{-1}, which means they are lower than typical mantle velocities. It was considered important to estimate the limits of the size of the two bodies that manifest as the HVSCB. Increasing the depth of the base of the HVSCBs caused instabilities in the ray tracing algorithm, so the results presented in Figure 3.28 show only negative perturbations of the horizon. This is more useful, as it is important to estimate the minimum dimensions of the bodies. This testing showed that the depth of the base of the bodies can be reduced by up to 300 m before the model no longer fits the data. Depth uncertainties for the base of the crust are plotted in Figure 3.29. The base of the crust can be perturbed by $+0.80/-0.20$ km before a significantly different model is achieved.
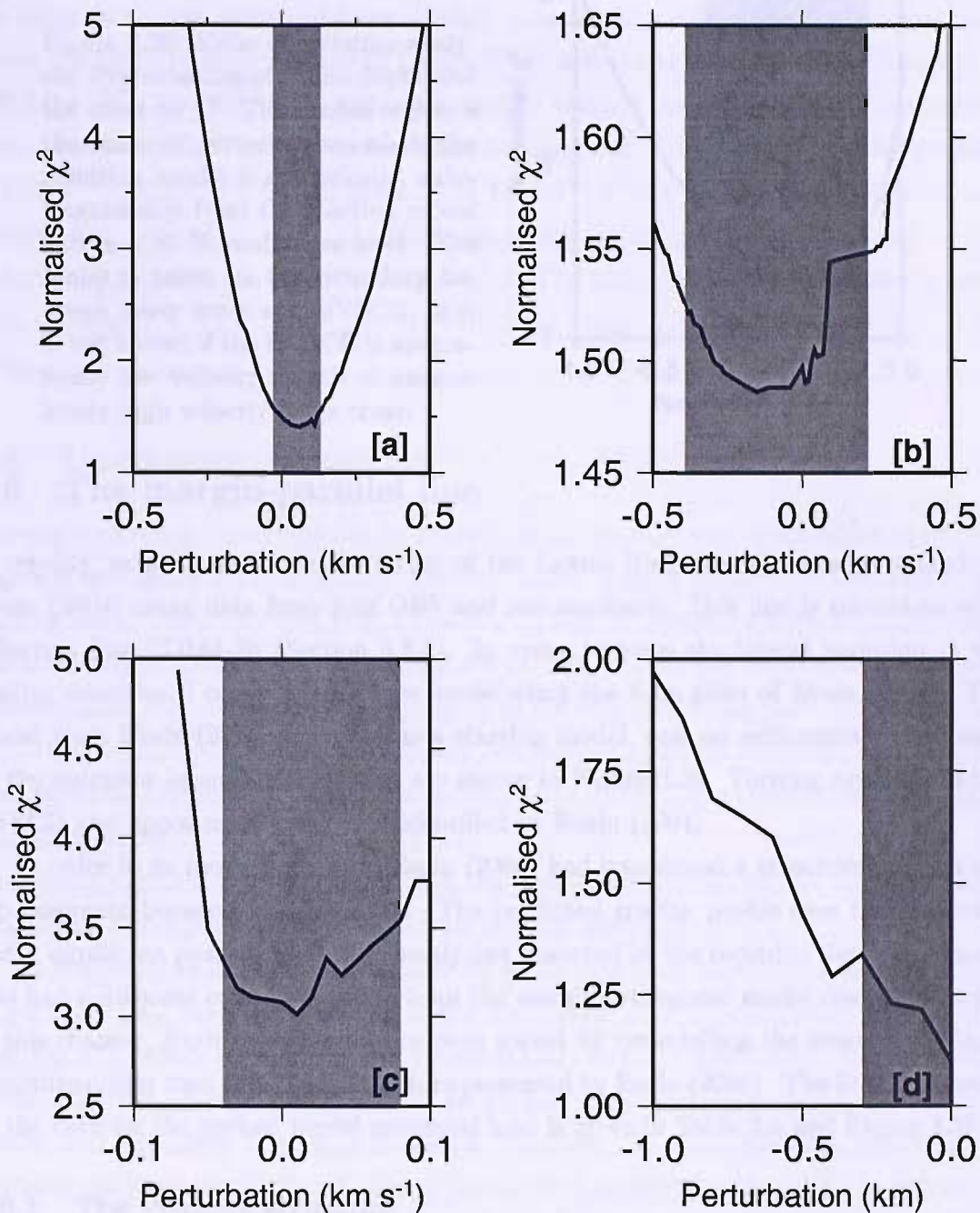
Figure 3.28: Model uncertainty analysis: Perturbation of model depth or velocity values and the effect on χ^2. On each plot, the shaded region is the range of perturbations where the resulting model is statistically indistinguishable from the starting model within a 95 % confidence level. Uncertainty of *a)* velocities in the deep crust, *b)* velocities in the HVSCB, *c)* mantle velocities and *d)* the depth of the base of the HVSCB are plotted.
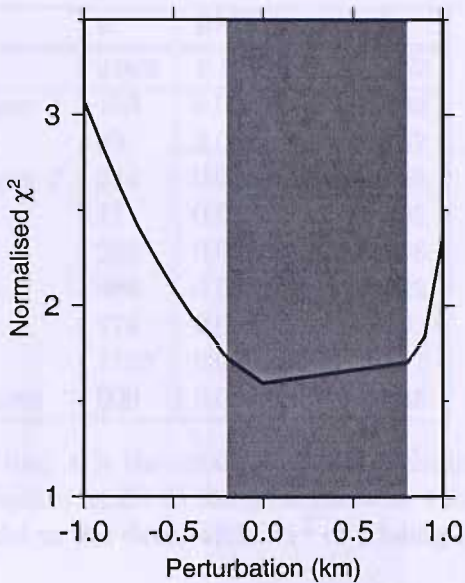
Figure 3.29: Moho uncertainty analysis: Perturbation of Moho depth and the effect on χ^2. The shaded region is the range of perturbations where the resulting model is statistically indistinguishable from the starting model within a 95 % confidence level. The Moho is taken as the boundary between lower crust and HVSCB, as it is not known if the HVSCB is anomalously low velocity mantle or anomalously high velocity lower crust.

3.6 The margin-parallel line

A velocity model parallel to the strike of the Laxmi Ridge margin was generated by Evain (2004) using data from four OBS and one sonobuoy. This line is coincident with reflection line CD144-3b (Section 5.2.3). In order to asses the lateral variation in the crustal velocities, I constructed a new model using the time picks of Evain (2004). The model from Evain (2004) was used as a starting model, and no refinements were made to the sediment layers. Both models are shown in Figure 3.30. Turning rays within the HVSCB and upper mantle were not identified by Evain (2004).

In order to fit the seismic data, Evain (2004) had introduced a structural high in the top basement between 25 and 60 km. The predicted gravity profile over this structure had a significant positive gravity anomaly not observed in the recorded data. His model also had a different crustal thickness from the margin-orthogonal model discussed earlier in this chapter. Both these limitations were solved by remodelling the crust as a 3 layer structure rather than the 2 layer structure presented by Evain (2004). The fit of the model to the data for the revised model presented here is given in Table 3.4 and Figure 3.31.

3.6.1 The velocity structure

Figure 3.30 shows that the velocity structure of Laxmi Ridge is homogeneous along-strike, at least at the scale of the model. The model consists of four layers, each with a relatively simple geometry and velocity structure. The sediments are up to 4 km thick, and reach P-wave velocities of 3.6 km s^{-1} at the base. The upper crust is approximately 3 km thick, and thins to 2 km at 35 km and 65 km. This thinning may be due to extension of this layer. The velocities in the upper crust range from 4.95 km s^{-1} at its upper surface to

Phase	n	RMS (ms)	χ^2
All	*4002*	*0.077*	*1.075*
Reflection from base of sediment layer 1	183	0.014	0.893
Refraction within sediment layer 1	83	0.013	0.757
Reflection from base of sediment layer 2	214	0.020	1.059
Refraction within sediment layer 2	71	0.017	0.692
Reflection from top basement	286	0.022	1.168
Refraction within upper basement	486	0.067	1.222
Reflection from mid-crust	176	0.085	0.733
Refraction within lower crust	1703	0.099	1.211
Reflection from base of the underplate	900	0.064	0.845

Table 3.4: Model misfit of the margin-parallel line: n is the total number of picks modelled for the instrument; RMS is the Root Mean Square misfit of the pick times to the model; χ^2 is a measure of the statistical fit of the model to the data, with a χ^2 of 1 being optimal.

5.49 km s^{-1} at the interface with the lower crust, although these velocities are poorly constrained. The lower crust is 7 km thick, with velocities ranging from 6.5 km s^{-1} to 7.3 km s^{-1}. The HVSCB is 6 km thick and is modelled with a constant velocity of 7.50 km s^{-1}. A constant velocity is used because no turning rays have been picked that constrain this part of the model. Reflections from the base of the HSVCB beneath Laxmi Ridge are much clearer on this line than on the margin-orthogonal line, perhaps because the structure is laterally more continuous along the strike of the ridge. The unequivocal strong reflections from the base of the HVSCB on this line provide clear evidence for the existence of this body and support the interpretations of less convincing reflections from this horizon on the margin-orthogonal line.

The thickness of the HVSCB is an estimate based on the velocities from the orthogonal model and rays reflected from its base; no turning rays are identified in this part of the model. The velocity structure predicted by this model matches that of the orthogonal model well (Fig. 3.32); the two models have a very similar velocity structure in the sediments and crust. The total crustal thickness of the two models differs by 3 km. This is larger than the expected uncertainty of the Moho depth for either model, but probably reflects the complexity of the deep structure in the margin-orthogonal model and the lack of reflections from the top of the underplate in the margin-parallel model.

3.6.2 Error analysis

Alternative models were generated for the margin-parallel line to test the amount of uncertainty in the velocity structure using the method described in Section 3.5. Both the velocity of the lower crust and the depth of the Moho were perturbed, and the results are shown in Figure 3.33. The figure shows that the lower crust has a velocity uncertainty of $+0.06/-0.03$ km s^{-1} and the Moho has a depth uncertainty of $+0.20/-0.35$ km.
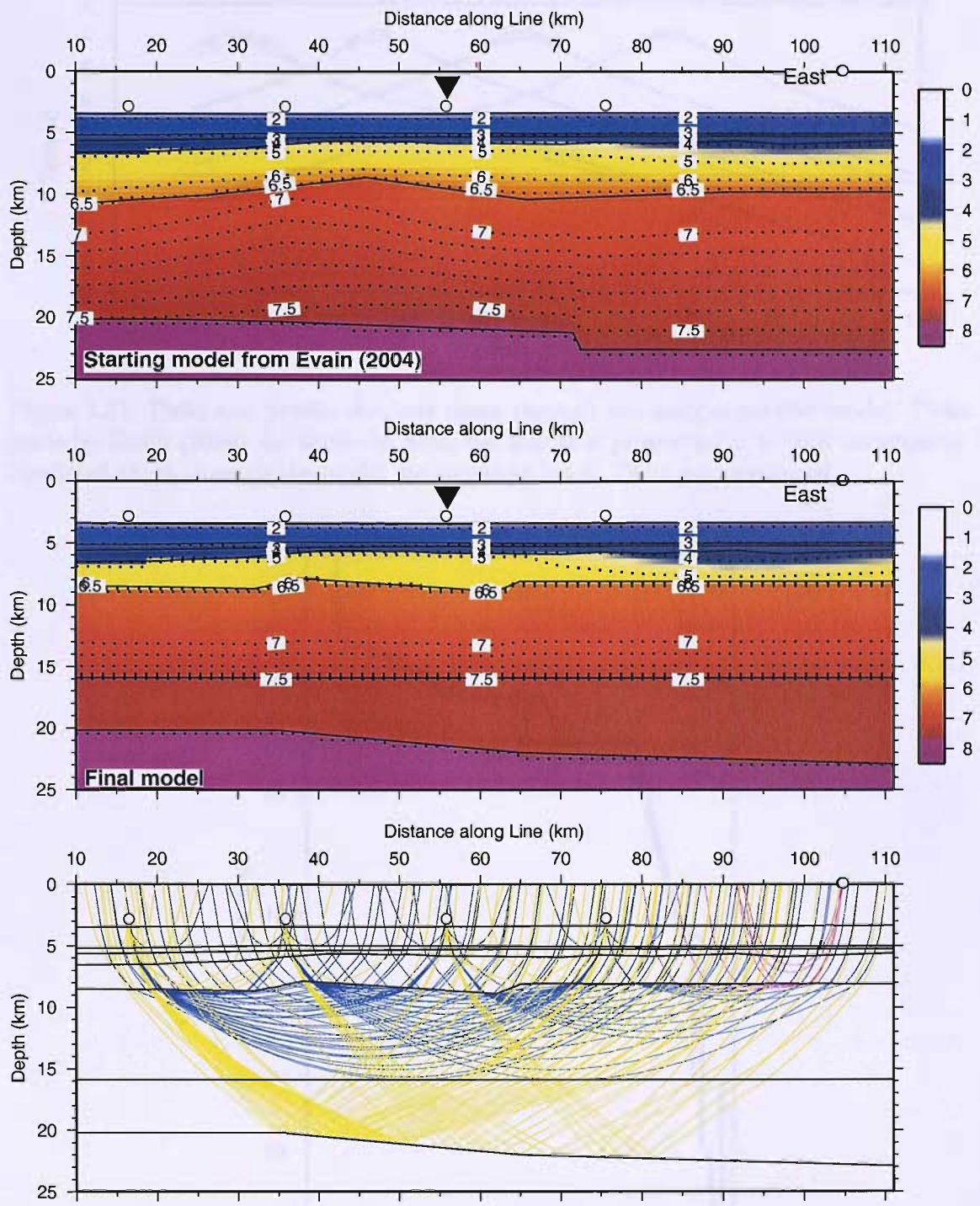
Figure 3.30: The wide-angle velocity structure along-strike of Laxmi Ridge: *Top:* starting model from Evain (2004). The crossing point with the margin-orthogonal model is shown by a black inverted triangle. Instrument locations are given by white circles. The crust was remodelled in order to remove the basement hump between 25 and 60 km, which contradicted coincident gravity data, and to introduce a three-layer crust in common with the margin-orthogonal model. *Middle:* The resulting refined model and *bottom:* rays traced through it. The crossing point with the margin-orthogonal model is at 56 km.
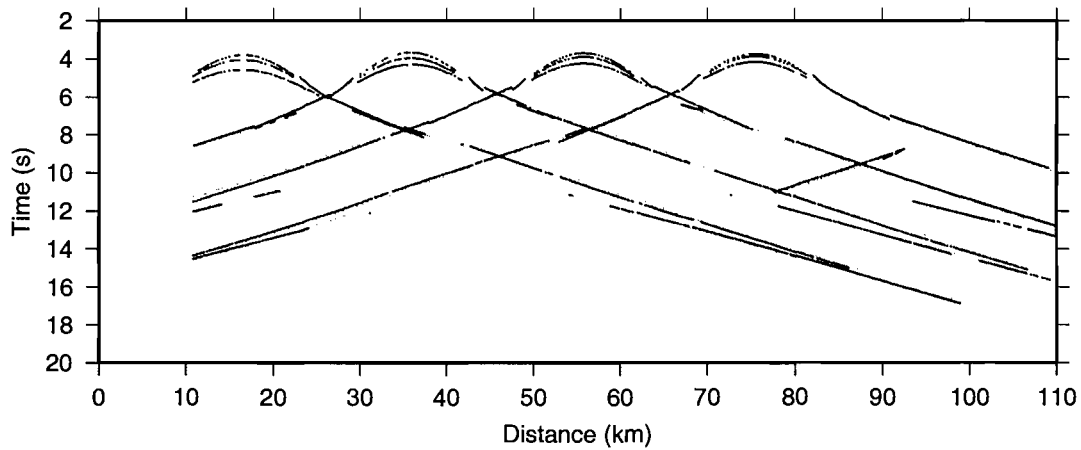
Figure 3.31: Picks and predicted travel times through the margin-parallel model. Picks made by Evain (2004) are shown in blue; bar height is proportional to pick uncertainty. Predicted times through the model are shown in black. Data are unreduced.
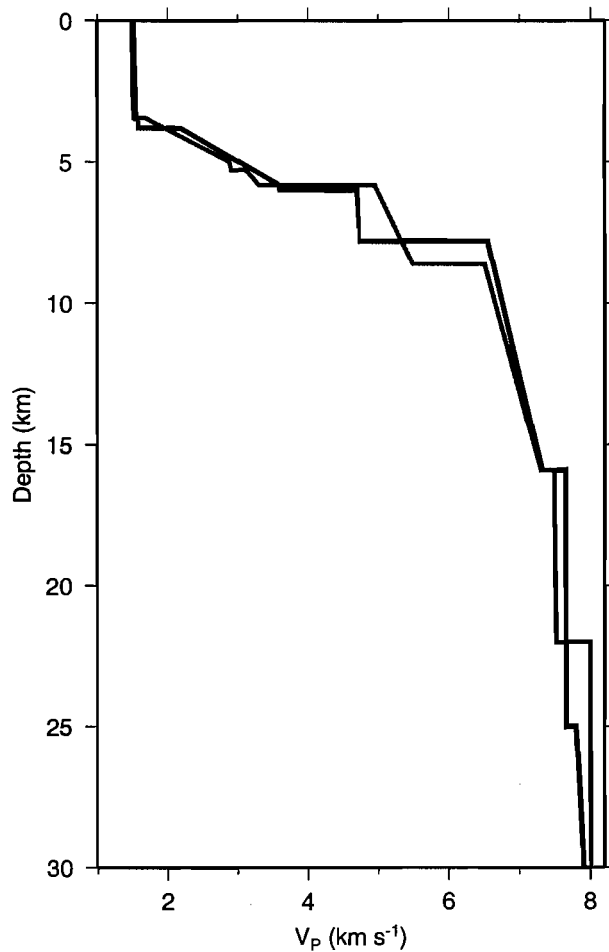
Figure 3.32: Comparison of velocity structures of the two models: Grey line is the margin-parallel model and black line is the margin-orthogonal model. 2d velocity profiles are taken from the crossing point of the two models (56 km and 194.2 km respectively).

Figure 3.33: Model uncertainty analysis for the margin-parallel model. Perturbation of model depth or velocity values and the effect on χ^2. On both plots, the shaded region is the range of perturbations where the resulting model is statistically indistinguishable from the starting model within a 95 % confidence level. Uncertainty of *a)* velocities in the crust, *b)* depth of the Moho are plotted.

3.7 Discussion

In this section I discuss some of the unusual features at the Laxmi Ridge margin, their implications for magmatic accretion and architecture of this margin, and the wider implications of the findings. The relationship of Laxmi Ridge and its conjugate, the Seychelles Bank, is also discussed. Finally, a model to explain the sequence of events that lead to the present-day configuration of the conjugates is presented.

3.7.1 The thin post-Chron 27 oceanic crust: mechanisms and implications

The OCB between Laxmi Ridge and the Chron 27 and younger oceanic crust is inferred to be between 120 km to 140 km based on the change in normal incidence reflectivity and basement structure (Section 5.2.2), the change in remenant magnetisation strength, the reduction in the velocity gradient of the deep crust and the limit of the HVSCB beneath Laxmi Ridge. This means that the first formed oceanic crust south of Laxmi Ridge is unusually thin (White et al., 1992), with thickness ranging from 4.5 km at the southern end of the profile to 6 km at the OCB. These thicknesses are anomalous, but are well constrained by the low uncertainty (Section 3.5) and high resolution (Section 3.3) of the deep crust. Further support is provided by the excellent match in crustal structure and thickness to the early oceanic crust on the conjugate Seychelles Bank margin (Section 3.7.4) and the close fit of the gravity profile predicted from the velocity model (Section 4.1.1) to observed gravity.

These observations are crucial to understanding the thermal evolution of the margin, as the thin first-formed crust and weak syn-rift magmatism (Section 5.3.2) provide no evidence for the presence of a mantle thermal anomaly during final rifting, and therefore no influence from the Deccan hotspot. Despite this, Gop Rift, which formed prior to the Seychelles- India breakup, appears to have been influenced by the Deccan hotspot (Section 3.7.3). This implies that magmatism in Gop Rift was fed by a short duration pulse from the thermal anomaly. This kind of mechanism, where a finite amount of hot material is delivered to the base of the lithosphere and then rapidly cools by advection, is also hypothesised on the U.S Mid-Atlantic margin by Lizarralde and Holbrook (1997). They infer that the mantle cooled from $1500^{\circ}C$ to $1300^{\circ}C$ over 20 Ma from the subsidence history of the margin. This mechanism of advective cooling of a finite pulse of hot material is successfully modelled by Nielsen and Hopper (2002). If a Deccan input of hot material beneath the margin is the source of the magmatic characteristics of the rifting observed in Gop Rift, the mantle will have to have cooled within less than 5 Ma to allow for the non-volcanic features of the rifting between Laxmi Ridge and the Seychelles. This would either require a thermal anomaly 4 times smaller than that observed by Lizarralde and

Holbrook (1997), or a more efficient method of cooling the asthenosphere. This is not unreasonable since the thick Indian lithosphere would provide a cool, conductive layer to channel heat away from the anomaly site.

While the above discussion can explain the transition of the margin from a volcanic to non-volcanic state, it does not explain why the Chron 27 crust is unusually thin. This requires that there was no enhanced melting, e.g., by small-scale convection (Mutter et al., 1988) or active upwelling (Holbrook et al., 2001). The thin crust could simply be a consequence of the rapid rate of accretion: oceanic crust between 5.1 and 5.7 km thick is observed at the fast-spreading East Pacific Rise (Canales et al., 1998). If spreading rate is not the controlling factor, some mechanism is required to suppress melting sufficiently to limit the crustal thickness of the oceanic crust to a thickness less than that expected from simple decompression melting of the mantle. This could simply be because the Indian continental mantle is an evolved, depleted source which is not sufficiently fertile to generate 7 km thick crust by decompression melting. Alternatively, there may be an extensional control on the suppression of melting. This possibility is discussed below.

Rift duration and melt suppression

The rapid extension of the crust prior to breakup (Royer et al., 2002) was expected to generate significant amounts of syn-rift magmatism (Bown and White, 1995) by rapid upwelling of the mantle. However, this theory is not supported by the observations on the Laxmi Ridge/ Seychelles conjugate margins. This implies that there are other, more important, controls on syn-rift magmatism.

Geochemical data from Greenland is interpreted as showing that thick lithosphere can act as a cooling cap, which allows conductive cooling of the lithosphere and subsequent suppression of deep melting (Hellebrand and Snow, 2003). These data were from a region of slow spreading, but the principle may be applicable here too.

A theory that also invokes conductive cooling of the asthenosphere is that of Bown and White (1995). They suggest that melting is controlled by the duration of continental rifting, with longer periods of rifting allowing the mantle more time to cool against the cold lithosphere.

Assuming that sedimentation occurred at a constant rate during rifting and sediment accumulated parallel to the basement surface over Gop Rift and the Chron 27 oceanic crust, the ratio of Paleogene reflectors over both areas (Section 5.1.2) can be used to give a relative age of Gop Rift and the Chron 27 oceanic crust. These reflectors appear to be post-rift with respect to Gop Rift and contemporaneous with the continued extension of the margin. An upper estimate for rift duration is obtained by assuming rifting south of Gop Rift began at the start of the Paleogene, and that rifting ended with break up south

of Laxmi Ridge and the formation of the Chron 27 oceanic crust. The thinner sequence of reflectors over the oceanic crust is due to the younger age of this structure. Assuming the whole sequence of the Paleogene is present and taking the ratio of the two sets of reflectors infers a rift duration of 7 Myr.

Figure 3.34 uses the method of Bown and White (1995) to show that this rift duration is sufficiently long to suppress melting enough to generate the crustal thickness observed, assuming an initial lithospheric thickness of 150 km and a β of 5. These assumptions are reasonable since Reddy et al. (1999) report a crustal thickness of 45 km for peninsular India, and the current thickness of Laxmi Ridge is 9 km, excluding the HVSCB. It was assumed that any earlier thermal input from the 90 Ma episode of rifting between the Seychelles and Madagascar had dissipated. The method of Bown and White (1995) is generally invoked to predict volumes of syn-rift magmatism rather than thickness of magmatic crust, but it is considered valid for this purpose since there appears to be no component of active upwelling involved in the crustal accretion at this margin. Figure 3.34 shows predicted melt thicknesses for an elevated mantle temperature, but the temperature of the mantle at rifting is not known. This study infers that rift duration and the subsequent mantle cooling is a more important control on syn-rift magmatism than initial mantle temperature because an elevated mantle temperature may not generate significant syn-rift magmatism if the rift duration is sufficiently long.

3.7.2 Anomalous velocities in the mantle and deep crust

Mantle velocities are poorly constrained, but they seem to be low, particularly under the Chron 27 oceanic crust. Possible causes for the low velocities are listed below:

1. The low velocities could be due to remnant heat from the Deccan hotspot or lateral heat conduction from the current day spreading centre, the Carlsberg Ridge. If the thermal anomaly is from the Carlsberg Ridge, this could explain why there is a lateral density gradient in the mantle (Section 4.1.1), and also why the velocities are lower to the south (closer to the ridge). This velocity gradient could be due to a lateral mantle temperature gradient of the order of $0.02^\circ C$ km^{-1}, although this depends on the composition of the source mantle (Farnetani et al., 1996). The study area is probably too far from the current day location of the Carlsberg Ridge to experience a lateral conducted heat flow from the Ridge, but the possibility can not be ruled out.

2. The reflection modelled as the Moho could actually be a deep crustal reflector, implying that what was interpreted here as low velocity upper mantle is actually deep oceanic crust whose base is not imaged. This seems unlikely since a velocity of 7.7 km s^{-1} is too high to be deep oceanic crust (White et al., 1992).
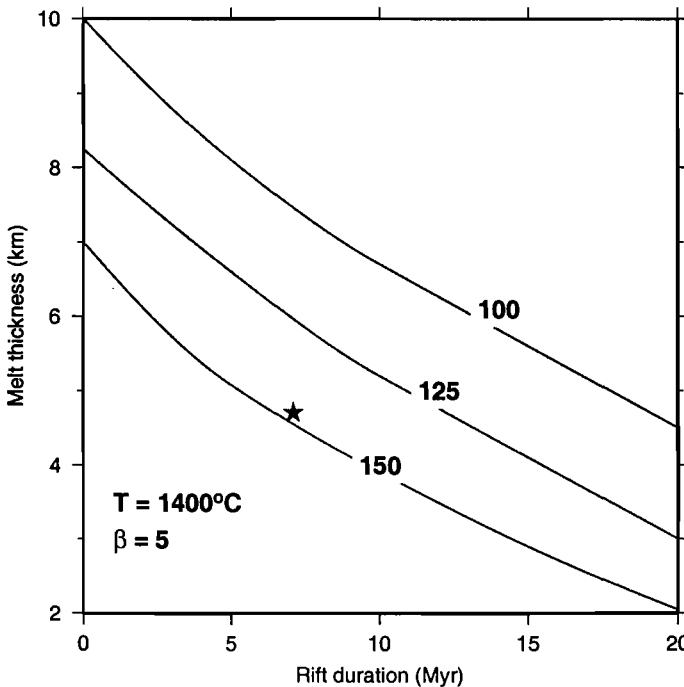
Figure 3.34: Rift duration and melt generation: Rift duration versus total melt thickness for a warm (1400°C) mantle and a β of 5. Numbers on curves are initial lithosphere thickness in km. The star is the average thickness of the Chron 27 oceanic crust. The rift duration is approximated from the syn-rift stratigraphy discussed in Section 5.1.2.

3. Conversely, what has been interpreted as oceanic layer 3 could actually be partially serpentinised mantle, with the Moho a serpentinisation front. Serpentinisation occurs when crustal scale faults act as conduits for seawater to enter the mantle. The seawater can hydrate olivine, transforming it to lower density serpentinite (O'Hanley, 1996). A 3 km thick oceanic layer 2 underlain by 3 km of materials with velocities of 7.2 km s^{-1} to 7.6 km s^{-1} has been modelled across the Newfoundland margin. This was interpreted as 3 km thick oceanic crust underlain by 3 km of partially serpentinised mantle (Reid, 1994). This hypothesis seems unlikely to apply to the Laxmi Ridge margin, since this would require serpentinite to form at shallower depths than its stability zone (Fowler, 1990).

4. The low velocity upper mantle could be partially serpentinised. A velocity of 7.7 km s^{-1} equates to a serpentinisation of 10 % (Miller and Christensen, 1997).

The serpentinisation of the upper mantle or remnant thermal energy hypotheses (1 and 4) are preferred, as they are the simplest explanations for the observations.

Unusual velocities are also seen in the deep crust at two locations; beneath Laxmi Ridge and the continental rise. These are interpreted in Section 4.2.3 as a single body of magmatic underplate that had accreted to the base of the crust during the initiation of Deccan volcanism, only to be separated by later spreading in Gop Rift. Bodies in

the deep crust with velocities greater than 7 km s^{-1} have been interpreted as magmatic underplate associated with rifting on many continental margins, including the East Coast of the U.S.A. (Kelemen and Holbrook, 1995) and parts of the North Atlantic, e.g., Hatton Bank (Barton and White, 1995) and Edoras Bank (Barton and White, 1997). High velocity bodies are derived from melts formed either by high temperature melting leading to increased Mg content of the melt (White and McKenzie, 1989), or by melt fractionation forming cumulates. According to Farnetani et al. (1996), magmatic underplate forms because crystal fractionation is an important processes in plume volcanism. Petrological modelling shows that crystal fractionation within a picritic, plume influenced mantle generates olivine rich cumulates, which can have seismic velocities 7.5 - 7.9 km s^{-1} (Farnetani et al., 1996).

An alternative explanation for the HVSCBs beneath the Laxmi Ridge margin is that they are serpentinised bodies resulting from the lateral diffusion of seawater from faulting within Gop Rift. This seems unlikely since the HVSCBs are present beneath thick crust and absent beneath thin crust: the opposite pattern would be expected if they are serpentinite. The magmatic underplate hypothesis is preferred because it agrees with conclusions drawn on other volcanic margins. In addition, the whole of the Laxmi Ridge margin was extending, so serpentinisation would be expected across the whole margin rather than localised about one fault system.

3.7.3 Controls on extension and magmatism in Gop Rift

In Section 4.2.3, it is shown that the opening of Gop Rift could coincide with the extrusion of the Deccan Traps. Spreading began shortly after the initiation of the Deccan lavas, and ended at around the time the hotspot ceased. This suggests that the seafloor spreading initiated because of thermal weakening by the hotspot and did not continue to steady state, self-sustaining accretion, so was dependant on the thermal anomaly for melt supply. Accretion was asymmetric, with thicker, more rapid formation in the northern basin, which would have been closer to the Deccan hotspot. Underplate formed by the Deccan hotspot probably predates spreading in Gop Rift (Section 4.2.3).

The underplate beneath the continental rise is $\sim$3 km thicker than the underplate beneath Laxmi Ridge. Figure 3.35 uses the calculations of White (1992) to show how, for a given magnitude of crustal extension (β), increasing the mantle potential temperature by 40°C can replicate this pattern. This is further evidence for asymmetry of Gop Rift being due to the influence of the Deccan hotspot to the north.
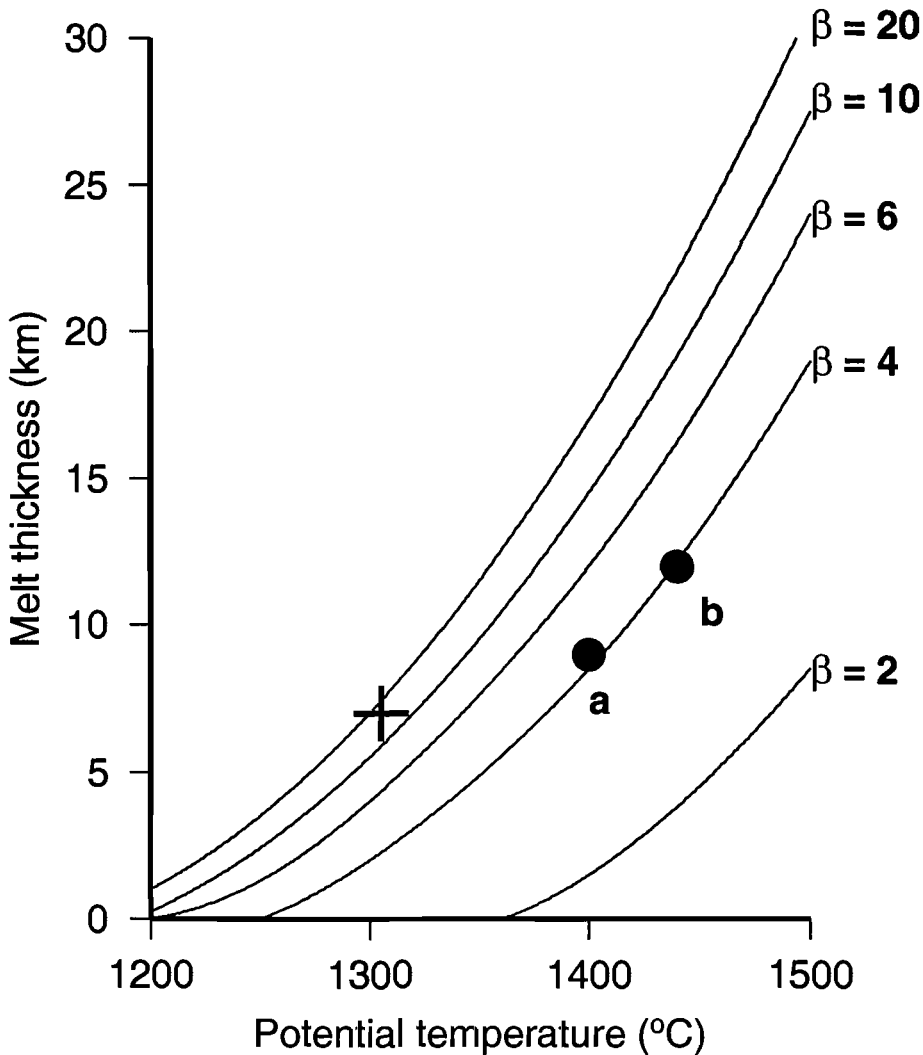
Figure 3.35: Potential temperature vs. melt thickness for Gop Rift underplate: curves are different stretching factors (β). The cross is the thickness of magmatic crust generated by decompression melting of normal mantle. Black circles are the thicknesses of the underplated material beneath Laxmi Ridge (a) and the continental rise (b). β is assumed to be approximately 4 because the full thickness of the Indian crust is 45 km (Reddy et al., 1999) and the continental crust immediately north of Gop Rift is 11 km. To maintain a β of 4, the temperature anomaly must be increased by 40°C to accrete the observed thickness of underplate beneath the continental rise.

3.7.4   The Seychelles Bank margin

In Figure 3.36, the velocity structure of the conjugate Seychelles Bank margin (Collier, pers. comm.) is joined to the Laxmi Ridge margin at the approximate location of Chron 27 on both margins. The depth scale is relative to the Seychelles margin; the Laxmi Ridge profile has been shifted by 940 m so that the profiles are aligned on top basement. Isostatic calculations that compensate for the extra sediment loading on the Laxmi Ridge crust predict a depth to basement of 7.42 km for the Seychelles margin, which matches the observed mean depth to basement of 7.41 km. This shows that the extra sediment loading on the Laxmi Ridge margin can explain the difference in basement depth. The excellent match in both crustal thickness and velocity structure of the two models provides support for the reliability of both models. In particular, unusual features such as the thin first-formed oceanic crust and high velocities at the base of the crust are independently verified. The crust has an asymmetric morphology. Bassi (1995) predicted that rapidly strained lithosphere would yield symmetrical margins, but strain rate is only a control if the the upper mantle is weak and viscous. Even if Gop Rift is closed and it is assumed that the phase of extension that lead to the eventual separation of Laxmi Ridge and the Seychelles began south of Laxmi Ridge, the Moho morphology is still obviously asymmetric.

Velocities greater than 7 km s^{-1} beneath the shelf break on the Seychelles margin were interpreted by Collier (pers. comm) as magmatic underplate. Around 2 km of this high velocity material is modelled, which matches predictions by McKenzie and Bickle (1988) for melt generation by instantaneous rifting if a β of 5 is assumed. However, the continuation of these high velocities onto the Laxmi Ridge margin suggests that they are related to oceanic crust on these margins; perhaps the high velocity region under the foot of the slope off the Seychelles Plateau is the OCB on this margin.

3.7.5   Sequence of events

Given the evidence for the distribution and timing of magmatism and the timing of breakup, the following sequence of events is suggested:

1. The Deccan hotspot arrives at the base of the extending Indian lithosphere. The Deccan Traps are extruded around 67 Ma ago (Vandamme et al., 1991) over the Indian continent, with some reaching the Seychelles (Müller et al., 2001), and magmatic material is accreted to the base of the crust beneath India (Krishna et al., 1991), including Laxmi Ridge (Pandey et al., 1995; Miles et al., 1998; Krishna et al., 2006). A combination of thermal weakening and extension cause a weak spot in what will become Gop Rift.
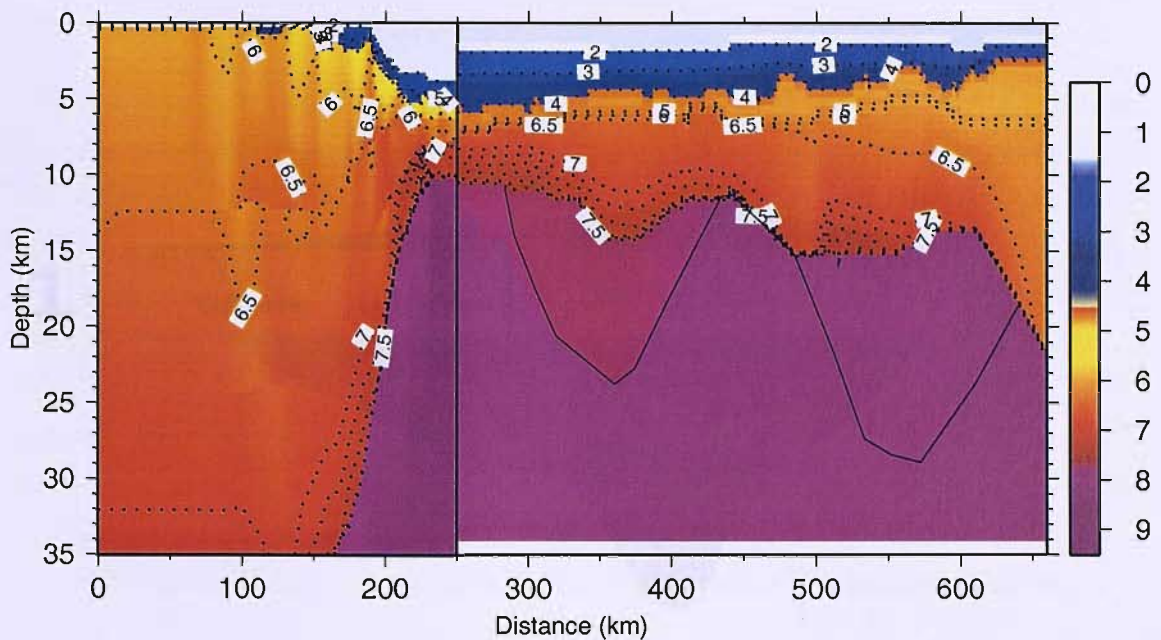
Figure 3.36: Laxmi Ridge and Seychelles Bank conjugate rifted margins: Laxmi Ridge is joined to the Seychelles Bank at the Chron 27 magmatic crust. The Laxmi Ridge model is shifted down by 940 m to compensate for depression of the crust by the thick Indus Fan sediments. There is a good match in both crustal thickness and velocity structure at the join.

2. Continuing extension shapes the basement structure by faulting. Gop Rift progresses to seafloor spreading, exploiting the weakness in the lithosphere caused by the magmatic material at the base of the crust. Accretion is asymmetric, with more new crust formed in the north, near the waning Deccan hotspot.

3. Once the pulse from the hotspot is exhausted, spreading ceases in Gop Rift. After continued rapid extension of the crust, a new spreading centre formed at 62 Ma south of Laxmi Ridge; the Carlsberg Ridge. The rift may have exploited the weakness associated with the change in lithospheric rheology caused by underplating the crust. Shear-wave splitting due to anisotropy beneath the Seychelles (Hammond et al., 2005) may indicate that the underplate extends as far as the Seychelles Bank (Minshull, pers. comm.). Oceanic crust formed south of Laxmi Ridge is thin despite the rapid extension because the rift duration of 7 M.yr is sufficiently long to allow conductive cooling of the upwelling lithosphere. There is some extrusive magmatism on breakup, which manifests as weak SDRs on both the Laxmi Ridge and Seychelles Bank margins.

This sequence is illustrated in Figure 3.37.
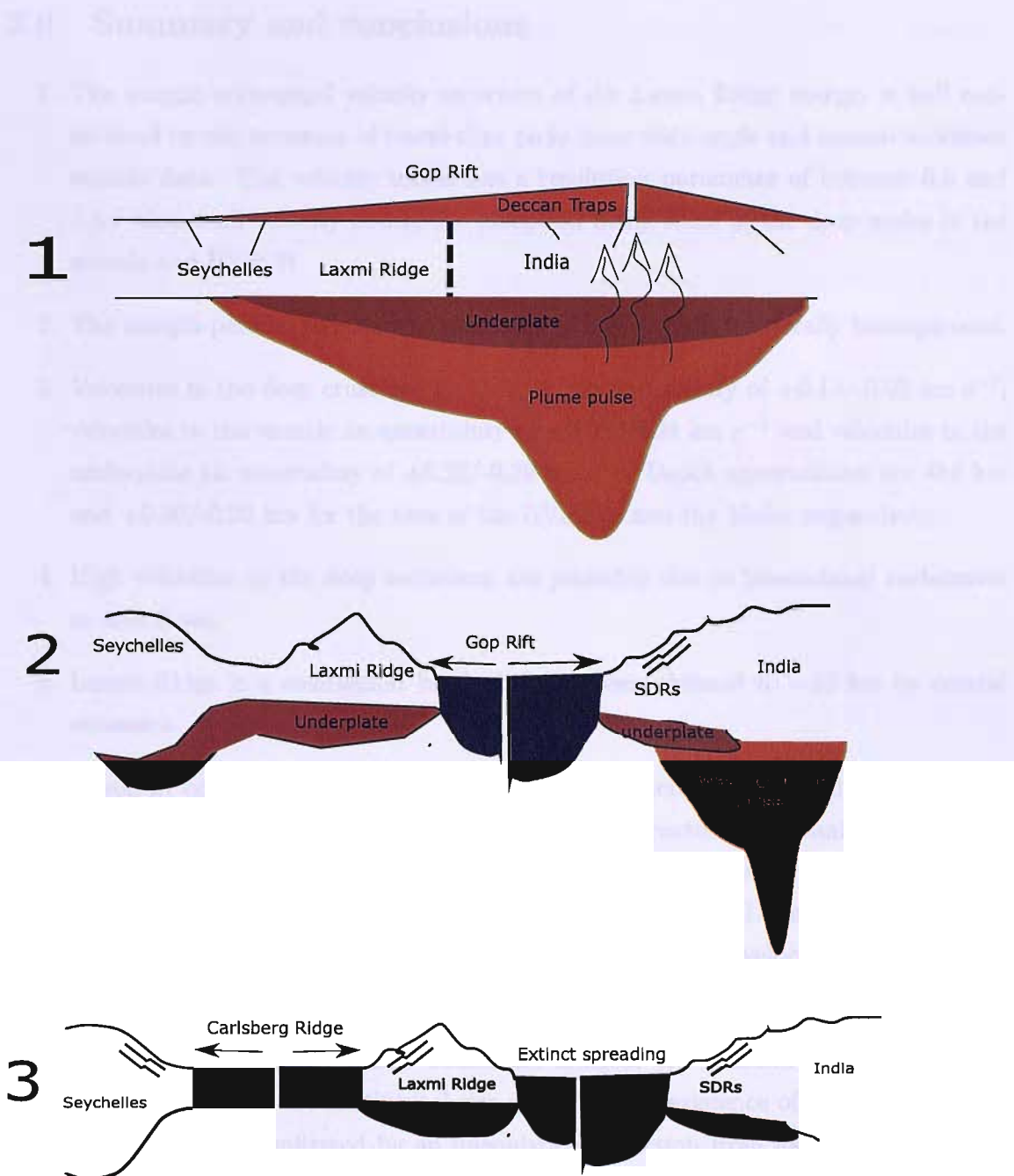
Figure 3.37: Sequence of events forming the Laxmi Ridge margin: *1)* The Deccan hotspot arrives at the base of the extending lithosphere, causing extrusion of the Deccan traps and magmatic underplating of the crust, which may extend beneath the Seychelles (Hammond et al., 2005). *2)* Asymmetric accretion in Gop Rift, breakup occurs in weakened underplated lithosphere. *3)* The hotspot exhausted, spreading halts in Gop Rift. A new spreading centre is established south of Laxmi Ridge, separating India from the Seychelles. No scale implied. For a full description, see text.

3.8 Summary and conclusions

1. The margin-orthogonal velocity structure of the Laxmi Ridge margin is well constrained by the inversion of travel-time picks from wide-angle and normal incidence seismic data. The velocity model has a resolution parameter of between 0.5 and 1 for almost all velocity nodes, the exception being some of the deep nodes in the mantle and HVSCB.

2. The margin-parallel structure of the Laxmi Ridge margin is laterally homogeneous.

3. Velocities in the deep crust can be assigned an uncertainty of $+0.13/-0.03$ km s^{-1}; velocities in the mantle an uncertainty of $+0.08/-0.04$ km s^{-1} and velocities in the underplate an uncertainty of $+0.22/-0.39$ km s^{-1}. Depth uncertainties are -0.3 km and $+0.80/-0.20$ km for the base of the HVSCBs and the Moho respectively.

4. High velocities in the deep sediments are probably due to intercalated carbonates or lava flows.

5. Laxmi Ridge is a continental block that has been thinned to $\sim$10 km by crustal extension.

6. Chron 27 oceanic crust has an unusual velocity structure, with a thin, low velocity gradient layer 2 and thin layer 3. The velocity structure of oceanic crust within northern Gop Rift matches Atlantic averages for plume influenced accretion. Despite broad similarities in the velocity structure of Gop Rift and Laxmi Ridge, Gop Rift is interpreted as being of oceanic provenance based on its velocity structure, high magnetisation and seismic reflection characteristics.

7. Two high velocity sub-crustal bodies are imaged, one beneath Laxmi Ridge and the other beneath the continental rise of India. The existence of the body beneath Laxmi Ridge is confirmed by an unequivocal reflection from its base observed on the margin-parallel wide-angle line. They are interpreted as magmatic underplate formed prior to seafloor spreading in Gop Rift.

8. Asymmetric accretion of both underplate beneath the Laxmi Ridge margin and oceanic crust within Gop Rift was driven by the proximity of the Deccan hotspot. The mantle beneath the northern limit of the underplate was around 40°C hotter than the southern limit.

9. Oceanic crust formed south of Laxmi Ridge is around 5 km thick, which indicates that the Deccan hotspot was not active in the region by Chron 27 time. The mantle may have cooled due to a combination of heat conducting through the thick,

cool lithosphere and having a sufficiently long rift duration to allow new upwelling material time to cool.

10. Low mantle velocities beneath the Chron 27 oceanic crust could be an indicator of 10% serpentinisation of the mantle, or a remnant thermal anomaly from breakup.

11. The Laxmi Ridge and Seychelles Bank conjugate margin velocity models are an excellent match when joined at the OCB, in terms of crustal thickness and velocity structure.

4

Potential field modelling

4.1 Free-air gravity over Laxmi Ridge margin

Laxmi Ridge is characterised by a negative free-air gravity signature (Fig. 4.1), which suggests that it is underlain by thick crust. To the north of Laxmi Ridge are Gop Rift and, further east, Laxmi Basin. Both have a positive free-air anomaly. Sedimentary basins like Gop Rift generally have negative free-air signature due to their low density sedimentary fill, and conversely, basement highs like Laxmi Ridge generally have a positive free-air anomaly. This kind of gravity inversion is also observed in the Ross Sea (e.g., Karner et al., 2005), the western platform of New Zealand (Holt and Stern, 1991) and the 85° East ridge in the Central Indian Ocean (Liu et al., 1982). Davey and Cooper (1987) and Davey (1981) attribute the positive anomaly over a basement low in the Ross Sea to the addition of high density magmatic material to the lower crust. An alternative model, proposed by Karner et al. (2005), shows how changes in flexural strength of the lithosphere can change the direction of the gravity signature of a basin: an extensional basin forms in a relatively weak lithosphere; this has a negative free-air anomaly. The lithosphere then cools and so its flexural strength increases. Sediment loading adds to the density of the basin (by replacing the lower density water), but the load is not isostatically compensated due to the rigidity of the lithosphere, so a positive anomaly is retained. This case is only valid if there is a delay between basin formation and sediment loading, which probably is not the case for the Laxmi Ridge margin (Section 5.3.1).

In order to discover the provenance of the observed anomalies over Laxmi Ridge, a gravity model was constructed by converting the calculated velocity structure of the margin (Section 3.4) into a density model. The conversion was made using equation 4.1, which is a fourth order polynomial fit (Ludwig et al., 1970) to the velocity-density relationship of sediments and crystalline rocks, measured by lab and in-situ seismic methods (e.g., Christensen and Mooney, 1995).

$$\rho = -0.6697 + 2.2302V_p - 0.598V_p^2 + 0.07036V_p^3 - 0.0028311V_p^4 \qquad (4.1)$$

Density is measured in g cm^{-3}; velocities are in kms^{-1}. This relationship is only valid for crustal rocks; a density of 3.3 g cm^{-3} was used for the upper mantle (Anderson, 1989) and 1.033 g cm^{-3} was used for seawater.

After the construction of a density model, a synthetic gravity profile can be generated. The models presented in this chapter were made using the software *grav2d*, which uses
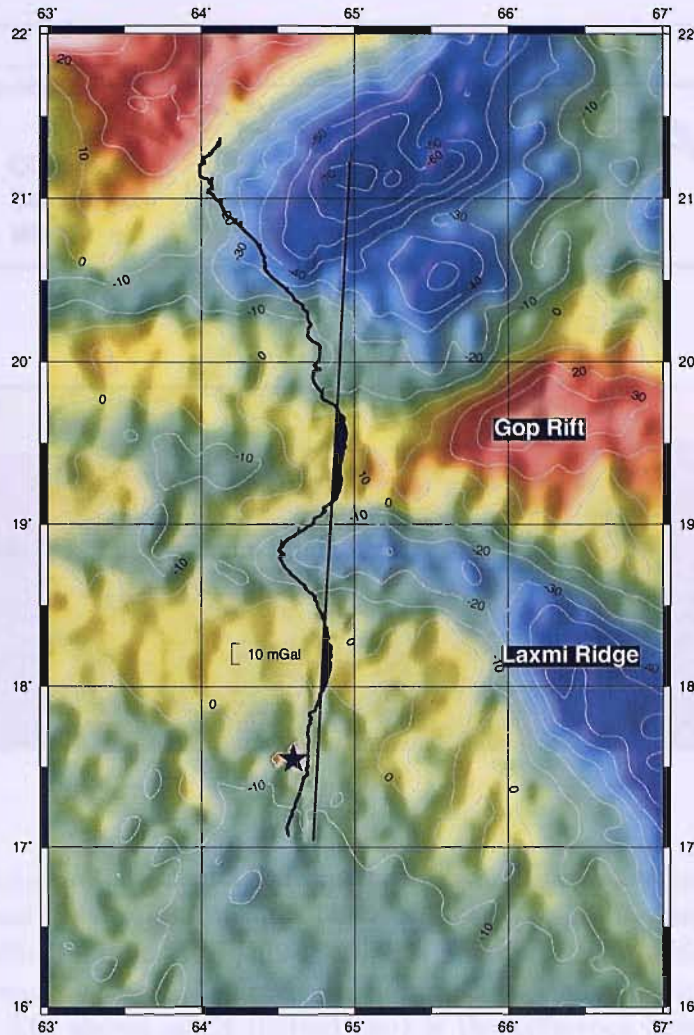
Figure 4.1: Free-air gravity: Negative free-air anomalies associated with Laxmi Ridge and the continental rise of India are separated by a positive anomaly over Gop Rift. Contours are in mGal. The extracted gravity along the main CD144 profile (black line) is shown as a wiggle plot; positive values are to the right of the profile. The 12 mGal positive anomaly discussed in Section 4.1.3 is indicated with a star.

the 2d line integral method developed by Talwani et al. (1959).

4.1.1 The gravity models

The gravity profile generated by a direct conversion of the velocity model (Section 3.4) to a density model is given in Figure 4.2. The misfit between the predicted and observed curves over the oceanic (southern) end of the model is substantially reduced if a best-fitting linear trend is removed from the data. This implies that the gravity signature of the margin has a linear component with its source deeper than the crust. This is because the mantle temperature, and therefore density, changes laterally. This effect decreases linearly to the north, away from the spreading centre at Carlsberg Ridge. Gradients in
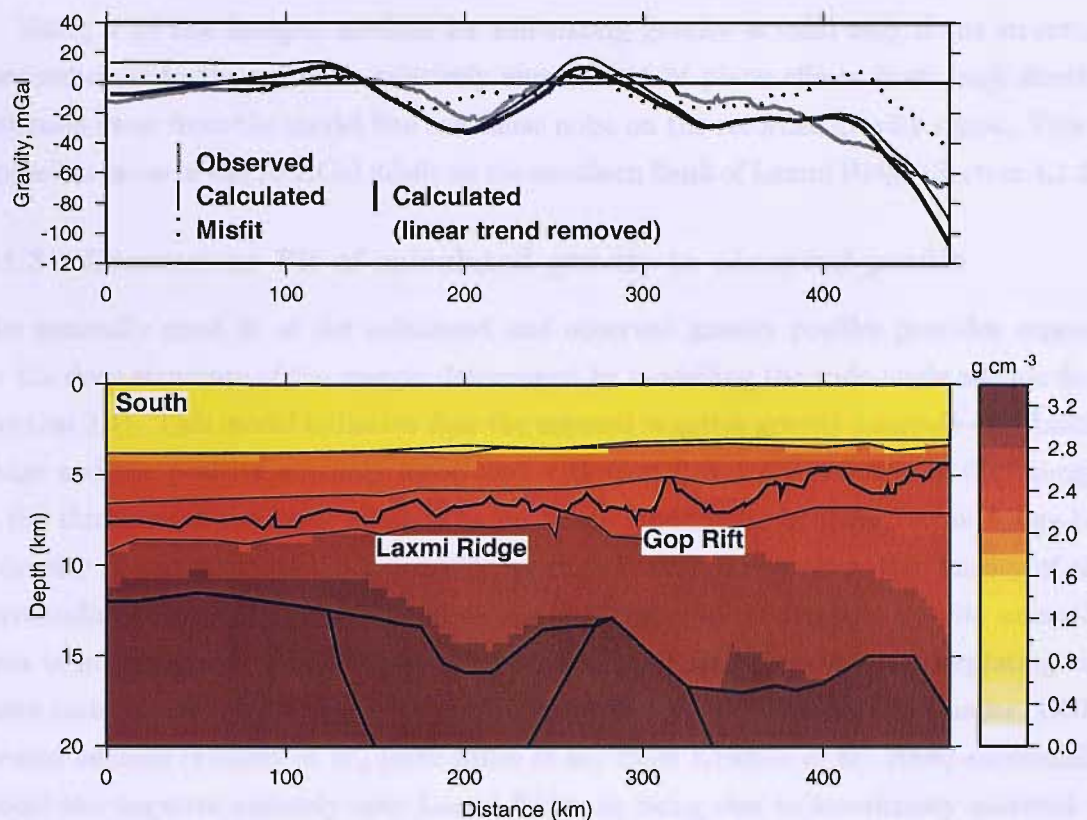
Figure 4.2: Gravity profile calculated from the wide-angle velocity model: *Top*: Calculated and observed gravity and misfit. The calculated profile becomes more similar to the observed profile if a best-fitting linear trend is removed from the data, implying that there is a linear component to the gravity signature that originates from a deeper source than the crust. The shown misfit (dotted line) is the difference between the observed gravity and the calculated gravity once this trend has been removed. The RMS misfit is 9.49 mGal. *Bottom*: Density structure of the model, units are g cm^{-3}. Boundaries are horizons from the wide-angle velocity model (Section 3.4), which are constrained both by velocity discontinuities and seismic reflections.

mantle density are also inferred on the conjugate Seychelles Bank margin from gravity modelling (Vardy, 2005, Collier, per. comm).

This model generally fits the data well (the RMS misfit is 9.49 mGal). There is a 10 mGal misfit over the southern flank of Laxmi Ridge.

4.1.2 Limitations of the gravity model

The conversion of seismic velocity to density is an approximation based on lab measurements. This approximation can break down if there has been an alteration of the density of the rocks, for example by thermal alteration of the constituent minerals. This is discussed in more detail in Section 4.1.3.

The velocity-density conversion used is only valid for crustal rocks, so a constant mantle density of 3.3 g cm^{-3} was used.

Using a 2d line integral method for calculating gravity is valid only if the structure perpendicular to the model is relatively simple: out of plane effects from large density contrasts away from the model line can cause noise on the recorded gravity signal. This is a possible cause of the 10 mGal misfit on the southern flank of Laxmi Ridge (Section 4.1.3).

4.1.3 Discussion: Fit of calculated gravity to observed profile

The generally good fit of the calculated and observed gravity profiles provides support for the deep structure of the margin determined by modelling the wide-angle seismic data (Section 3.4). This model indicates that the unusual negative gravity anomaly over Laxmi Ridge and the positive anomaly associated with Gop Rift are a function of the changes in the thickness of the lower crust. The magmatic underplate beneath Laxmi Ridge has a density of approximately 3.2 g cm^{-3}, which is slightly lower than the density of the surrounding mantle (3.3 g cm^{-3}) and so may contribute to the negative gravity anomaly. This is in agreement with the theory that magmatic intrusions and underplating can cause such counter-intuitive gravity profiles (e.g., Davey, 1981; Davey and Cooper, 1987). Several authors (Pandey et al., 1995; Miles et al., 1998; Krishna et al., 2006) successfully model the negative anomaly over Laxmi Ridge as being due to low-density material in the deep crust/ shallow mantle. Magmatic underplate has been modelled under the Eastern Basin and at depths of 45-60 km beneath the western coast of continental India using gravity inversions (Negi et al., 1994), and beneath the Deccan Traps using seismic inversions (Krishna et al., 1991). In fact, gravity inversions shows that up to two-thirds of India may be underplated (Negi et al., 1989). The small misfit between the observed and measured gravity on the southern flank of Laxmi Ridge could be due to an out of plane high density body adding its signature obliquely to the observed gravity. This scenario is examined in the following section.

Offline density contribution

A 12 mGal free-air anomaly high exists adjacent to the gravity misfit over Laxmi Ridge (Fig. 4.1). This could potentially contribute an out of plane positive component to the measured gravity over the main line, and could therefore be the cause of the misfit between the observed and predicted curves.

The depth of the source of this 12 mGal anomaly can be approximated from the width of the observed anomaly shape (e.g., Fowler, 1990) from equation 4.2:

$$gz_{anomaly} = \frac{G\frac{4}{3}\pi R^3 (\rho - \rho')}{z^2 (1 + \frac{x}{z}^2)^{\frac{3}{2}}} \tag{4.2}$$

where $gz_{anomaly}$ is the vertical component of the gravity anomaly, G is the gravitational

constant, ρ is the background density and ρ' is the density of the body causing the anomaly. R and z are the radius and depth of the body respectively, both in kilometres.

Since the constant $G\frac{4}{3}\pi = 27.95$, then

$$gz_{max} = 27.95(\rho - \rho')\frac{R^3}{z^2} \tag{4.3}$$

If the anomaly is plotted normalised to gz_{max}, the half-width of the profile, x_{half} can be measured to give an estimate of the depth *(z)* of the body. g=gz_{max}/2 occurs at x_{half}:

$$\frac{gz_{max}}{gz_{max}/2} = 2 = [1 + (\frac{x_{half}}{z})^2]^{\frac{3}{2}} \tag{4.4}$$

so,

$$z \sim 1.3 \cdot x_{half} \tag{4.5}$$

In the case of this anomaly, the half width is observed to be approximately 0.075^o (8.3 km), so the depth of the source body is ~ 11 km.

Knowing the depth and position of the source of this anomaly allows the effect on the adjacent main Laxmi Ridge profile to be calculated, using equation 4.6:

$$gz = \frac{27.95R^3(\rho - \rho')}{z^2(1 + \frac{x}{z}^2)^{3/2}} \tag{4.6}$$

where z is the depth of the source body calculated from equation 4.5, x is the horizontal offline distance from the body to the Laxmi Ridge main profile (approximately 100 km; Fig. 4.1.3), R is the radius of the anomaly source body (if it is approximated to a sphere then R=$[(z^2gz_{max})/27.9]^{1/3}$) gz_{max} is the measured maximum anomaly, (12 mGals); R is approximately 17 km. ρ and ρ' are the body density and background density respectively. These quantities are estimated for a depth of 11 km, from the velocity-density conversion (Fig. 4.2), to be 3.0 g cm^{-3} and 3.01 g cm^{-3}.

Using these figures gives the offline contribution of the high density body adjacent to the Laxmi profile as 1.8 mGals. This figure is approximate, as it is based on the assumptions discussed above. However, it is clearly an order of magnitude too low to be the cause of the 10 mGal misfit over the southern flank of Laxmi Ridge.

4.2   Magnetic modelling

The pattern of magnetic anomalies along the Laxmi Ridge main (north-south) profile was matched by magnetic modelling using constant polarity blocks. The aim of this study was to better understand the provenance of the observed linear magnetic anomalies across the margin (Fig. 4.3), particularly those of disputed origin within Gop Rift (e.g., Naini and Talwani, 1982; Miles et al., 1998; Talwani and Reif, 1998). This modelling provides not only an understanding of the nature of the crust, but also some clues as to the timing of the tectonic events that have affected the present day morphology of the margin.
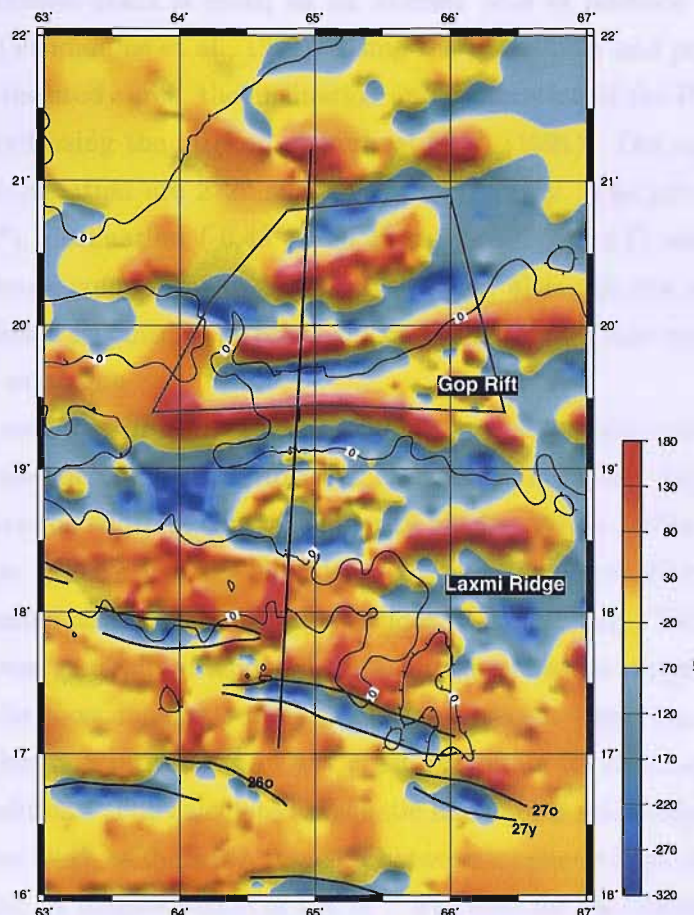
Figure 4.3: Magnetic anomaly map over Laxmi Ridge: Red shades are positive anomalies and blues are negative; scale is in nT. The Chron 27 and Chron 26 seafloor spreading anomaly picks of Miles et al. (1998) are marked with black lines. The linear anomalies in Gop Rift are outlined with a grey box; their provenance is disputed (e.g., Naini and Talwani, 1982; Talwani and Reif, 1998). The southern-most of the three linear positive anomalies in the grey box corresponds to the basement high, Palitana Ridge (Fig. 5.11). The 0 mGal gravity contour is marked: Laxmi Ridge is enclosed by a gravity low; Gop Rift has a positive free-air anomaly.

4.2.1 Forward modelling technique: Oceanic crust

The magnetic field is calculated by summing the contribution from individual fields generated by polygons of constant polarity. The *Magsmr* executable was used (Russell, 1999), which is an implementation of the method devised by Talwani (1965). The remenant magnetisation of the crust was assumed to be acquired during the Paleogene, contemporary with early seafloor spreading (Royer et al., 2002). The appropriate geomagnetic palaeopole was taken from a compilation by Van der Voo and McElhinny (1989). Three possible palaeopoles have been calculated for Paleocene samples from the Indian Plate; the difference between them is small so an average pole of latitude 36.9°N, longitude 281.3° was used (Vandamme et al., 1991). Using the palaeopole and present day latitude and longitude of the study area, the inclination and declination of the Paleocene magnetic field was calculated using the method of Verhoef et al. (1991). The values for remenant declination and inclination are 272° and -68.7° respectively. The present-day magnetic inclination (26.8°), declination (-0.48°) and intensity (37,771 nT) are also required to calculate the induced component of the magnetisation, although the main source of the magnetic anomalies is assumed to be remenant magnetisation. These values were obtained from the NGDC catalogue.

Unequivocal seafloor spreading anomalies (Miles et al., 1998) were modelled by using the appropriate spreading rate (Royer et al., 2002) and Chron duration (Cande and Kent, 1995) to give the width of constant polarity blocks. Whole thickness magnetisation was used, i.e., the whole crust was considered to be magnetised (Harrison, 1987, 1981) rather than assuming all the magnetisation resides in layer 2 (e.g., Talwani et al., 1971). The lower crust was generally considered to be amagnetic as its temperatures are above the Curie point for most magnetic phases. However, recent work (e.g., McEnroe et al., 2004) indicates that haematite in the lower crust can retain its structural stability under lower crustal conditions. The calculated magnetic anomaly is relatively insensitive to the magnetic thickness used, as there is a trade off between magnetic layer thickness and magnetisation strength. A magnetisation of 1 A m^{-1} was used for the Chron 27 oceanic crust. A magnetic susceptibility of 0.2 (Harrison, 1987) was used for all blocks in the model. Although the susceptibility changes the degree to which the crust acquires an induced magnetisation, testing showed that the predicted anomaly waveform and magnitude is relatively insensitive to the actual susceptibility value used. Modelling the oceanic crust using the magnetic data presented in this thesis gives a good match for the published Chron durations and seafloor spreading rates (Table 4.1). Seafloor spreading is observed to commence at around 60.75 Ma, 0.55 Myr after the start of Chron 27r time (Table 4.1). The magnetic model for the oceanic end of the profile and its fit to the observed data is shown in Figure 4.4.

Block	Youngest age[1]	Duration[1]	Implied spreading rate	Spreading rate[2]
26r	58.4 Ma	5.397 Myr	full thickness not seen	118 mm yr^{-1} full rate
27n	60.9 Ma	0.356 Myr	118 mm yr	118 mm yr^{-1} full rate
27r	61.3 Ma	1.223 Myr	full thickness not seen	118 mm yr^{-1} full rate
[1]Cande and Kent (1995)			[2]Royer et al. (2002)	

Table 4.1: Age, duration and spreading rate of observed seafloor spreading anomalies: Chron 27n models as a 21 km wide block; for a Chron duration of 0.356 Myr this gives a half-spreading rate of 59 mm yr^{-1}. Chron 27r should be 160 km wide, but is only 88 km wide (Figure 4.4). This means that either the spreading rate was substantially slower than that previously published, or that seafloor spreading did not commence until 0.55 Myr after the start of Chron 27r; 60.75 Ma.

4.2.2   Modelling Laxmi Ridge and Gop Rift

Crust of disputed origin was modelled by attempting to match the observed anomaly waveform using a variety of configurations of constant magnetisation blocks. Due to the non-uniqueness of the solution, a minimum structure model is preferred. In an effort to produce a minimum structure model, small-scale features such as intrusions are not modelled. This approach accounts for the smoothness of the modelled anomaly profile compared to the measured anomalies.

Laxmi Ridge is well modelled as a block of low (0 to 0.5 A m^{-1}) normal polarity magnetisation (Fig. 4.5), confirming its continental provenance (Talwani and Reif, 1998). The fit of the observed and modelled magnetic anomaly is improved if a component of the magnetisation over Laxmi Ridge is sourced within the magmatic underplate observed beneath the crust (Section 3.4.5). This underplate component of magnetisation is not required by the data, but is consistent with both the magnetic an wide-angle data. The underplate is modelled with a normal polarity, which places constraints on its likely age of formation (Section 4.2.3).

Palitana Ridge marks the boundary between the weakly magnetised Laxmi Ridge and the high amplitude anomalies in Gop Rift. If Gop Rift is proved to be of oceanic provenance, then Palitana Ridge can be said to form the OCB between stretched continental crust within Laxmi Ridge and oceanic crust in the northern part of Gop Rift. Its high magnetisation and basement topography may indicate that it is a volcanic construct.

In the literature, Gop Rift generally begins immediately north of Laxmi Ridge and ends at the large seamount 315 km along the profile (Fig. 4.6). However, the pattern of high amplitude anomalies within Gop Rift continue to the north, and are symmetrical about the seamount. This suggests that the basin to the north is a continuation of Gop Rift. Between Laxmi Ridge and Palitana Ridge, the crustal provenance appears to be different from that in northern Gop Rift. This means that the geographical feature called Gop Rift is actually two structures: weakly magnetised normal polarity crust to the
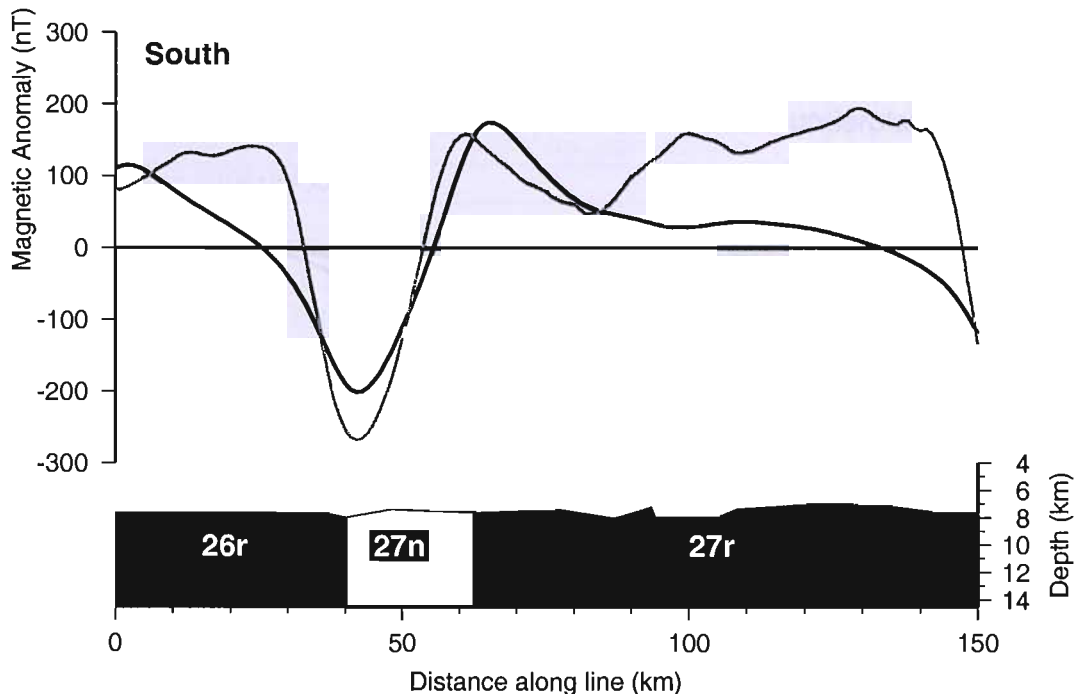
Figure 4.4: Magnetic model for the oceanic crust: *bottom:* magnetic blocks of uniform polarity are used to model observed magnetic anomalies. The base of the crust is modelled as a flat layer for simplicity; the thickness of the blocks is around 6 km, which is appropriate for full thickness oceanic crust on this margin (Section 3.4.2). Distance scale starts at the southern end of the Laxmi Ridge main profile. Magnetisation was acquired in the southern hemisphere, hence the negative anomaly over the normal polarity block. The magnetisation of the blocks is 1 A m^{-1} for the positive (white) block and -1A m^{-1} for the negative (black) blocks. *Top:* magnetic anomalies; observed (grey line) and modelled (black line). The fit of the modelled profile to the observed data are reasonable; the RMS misfit is 62.6 nT. The model does not terminate at 150 km, but continues north (Fig. 4.5).

south and the southern half of a basin filled with strongly magnetised reversed polarity crust to the north. If Gop Rift is proved to be of oceanic origin, the large seamount identified may be the extinct spreading centre. If Gop Rift and the basin north of the seamount are not of oceanic origin, the crust must be heavily intruded to retain such a high remenant magnetisation. To avoid confusion, Gop Rift is here considered to be the section of strongly magnetised crust between Palitana Ridge and the start of the weakly magnetised continental rise.

The magnetic stripes in Gop Rift are caused by the interaction of a high magnetisation with topography, and edge effects due to lateral magnetisation contrasts. They do not require polarity reversals within Gop Rift (Fig. 4.6). Sansom (pers. comm.) uses a polarity reversal in Gop Rift to improve the fit of one of the negative swings observed in the magnetic signal (Fig 4.7). This approach is not adopted here because the single polarity model generates peaks and troughs in the right locations simply by interaction
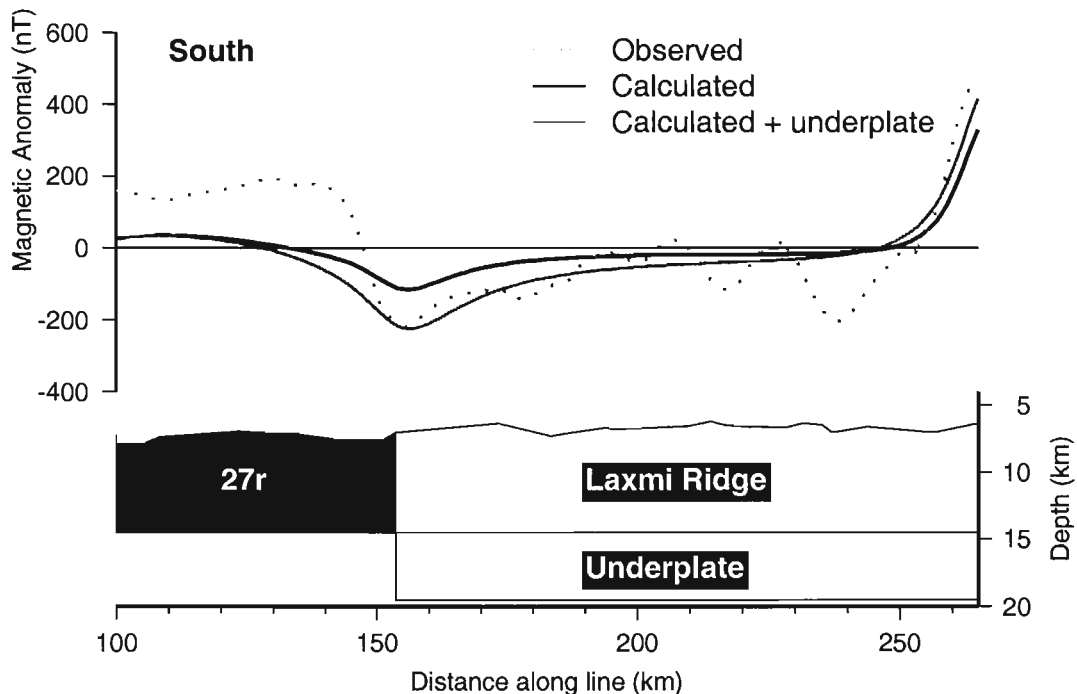
Figure 4.5: Magnetic model for Laxmi Ridge: Laxmi Ridge has 0 - 0.5 A m^{-1} normal polarity magnetisation. *Top:* the fit of the modelled anomaly (black line) to the observed anomaly (grey dashed line) is improved if the component of the magnetic signature generated by an underplate with a magnetisation of 2 A m^{-1} is included (grey solid line).

of the magnetic field with topography. Adding opposite polarity blocks to improve the fit would render the model more complex than is justified by non-unique forward modelling. Sansom's method reduces the RMS misfit of the modelled and observed magnetic anomaly over Gop Rift from 96 nT to 89 nT, which is an improvement less than the internal crossover errors of the dataset (Section 2.4.2). An alternative model presented by Sansom (pers. comm.) has a comparable statistical fit to the data using a single polarity solution for Gop Rift. Sansom's reversal model requires a very high magnetisation within Gop Rift, and is not interpreted as being of oceanic origin because the modelled reversals are not symmetrical within the basin (Sansom, pers. comm.).

Gop Rift can be modelled as having either an oceanic or continental provenance (Fig. 4.6). In the continental scenario, the best fit of the modelled and observed anomalies occurs when the magnetisation is produced both by a 2 km thick sub-crustal layer with a magnetisation of -2 A m^{-1}, and an approximately 2 km supra-crustal layer with a magnetisation of -6 A m^{-1}, which is appropriate for Paleocene basalts (Juárez et al., 1989). This model is considered valid because a bright reflector, which may be a thin layer of extrusives, is imaged on the coincident multichannel seismic profile (Section 5.2.2), and the high velocities at the base of the crust in Gop Rift seen in Section 3.4.4 are consistent with the presence of magmatic underplate. However, Gop Rift can also be modelled

with an oceanic provenance; the best fit model has a 2 km thick oceanic layer two with a magnetisation of -2.5 A m^{-1} overlying layer three magnetisation of -1.5 A m^{-1}. A magnetisation of -2.5 A m^{-1} is not high for Paleocene basalts (Juárez et al., 1989), but it is slightly higher than the magnetisations modelled in the younger oceanic crust on this margin (Section 4.2.1).

The oceanic hypothesis is the simplest scenario that gives a reasonable fit to the data. Both models give an equally good fit to the data, so Gop Rift cannot be conclusively proved to be of continental or oceanic origin by magnetic modelling alone (Fig. 4.8). Malod et al. (1997) hypothesised a pre- Chron 28 oceanic provenance for Gop Rift based on magnetic anomalies.

The continental rise is best modelled as a block with zero magnetisation. In common with Laxmi Ridge, the modelled anomaly over the continental rise matches the observed anomaly more closely if a magnetic component from a sub-crustal normal polarity layer with a magnetisation of 2 A m^{-1} is considered (Fig. 4.6). The continental rise is difficult to model as it is on the northern limit of the data: its magnetisation will be affected by lateral magnetisation contrasts from adjacent crust north of the model line, and these effects are not considered in this model as the basement topography further north is unknown.
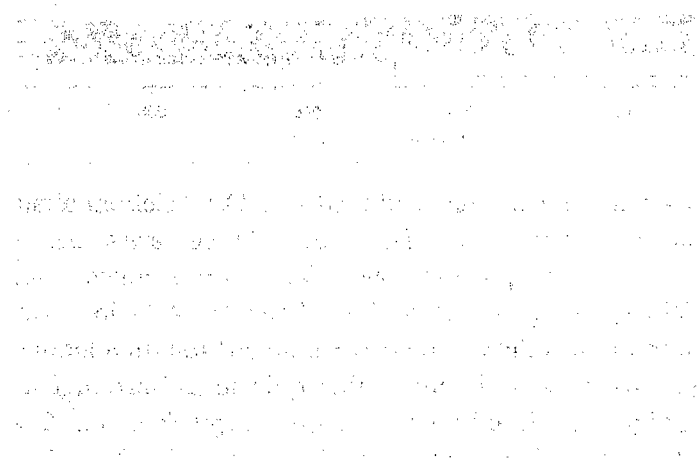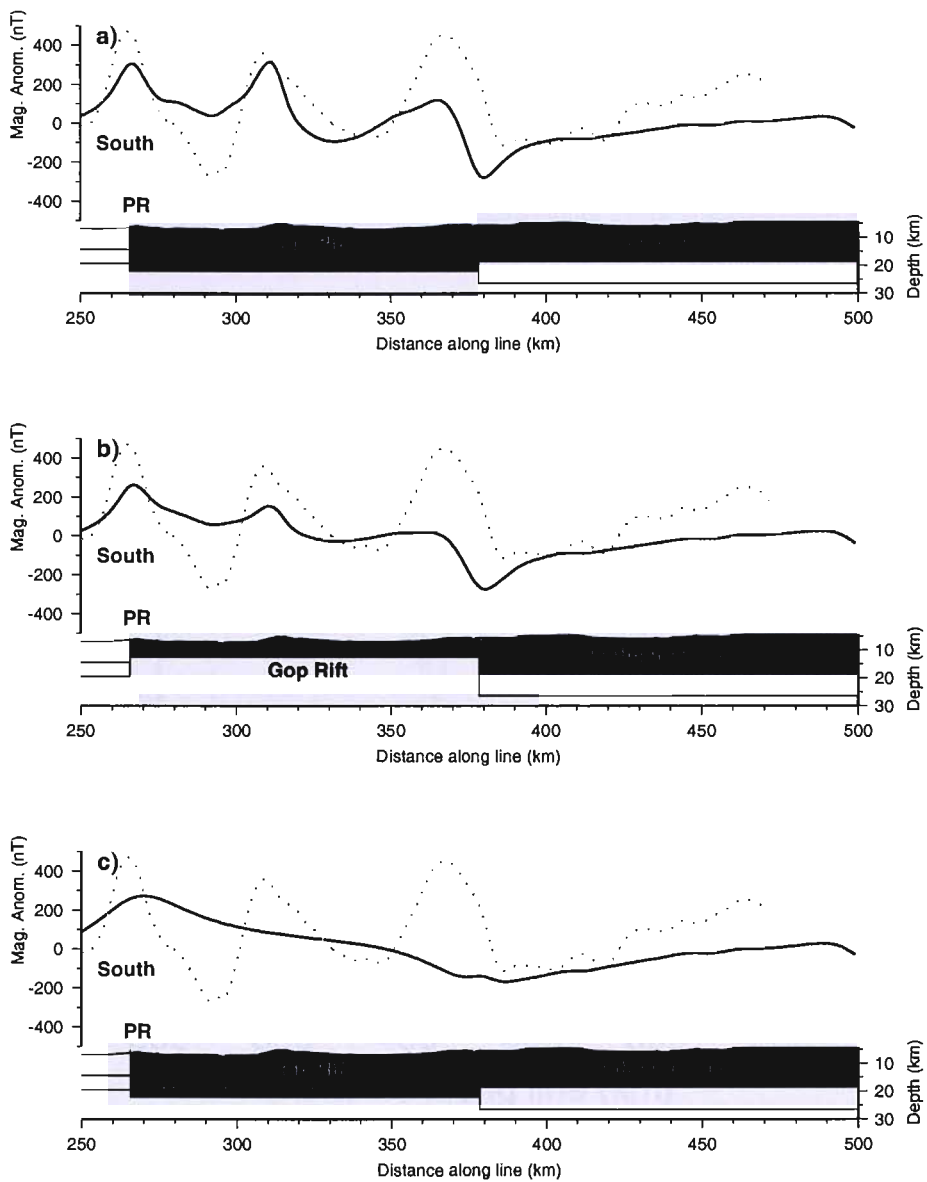
Figure 4.6: Magnetic models for Gop Rift: The magnetic anomaly observed over Gop Rift is modelled in several ways. *a)* The crust within Gop Rift has a magnetisation of zero. The magnetisation causing the anomaly has two components: a 2 km thick underplate with a magnetisation of -2 A m^{-1} and a thin extrusive package with a magnetisation of -6 A m^{-1}. This model matches the data reasonably well, but is not a minimum structure model. *b)* The magnetisation of Gop Rift is mainly due to the high magnetisation (-2.5 A m^{-1}) of $\sim$ 2 km thick layer 2 oceanic crust basalts overlying layer three gabbros with a magnetisation of -1.5 A m^{-1}. This model matches the data adequately, and is a minimum structure model. *c)* Gop Rift has a magnetisation of zero, and the only component of magnetisation is provided by the underplate. This does not recreate the high amplitude peaks and troughs of the observed data. In all models, the continental rise has a magnetisation of zero, and its underplate has a magnetisation of 2 A m^{-1}. PR is Palitana Ridge.
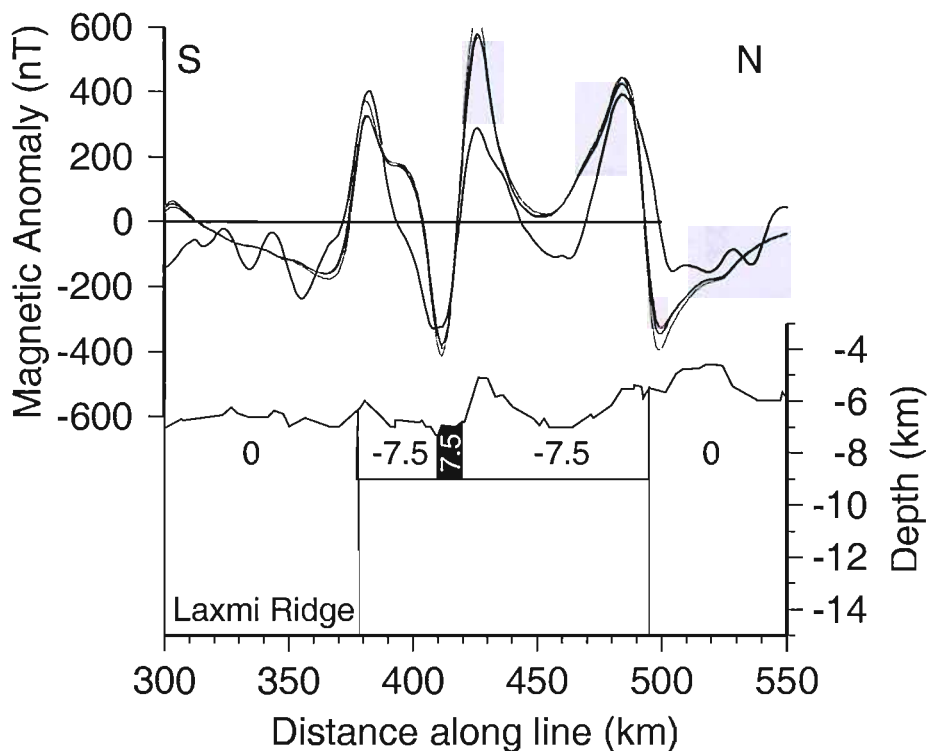
Figure 4.7: Alternative model for Gop Rift: modelling Gop Rift with a polarity reversal south of the central basin high improves the fit of the observed (black line) and modelled (coloured line) magnetic anomalies over Gop Rift at the cost of using a model that is not minimum structure. Magnetisations are in A m^{-1}; different coloured lines are predicted curves using different palaeopoles. From Sansom (pers. comm.)
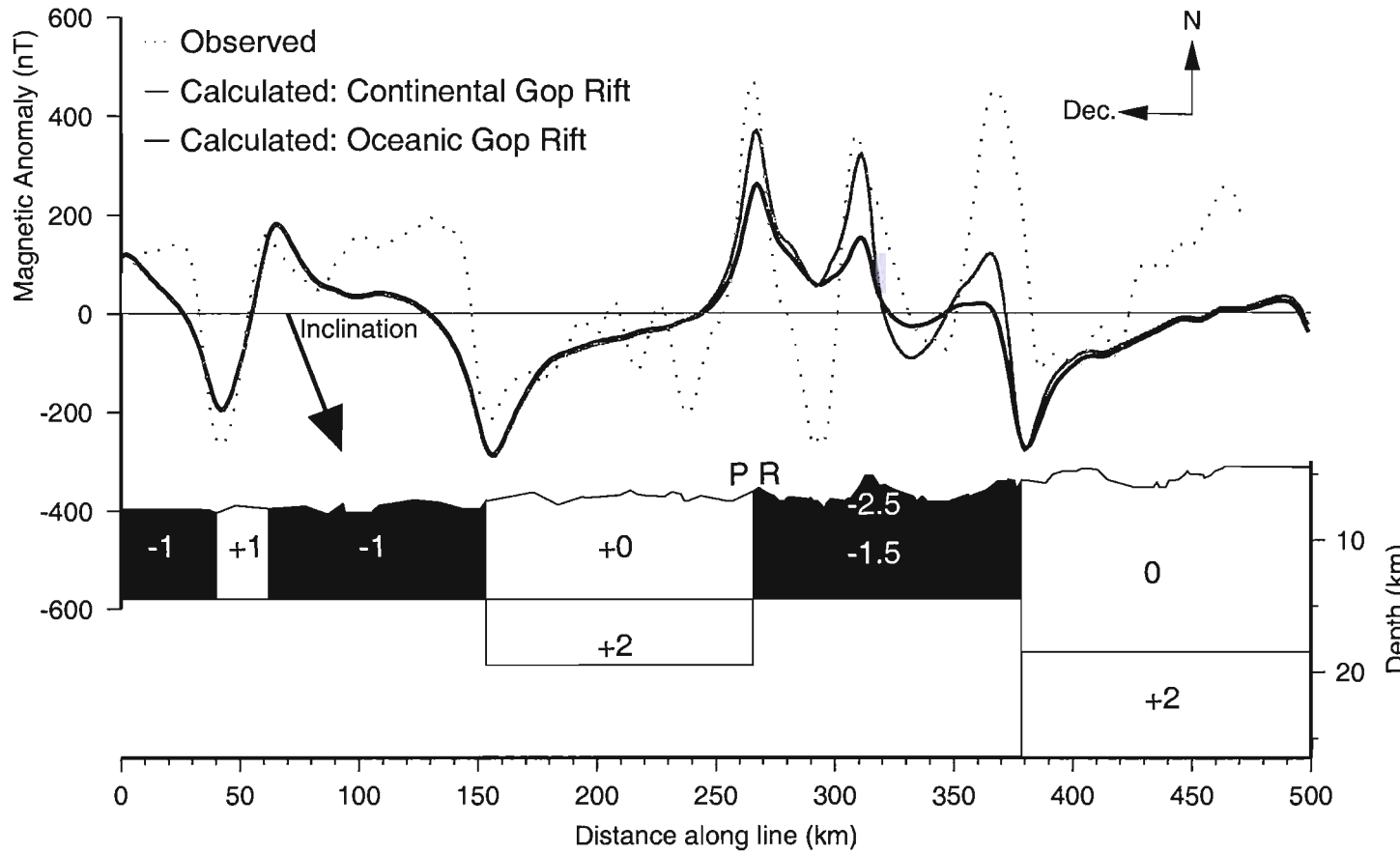
Figure 4.8: Laxmi Ridge margin magnetic model: White blocks have normal polarity and black blocks have reversed polarity. The blocks are labelled with their magnetisation contrast in A m^{-1}. The base of the blocks is flat to simplify the modelling; the block thicknesses are based on the crustal thicknesses modelled in Section 3.4. Palitana Ridge is labelled PR. *Top:* The observed (grey dashed line) and modelled (solid lines) magnetic anomalies. The model shown here attributes an oceanic provenance to Gop Rift, with a magnetisation of -2.5 A m^{-1} in layer 2 and -1.5 A m^{-1} in layer 3. Layer 2 is an approximately 2 km thick block. However, Gop Rift can also be modelled as a continental block with its magnetic signature generated by underplate and supra-crustal magmatic material (Fig. 4.6; solid black line). Arrows indicate the Paleocene magnetic declination (dec.) and inclination directions.

An alternative model of the whole margin, which uses thin (< 3 km) blocks in the oceanic parts of the model to simulate magnetisation originating in layer 2 only (Talwani et al., 1971), is shown in Figure 4.9. This model slightly improves the fit of the width of the anomalies over the oceanic crust south of Laxmi Ridge and within Gop Rift. In order to match the amplitudes of the anomalies, the magnetisations of the Chron 27 oceanic crust and Gop Rift were increased to 2 A m^{-1} and -4.5 A m^{-1} respectively.
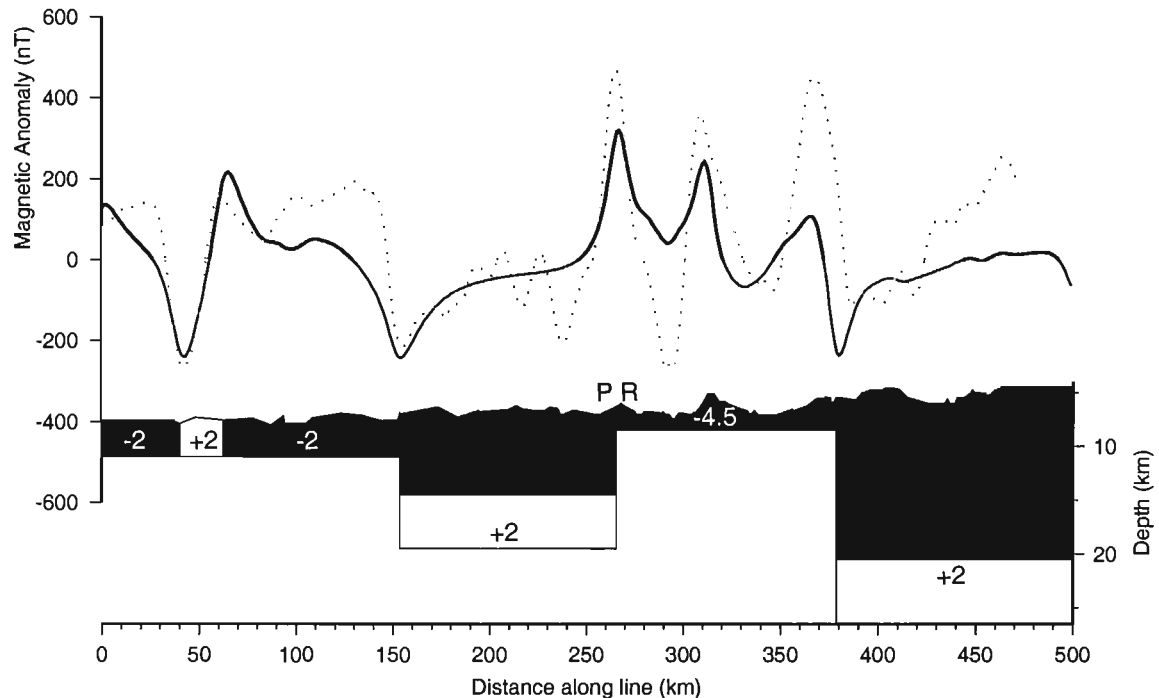
Figure 4.9: Magnetisation within layer 2 only: assigning all the magnetisation the the upper crust of the areas of the model that are interpreted as oceanic (south of Laxmi Ridge and within Gop Rift). Black blocks are negatively magnetised, white blocks are positively magnetised and grey blocks have no significant magnetisation.

4.2.3 Discussion: Implications for the provenance of Gop Rift and the magmatic material

Magnetic modelling has led to a number of hypotheses for the formation of Gop Rift. These hypotheses are discussed in the following sections.

Gop Rift as oceanic crust

If Gop Rift is of oceanic provenance, then an appropriate reversed polarity period needs to be suggested for its formation to fit the negative magnetisation modelled in Section 4.2.2. The possibilities are discussed below.

Gop Rift could have formed during either Chrons 26r or 27r, making it contemporaneous with spreading on the Carlsberg Ridge. However, due to the low yield strength of

spreading ridges, it is unlikely that spreading took place in two adjacent basins at once. If this was the case, one would expect to observe wedge-shaped magnetic anomalies in both basins due to the gradual extinction of the spreading centre in Gop Rift and the propagation of the proto-Carlsberg Ridge in the Arabian Basin. Since this pattern of anomalies is not observed, these theories are discounted.

Several authors have suggested that Gop Rift was formed by seafloor spreading prior to Chron 28 time (Biswas and Singh, 1988; Bhattacharya et al., 1994; Malod et al., 1997; Talwani and Reif, 1998). Attempts to model Gop Rift as Chron 28 were not successful (Fig. 4.10). This is because the anomalies recorded in Gop Rift were formed during a period of constant reversed polarity. Chron 28r was only active for 0.026 Myr (Cande and Kent, 1995); at 118 mm yr^{-1} full spreading rate (Royer et al., 2002), this gives a total width of 3.1 km. Gop Rift is around 100 km wide, so a spreading centre within Gop Rift would have to be active for 0.847 Myr at 118 mm yr^{-1}. If the crust was formed during Chron 28r time, the spreading rate would have to be increased to an unrealistic 26 m yr^{-1}.

Bernard and Munschy (2000) use the geometry of fracture zones in the Mascarene Basin and Laxmi Basin to show how the Mascarene Basin opened with a progressive southward migration of the ridge axis. An eastward ridge jump moved the spreading centre to the Laxmi Basin around Chron 30 time for the northern end of the Ridge and at Chron 27 time for the southern end of the ridge. According to this theory, if Gop Rift is a continuation of the Laxmi Basin then oceanic crustal accretion in Gop Rift should have occurred around Chron 30 time.

Malod et al. (1997) suggested that Gop Rift was formed by a short period of seafloor spreading during Chron 29 time, which was halted when the spreading centre jumped south to form Carlsberg Ridge, where spreading commenced 60.75 Ma (Table 4.1). They located the spreading centre at the basement high in the middle of Gop Rift, the Palitana Ridge. They assumed that the pattern of positive and negative anomalies recorded in Gop Rift were due to a reversal from Chron 29r to Chron 29n, but Figure 4.8 shows that the waveform of the anomaly is an interaction between topography and high magnetisation and no polarity reversals are required. The duration of Chron 29r is about 0.833 Myr (Cande and Kent, 1995), and assuming a spreading rate of 118 mm yr^{-1} gives a duration for Gop Rift of 0.847 yr, so accretion of the crust within Gop Rift could feasibly have occurred during this Chron. If spreading in Gop Rift occurred around Chron 29, then it is contemporaneous with the eruption of the Deccan Traps (e.g., Vandamme et al., 1991, Section 1.4.1).

Bhattacharya et al. (1994) postulate that the magnetic lineations in Gop Rift are consistent with the basin opening either between Chrons 33 and 34 (Talwani and Reif, 1998) or between Chrons 31 and 32. This model does not agree with the findings presented
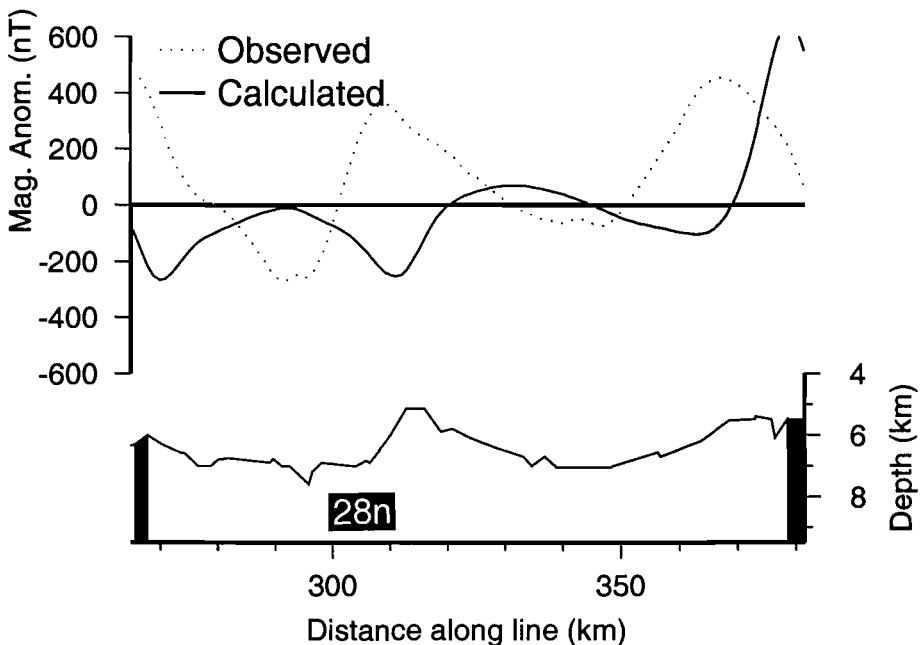
Figure 4.10: Gop Rift as Chron 28: Using the published spreading rate (Royer et al., 2002) and Chron durations (Cande and Kent, 1995), it is not possible to satisfactorily model Gop Rift as Chron 28 oceanic crust.

here, as it does not use a single polarity solution. It also requires highly variable spreading rates; from 2.6 to 40.3 mm yr^{-1}. If Gop Rift opened between Chrons 33 and 34, then spreading would predate the Deccan Traps by 12 Myr. An alternative explanation for the 12 km thick igneous crust accreted within the Rift (Section 3.4.4) would therefore be required.

The magnitude of the remenant magnetisation required to match the high amplitude anomalies observed over Gop Rift is large compared to the remenant magnetisation of the Chron 27 oceanic crust on this margin. This may be a consequence of its hypothesised hotspot source, since melting of hotter mantle can change the geochemistry of the resulting melt by increasing the ratio of MgO to SiO_2 (Holbrook et al., 2001). There is also a significant change in the trace element composition of melts generated over present day hotspots such as Hawaii compared to melts from normal mantle (Norman et al., 2002). However, there is no compelling evidence for hotspot influenced magmatic crust retaining a higher magnetism than 'normal' oceanic crust, so the observation of high remenant magnetisation in Gop Rift is probably due to the unusually high magnetic field strength recorded during the Cretaceous (Wang et al., 2005). The magnetisation of -2.5 A m^{-1} is a conservative estimate; a better fit to the observed magnetic anomalies is obtained with a full thickness magnetisation of -4.5 A m^{-1} in Gop Rift (Fig. 4.11). This observation of high amplitude anomalies provides additional evidence for the opening of Gop Rift being synchronous with the Cretaceous Deccan Traps.
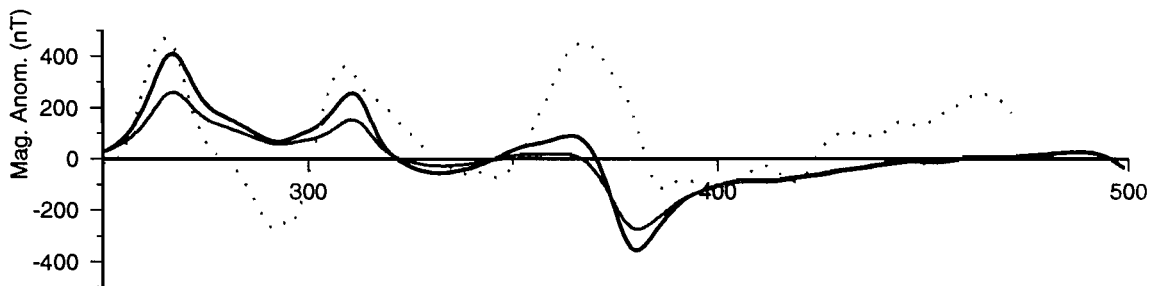
Figure 4.11: High magnetisation in Gop Rift: The measured magnetic anomalies (dashed grey line) are better matched if the remenant magnetisation in Gop Rift is increased from -2.5 A m^{-1} (grey solid line) to -4.5 A m^{-1} (black solid line). This is a consequence of the crusts' formation during a period of high magnetic field strength during the Cretaceous.

In order to test the validity of an oceanic provenance for Gop Rift, the effect spreading within the basin has on the regional plate tectonic reconstruction needs to be considered. This has not been studied in detail previously; the most recent plate reconstruction (Royer et al., 2002) begins at Chron 27, after the formation of Gop Rift. Bernard and Munschy (2000) reconstruct the opening in the Laxmi Basin, and do not consider Gop Rift as a separate structure (e.g., Mishra et al., 2004). Figure 4.12 shows that rotating the continental rise and Laxmi Ridge back to a fixed Palitana Ridge (Malod et al., 1997) gives a good geometric fit. The oblique opening of Gop Rift has forced the strike of Laxmi Ridge from a NNE-SSW orientation, to east-west. The Euler pole used to perform this rotation was based on those used by Royer et al. (2002).

Palitana Ridge is a basement high that divides stretched continental crust in the south of Gop Rift and oceanic crust in the north: it is the OCB. The south of Gop Rift can be considered a failed rift. The modelled geometric fit of the continental rise and Laxmi Ridge support an oceanic provenance for Gop Rift, and does not exclude the possibility that Gop Rift is an extension of the Laxmi Basin (Bernard and Munschy, 2000). However, observed magnetic anomalies in the Laxmi Basin are of the order of 100 nT weaker than those in the north of Gop Rift (Krishna et al., 2006), so it seems unlikely that the two basins are contemporaneous. This supports the interpretation by Krishna et al. (2006) of Laxmi Basin as a failed rift.

After the Chron 29 upwelling of the thermal anomaly was exhausted, spreading stepped south from northern Gop Rift to the Arabian Basin seaward of Laxmi Ridge. This suggests that enhanced mantle melting above the hotspot was providing material for crustal accretion in Gop Rift and once the supply was exhausted, accretion stopped. Breakup seaward of Laxmi Ridge probably exploited the weakening of the lithosphere caused by magmatic underplating of the crust: shear wave splitting beneath the Seychelles Plateau (Hammond et al., 2005) may be the result of the continuation of the Laxmi Ridge underplate beneath the Seychelles (Minshull, pers. comm.).
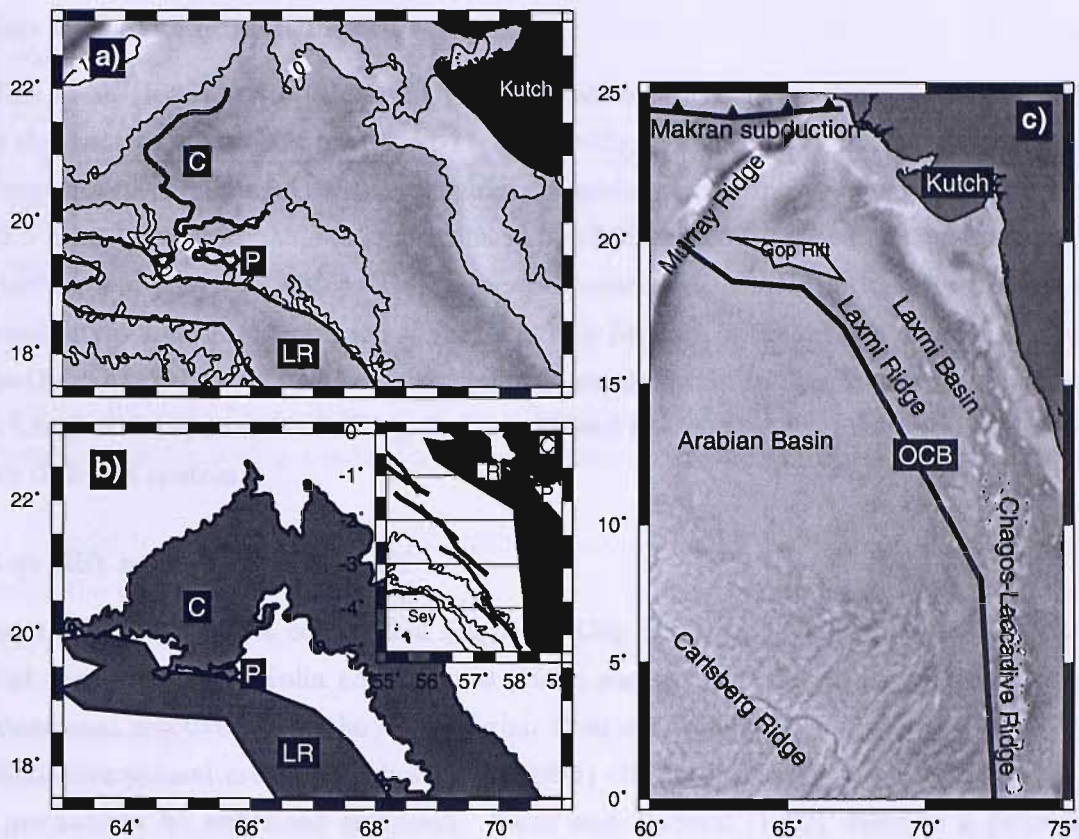
Figure 4.12: Closing Gop Rift: Keeping Palitana Ridge fixed, the continental rise and Laxmi Ridge can be rotated to close Gop Rift. This gives a good geometric fit. On all figures, LR = Laxmi Ridge, P = Palitana Ridge and C = continental rise. *a)* The present day configuration of Laxmi Ridge and Gop Rift. The -10 mGal gravity contour is plotted as a fine black line. The morphology of Palitana Ridge and the continental rise (Section 5.2.4) are plotted as heavy black lines. Depth to basement information is only known for a limited part of the margin, but the -10 mGal contour is observed to be a good analogue for the edge of both Laxmi Ridge and the continental rise. *b)* The continental rise and Laxmi Ridge rotated back to Palitana Ridge to close Gop Rift. Palitana Ridge marks the boundary between stretched continental crust to the south and oceanic crust to the north. The continental rise is approximated by the -10 mGal gravity contour. This closure gives a geometrically good fit of the two blocks. The gap to the east of Gop Rift may be due to alteration of the gravity field by sediment accumulation, or to the oversimplification of the reconstruction: opening of Gop Rift is clearly responsible for the change in orientation of Laxmi Ridge, from NNW-SSE to east-west, but this additional rotation is left out of the reconstruction for simplicity. The gap could also be due to the continuation of extension to the southeast; opening in Gop Rift may be contemporaneous with opening of the Laxmi Basin (Bernard and Munschy, 2000). However, Laxmi Basin could alternately be a failed rift (Krishna et al., 2006). *Inset:* The reconstruction in appropriate geographical coordinates (Royer et al., 2002). Gop Rift is closed, and Laxmi Ridge is rotated back to the Seychelles Plateau. The contours are bathymetry in 1000 m increments. Heavy black and grey lines are the magnetic picks for Chron 27 for Laxmi Ridge and the Seychelles respectively (Miles et al., 1998). *c)* The regional context of the margin. North of Palitana Ridge, Gop Rift is a wedge of oceanic crust within stretched continental crust. The OCB on this margin is located at the limit of stretched continental crust, where accretion from the Carlsberg Ridge begins.

Gop Rift as exhumed mantle

Miles et al. (1998) attribute the high magnetisation of the Laxmi Spur, a basement high to the west of the profile modelled here, as being evidence of it having a serpentinite composition. The magnetisation required to model Gop Rift as a single polarity block (-2.5 A m^{-1}) is comparable to serpentinised peridotites recovered by drilling and dredging (Hayling and Harrison, 1986). The magmatic nature of this margin does not exclude the possibility of mantle exhumation as the magmatic features of the margin may be related to the Deccan hotspot, which predates the final, amagmatic breakup. However, it is difficult to imagine the dynamics of rifting that would lead to synchronous mantle exhumation at two different centres.

Gop Rift as continental crust

Some authors favour a continental origin for Gop Rift (e.g., Naini and Talwani, 1982; Mishra et al., 2004). Kolla and Coumes (1990) suggest that Laxmi Ridge was rifted by extensional reactivation of the Precambrian Dharwar trend. They interpret Gop Rift as rifted, transitional crust. Gombos et al. (1995) cite uplift from the Deccan hotspot as a mechanism for enhanced extension. Naini and Talwani (1982) describe a process of extension and dike injection, which attributes the linear magnetic anomalies in Gop Rift to margin-parallel intrusions. Miles and Roest (1993) describe Gop Rift as transitional, underplated crust, based on analysis of seismic and gravity data. They identify Chron 28 south of Laxmi Ridge, and on that basis, attribute the initiation of seafloor spreading to the Deccan hotspot. However, Miles et al. (1998) show that the Chron 28 anomaly is actually a magnetised basement feature. A continental provenance for Gop Rift is feasible if the observed magnetisation is generated by underplate and extrusive magmatism (Fig. 4.8).

Provenance of magmatic material

The polarity of the magmatic crust across the margin can give clues as to the timing and nature of its formation. This is summarised in Figure 4.13. The observation that underplate beneath the continental rise and Laxmi Ridge both have a normal polarity magnetisation suggests that they might have the same source, and perhaps were once laterally adjacent. Since the magnetic crust in Gop Rift is of the opposite polarity, the architecture observed in Gop Rift cannot simply be caused by thinning of both the crust and underplate after emplacement. This observation suggests that Gop Rift is of oceanic origin. The most likely age for Gop Rift then is Chron 29r (Malod et al., 1997) or Chron 30r (Bernard and Munschy, 2000), which are within the range of ages of eruption of the Deccan Traps (e.g., Vandamme et al., 1991). The underplate adjacent to Gop

Rift has normal polarity, so was probably formed during Chron 30n, at the initiation of Deccan magmatism. The underplating has weakened the lithosphere sufficiently to allow spreading to occur in Gop Rift. Since the underplating almost certainly pre-dates the spreading in Gop Rift, and both appear to have formed while the Deccan hotspot was active in this region, Chron 29r is the most likely period for the opening of Gop Rift. The small peaks in the anomaly over Laxmi Ridge could also be due to intrusions from this time. The very high magnetisation required to model Gop Rift as a constant polarity block is anomalous. This could be an effect of the high temperature of the mantle during accretion, caused by the Deccan hotspot. Final continental breakup occurs around Chron 27 time, after the end of the Deccan magmatism.
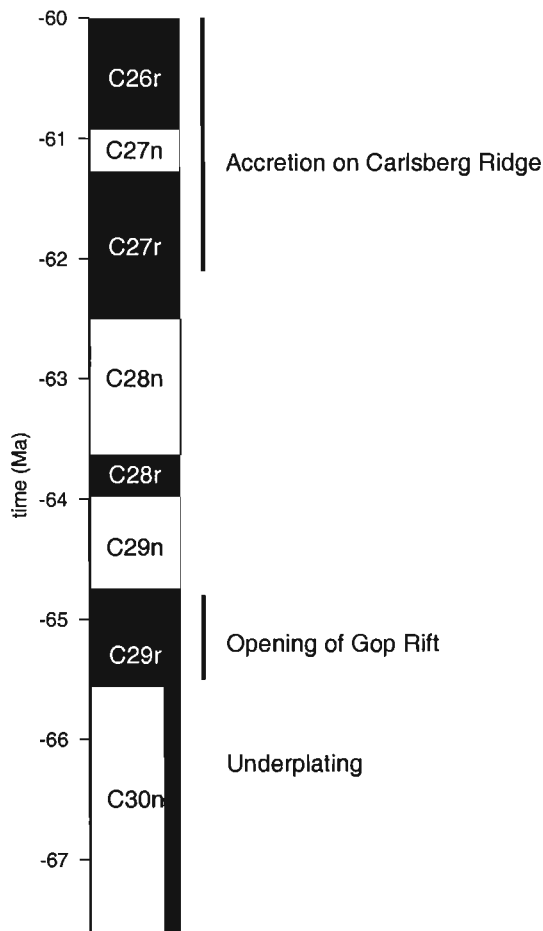
Figure 4.13: Geomagnetic timescale and magmatic events: Periods of normal (white) and reversed (black) magnetisation (Cande and Kent, 1995) and associated magmatic events. Thick grey bar is the duration of the Deccan Traps magmatism (Biswas and Thomas, 1992). It can be seen that underplating beneath the margin and seafloor spreading within Gop Rift are associated with the Deccan hotspot. Once the hotspot has waned, there is no supply of magma to sustain accretion in Gop Rift, and the spreading halts. After continued stretching, a relatively amagmatic continental margin (Section 3.7.1) is formed south of Laxmi Ridge prior to spreading on the Carlsberg Ridge.

4.3   Summary and conclusions

1. The negative gravity anomaly associated with Laxmi Ridge is a consequence of the thick crust beneath the Ridge.

2. Laxmi Ridge has magnetisation of less than 0.5 A m^{-1}, which is consistent with a continental origin.

3. Gop Rift has a large reversed polarity magnetisation. The anomaly pattern can be matched with either a continental or oceanic model, but the simplest model implies an oceanic provenance. Matching the magnetic anomaly pattern in Gop Rift requires a magnetisation of at least -2.5 A m^{-1} in layer 2 and -1.5 A m^{-1} in layer 3. This relatively high magnetisation is a symptom of the crust being formed during the Cretaceous, which was a period of high magnetic field strength.

4. Palitana Ridge occurs at the limit of stretched continental crust and oceanic crust within Gop Rift; it marks an OCB on this margin between stretched continental crust in the south of Gop Rift and oceanic crust in the north.

5. The magnetic anomalies in Gop Rift are much higher than those in the Laxmi Basin, suggesting that the two structures have a different origin.

6. The underplate beneath Laxmi Ridge and the continental rise are consistent with, but not required by, the magnetic data. They may have been formed during Chron 30n, and would therefore be related to the Deccan magmatism. They were once laterally adjacent, but were separated by spreading in Gop Rift.

7. Seafloor spreading in Gop Rift is most likely Chron 29 in age and contemporaneous with the Deccan magmatism.

8. Normal seafloor spreading commenced south of Laxmi Ridge 0.55 Myr after the commencement of Chron 27r. This post-dates emplacement of the Deccan Traps, hence the apparent lack of underplating of the conjugate Seychelles margin, and the thin oceanic crust seaward of both margins.

5

Stratigraphy and upper-crustal structure from seismic reflection profiles

Multichannel seismic lines collected during the research cruise *Charles Darwin 144* are interpreted here with the aim of describing the reflection characteristics of both the sediments and crust at the Laxmi Ridge rifted continental margin. These data are important as they are of higher resolution than the refraction data collected using ocean-bottom instruments (Chapter 3). Seismic imaging of the sediments can provide constraints on their age, and may help infer the age of tectonic processes that have affected the margin. Deep reflections can provide evidence for both crustal structure and, where the Moho is imaged, crustal thickness.

The processing of the CD144 MCS lines (Fig. 5.1) is described in Section 2.3. Line 6 (CD144-6) is of good quality, and is coincident to part of the wide-angle line (Section 3.4). CD144-5 is also of good quality, and gives additional information on the nature of the rifting that formed the margin. CD144-3 is of poor quality, but it is included here as it gives an indication of the along-strike variability of margin-parallel features. Stratigraphic horizons are correlated with those observed on seismic line *Sonne SO12* (Gaedicke et al., 2002b), which crosses CD144-2. These horizons are tied to dated lithologies logged in the industry well, *Indus Marine-A1* (Clift et al., 2000, Clift, pers. comm.).

5.1 Reflection characteristics of sedimentary units

The basement of the Laxmi Ridge continental margin is overlain by up to 2.5 s of Indus Fan sediments. These sediments can be broadly divided into three packages, which represent different tectonic controls on sediment supply and subsequent erosion. The post-rift megasequences *M1* and *M2* were first identified by Droz and Bellaiche (1991). The megasequences can be subdivided into stratigraphic units by correlating horizons with those identified on seismic line *Sonne SO12* (Gaedicke et al., 2002a,b). These horizons are dated using ties from industry well *Indus Marine-A1* (Clift et al. (2000); Clift, pers. comm.), which reached the base of the Middle Miocene at 2725 m (Shuaib, 1982). The stratigraphic units are initially described for CD144-6 (Fig. 5.2).

5.1.1 Pre-rift sediments (*P*)

The *P* package are the oldest sediments in the sequence. They are Cretaceous pre-rift sediments that predate the breakup of India and the Seychelles (Gaedicke et al., 2002b).

They are observed on CD144-6 as strong, sub-parallel reflections up to 0.5 s two-way time (TWT) thick, which are preserved on basement highs of continental provenance (Fig. 5.2).

5.1.2 Oldest post-rift sediments (*M1*)

The *M1* sedimentary unit (Fig. 5.2) is a sub-horizontal sequence of parallel reflectors, which onlaps the basement, draping basement highs in places. It is up to 1.5 s TWT thick. Its draping nature indicate that it is probably formed from hemipelagic settling, intercalated with distal turbidites from the proto-Indus Fan. M1 is Paleocene to Lower Miocene in age, although precise dating of these horizons is not possible as these units are deeper than the base of well *Indus Marine-A1* (Shuaib, 1982). The Indus Fan initiated during the Early Eocene, shortly after the collision of India and Asia (Clift et al., 2002). The collision and subsequent uplift may be the cause of the unconformity observed in the Paleogene sediments (E-U, Fig. 5.2).

5.1.3 Youngest post-rift sediments (*M2*)

Sequence *M2* is an almost 2 s TWT thick package of overlapping channel levee structures, separated from M1 by regional unconformity *U*, which is a hiatial surface associated with the uplift of the northern margin of the Arabian plate (Gaedicke et al., 2002b). The channel levees characteristically consist of a bright, sub-parallel channel fill bounded by transparent levee shoulders. The chaotic reflectivity of this package is a consequence of the overlapping of many meandering channel systems. The oldest sediments in this megasequence are Middle-Miocene in age, and the megasequence can be subdivided into 4 units based on well ties (Fig. 5.2). The increase in energy of deposition responsible for the transition from hemipelagic to channel levee sedimentation may be due to a number of factors: the convergence of the Indian and Arabian plates and the subsequent uplift of the Karakorum (Gaedicke et al., 2002b) increasing sediment supply to the Indus river system and sea-level lowering causing the environment of deposition to prograde to a shallower deltaic system (Clift et al., 2002).
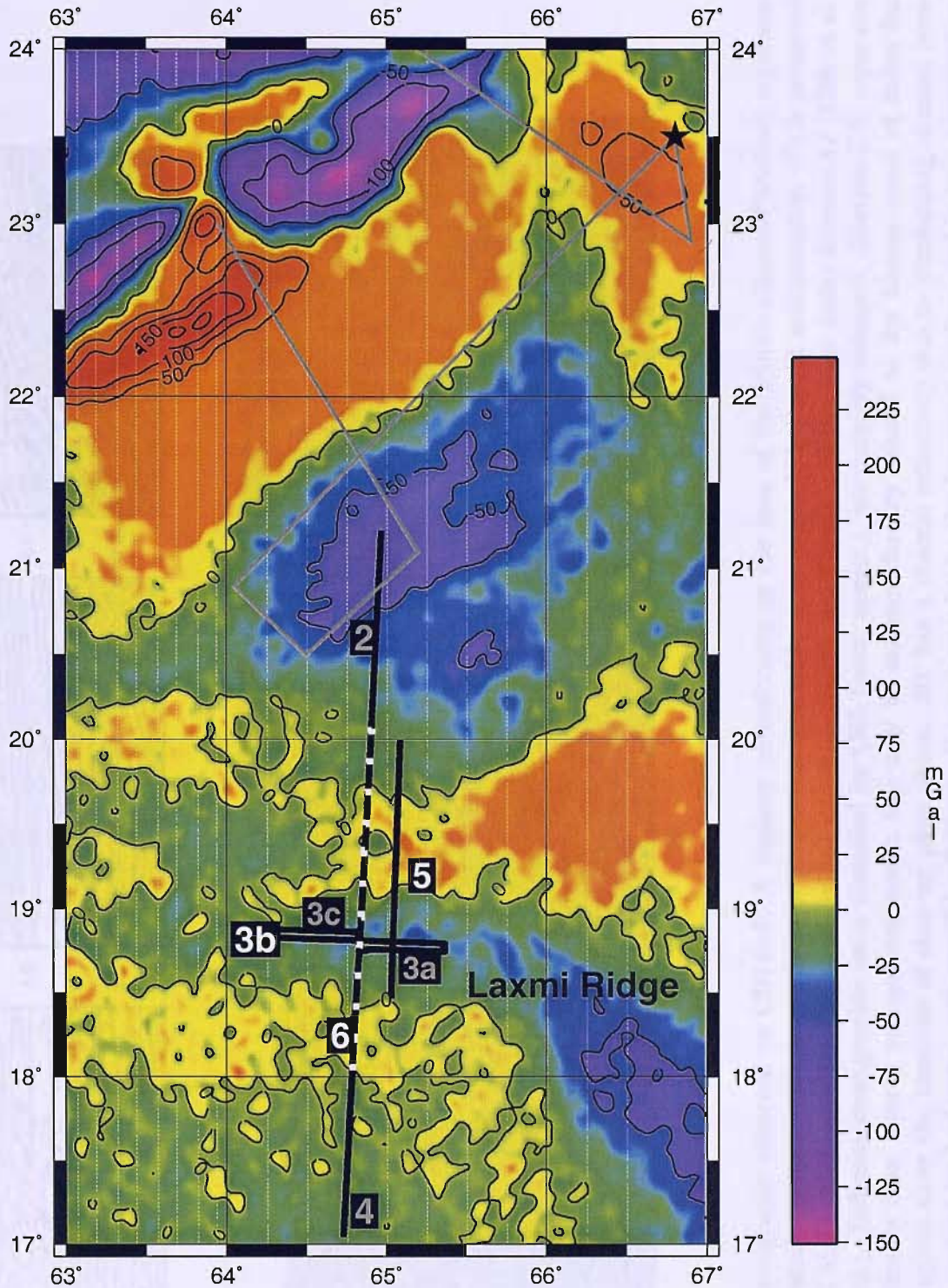
Figure 5.1: MCS profiles: CD144 profiles are indicated by heavy black lines. CD144-6 (dashed white line) is a partial re-shoot of lines 2 and 4. Lines interpreted in this chapter are indicated by a white number; those processed but not interpreted are indicated with a grey number. Stratigraphic ties from industry well *Indus Marine-A1* (star) can be made by following horizon ties made on the *Sonne SO12* profile (grey line; Gaedicke et al., 2002a,b), which crosses CD144-2. Background field is free-air gravity (Sandwell and Smith, 1997).
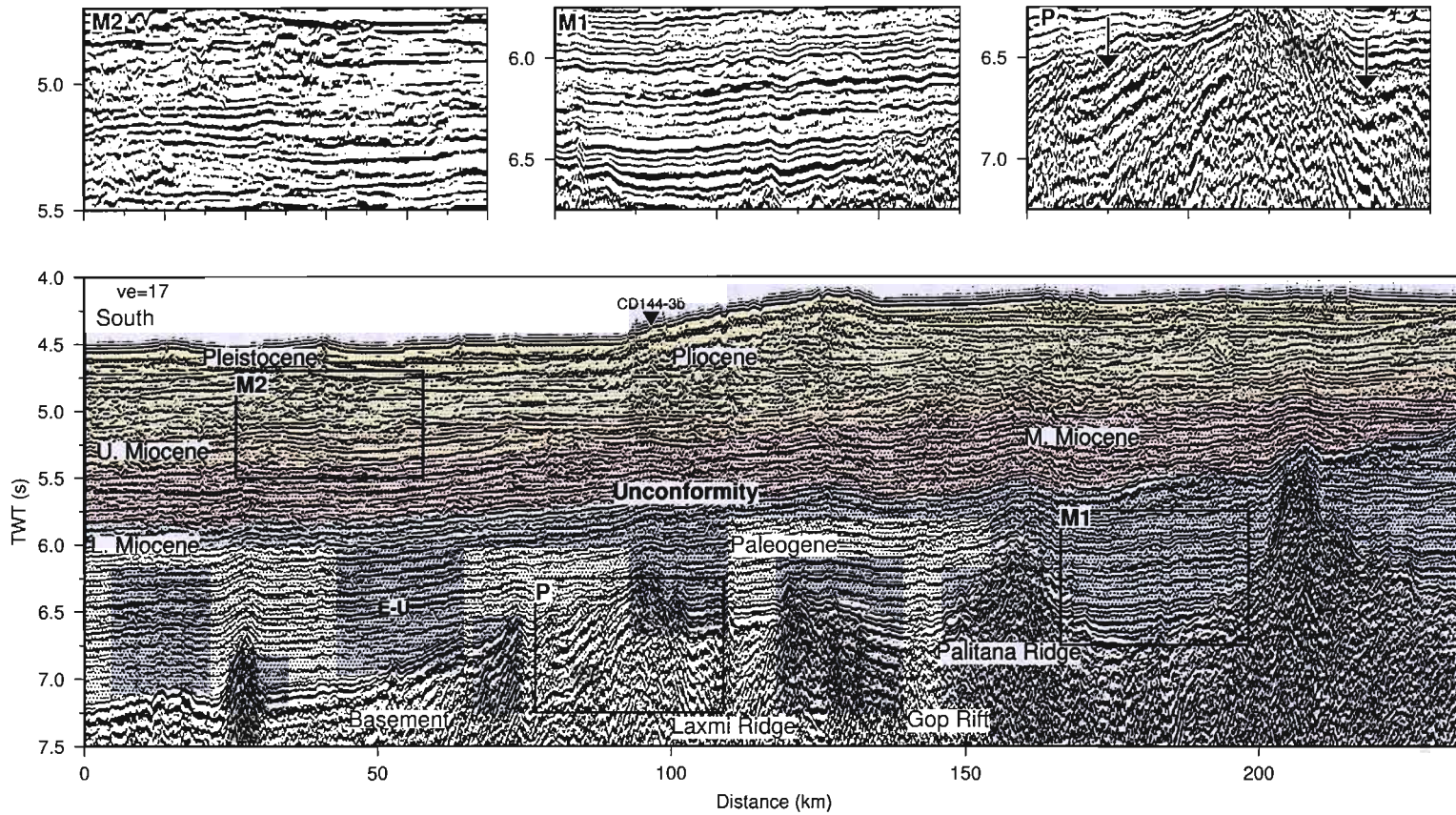
Figure 5.2: Sequence stratigraphy observed on CD144-6: A regional unconformity at the base of the Middle-Miocene(labelled) separates Paleogene distal sedimentation sequence M1 from Miocene- Pleistocene channel levee sequence M2. Pre-rift sedimentation (P) is preserved on continental basement highs. Megasequence M2 is subdivided into stratigraphic units using well ties from *Indus Marine-A1* (Clift et al. (2000); Clift pers. comm.). Different stratigraphic units identified by Clift (pers. comm.) are uniquely coloured. Horizon E-U separates older less reflective sediments from layered younger sediments; this may be an unconformity related to the Eocene onset of Indus fan sedimentation. Boxed regions show the locations of close-up plots above: *M2* has a chaotic reflectivity due to overlapping channel levee structures. *M1* is characterised by horizontal, sub parallel reflectors. *P* is sub-parallel to the basement surface, and is only preserved on continental basement (arrowed).

5.1.4 Sedimentary characteristics of CD144-5

CD144-5 is $\sim$ 20 km east of CD144-6, and is in shallower water. The same megasequences can be traced as in CD144-6. The depth of the seabed and sedimentary horizons are slightly different from those observed in CD144-6, probably as a consequence of the change in water depth. A 1 s syn-tectonic package (large arrowhead, Fig. 5.3) that abuts the northern limit of Laxmi Ridge is observed on this line and is not seen elsewhere. The RMS stacking velocities (Fig. 5.3; Section 2.3) in the sediments are comparable to sediment velocities modelled using wide-angle seismic data (Section 3.4.1) once the RMS stacking velocities have been converted into interval velocities using the Dix equation (Dix, 1952):

$$V_{int}(n) = \sqrt{\frac{V_{RMS}(n)^2 t(n) - V_{RMS}(n-1)^2 t(n-1)}{t(n) - t(n-1)}} \qquad (5.1)$$

where $V_{int}(n)$ is the interval velocity in the nth layer, $V_{RMS}(n)$ is the RMS (stacking) velocity in the nth layer, $V_{RMS}(n\text{-}1)$ is the RMS (stacking) velocity in the $n\text{-}1^{th}$ layer, and $t(n)$ and $t(n\text{-}1)$ are the times to the base of the nth and $n\text{-}1^{th}$ layer respectively.

5.1.5 Sedimentary characteristics of CD144-3b

CD144-3b (Fig. 5.4) is of inferior quality to CD144-5 and 6, but it is important as it gives constraints on the along-strike variability of both the crustal structure and sediment thickness. The total sediment thickness is observed to thicken to greater than 2 s TWT to the west as the basement depth increases. The regional unconformity, U is easily observed on this section, and the morphology of the channel levees in sequence M2 are also clear as they are often bisected orthogonal to the down stream direction.

5.2 Reflection characteristics of acoustic basement

The broad pattern of reflectivity changes within acoustic basement across the Laxmi Ridge Margin can be used to infer changes in crustal provenance. However, this information should be used with caution, since the reflectivity of the deep structure is a product of both that structure, and the reflection characteristics of any overburden. CD144-5 is the profile with the most clearly imaged basement structure, so it is considered first:

5.2.1 CD144-5

A change in reflectivity is observed across the ocean-continent boundary separating the ocean basin within northern Gop Rift (Section 4.2.3) from the continental blocks of Palitana and Laxmi Ridge and the continental rise of India (Fig 5.5). A summary of the identified basement features is given in Figure 5.6.
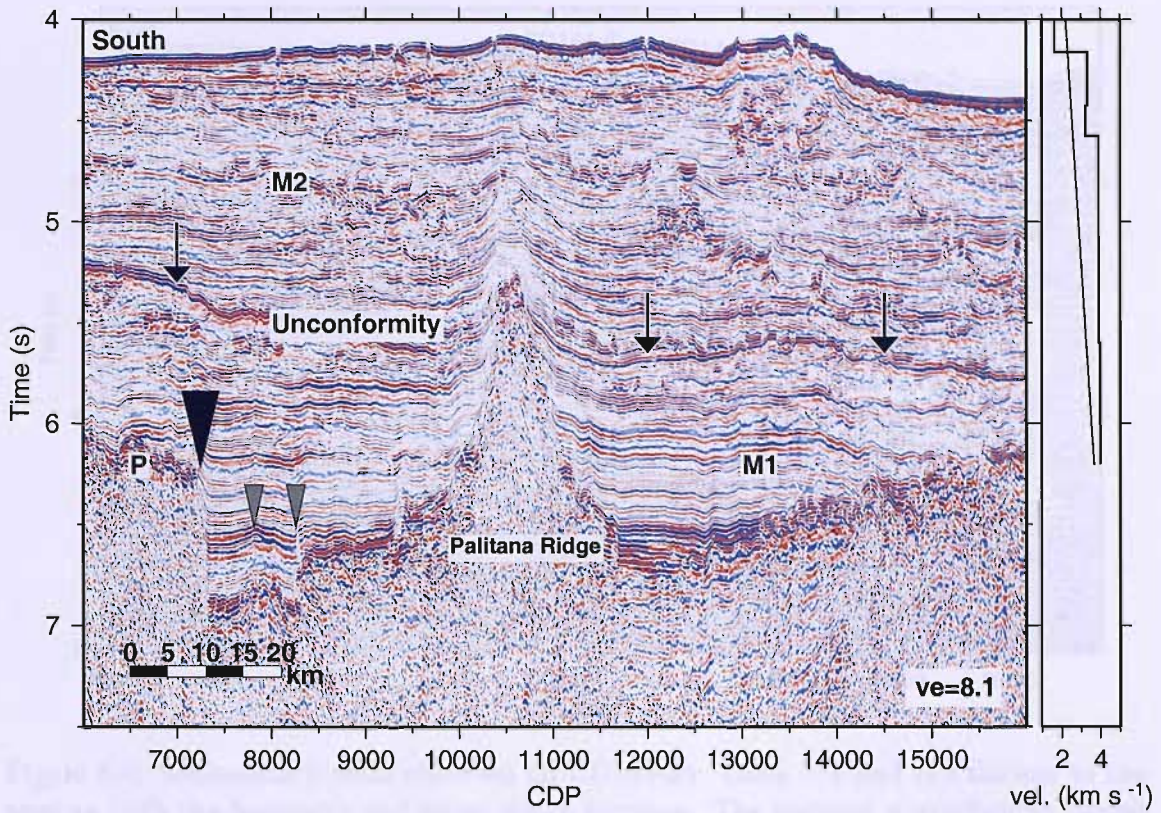
Figure 5.3: Sedimentary units on CD144-5: M1 and M2 are separated by regional unconformity *U* (small arrows). A 1 s TWT package of post-rift sediments abuts the northern limit of Laxmi Ridge (large arrow head). Smaller faults (grey arrowheads) are observed in the basin south of the Palitana Ridge, which disrupt both the basement and syn-tectonic sediments above. *Right:* Typical interval velocities derived from sediment stacking velocities (black line) and interval velocities derived from the wide-angle model (Section 3.4.1; grey line). Both sets of velocities reach almost 4 km s^{-1} at the base of the sediments. A small jump is recorded in the stacking velocities across the regional unconformity *U*.

The continental blocks have a rough basement topography and a highly reflective character. Oceanic crust north of Palitana Ridge has a lower amplitude, layered reflectivity, and the basement surface is, in parts, much smoother (e.g., between CDPS 11700 and 12600). This contrast between the two types of crust is most striking between the apparently continental Palitana Ridge and the oceanic crust in northern Gop Rift (Section 4.2.2). Palitana Ridge appears to be a horst structure marking the ocean-continent boundary (OCB) between Laxmi Ridge and northern Gop Rift.

Within northern Gop Rift, the top 0.8 s TWT of the oceanic crust have a low amplitude and layered reflectivity, while the continental crust is more reflective with a chaotic character. This is in common with the findings of Malod et al. (1997). Bright reflectors, 0.4 s TWT thick, on top of the basement in Gop Rift are another characteristic of oceanic crust on this margin. These reflectors have been interpreted as lava flows (Malod et al., 1997; Gaedicke et al., 2002a) and carbonate sediments (Gaedicke et al., 2002a), but they
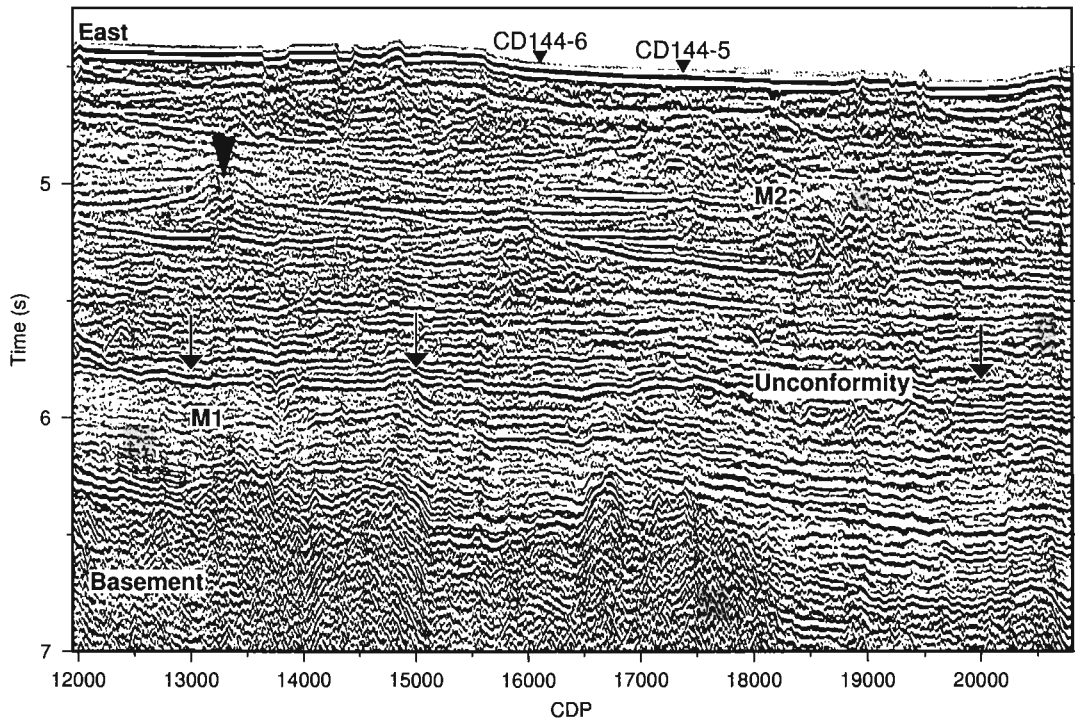
Figure 5.4: Sedimentary units observed on CD144-3b: Units M1 and M2 thicken to the west as both the basement and water depth increase. The regional unconformity (small arrows) is easier to pick out on this section than on CD144-5 or 6. The sediments are generally adequately resolved, but the basement is poorly imaged. Channel levees are easy to identify as as they are often bisected orthogonally to the down stream direction. An example is indicated with a black arrowhead; the coarse channel fill is strongly reflective and the levee shoulders are semi-transparent.

appear to be a feature of the oceanic crust at this margin. The implied crustal thickness for the oceanic crust in Gop Rift is 11.0 km (2.0 s TWT). A thickness of 11 km is computed for this crust in Section 3.4.4.

The reflection Moho is poorly imaged, but it is observed as a low frequency reflector, which is approximately coincident with the base of the crust modelled in Section 3.4. The reflector shallows from 9.2 s under Laxmi Ridge to 8.3 s under Palitana Ridge. The Moho does not shallow under Palitana Ridge in the wide angle model. This difference could be either due to a lateral variation in Moho depth (CD144-5 is not coincident with the wide-angle model) or could be because the MCS reflection Moho is actually a reflection from the top of an underplate that does not have a sufficient velocity contrast with the surrounding mantle to be detected by wide-angle seismic methods. North of Palitana Ridge, the Moho deepens to approximately 8.75 s under Gop Rift and shallows again to 8.4 s under the continental rise. The character of the reflection Moho is observed to change from a low frequency reflector under Laxmi Ridge and Palitana Ridge to a higher frequency double reflector under northern Gop Rift (CDPs 11000-13000, Fig. 5.5).
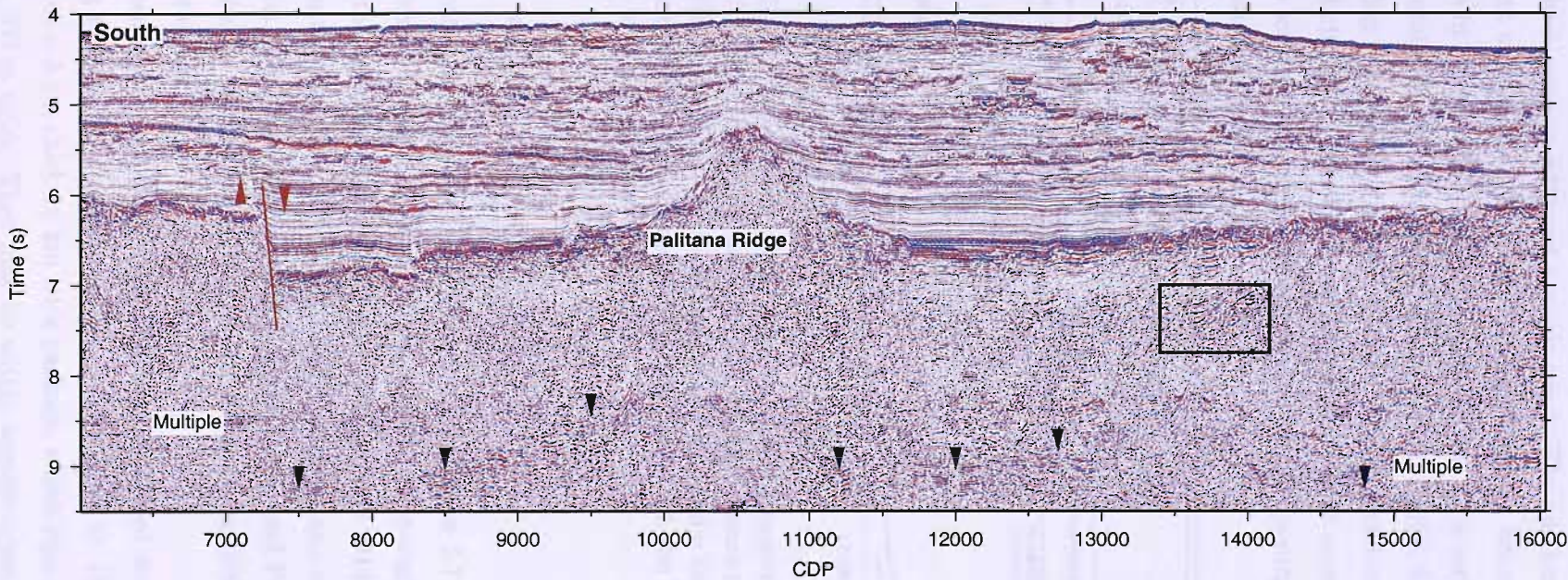
Figure 5.5: CD144-5 Basement structure: Between CDPs 6000 and 11500 the basement has a chaotic reflectivity beneath an irregular, faulted surface. The Moho at the base of this crust (black arrows) is an approximately 0.5 s TWT thick low amplitude reflection. In northern Gop Rift (CDPs 11500 to 14250) the basement surface is smoother, and is overlain by a 0.4 s TWT thick package of bright reflectors. Immediately beneath the basement surface there is a 1 s TWT thick area of low amplitude layered crust. The Moho here (arrowed) is a higher frequency reflection than the Moho to the south, and appears as a double reflector. The crust in northern Gop Rift is separated from faulted, rough basement of the continental rise by a 15 km wide 0.6 s TWT thick package of dipping reflectors (black box). The red line marks the abrupt boundary between Laxmi Ridge and Gop Rift. This boundary may be a normal fault; the apparent sense of motion is shown by red arrowheads.

The southern OCB of northern Gop Rift is marked by an abrupt transition from continental crust to adjacent oceanic crust. The northern margin is more complex: The basement surface changes from a smooth reflector below a 0.4 s bright, high amplitude package in northern Gop Rift to a horizon cut by a series of horsts and grabens on the continental rise. At around 7 s TWT, a 15 km wide, 0.6 s TWT (2.7 km) thick wedge of dipping reflectors are imaged within the basement beneath this transition of basement types. Individual reflectors are divergent and dip at around 12°. These reflector packages may be seaward dipping reflectors related to the opening of Gop Rift. Their provenance is discussed further is Section 5.3.2.
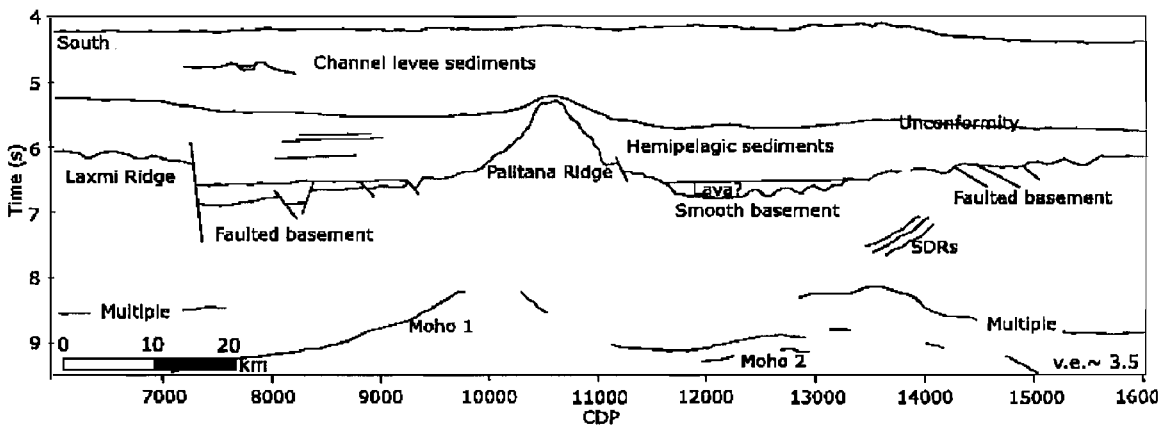
Figure 5.6: Interpretation of CD144-5 basement structure: Smooth basement in northern Gop Rift is sandwiched between faulted, rough basement in Palitana Ridge and the continental rise. The Moho is subdivided into *Moho 1*, the low frequency reflector observed at the base of the rough continental crust, and *Moho 2*, the higher frequency double reflector imaged beneath northern Gop Rift.

5.2.2   CD144-6

Basement structure on CD144-6 is shown in Figure 5.7, with an interpretation of these structures in Figure 5.8. Comparison with the wide-angle model are made in Figure 5.9. Where the basement differs from that observed on CD144-5, it is described here. Oceanic crust south of Laxmi Ridge (south of CDP 11000) has a smooth, high amplitude basement reflection. Continental crust within Laxmi Ridge and Palitana Ride has a rough surface cut by faults. In northern Gop Rift (CDPs 19000 to 21000) the basement surface is again a smooth, high amplitude reflector.

Oceanic crust south of CDP 11000 is separated from Laxmi Ridge by two sets of dipping reflectors. The seaward set (CDPs 9500 to 11500) are weakly imaged. They consist of a 3 km thick 18 km wide package, which dips at 10°. Individual reflections are around 200 m thick. They may be within oceanic crust, but this is not clear from these data. This set is separated from the landward set by a basement high. The landward set

of dipping reflectors (CDPs 12000 to 13100) have a much higher amplitude, and occur within the stretched continental crust of Laxmi Ridge. The package consists of divergent reflectors in a wedge shape, which increases in thickness from 1.2 km at the crest of Laxmi Ridge to 3 km to the south. The total length of the package is 13 km, and the average dip of the reflectors is 14°. This pattern of weak seaward and strong landward SDRs separated by a basement high is typical of the volcanostratigraphy of SDRs at the OCB of volcanic rifted margins (Planke et al., 2000). This is discussed in more detail in Section 5.3.2.

A 40 km wide SDR wedge is reported on the cross-cutting *Sonne* line by Gaedicke et al. (2002a), which is at the approximate latitude of a 3.75 km wide package of dipping reflectors observed between Gop Rift and the continental rise (CDPs 20100 and 21100). The SDRs observed here are weaker than on CD144-5. The provenance of these reflections are discussed in Section 5.3.2. Locations of these reflectors are plotted on Figure 5.11.

Although SDRs are often thought to be a consequence of rifting over a thermal anomaly, they can be due to rapid decompression melting during fast rifting (Bown and White, 1995). Keen and Potter (1995) attribute those observed on the Nova Scotia margin to small-scale convection increasing melting during rifting. These theories are relevant to the Laxmi Ridge margin as there is no evidence that the thermal anomaly that formed Gop Rift was still present during the separation of India and the Seychelles (e.g., Section 3.7.1); the magmatism associated with this rifting event is assumed to be a function of the rapid extension (Royer et al., 2002; Bown and White, 1995).

The oceanic crust south of Laxmi Ridge is 1.4 s ($\sim$ 7 km) thick. It has a layered reflectivity but lacks the dipping events observed in some locations within fast spreading oceanic crust in the Pacific (e.g., Ranero et al., 1995; Reston et al., 1999). The crest of Laxmi Ridge is cut by a number of grabens, which are orthogonal to the direction of continental extension. Kolla and Coumes (1990) also describe the morphology of Laxmi Ridge as a block faulted, horst and graben complex.

The Moho is imaged across most of the margin as a low frequency reflector, which is approximately coincident with the base of the crust computed in Section 3.4 (Fig. 5.9). Under Laxmi Ridge, a deep crustal reflector is seen 2 s TWT (6.75 km) beneath the basement surface. This reflector is shallower than the reflection Moho, and where it occurs the amplitude of the Moho reflection beneath it is slightly reduced. It appears to coincide with the top of the sub-crustal high velocity layer sampled by wide-angle seismic methods in Section 3.4.5.
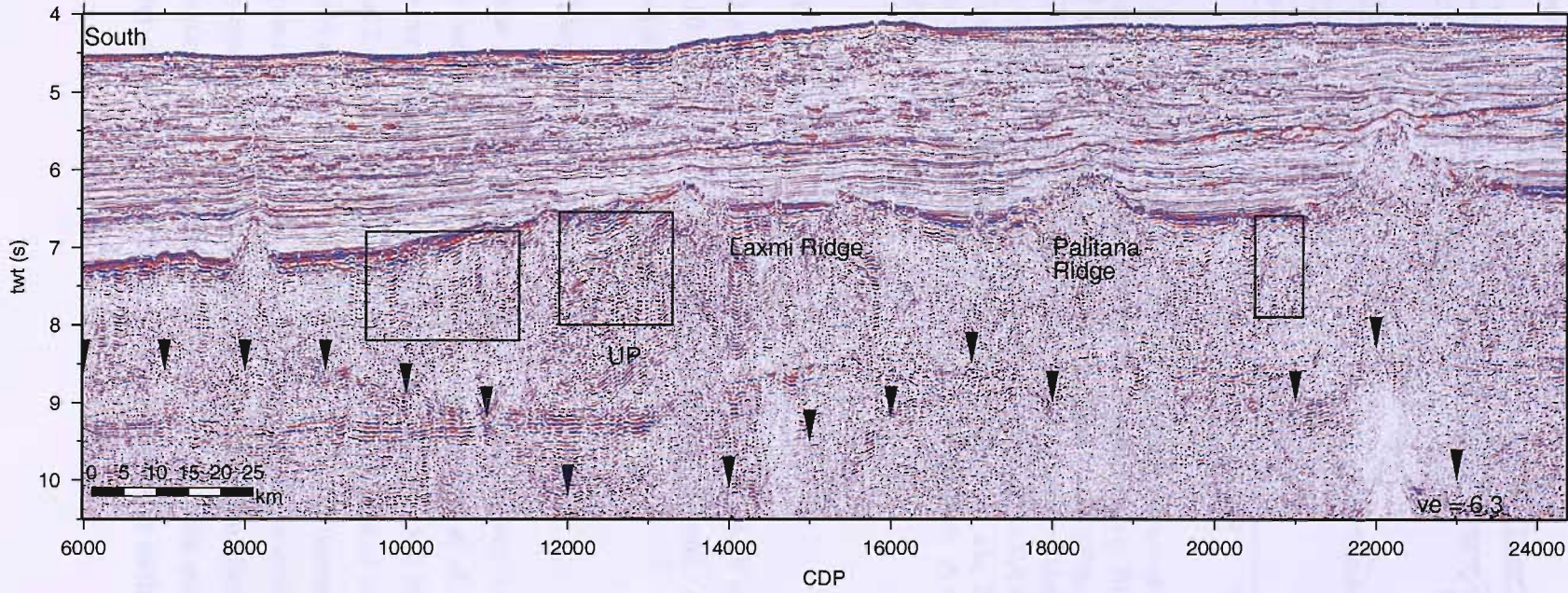
Figure 5.7: CD144-6 Basement structure: The bright top basement reflector observed between CDPs 6000-10000 and 19000-21000 is a feature of oceanic crust on this margin. Reflections that may be seaward dipping reflectors (SDRs) are indicated by boxes. The strong intra-basement reflectors seen within the top 0.5 s of continental crust between CDPs 12000 and 13000 are probably pre-rift sediments. The crest of Laxmi Ridge is cut by a number of grabens. A reflection from the Moho (black arrows) is flat beneath oceanic crust at the southern end of the profile and dips down at approximately 7° beneath the southern flank of Laxmi Ridge. The Moho is hard to detect beneath northern Gop Rift, but it reappears at 8.2 s beneath the continental rise. Beneath CDPs 12000 and 13100, a strong lower crustal reflector is imaged (labelled UP); this reflector coincides with the top of the high velocity sub-crustal body modelled in Section 3.4.5.
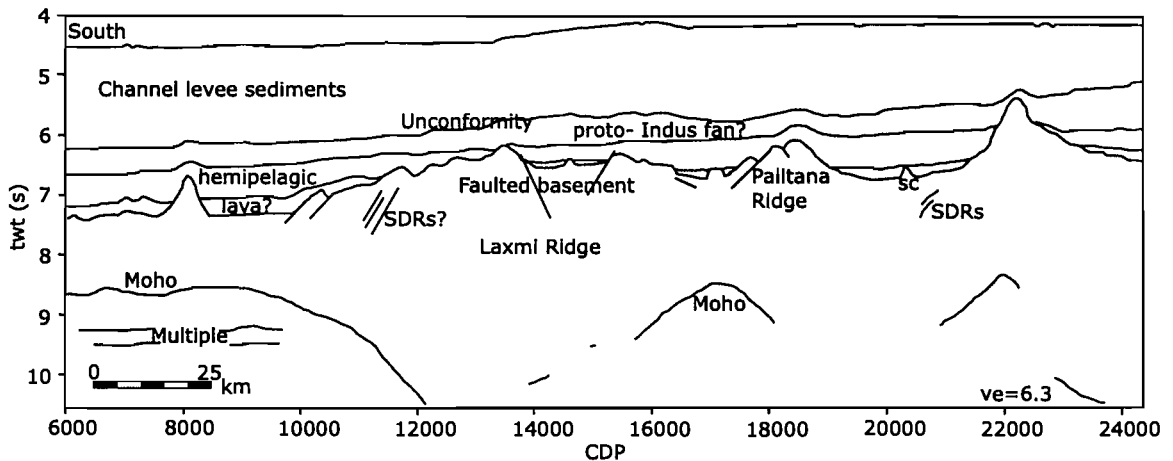
Figure 5.8: Interpretation of CD144-6 basement structure: Both oceanic crust south of Laxmi Ridge and oceanic crust within northern Gop Rift are separated from faulted, extended continental crust by weak packages of dipping reflectors (tentatively labelled SDRs). The reflection Moho is imaged beneath most of the margin, but is absent beneath northern Gop Rift. Top basement is overlain by up to 0.4 s TWT of bright reflectors that may be lava flows (Malod et al., 1997; Gaedicke et al., 2002a), or could be due to the reverbatory nature of the reflection from that horizon. A seamount within northern Gop Rift is labelled *sc*.

5.2.3   CD144-3b

Basement structure is poorly imaged on profile CD144-3b due to the low fold (Section 2.2). Figure 5.10 shows that Laxmi Ridge shallows to the east. A 25 km graben with bounding faults that dip at $\sim 25^o$ is imaged.

5.2.4   Depth to basement map

Travel time picks for depth to acoustic basement were made on all profiles. They were combined with picks from previous cruises (Malod et al., 1997; Miles et al., 1998) and depth converted using an average water velocity of 1.503 km s^{-1} and an average sediment velocity of 2.65 km s^{-1} (Section 3.4.1). After removal of bad datapoints, depths were averaged onto a 1 minute grid to generate the depth to basement map shown in Figure 5.11. Mapping the approximate location of the ocean basin within northern Gop Rift onto the basement map from changes in crustal magnetisation (Section 4.2.2) and the location of SDRs (Section 5.3.2) infers an asymmetric basin, with more accretion in the west. This asymmetry suggests that spreading was progressively extinguished from the east.
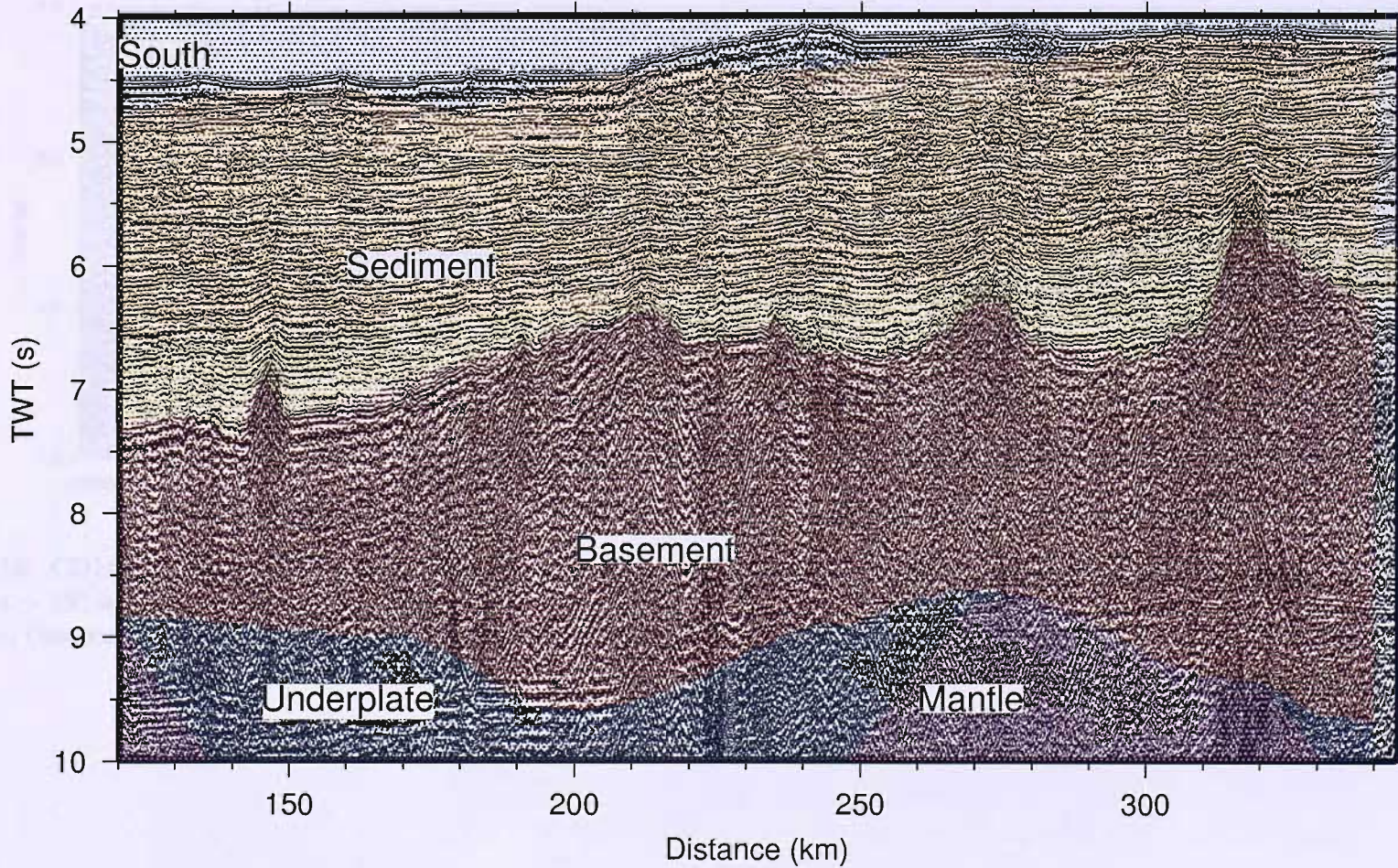
Figure 5.9: CD144-6 and the wide-angle velocity model: horizons from the wide-angle velocity model (Section 3.4) are converted from depth to time and overlain on CD144-6. The water column is coloured blue; sediments are yellow, basement is red and the mantle is purple. The lower crustal high velocity layer is blue. The velocity horizon observed within the sediments corresponds to the Miocene U unconformity. Between 200 and 250 km, the reflection Moho is observed to correspond to the top of the high velocity sub crustal layer, rather than the upper mantle. No reflection Moho is imaged beneath northern (oceanic) Gop Rift.
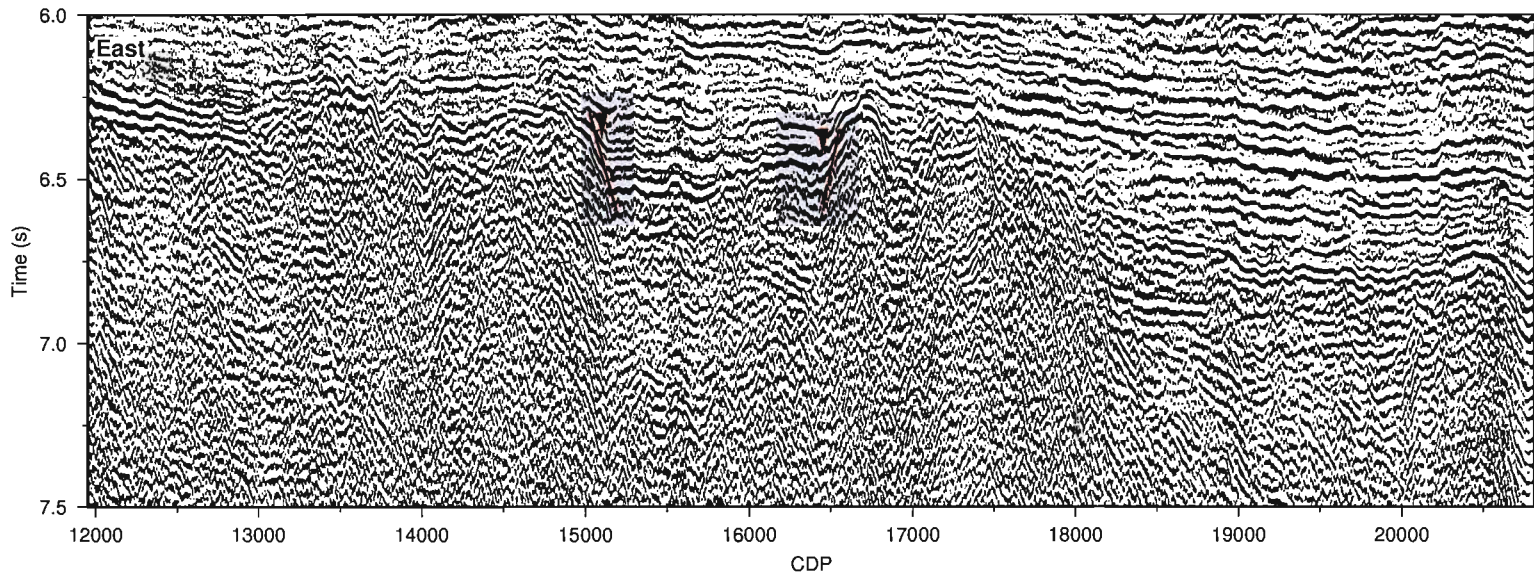
Figure 5.10: CD144-3b basement structure: Laxmi Ridge shallows to the east. A 25 km wide graben with bounding faults (red lines) dipping at $\sim 25^\circ$ is imaged between CDPs 15000 and 16500. Image is poor due to the low fold of the data (8), and the errors made during acquisition (Section 2.2).
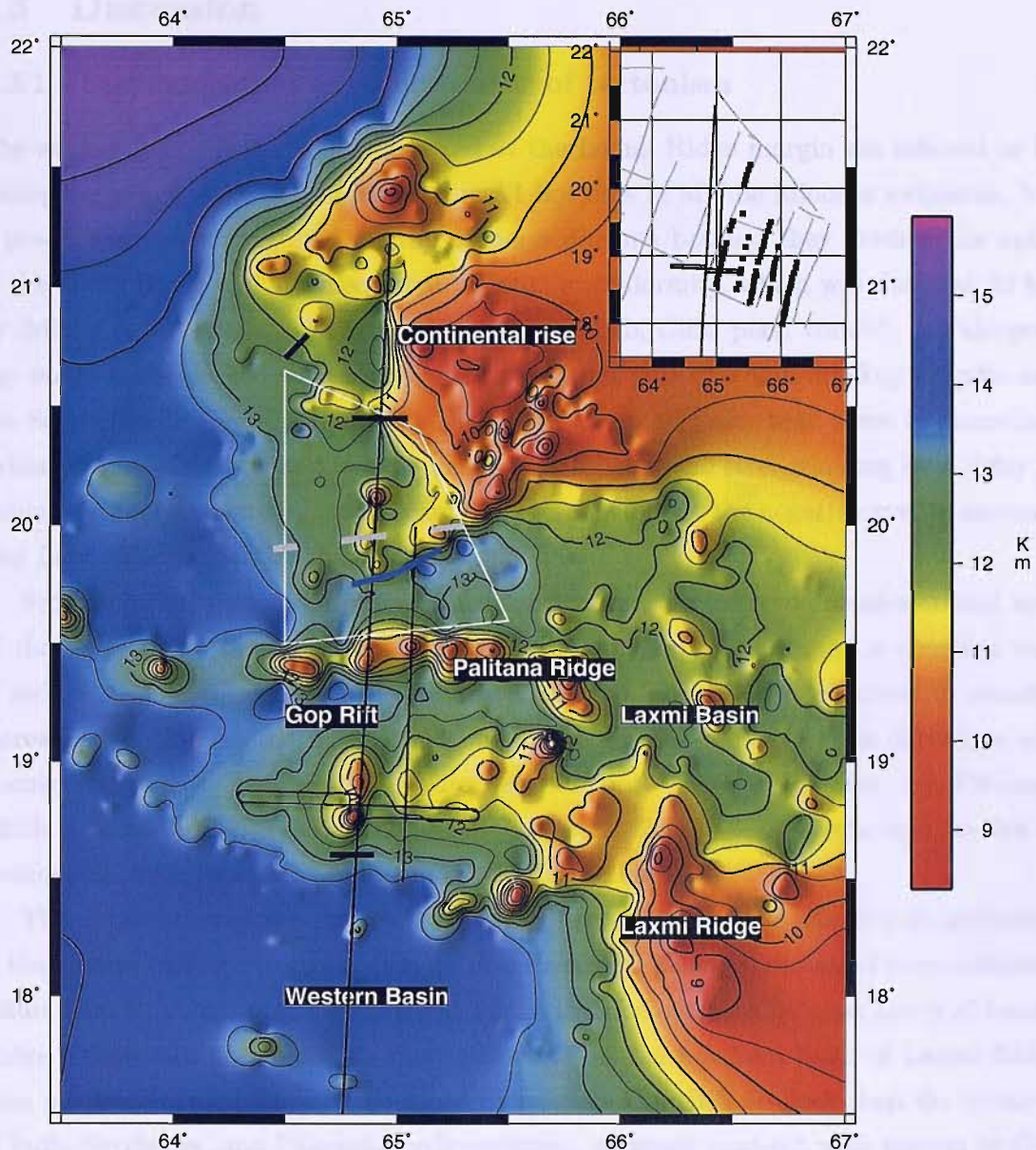
Figure 5.11: Depth to basement map, compiled from single-channel reflection data from previous cruises (Malod et al., 1997; Miles et al., 1998) combined with basement picks from CD144 MCS data. Two-way travel time picks are converted to depths by using an average water velocity of 1.503 km s^{-1} and an average sediment velocity of 2.65 km s^{-1} (Section 3.4.1). Depth scale is in km. Gop Rift is bisected by a basement high; the Palitana Ridge. The locations of SDRs identified in this chapter and by Gaedicke et al. (2002b) are marked with heavy black lines. The interpreted extinct spreading centre is marked by a dashed grey line, and associated axial lava flows are marked with a heavy blue line. The approximate bounds of the northern Gop Rift ocean basin are marked by a white line. The basin is wider to the west, which suggests that spreading was progressively extinguished from the east. *Inset:* Data used in compiling the map: black lines are CD144 picks; grey lines are picks from single channel *Profindus* data (Malod et al., 1997) and black squares are picks from single channel *CD20* reflection profiles (Miles et al., 1998). Lines are only plotted where reliable basement picks exist.

5.3 Discussion

5.3.1 Sedimentation as an indicator of tectonism

The earliest post-rift sediments observed at the Laxmi Ridge margin are inferred to be Paleogene in age. The well Indus Marine A1 bottoms in Middle Miocene sediments, but a pre-20 Ma age is suggested for the deeper sediments because they predate the uplift of the Owen Ridge and the associated regional unconformity, which was dated at 20 Ma by drilling (Clift et al., 2000; Gaedicke et al., 2002a,b, Clift, pers. comm). A Paleogene age would make the sedimentation contemporaneous with the final breakup of India and the Seychelles (Royer et al., 2002). This observation suggests that there is immediate sedimentation after breakup, which means that lithospheric strengthening by a delay in sedimentation (Karner et al., 2005) cannot be responsible for the negative gravity anomaly over Laxmi Ridge (Section 4.1).

Sedimentation rates are approximated by dividing the observed cross-sectional area of the package by the duration of the depositional period, assuming a constant rate of sedimentation. Generally, the sedimentation rate (Fig. 5.12) is observed to steadily increase with time in the basin, reflecting the increasing erosion of the Himalaya and Karakorum ranges. Sedimentation rate peaks in both the mid Miocene and Pliocene, which is consistent with earlier findings (Clift et al., 2000); both events may be due to continental uplift increasing sediment supply to the basin.

The distribution of the earliest (Paleogene) post-rift sediments can give an indication of the relative timing of tectonic events. This Paleogene package consists of more reflectors within Gop Rift than over Laxmi Ridge or the first formed oceanic crust south of Laxmi Ridge. There are also generally more reflectors on the northern flank of Laxmi Ridge than on the southern flank. This could be because Gop Rift is older than the breakup of India-Seychelles, and Paleogene sedimentation, although post-rift with respect to Gop Rift, was synchronous with the continued extension and ultimate breakup of the Laxmi Ridge- Seychelles conjugate pair (Fig. 5.13).

A summary of the main tectonic events and their influence on the sedimentary history of the basin is give in Figure 5.12.

5.3.2 Seaward dipping reflections and their provenance

Three packages of seaward dipping reflections were identified on CD144-6 (Fig. 5.7): two at the margin of Laxmi Ridge and Chron 27 oceanic crust, and one at the northern margin of northern Gop Rift. The provenance of these sets of reflectors is discussed here.
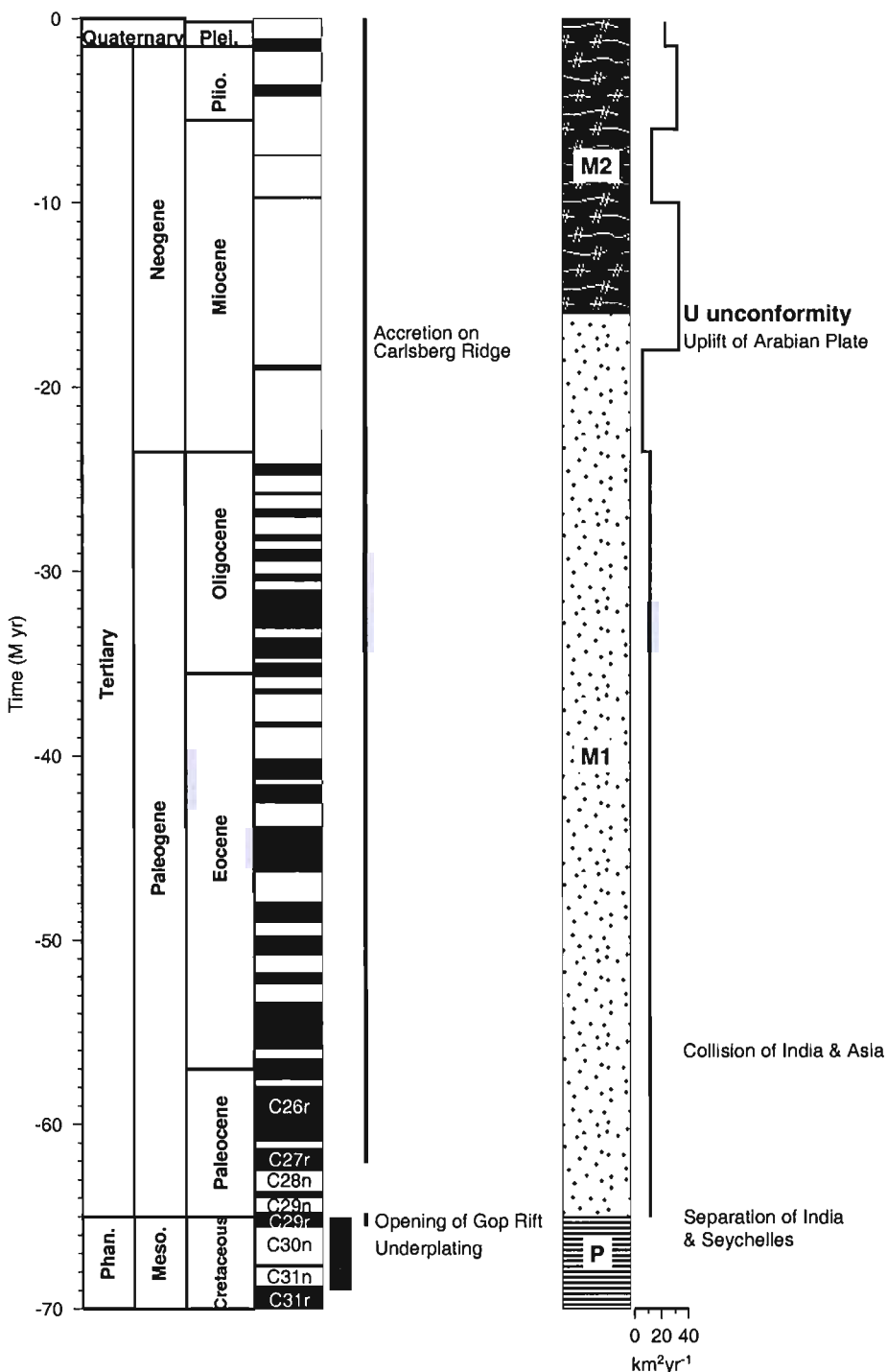
Figure 5.12: A comparison of magmatic (Section 4.2.3), tectonic and sedimentary events at the Laxmi Ridge margin. Magnetic Chrons are from Cande and Kent (1995); geological timescale is from Harland et al. (1990). The opening of Gop Rift occurs during the life of the Deccan hotspot (e.g., Vandamme et al., 1991), and causes the initiation of the separation of India and the Seychelles. This is manifest in the sedimentary record as the beginning of hemipelagic sedimentation during the Paleogene (Gaedicke et al., 2002a). *Right)* The relative rate of sedimentation peaks in both the mid Miocene and Pliocene. The Miocene peak may be due to uplift of the Arabian plate and subsequent unroofing of the Himalaya/ Karakorum.
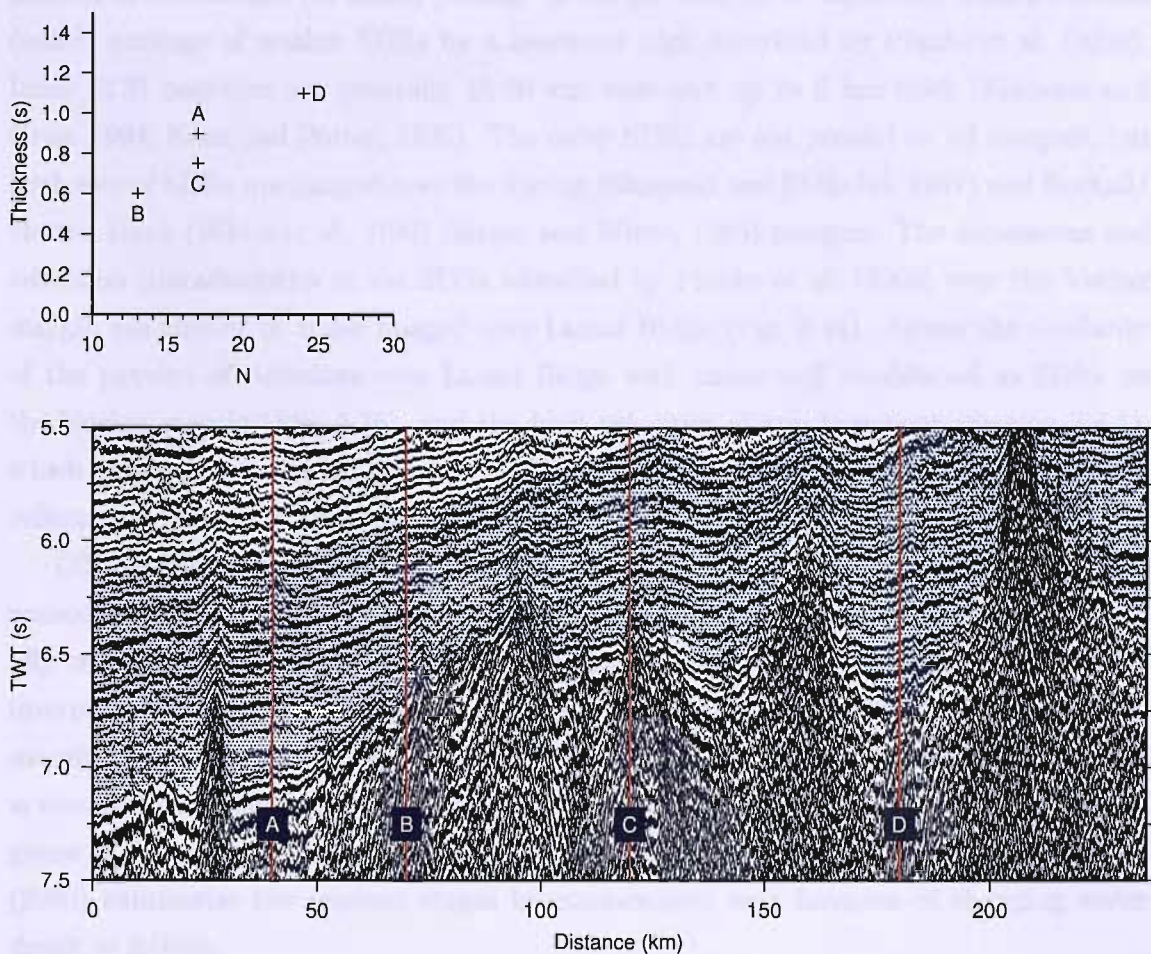
Figure 5.13: Paleogene sequences as an indicator of relative age: Thickness and number of discrete reflectors within the Paleogene sequence (blue) are compared along profiles A-D (red lines) as an analogue for relative age of tectonic features. *Top:* relative number of reflectors (N) and thickness in seconds (two way time) along profiles A-D. Northern Gop Rift (*D*) has more and thicker Paleogene reflectors. This is consistent with it being formed by seafloor spreading which predates the final breakup of the Laxmi Ridge margin and the spreading south of Laxmi Ridge. Oceanic crust south of Laxmi Ridge (*A*) has less reflectors than northern Gop Rift (*D*) so it is a younger structure. The profiles over Laxmi Ridge (*B* and *C*) have different numbers and thicknesses of packages, suggesting that extension of Laxmi Ridge was ongoing during Paleogene sedimentation. Profile *B* has fewer reflectors than profile *A*; this is probably due to a lack of accommodation space over this structural high rather than a younger age, as it is unlikely that the extension of Laxmi Ridge continued after seafloor spreading started to the south, as the spreading centre would have had a lower yield strength than the stretched continental crust.

Laxmi Ridge dipping reflections

The seaward dipping reflections identified seaward of the crest of Laxmi Ridge exhibit the pattern of a landward (or inner) package of unequivocal SDRs separated from a seaward (outer) package of weaker SDRs by a basement high described by Planke et al. (2000). Inner SDR packages are generally 15-50 km wide and up to 6 km thick (Eldholm and Grue, 1994; Keen and Potter, 1995). The outer SDRs are not present on all margins, but both sets of SDRs are imaged over the Vøring (Skogseid and Eldholm, 1987) and Rockall/Hatton Bank (White et al., 1987; Barton and White, 1995) margins. The dimensions and reflection characteristics of the SDRs identified by Planke et al. (2000) over the Vøring margin are similar to those imaged over Laxmi Ridge (Fig. 5.14). Given the similarity of the pattern of reflectors over Laxmi Ridge with those well established as SDRs on the Vøring margin (Fig. 5.14), and the high velocities at top basement (Section 3.4.1), which preclude a sedimentary origin for these reflectors, it seems likely that the dipping reflectors imaged over Laxmi Ridge are SDRs.

Differences between the reflection characteristics of the inner and outer SDRs is a consequence their different extrusive modes. Inner SDRs have been confirmed as subaerially emplaced flood basalts by drilling (Larsen and Saunders, 1998). Outer SDRs were interpreted as deep marine sheet flows formed during the initial drift stages of a volcanic margin by Planke et al. (1995). The basement high separating the two packages of SDRs is though to be a shallow marine volcanic construct formed after subsidence and submergence of the margin, based on evidence from drilling (Planke et al., 1995). Planke et al. (2000) summarise the relevant stages in emplacement as a function of changing water depth as follows:

1. Effusive subaerial volcanism forming the inner SDRs.

2. Rifting and subsequent flooding.

3. Explosive shallow marine volcanism forming the basement high.

4. Effusive deep marine volcanism forming the outer SDRs.

5. Subsidence leading to dip reversal of SDRs.

Up to 30 km wide packages of unequivocal SDRs are identified on the conjugate Seychelles Bank margin, both by their wedge-shaped, internally divergent morphology and by their stacking velocities, which are too high to interpret the reflectors as faults or pre-rift sediments (Sansom, pers. comm.). Not all seismic lines image such high amplitude, unequivocal SDRs, but where weak SDRs are imaged, their provenance is confirmed by the presence of more convincing SDRs on adjacent lines.
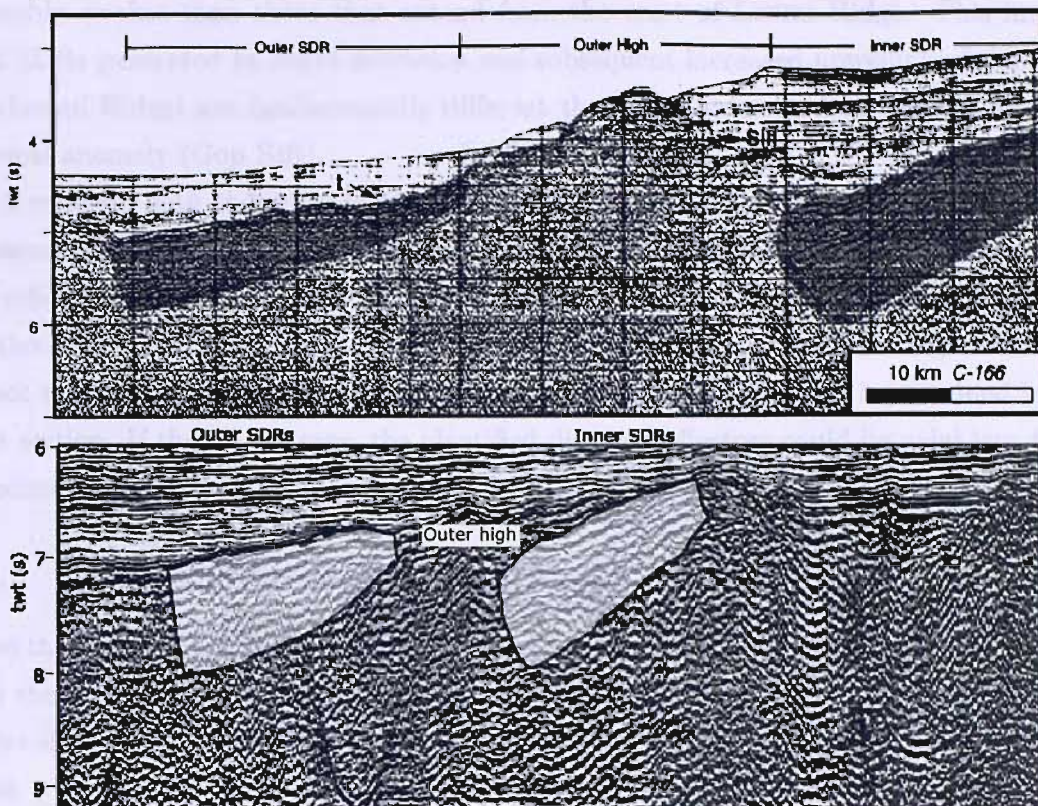
Figure 5.14: Comparison of SDRs on the Laxmi Ridge and Vøring Margins: The morphology and distribution of SDRs (shaded regions) on the Vøring margin (top; Planke et al., 2000) are similar to those observed on the Laxmi Ridge margin (bottom). Both plots are at the same scale.

The SDRs imaged both over Laxmi Ridge and on the conjugate Seychelles Bank margin (Sansom, pers. comm.) must be a consequence of rapid extension of this margin (Royer et al., 2002), as final breakup occurred after the waning of the Deccan hotspot (Section 4.2.3; Vandamme et al., 1991; Cande and Kent, 1995; Royer et al., 2002).

Gop Rift dipping reflections

Bright, diverging southward dipping reflectors have been identified at the junction of oceanic crust in northern Gop Rift and faulted continental crust on the continental rise on profile CD144-5 (Fig. 5.5). They appear to be preserved within oceanic crust. Less compelling dipping reflectors are seen in approximately the same location on profile CD144-6 (Fig. 5.7). The provenance of these reflectors is assumed to be magmatic, as they occur within an area of basement with high P-wave velocities (Section 3.4.4), which makes them unlikely to be pre-rift sediments. If these reflectors are SDRs then they are con-

siderably weaker than those that extend from the crest of Laxmi Ridge. This implies that SDRs generated by rapid extension and subsequent increased upwelling of the mantle (Laxmi Ridge) are fundamentally different that those generated by extension over a thermal anomaly (Gop Rift).

A problem with the interpretation of the Gop Rift dipping reflectors as SDRs is the apparent continuation of the northern Gop Rift ocean basin north of the basement high the reflectors originate on (Section 4.2.2). This may mean that northern Gop Rift is the southern half of an ocean basin, which is symmetrical about the basement high. Whether or not this basement high is the extinct spreading centre in this basin is examined in the next section. If that is the case, the identified dipping reflectors could be axial lava flows associated with the spreading ridge.

5.3.3 Is there an extinct spreading centre in Gop Rift?

From the evidence presented in this chapter and Sections 3.4.4 and 4.2.2, it seems plausible that the crust within northern Gop Rift is oceanic. If this is the case, an extinct spreading centre should still be identifiable as a volcanic construct in the approximate centre of this crust.

From the magnetic model of the Laxmi Ridge margin (Figure 4.8), it appears that the oceanic crust within northern Gop Rift continues to the north of a large basement high, seen here on reflection profile CD144-6 between CDPs 21000 and 23500 (Fig. 5.7). It is not clear from the basement map (Fig. 5.11) exactly where the boundaries of this ocean basin are. The continuation of the basin to the north is illustrated on CD144-2 (Fig. 5.15), although the quality of the data are poor. On CD144-2, crust in northern Gop Rift appears to be symmetrical about the basement high, which is between CDPs 14000 and 17000 on this line. This basement high rises almost 3 km above the surrounding basement and is 31 km wide. It is hard to describe due to the poor quality of CD144-2, but it is an asymmetric feature, with lower relief to the north. There appears to be a package of SDRs between the ocean basin and the continental rise (CDP 20000). Although the data are poor, we can have confidence in the identification of these SDRs due to the observation of SDRs on the cross cutting *Sonne* line (Gaedicke et al., 2002b).

In common with the extinct spreading centre in the Labrador Sea (Louden et al., 1996), the Moho shallows under the basement high. The basement high appears to be a single seamount (Fig. 5.11), but this may be a consequence of sparse data. The basement high is tall compared to a modern analogue, the fast-spreading East Pacific Rise, which is around 200 m high (Franchetau and Ballard, 1983), but it is similar in its apparent lack of axial trough and evidence of axial lava flows (Fornari et al., 2004). Both its asymmetry, with the northern flank lower than the southern, and its height give it more in common

with the axial volcano observed on the Juan de Fuca Ridge. The Juan de Fuca axial volcano is flanked by numerous sheet flows, 5 kyr to 9 kyr in age (Barker et al., 1999). This is an intermediate spreading centre caused by ridge-hotspot interaction so may be a good modern analogue.

Seafloor spreading between Palitana Ridge and the continental rise explains the apparent lack of lateral continuity of Gop Rift with the Laxmi Basin; Laxmi Basin is a failed rift (Section 4.2.3; Krishna et al., 2006), whereas Gop Rift continued to continental breakup and seafloor spreading.
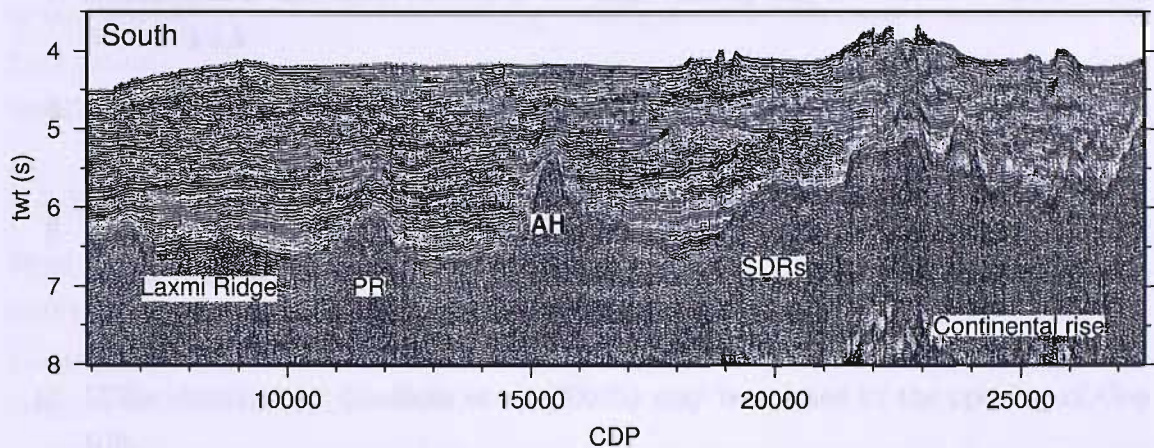
Figure 5.15: Basement structure on CD144-2: PR is Palitana Ridge and AH is the basement high separating what appears to be oceanic crust in northern Gop Rift and a continuation of this crust to the north. This means the basement high may be an axial high; a fossil spreading centre. Between the ocean basin and the continental rise there appears to be a package of SDRs, which are geographically close to those identified by Gaedicke et al. (2002b).

5.4 Summary and conclusions

1. The sedimentary sequence on the Laxmi Ridge margin consists broadly of three packages: *P*, which is a Cretaceous pre-rift sequence preserved on continental basement highs; *M1*, which represents Paleocene to Oligocene hemipelagic settling and distal turbidites from the proto-Indus Fan and *M2*, which are Miocene to Quaternary Indus Fan channel levee complexes.

2. Paleogene sediments are post-rift with respect to the opening of Gop Rift, but synchronous with the breakup of India and Seychelles.

3. Extension in northern Gop Rift predates seafloor spreading south of Laxmi Ridge.

4. Continental crust has a chaotic, highly reflective character underneath a rough basement surface, while oceanic crust has a low amplitude parallel reflectivity overlain

by up to 0.4 s TWT of parallel, bright reflectors.

5. Crustal structure observed on CD144-6 can be tied to major velocity discontinuities in the wide-angle velocity model (Section 3.4).

6. The Moho is imaged as a low frequency reflector beneath both the continental crust and oceanic crust south of Laxmi Ridge. Beneath northern Gop Rift, it is either absent or a higher frequency double reflector.

7. A reflection is seen from the top of the high velocity sub-crustal body discussed in Section 3.4.5.

8. Seward dipping reflectors generated by rapid extension are observed on this margin and on the conjugate Seychelles Bank margin.

9. The basement high at approximately 20.1°N 64.9°E may be an extinct spreading centre from oceanic crustal genesis within northern Gop Rift. It is flanked by a seismically bright package of axial lava flows.

10. SDRs identified by Gaedicke et al. (2002b) may be related to the opening of Gop Rift.

6 ‖ Conclusions and wider context of this work

This chapter summarises the main results and conclusions from this thesis, and discusses the wider context of the work. Suggestions are also made for further research to support some of the theories presented here and address some of the outstanding questions.

6.1 Major conclusions of this work

The Laxmi Ridge continental margin has features common to both amagmatic and volcanic rifted margins. This apparent disparity is resolved by considering two distinct phases of rifted margin formation: a Deccan volcanic phase characterised by asymmetric extension in Gop Rift and voluminous magmatism, followed by rapid mantle cooling and a relatively amagmatic phase that led to breakup between Laxmi Ridge and the Seychelles (Fig. 3.37).

Gop Rift was interpreted as an ocean basin based on its high amplitude magnetisations of at least -2.5 A m^{-1} in layer 2 and -1.5 A m^{-1} in layer 3 (Section 4.2.2) that provide evidence for a magmatic (oceanic) origin. These magnetisations are high compared to those modelled for the oceanic crust south of Laxmi Ridge, which may be suggestive of formation at the end of the Cretaceous, a period of high magnetic field strength (Wang et al., 2005). A change in crustal provenance from continental at Laxmi ridge to oceanic at Gop Rift is indicated also by a change in the character of the normal incidence reflectivity of both the crust and Moho (Fig. 5.5). Oceanic crust within northern Gop Rift matches Atlantic averages for P-wave velocity structure of plume influenced accretion (Fig. 3.27; White, 1992). Seaward-dipping reflectors identified by Gaedicke et al. (2002b) and in this work (Section 5.3.3) may be associated with the opening of Gop Rift as they are at the approximate latitude where the OCB between Gop Rift and the continental rise of India is inferred from a change in remanent magnetisation of the crust (Section 4.2.2). SDRs are observed at the northern limit of Gop Rift on MCS line CD144-2, but they are hard to identify due to poor data quality. The southern OCB between Gop Rift and Laxmi Ridge has a different character: there are no obvious SDRs or transitional crust; oceanic crust in Gop Rift abuts against stretched continental crust at Palitana Ridge. Palitana Ridge is a basement high that may be an isolated fault block. The basement high within Gop Rift, at approximately 20.1°N 64.9°E, is most likely the extinct spreading centre from oceanic crustal genesis within Gop Rift (Section 5.3.3). It is flanked by seismically bright reflectors that are interpreted as a package of axial lava flows. A Chron 29 age is

suggested for spreading in Gop Rift based on magnetic modelling (Section 4.2.3) and the voluminous magmatism (Sections 3.4.5; 3.7.2), which allows us to infer that extension was contemporaneous with the lifespan of the Deccan hotspot (e.g., Vandamme et al., 1991).

High velocity lower crustal bodies (Section 3.4.5) beneath Laxmi Ridge and the continental rise of India are broadly symmetrical about Gop Rift and they are interpreted to be up to 13 km thick wedges of magmatic underplate related to the Deccan phase of extension. Velocities in the HVSCBs reach 7.4 km s^{-1} +0.22/-0.39 km s^{-1} (Section 3.4.5), which is high compared to normal lower continental crust and leads to the conclusion that they are underplate. The HVSCB beneath Laxmi Ridge is very well constrained by wide-angle reflections on the margin-parallel line (Section 3.6.1). Discontinuous but strong wide-angle reflections are seen on the margin-orthogonal line (Section 3.4.5). Normal-incidence reflections are also identified from the upper surface of the body beneath Laxmi Ridge (Section 5.2.2). The HVSCB north of Gop Rift is constrained by sporadic wide-angle reflections from its base. The two HVSCBs are consistent with, but not required by, coincident free-air gravity and magnetic anomaly data.

A Chron 30 age is suggested, with both underplates forming as one body prior to oceanic crustal accretion in Gop Rift and were split into two bodies by the spreading (Sections 4.2.3; 3.7.3). Asymmetric accretion of both underplate beneath the Laxmi Ridge margin and oceanic crust within Gop Rift was driven by the proximity of the Deccan hotspot. Mantle beneath the northern limit of the underplate was around 40°C hotter than the southern limit (Section 3.7.3).

Basement within the Laxmi Basin, which is adjacent to Gop Rift, has been previously interpreted as thinned continental crust (Krishna et al., 2006) and oceanic crust (Bernard and Munschy, 2000). Magnetic anomalies in Gop Rift have much larger amplitude than those in the Laxmi Basin (Section 4.2.3), which, assuming contemporaneous extension, suggests that the two structures have a different origin, so Laxmi Basin is most likely intruded, stretched continental crust.

Laxmi Ridge is generally accepted to be stretched continental crust (e.g., Naini and Talwani, 1982; Talwani and Zelt, 1998). This work supports a continental provenance; crust in Laxmi Ridge has a low remenant magnetisation (less than 0.5 A m^{-1}; Section 4.2.2) and low P-wave velocities relative to normal oceanic crust (Section 3.4.3). The negative gravity anomaly associated with Laxmi Ridge is a consequence of the thick crust beneath the Ridge, but there may also be a small contribution from the magmatic underplate at the base of the crust, which has a low density compared to that of the surrounding mantle (Section 4.1.3). Excluding the underplate, Laxmi Ridge has a crustal thickness of almost 10 km (Section 3.4.3). Some SDRs are identified originating at the crest of Laxmi ridge and extending seaward for 100 km (Section 5.2.2). SDRs are also identified on the conjugate Seychelles Bank margin (Sansom, pers. comm.), suggesting

that this magmatism is extension related. The margin-parallel structure of the Laxmi Ridge margin is laterally homogeneous (Section 3.6; Evain, 2004).

Normal seafloor spreading commenced south of Laxmi Ridge 0.55 Myr after the commencement of Chron 27r (Section 4.2.1). This post-dates emplacement of the Deccan Traps (e.g., Vandamme et al., 1991), hence the thin (around 5 km thick) oceanic crust seaward of both margins (Section 3.7.4). The Chron 27 oceanic crust has an unusual velocity structure, with a thin, low velocity gradient layer 2 and thin layer 3 (Section 3.4.2).

Thick sediments from the Indus fan have been deposited over Laxmi Ridge, and isostatic compensation of those sediments accounts for the misfit in basement depth between the Seychelles Bank and Laxmi Ridge conjugate margins. Once the difference in sediment loading is taken into account, the velocity models over the two margins match exceptionally well (Section 3.7.4). The regional Miocene U unconformity manifests both as a clear normal incidence reflection (Section 5.1.3) and a step up in P-wave velocities (Section 3.4.1). The relative numbers of Paleogene reflectors observed on the MCS profiles can be used to approximate relative age of extension over parts of the Laxmi Ridge margin. The Paleogene stratigraphy provides further evidence that extension in Gop Rift predated final breakup south of Laxmi Ridge (Section 5.3.1).

6.2 Wider contexts of this work

The findings of this thesis have implications for the mechanisms and controls on continental rifting, early seafloor spreading and syn-rift magmatism.

This work has important implications for the nature of ridge-hotspot interactions: magnetic modelling implied that underplating associated with Gop Rift formed prior to extension (Section 3.7.3). This means that, rather than being a syn-rift product of excessive magmatism, underplate could actually be a primary stage of increased upwelling. Partially replacing the upper mantle with magmatic crust weakens the lithosphere, focusing strain caused by extension or thermal uplift sufficiently to cause rifting. Since spreading in Gop Rift ceased once the thermal influence of the hotspot dwindled, spreading initiated by thermal anomalies must require a period of time to progress to steady-state, self-sustaining accretion. Perhaps increased convection caused by a thermal anomaly is the driving process during early seafloor spreading. Asymmetry in the thickness of both the underplate and oceanic crust in Gop Rift (Section 3.7.3) indicates that the hotspot was north of the basin; upwelling and subsequent melting were asymmetric due to the thermal input being located away from the basin.

The major conclusion of this work is that the Laxmi Ridge continental margin is essentially two rifted margin systems: the hotspot-influenced Gop Rift and the amagmatic rifting between Laxmi Ridge and the Seychelles. The reconstructed conjugate Seychelles

Bank and Laxmi Ridge margins show that, despite high velocities at the base of the crust, the first-formed oceanic crust was anomalously thin (Section 3.4.2). This pattern of volcanic and amagmatic margin formation requires an isolated pulse of hot material from the hotspot, followed by rapid cooling of the mantle (estimated at around 20°C Myr^{-1}; Section 3.7.1). The mantle cooling is interpreted here as being due to a combination of the hotspot pulse cooling against the cold Indian lithosphere and a sufficiently long rift duration allowing any new upwelling material time to cool. The first-formed oceanic crust on the Laxmi Ridge-Seychelles Bank conjugate pair might reasonably be expected to be thicker than normal due to the rapid extension (Bown and White, 1995; Royer et al., 2002). The fact that it is thinner than normal implies that rift duration and associated lithospheric cooling is a major control on decompression melting. Strain rate does not seem to have been a major control on the architecture of the conjugate Laxmi Ridge and Seychelles Bank margins: the margins have a strong asymmetry in the Moho structure (Fig. 3.36), while modelling by Bassi (1995) predicted that only a weak and viscous lithosphere extended by very slow rates of strain would rupture asymmetrically.

6.3   Suggestions for further research

Some outstanding questions still remain that are beyond the scope of this work. These questions, and research that might allow their resolution, are discussed below.

Significant debate exists still about the exact timing and duration of the eruption of the Deccan Traps, and the longevity of the associated mantle hotspot. Although Gop Rift was irrefutably formed due to the interaction of rifting and some kind of mantle thermal anomaly, and although this must have occurred at approximately the same time as the Deccan eruptions, the link between Gop Rift and the Deccan hotspot is not unequivocally proved. The timing of the underplate that predates spreading in Gop Rift and accretion of the magmatic crust within the Rift are both constrained by ambiguous magnetic modelling. The relative age of Gop Rift is further constrained by Paleogene stratigraphy, but this method has large errors associated with it. In order to resolve this issue, both the timing of the Deccan magmatism and the age of Gop Rift need to be better constrained. The age of the Deccan Traps is an ongoing question that will ultimately be resolved by improved geochemical and geomagnetic dating methods. The age of Gop Rift would be better constrained by dating direct samples from the crust obtained by drilling. A more careful examination of the stratigraphy over the margin might provide clues about the age of the underplate, since evidence of uplift might be expected due to the addition of hot material to the base of the crust. However, this seems unlikely as there is a limited amount sedimentation that is pre-rift relative to Gop Rift (Section 5.1.1).

In addition to the vertical component hydrophone and geophone data used in this

thesis to construct a P-wave velocity model, data were also collected using horizontal geophones. These horizontal components record information about shear (S) wave propagation through the margin. Processing and modelling these data could give additional constraints on the impedance contrast at horizons beneath the margin by quantifying P-S wave conversions. The ratio of P to S wave velocities through the model is related to the Poisson's Ratio of the subsurface. The value of Poisson's ratio can be used to infer crust type. This would be particularly useful in the upper mantle beneath the Chron 27 oceanic crust, where low mantle velocities may be due to mantle serpentinisation of up to 10% (Miller and Christensen, 1997). Poisson's ratio can be a more reliable indicator of mantle serpentinisation than seismic velocity alone (e.g., Bullock and Minshull, 2005).

The exact nature of important features of the Laxmi Ridge margin that are at the limit of the resolution of wide-angle modelling, such as SDRs, the extinct spreading centre in Gop Rift and Palitana Ridge, are constrained by normal incidence reflections (Chapter 5). To improve the clarity of seismic images over such features, the multichannel data could be pre-stack depth migrated (PSDM). PSDM has the advantage of improved resolution and accurate mapping of structure to its correct subsurface location, but the method requires a very accurate velocity model, which is time-consuming to construct.

Given the presence of Deccan lava flows on the Seychelles Plateau (Müller et al., 2001), it seems reasonable expect Deccan lavas to be present on continental crust at the Laxmi Ridge margin. Lava flows might explain the high P-wave velocities modelled at the base of the sediments. This hypothesis could be tested by drilling, although the thick Indus Fan sediments would make drilling challenging.

Rapid cooling of the lithosphere is required between the two phases of margin formation on the Laxmi Ridge rifted margin. Rapid mantle cooling is discussed by Lizarralde and Holbrook (1997) to explain the subsidence patterns at the mid-Atlantic margin, but the exact method for cooling material supplied by a mantle thermal anomaly is not fully understood. To do this would require a better understand of the dynamics and cyclicity of the Deccan hotspot and the mechanics of mantle cooling. These uncertainties may be resolved through a combination of computer simulation and careful observation of patterns of magmatic material and uplift associated with the hotspot.

Bibliography

G. A. Abers. Evidence for seismogenic normal faults at shallow dips in continental rifts. *Non-Volcanic Rifting of Continental Margins: A Comparison of Evidence from Land and Sea. Geological Society, London, Special Publications*, 187:305–318, 2001.

C. J. Allégre, J. L. Birck, F. Campas, and V. Courtillot. Age of the Deccan traps using ^{187}Re-^{187}Os systematics. *Earth and Planetary Science Letters*, 170:197–204, 1999.

D. L. Anderson. *Theory of the Earth.* Blackwell Publications, 1989.

R. T. Bachman and E. L. Hamilton. Sediment sound velocities from sonobuoys: Arabian Fan. *Journal of Geophysical Research*, 85:849–852, 1980.

E. T. Barker, C. G. Fox, and J. P. Cowen. In situ observations of the onset of hydrothermal discharge during the 1998 submarine eruption of Axial Volcano, Juan de Fuca Ridge. *Geophysical Research Letters*, 26:3445–3448, 1999.

A. J. Barton and R. S. White. The Edoras bank margin: continental break-up in the presence of a mantle plume. *Journal of the Geological Society of London*, 154:971–974, 1995.

A. J. Barton and R. S. White. Crustal structure of Edoras Bank continental margin and mantle thermal anomalies beneath the North Atlantic. *Journal of Geophysical Research*, 102, 1997.

G. Bassi. Relative importance of strain rate and rheology for the mode of continental extension. *Geophysical Journal International*, 122:195–210, 1995.

A. Bernard and M. Munschy. Le bassin des Mascareignes et le bassin de Laxmi (océan Indien occidental) se sont-ils formés à l'axe d'un même centre d'expansion? *C. R. Acad. Sci. Paris, Sciences de la Terre et des planetes*, 330:777–783, 2000.

N. Bhandari, P. N. Shukla, Z. G. Ghevariya, and S. M. Sundaram. Impact did not trigger Deccan volcanism: evidence from Anjar K/T boundary intertrappean sediments. *Geophysical Research Letters*, 22(4):433–436, 1995.

G. C. B. Bhattacharya, A. K. Chaubey, G. P. S. Murty, S. Srinivas, K. V. L. N. S. Sarma, V. Subrahmanyam, and K. S. Krishna. Evidence for seafloor spreading in the Laxmi Basin, northeastern Indian Ocean. *Earth and Planetary Science Letters*, 125:211–220, 1994.

L. D. Bibee and G. G. Shor. Compressional wave anisotropy in the crust and upper mantle. *Geophysical Research Letters*, 3:639–642, 1976.

S. K. Biswas and N. K. Singh. Western continental margin of India and hydrocarbon potential. *Proceedings of the 7ᵗʰ Offshore South East Asia Conference, Singapore, 2-5 Feb.*, 1988.

S. K. Biswas and J. Thomas. The Deccan Traps and Indian Ocean volcanism. *First Indian Ocean petroleum seminar: Seychelles, United Nations Department of Technical Co-operation for Development*, 1992.

I. T. Bjarnason, W. Menke, F. O. G., and D. Caress. Tomographic image of the Mid-Atlantic plate boundary in south-west Iceland. *Journal of Geophysical Research*, 98: 6607–6622, 1993.

J. H. Bodine, M. S. Steckler, and A. B. Watts. Observations of flexure and rheology of the oceanic lithosphere. *Journal of Geophysical Research*, 86:3695–3707, 1981.

M. H. P. Bott. Modelling the loading stresses associated with continental rift systems. *Tectonophysics*, 182:99–115, 1992.

M. H. P. Bott and N. J. Kusznir. Stress distribution associated with compensated plateau uplift structures with application to the continental splitting mechanism. *Geophysical Journal of the Royal Astronomical Society*, 56:451–459, 1979.

J. W. Bown and R. S. White. Variation with spreading rate of oceanic crustal thickness and geochemistry. *Earth and Planetary Science Letters*, 121:435–449, 1994.

J. W. Bown and R. S. White. Effect of finite extension rate on melt generation at rifted continental margins. *Journal of Geophysical Research*, 100:18011–18029, 1995.

N. Bruguier. Inversion of first-arrival travel-times from the Chicxulub impact crater. *Journal of Conference Proceedings, Vol. 1, CCSS Workshop June 4th-6th, Cambridge Publications, Cambridge, UK.*, 1:47–52, 1996.

J. P. Brun and M. O. Beslier. Mantle exhumation at passive margins. *Earth and Planetary Science Letters*, 142:161–173, 1996.

S. K. Buchanan, R. A. Scrutton, R. A. Edwards, and R. B. Whitmarch. Marine magnetic data processing in equatorial regions off Ghana. *Geophysical Journal International*, 125:123–131, 1996.

A. D. Bullock. *From continental thinning to sea-floor spreading: a geophysical study of rifted margins southwest of the UK*. Ph.D. Thesis, School of Ocean and Earth Science, University of Southampton, Southampton, UK, 2004.

A. D. Bullock and T. A. Minshull. From continental extension to sea-floor spreading: Crustal structure of the Goban Spur rifted margin, southwest of the UK. *Geophysical Journal International*, 163(2):527–546, 2005.

K. Burke and A. J. Whiteman. Uplift, rifting and the break-up of Africa. *In: D. H. Tarling, S. K. Runcorn (Eds.), Implications of continental drift to the Earth Sciences, Academic Press, New York*, pages 735–755, 1973.

J. P. Canales, R. S. Detrick, S. Bazin, A. J. Harding, and J. A. Orcutt. Off-axis crustal thickness across and along the East Pacific Rise within the MELT area. *Science*, 280 (5367):1218–1221, 1998.

S. C. Cande and D. V. Kent. Revised calibration of the geomagnetic polarity timescale for the Late Cretaceous and Cenozoic. *Journal of Geophysical Research*, 100:6093–6095, 1995.

J. R. Cann. A model for oceanic crustal structure developed. *Geophysical Journal of the Royal Astronomical Society*, 39:169–187, 1974.

R. L. Carlson. Seismic velocities in the uppermost oceanic crust: age dependence and the fate of Layer 2A. *Journal of Geophysical Research*, 103:7069–7077, 1998.

A. K. Chaubey, J. Dyment, G. C. Bhattacharya, J.-Y. Royer, K. Srinvas, and V. Yatheesh. Paleogene magnetic isochrons and paleo-propagators in the Arabian and Eastern Somali basins, NW Indian Ocean. *The tectonic and climatic evolution of the Arabian Sea region. Special publication of the Geological Society of London, UK*, 195:71–85, 2002a.

A. K. Chaubey, D. G. Rao, K. Srinivas, M. V. Ramana, and V. Subrahmanyam. Analysis of multichannel seismic reflection, gravity and magnetic data along a regional profile across the central-western continental margin of India. *Marine Geology*, 182(3-4):303–323, 2002b.

D. Chian, C. Keen, I. Reid, and K. E. Louden. Evolution of nonvolcanic rifted margins: New results from the conjugate margins of the Labrador Sea. *Geology*, 23(7):589–592, 1995.

D. Chian and K. E. Louden. Crustal structure of the Labrador Sea conjugate margin and implications for the formation of nonvolcanic continental margins. *Journal of Geophysical Research*, 100:24239–24253, 1995.

N. I. Christensen and W. D. Mooney. Seismic velocity structure and composition of the continental crust: A global view. *Journal of Geophysical Research*, 100:9761–9788, 1995.

N. I. Christensen and J. D. Smewing. Geology and seismic structure of the northern section of the Oman ophiolite. *Journal of Geophysical Research*, 86:2545–2555, 1981.

J. F. Claerbout. Snell waves: Stanford exploration project report no. 15. *Stanford University*, pages 57–72, 1978.

P. Clift, A. Carter, M. Krol, and E. Kirby. Constraints on India-Eurasia collision in the Arabian Sea region taken from the Indus Group, Ladakh Himalaya, India. *The tectonic and climatic evolution of the Arabian Sea region. Special publication of the Geological Society of London, UK*, 195:97–116, 2002.

P. Clift, N. Shimizu, G. Layne, C. Gaedicke, H.-U. Schluter, M. Clark, and S. Amjad. Fifty-five million years of Tibetan evolution recorded in the Indus Fan. *EOS, Transactions, American Geophysical Union*, 81, 2000.

P. D. Clift and J. Turner. Paleogene igneous underplating and subsidence anomalies in the Rockall-Faeroe-Shetland area. *Marine and Petroleum Geology*, 15:223–243, 1998.

M. F. Coffin and O. Eldholm. Scratching the surface: estimating dimensions of large igneous provinces. *Geology*, 21:515–518, 1993.

J. S. Collier. Cruise Report, R.R.S. Charles Darwin Cruise 144: Structure of the Seychelles-Laxmi Ridge conjugate rifted continental margins. Muscat, Sultanate of Oman to Victoria, Mahe, Republic of Seychelles. 13 January- 22 February, 2003.

F. A. Darbyshire, I. T. Bjarnason, R. S. White, and O. G. Flóvenz. Crustal structure above the Iceland mantle plume imaged by the ICEMELT refraction profile. *Geophysical Journal International*, 135:1131–1149, 1998.

F. J. Davey. Geophysical studies in the Ross Sea region. *Journal of the Royal Society of New Zeland*, 11:465–479, 1981.

F. J. Davey and A. K. Cooper. Gravity studies of the Victoria Land basin and Iselin bank. *in: The Antarctic Continental Margin: Geology and Geophysics of the Western Ross Sea, Earth Science Series*, 5B:119–138, 1987.

M. Davis and N. Kusznir. Depth-dependant lithospheric stretching at rifted continental margins. *NSF Margins Program Special Publication on Rifted Margins, (ed. G. Karner)*, 2003.

S. M. Dean. Structure of the ocean-continent transition in the Southern Iberia abyssal plain. *Ph.D. Thesis, Robinson College, Cambridge*, 1999.

S. M. Dean, T. A. Minshull, R. B. Whitmarsh, and K. E. Louden. Deep structure of the ocean-continent transition in the southern Iberia Abyssal Plain from seismic refraction profiles: The IAM-9 transect at 40°20 N. *Journal of Geophysical Research*, 105:5859–5855, 2000.

N. Den. Seismic refraction measurements in the northwest Pacific basin. *Journal of Geophysical Research*, 74:1421–1434, 1969.

R. Detrick, J. Collins, R. Stephen, and S. Swift. In situ evidence for the nature of the seismic layer 2/3 boundary in oceanic crust. *Nature*, 370:288–290, 1994.

C. W. Devey and W. E. Stephens. Tholeiitic dykes in the Seychelles and the original spatial extent of the Deccan. *Journal of the Geological Society of London*, 148:979–983, 1991.

J. F. Dewey and K. Burke. Hot-spots and continental break-up. *Geology*, 2:57–60, 1975.

C. H. Dix. Seismic prospecting for oil. *Harper and Brothers*, 1952.

L. Droz and G. Bellaiche. Seismic facies and geological evolution of the central portion of the Indus Fan. *Seismic Facies and Sedimentary Processes of Submarine Fans and Turbidite Systems. Springer Verlag, New York.*, pages 383–402, 1991.

R. K. Dube, J. C. Bhayana, and H. M. Chaudhury. Crustal structure of the peninsular India. *Pure and Applied Geophysics*, 109:1718–1727, 1973.

J. Dyment. Evolution of the Calsberg Ridge between 60 and 45 Ma: Ridge propagation, spreading asymmetry and the Deccan-Reunion hotspot. *Journal of Geophysical Research*, 103:24067–24084, 1998.

O. Eldholm and K. Grue. North Atlantic volcanic margins: Dimensions and production rates. *Journal of Geophysical Research*, 99:2955–2968, 1994.

P. England. Constraints on extension of continental lithosphere. *Journal of Geophysical Research*, 88(B2):1145–1152, 1983.

M. M. Evain. Crustal structure of the NW Indian continental margin at Laxmi Ridge. *M.Sc. Dissertation, University of Southampton*, 2004.

C. G. Farnetani, M. A. Richards, and M. S. Ghiorso. Petrological models of magma evolution and deep crustal structure beneath hotspots and flood basalt provinces. *Earth and Planetary Science Letters*, 143:81–94, 1996.

D. Fornari, M. Tivey, H. Schouten, M. Perfit, D. Yoerger, A. Bradley, M. Edwards, R. Haymon, D. Scheirer, K. Von Damm, T. Shank, and A. Soule. Submarine lava emplacement at the East Pacific Rise 9° 50′N: implications for uppermost ocean crust stratigraphy and hydrothermal fluid circulation. *The Thermal Structure of the Ocean Crust and the Dynamics of Hydrothermal Circulation, Geophysical Monograph 148, American Geophysical Union*, pages 187–217, 2004.

D. J. Forster and C. C. Mosher. Suppression of multiple reflections using the radon transform. *Geophysics*, 57:386–395, 1992.

C. M. R. Fowler. *The solid earth: An introduction to global geophysics.* Cambridge University Press, 1990.

J. Franchetau and R. D. Ballard. The East Pacific Rise near 21°N 13°N and 20°S: inferences for along-strike variability of axial processes of the mid-ocean ridge. *Earth and Planetary Science Letters*, 64:93–116, 1983.

T. J. G. Francis and G. G. Shor. Seismic refraction measurements in the northwest Indian ocean. *Journal of Geophysical Research*, 71:427–449, 1966.

T. Funk, K. E. Louden, and I. D. Reid. Crustal structure of the Grenville Province in southeastern Labrador from refraction seismic data: evidence for a high-velocity lower crustal wedge. *Canadian Journal of Earth Science*, 38:1463–1478, 2001.

C. Gaedicke, A. Prexl, H.-U. Schluter, H. Meyer, H. Roeser, and P. Clift. Seismic stratigraphy and correlation of major regional unconformities in the northern Arabian Sea. *The tectonic and climatic evolution of the Arabian Sea region. Special publication of the Geological Society of London, UK*, 195:25–36, 2002a.

C. Gaedicke, H.-U. Schluter, H. A. Roeser, A. Prexl, B. Schreckenberger, H. Meyer, C. Reichert, P. Clift, and S. Amjad. Origin of the northern Indus Fan and Murray Ridge, Northern Arabian Sea: interpretation from seismic and magnetic modelling. *Tectonophysics*, 355:127–143, 2002b.

A. Ghods. Is small scale convection responsible for the formation of thick igneous crust along volcanic passive margins? *Geophysical Research Letters*, 29(10), 2002.

A. M. Gombos, W. G. Powell, and I. O. Norton. The tectonic evolution of western India and its impact on hydrocarbon occurrences: an overview. *Sedimentary Geology*, 96, 1995.

I. Grevemeyer and W. Weigel. Seismic velocities of the uppermost igneous crust versus age. *Geophysical Journal International*, 124:631–635, 1996.

I. Grevemeyer, W. Weigel, and C. Jennrich. Structure and ageing of oceanic crust at 14°S on the East Pacific Rise. *Geophysical Journal International*, 135:573–584, 1998.

E. L. Hamilton, R. T. Bachman, J. R. Curray, and D. G. Moore. Sediment velocities from sonobuoys: Bengal Fan, Sudan Trench, Andaman Basin and Nicobar Fan. *Journal of Geophysical Research*, 82(20):3003–3011, 1977.

J. O. S. Hammond, N. Teanby, P. Joseph, T. Ryberg, G. Stuart, J.-M. Kendall, G. Rümper, and J. Wookey. Upper mantle anisotropy beneath the Seychelles microcontinent. *Journal of Geophysical Research*, 110(11):1–12, 2005.

W. B. Harland, R. L. Armstrong, A. V. Cox, L. E. Craig, A. G. Smith, and D. G. Smith. A geologic time scale, 1989 edition. *Cambridge University Press*, pages 1–263, 1990.

C. G. A. Harrison. Magnetism of the oceanic crust. *in The Oceanic Lithosphere*, 7: 219–239, 1981.

C. G. A. Harrison. Marine magnetic anomalies - the origin of the stripes. *Annual Review of Earth and Planetary Sciences*, 15:505–543, 1987.

D. L. Harry and J. C. Bowling. Inhibiting magmatism on nonvolcanic rifted margins. *Geology*, 27(10):895–898, 1999.

K. Hayling and C. G. A. Harrison. Magnetization modelling in the North and Equatorial Atlantic Ocean using MAGSAT. *Journal of Geophysical Research*, 91:12423–12443, 1986.

E. Hellebrand and J. E. Snow. Deep melting and sodic metasomatism underneath the highly oblique-spreading Lena Trough (Artic Ocean). *Earth and Planetary Science Letters*, 216:283–299, 2003.

K. Hinz. A hypothesis on terrestrial catastrophes. Wedges of very thick oceanward dipping layers beneath passive continental margins - Their origin and palaeoenvironmental significance. *Geologisches Jahrbuch, Reihe E, Geophysik*, 22:3–28, 1981.

H. J. Hoffman and T. J. Reston. Nature of the S reflector beneath the Galicia Banks rifted margin: preliminary results from prestack depth migration. *Geology*, 20:1091–1094, 1992.

C. Hofmann, G. Feraud, and V. Coutillot. ^{40}Ar/^{39}Ar dating of mineral separates and whole rocks from the Western Ghats lava pile: further constraints on duration and age of the Deccan Traps. *Earth and Planetary Science Letters*, 180:13–27, 2000.

W. S. Holbrook and P. B. Keleman. Large igneous province on the U.S. Atlantic margin and implications for magmatism during continental breakup. *Nature*, 364:433–436, 1993.

W. S. Holbrook, H. C. Larsen, J. Korenaga, T. Dahl-Jensen, I. D. Reid, P. B. Kelemen, J. R. Hopper, G. M. Kent, D. Lizarralde, S. Bernstein, and R. S. Detrick. Mantle thermal structure and active upwelling during continental breakup in the North Atlantic. *Earth and Planetary Science Letters*, 190:251–266, 2001.

J. S. Holik, P. D. Rabinowitz, and J. A. Austin. Effects of the canary hotspot volcanism on structure of oceanic crust off morocco. *Journal of Geophysical Research*, 96:12039–12067, 1992.

W. E. Holt and T. A. Stern. Sediment loading on the western platform of the New Zeland continent: implications for the strength of a continental margin. *Earth and Planetary Science Letters*, 107:523–538, 1991.

J. R. Hopper and W. R. Buck. The effect of lower crustal flow on continental extension and passive margin formation. *Journal of Geophysical Research*, 101:20175–20194, 1996.

J. R. Hopper, T. Dahl-Jensen, W. S. Holbrook, H. C. Larsen, D. Lizarralde, J. Korenaga, G. M. Kent, and P. B. Kelemen. Structure of the SE Greenland margin from seismic reflection and refraction data: Implications for nascent spreading centre subsidence and asymmetric crustal accretion during North Atlantic opening. *Journal of Geophysical Research*, 108, 2003.

J. R. Hopper, T. Funck, B. E. Tucholke, H. C. Larsen, W. S. Holbrook, K. E. Louden, D. Shillington, and H. Lau. Continental breakup and the onset of ultraslow seafloor spreading off Flemish Cap on the Newfoundland rifted margin. *Geology (Boulder)*, 32 (1):93–96, 2004.

S. J. Horsefield, R. B. Whitmarsh, R. S. White, and J.-C. Sibuet. Crustal structure of the Goban Spur rifted continental margin, NE Atlantic. *Geophysical Journal International*, 119:1–19, 1993.

R. Houtz and J. Ewing. Upper crustal structure as a function of plate age. *Journal of Geophysical Research*, 81(14):2490–2498, 1976.

J. Jackson. Strength of the continental lithosphere: time to abandon the jelly sandwich? *GSA today*, 12(9):4–10, 2002.

J. A. Jackson. Active normal faulting and crustal extension. *Continental Extensional Tectonics, Geological Society Special Publications*, 28:3–17, 1987.

M. T. Juárez, L. Tauxe, J. S. Gees, and T. Pick. The intensity of the Earth's magnetic field over the past 160 million years. *Nature*, 394:878–881, 1989.

G. D. Karner, M. Studinger, and R. E. Bell. Gravity anomalies of sedimentary basins and their mechanical implications: Application to the Ross Sea basins, West Antartica. *Earth and Planetary Science Letters*, 235:577–596, 2005.

C. E. Keen, R. C. Courtney, S. A. Dehler, and M.-C. Williamson. Decompression melting at rifted margins: comparison of model predictions with the distribution of igneous rocks on the eastern Canadian margin. *Earth and Planetary Science Letters*, 102:403–416, 1994.

C. E. Keen and D. P. Potter. The transition from a volcanic to a nonvolcanic rifted margin off eastern Canada. *Tectonics*, 14(2):359–371, 1995.

P. B. Kelemen and W. S. Holbrook. Origin of thick, high-velocity crust along the U.S. East Coast Margin. *Journal of Geophysical Research*, 100:10077–10094, 1995.

H.-J. Kim, H.-T. Jou, H.-M. Cho, H. Bijwaard, T. Sato, J.-K. Hong, H.-S. Yoo, and C.-E. Baag. Crustal structure of the continental margin of Korea in the East Sea (Japan Sea) from deep seismic sounding data: evidence for rifting affected by the hotter than normal mantle. *Tectonophysics*, 364:25–42, 2003.

K. B. Knight, P. R. Renne, A. Halkett, and N. White. ^{40}Ar - ^{39}Ar dating of the Rajahmundry Traps, Eastern India and their relationship to the Deccan Traps. *Earth and Planetary Science Letters*, 208:85–99, 2003.

V. Kolla and F. Coumes. Extension of structural and tectonic trends from the Indian subcontinent into the Eastern Arabian Sea. *Marine and Petroleum Geology*, 7, 1990.

K. S. Krishna, D. Gopala Rao, and D. Sar. Nature of the crust in the Laxmi Basin (14°-20°N), western continental margin of India. *Tectonics*, 25, 2006.

V. G. Krishna, K. L. Kaila, and P. R. Reddy. Low velocity layers in the subcrustal lithosphere beneath the Deccan Traps region of western India. *Physics of the Earth and Planetary Interiors*, 67:288–302, 1991.

N. J. Kusznir and R. G. Park. The extensional strength of the continental lithosphere: its dependence on geothermal gradient, and crustal composition and thickness. *In M. P. Coward, J. F. Dewey and P. L. Hancock (Eds.), Continental extensional tectonics, Vol 28 of Geological Society Special Publications, Geological Society of London*, pages 35–52, 1987.

H. C. Larsen and A. D. Saunders. Tectonism and volcanism at the southeast Greenland margin: a record of plume inmpact and later continental rupture. *Proceedings of the Ocean Drilling Program, Scientific Results*, 152:503–533, 1998.

D. Latin and N. White. Generating melt during lithospheric extension: Pure shear vs. simple shear. *Geology*, 18:327–331, 1990.

X. Le Pichon and F. Barbier. Passive margin formation by low angle faulting within the upper crust: The northern Bay of Biscay margin. *Tectonics*, 6:133–150, 1987.

X. Le Pichon, P. Henry, and B. Goffé. Uplift of Tibet: from eclogite to granite- implications for the Andean Plateau and the Variscan belt. *Tectonophysics*, 132:215–231, 1997.

G. S. Lister and G. A. Davis. The origin of metamorphic core complexes and detachment faults formed during Tertiary continetal extension in the northern Colarado River region, U.S.A. *Journal of Structural Geology*, 11:65–94, 1989.

G. S. Lister, M. A. Etheridge, and P. A. Symonds. Detachment faulting and the evolution of passive continental margins. *Geology*, 14:246–250, 1986.

C. S. Liu, D. T. Sandwell, and J. R. Curry. The negative gravity field over the 85° E ridge. *Journal of Geophysical Research*, 87(B9):7673–7686, 1982.

D. Lizarralde and W. S. Holbrook. U.S. mid-Atlantic margin structure and early thermal evolution. *Journal of Geophysical Research*, 102:22855–22875, 1997.

K. E. Louden, J. C. Osler, S. P. Srivastava, and C. E. Keen. Formation of oceanic crust at slow spreading rates: new constraints from an extinct spreading center in Larador Sea. *Geology*, 24(9):771–774, 1996.

W. J. Ludwig, J. E. Nafe, and C. L. Drake. Seismic refraction. *in A. E. Maxwell (ed.), The Sea*, 4:53–84, 1970.

J. A. Malod, L. Droz, B. Mustafa Kemal, and P. Patriat. Early spreading and continental to oceanic basement transition beneath the Indus deep-sea fan: northeastern Arabian Sea. *Marine Geology*, 141:221–235, 1997.

S. A. McEnroe, F. Langenhorst, P. Robinson, G. D. Bromiley, and C. S. J. Shaw. What is magnetic in the lower crust? *Earth and Planetary Science Letters*, 226:175–192, 2004.

D. McKenzie. Some remarks on the development of sedimentary basins. *Earth and Planetary Science Letters*, 40:25–32, 1978.

D. McKenzie and M. J. Bickle. The volume and composition of melt generated by extension of the lithosphere. *Journal of Petrology*, 29:625–679, 1988.

L. C. McNeill, C. J. Cotterill, T. J. Henstock, J. M. Bull, A. Stefatos, R. E. L. Collier, G. Papatheoderou, G. Ferentinos, and S. E. Hicks. Active faulting within the offshore western Gulf of Corinth, Greece: Implications for models of continental rift deformation. *Geology*, 33(4):241–244, 2005.

P. R. Miles, M. Munschy, and J. Segoufin. Structure and evolution on the Arabian Sea and East Somali Basin. *Geophysical Journal International*, 134:876–888, 1998.

P. R. Miles and W. R. Roest. Earliest sea-floor spreading magnetic anomalies in the north Arabian Sea and the ocean-continent transition. *Geophysical Journal International*, 115:1025–1031, 1993.

D. J. Miller and N. I. Christensen. Seismic velocities of lower crustal and upper mantle rocks from the slow-spreading Mid-Atlantic Ridge, south of the Kane transform zone (MARK). *Proceedings of the Ocean Drilling Program, Scientific Results, vol. 153, Ocean Drilling Program, College Station, TX*, pages 437–454, 1997.

T. A. Minshull. Poisson's ratio of a seaward-dipping reflector series, Hatton Bank. *Geophysical Journal International*, 115:332–335, 1993.

T. A. Minshull, S. M. Dean, R. S. White, and R. B. Whitmarsh. Anomalous melt production after continental break-up in the southern Iberia Abyssal Plain. *Non-Volcanic Rifting of Continental Margins: A Comparison of Evidence from Land and Sea. Geological Society, London, Special Publications*, 187:537–550, 2001.

D. C. Mishra, K. Arora, and V. M. Tiwari. Gravity anomalies and associated tectonic features over the Indian Peninsular Shield and adjoining ocean basins. *Tectonophysics*, 379:61–76, 2004.

P. Molnar. Continental tectonics in the aftermath of plate tectonics. *Nature*, 335:131–137, 1988.

J. V. Morgan and P. J. Barton. A geophysical study of the Hatton Bank volcanic margin: a summary of the results from a combined seismic, gravity and magnetic experiment. *Tectonophysics*, 173:517–526, 1990.

M. R. Muller, T. A. Minshull, and R. S. White. Crustal structure of the Southwest Indian Ridge at the Atlantis II Fracture Zone. *Journal of Geophysical Research*, 105: 25809–25828, 2000.

R. D. Müller, C. Gaina, W. R. Roest, and D. Lundbek Hansen. A recipe for microcontinent formation. *Geology*, 29:203–206, 2001.

R. D. Müller, J.-Y. Royer, and L. Lawver. Revised plate motions relative to the hotspots from combined Atlantic and Indian Ocean hotspot tracks. *Geology*, 21:275–278, 1993.

C. Z. Mutter and J. C. Mutter. Variations in thickness of layer 3 dominate oceanic crustal structure. *Earth and Planetary Science Letters*, 117:295–317, 1993.

J. C. Mutter. Margins declassified. *Nature*, 364:393–394, 1993.

J. C. Mutter, W. R. Buck, and C. M. Zehnder. Convective partial melting 1. A model for the formation of thick basaltic sequences during the initiation of spreading. *Journal of Geophysical Research*, 93:1031–1048, 1988.

J. C. Mutter, M. Talwani, and P. L. Stoffa. Origin of seaward-dipping reflectors in oceanic crust of the Norwegian margin by 'subaerial sea-floor spreading'. *Geology*, 10:353–357, 1982.

J. C. Mutter, M. Talwani, and P. L. Stoffa. Evidence for thick oceanic crust adjacent to the Norwegian margin. *Journal of Geophysical Research*, 89:483–502, 1984.

B. R. Naini and M. Talwani. Sediment distribution and structures in the Indus Cone and the western continental margin of India (Arabian Sea). *Eos, Transactions, American Geophysical Union*, 58:405, 1977.

B. R. Naini and M. Talwani. Structural framework and the evolutionary history of the continental margin of Western India. *American Association of Petroleum Geologists*, pages 167–191, 1982.

H. Narain, K. L. Kaila, and R. K. Verma. Continental margins of India. *Canadian Journal of Earth Sciences*, 5:1051–1065, 1968.

J. G. Negi, P. K. Agrawal, and O. P. Pandey. Large scale underplating of serpentinised/ fractionated magma and supermobility of hot Indian lithosphere. 27th *General Assembly, Wellington: IASPEI, Jan. 10-21*, 1994.

J. G. Negi, P. K. Agrawal, and N. K. Thakur. Inversion of regional gravity anomalies and main features of the deep crustal geology of India. *Tectonophysics*, 165:155–165, 1989.

T. K. Nielsen and J. R. Hopper. Formation of volcanic rifted margins: Are temperature anomalies required? *Geophysical Research Letters*, 29(21), 2002.

M. D. Norman, M. O. Garcia, V. S. Kamenetsky, and R. L. Nielsen. Olivine-hosted melt inclusions in Hawaiian picrites: equilibration, melting and plume source characteristics. *Chemical Geology*, 183:143–168, 2002.

I. O. Norton and J. G. Sclater. A model for the evolution on the Indian Ocean and the breakup of Gondwanaland. *Journal of Geophysical Research*, 84:6803–6830, 1979.

J. Oh, J. Austin, J. A., J. D. Phillips, M. F. Coffin, and P. L. Stoffa. Seaward-dipping reflectors offshore the southeastern United States: Seismic evidence for extensive volcanism accompanying sequential formation of the Carolina trough and Blake Plateau basin. *Geology*, 23(1):9–12, 1995.

D. S. O'Hanley. Serpentinites. Records of tectonic and petrological history. *Oxford monographs on geology and geophysics, Oxford University Press, New York*, 34, 1996.

K. Pande. Age and duration of the Deccan Traps, India: a review of radiometric and paleomagnetic constraints. *Proceedings of Indian Academy of Science (Earth and Planetary Science)*, 111(2):115–123, 2002.

K. Pande. $^{40}Ar/^{39}Ar$ age of a lava flow from the Bhimashankar formation, Giravali Ghat, Deccan Traps. *Proceedings of Indian Academy of Science (Earth and Planetary Science)*, 113:755–758, 2004.

O. P. Pandey, P. K. Agrawal, and J. G. Negi. Lithospheric structure beneath Laxmi Ridge and late Cretaceous geodynamic events. *Geo-Marine Letters*, 15:85–91, 1995.

M. Perez-Gussinye and T. J. Reston. Rheological evolution during extension at nonvolcanic rifted margins: Onset of serpentinization and development of detachments leading to continental breakup. *Journal of Geophysical Research*, 106:3961–3975, 2001.

S. Planke and O. Eldholm. Seismic response and construction of seaward dipping wedges of flood basalts: Vøring volcanic margin. *Journal of Geophysical Research*, 99:9263–9278, 1994.

S. Planke, J. Skogseid, T. P. Gladczenko, and O. Eldholm. Seismic evidence of shallow marine volcanism during volcanic margin formation. *Norsk Geologisk Forenings XIV landsmøte, Norsk Geologisk Forenings, Trondheim, Norway, Jan 6-8*, 1995.

S. Planke, P. A. Symonds, E. Alvestad, and J. Skogseid. Seismic volcanostratigraphy of large-volume basaltic extrusive complexes on rifted margins. *Journal of Geophysical Research*, 105(B8):19335–19351, 2000.

W. H. Press, S. A. Teukolsky, W. T. Vetterling, and B. P. Flannery. *Numerical recipies in FORTRAN, 2nd edn.* Cambridge University Press, New York, 1992.

R. W. Raitt. The crustal rocks. *In M. N. Hill (Ed.) The Sea, Wiley-Interscience, New York*, 3:85–102, 1963.

M. V. Ramana, T. Ramprasad, K. A. Kamesh Raju, and M. Desa. Geophysical studies over a segment of the Carlsberg Ridge, Indian Ocean. *Marine Geology*, 115:21–28, 1993.

C. R. Ranero, T. J. Reston, I. Belykh, and H. Gnibidenko. Reflective oceanic crust formed at a fast-spreading centre in the Pacific. *Geology*, 25(6):499–502, 1995.

M. Recq, R. B. Whitmarsh, J. C. Sibuet, R. S. White, and D. Lyness. Seismic structure of the peridotite ridge west of the Galicia Bank, West Iberia. *Comptes Rendus de l'Academie des Sciences, Serie II. Sciences de la Terre et des Planetes*, 322(7):571–578, 1996.

P. R. Reddy, N. Venkateswarlu, P. Koteswara Rao, and A. S. S. S. R. S. Prasad. Crustal structure of peninsular shield, india from dss studies. *National Geophysical Research Institute, India*, 1999.

I. Reid and H. R. Jackson. Oceanic spreading rate and crustal structure. *Marine Geophysical Research*, 5:165–172, 1981.

I. D. Reid. Crustal structure of a nonvolcanic rifted margin east of Newfoundland. *Journal of geophysical Research*, 99:161–165, 1994.

T. J. Reston. The S reflector west of Galicia: The seismic signature of a detachment fault. *Geophysical Journal International*, 127:230–244, 1996.

T. J. Reston and J. Phipps Morgan. Continental geotherm and the evolution of rifted margins. *Geology*, 32:133–136, 2004.

T. J. Reston, C. R. Ranero, and I. Belykh. The structure of Cretaceous oceanic crust of the NW Pacific: Constraints on processes at fast spreading centres. *Journal of Geophysical Research*, 104:629–644, 1999.

A. Rietbrock, C. Tiberi, F. Scherbaum, and H. Lyon-Caen. Seismic slip on a low angle normal fault in the Gulf of Corinth: Evidence from a high-resolution cluster analysis of micorearthquakes. *Geophysical Research Letters*, 23:1817–1820, 1996.

J.-Y. Royer, A. K. Chaubey, J. Dyment, G. C. Bhattacharya, K. Srinivas, V. Yatheesh, and T. Ramprasad. Paleogene plate tectonic evolution of the Arabian and Eastern Somali basins. *The tectonic and climatic evolution of the Arabian Sea region. Special publication of the Geological Society of London, UK*, 195, 2002.

S. M. Russell. A magnetic study of the West Iberia and conjugate rifted continental margins: Constraints on rift-to-drift processes. *Ph.D. Thesis, University of Durham*, 1999.

M. H. Salisbury and N. I. Christensen. The seismic velocity structure of a traverse through the Bay of Islands ophiolite complex, Newfoundland, an exposure of ancient oceanic crust and upper mantle. *Journal of Geophysical Research*, 83:805–817, 1978.

D. T. Sandwell and W. H. F. Smith. Marine gravity anomaly from Geosat and ERS 1 satellite altimetry. *Journal of Geophysical Research*, 102:10039–10054, 1997.

R. A. Scrutton. The crustal structure of Rockall Plateau microcontinent. *Geophysical Journal of the Royal Astronomical Society*, 27:259–275, 1971.

M. A. Sellevoll and M. Mokhtari. An intra-ocean crustal seismic reflecting zone below the dipping reflectors on Lofoten margin. *Geology*, 16:666–668, 1988.

G. Sen, M. Borges, and B. D. Marsh. A case for short duration of Deccan Trap eruption. *Eos, Transactions, American Geophysical Union*, 87(20), 2006.

H. C. Sheth. Flood basalts and large igneous provinces from deep mantle plumes: fact, fiction and fallacy. *Tectonophysics*, 311:1–29, 1999.

H. C. Sheth, K. Pande, and R. Bhutani. ^{40}Ar - ^{39}Ar ages of Bombay trachytes: evidence for a Palaeocene phase of Deccan volcanism. *Geophysical Research Letters*, 28(18): 3513–3516, 2001.

S. M. Shuaib. Geology and hydrocarbon potential of offshore Indus Basin, Pakistan. *AAPG Bulletin*, 66:940–946, 1982.

J. C. Sibuet, V. Louvel, R. B. Whitmarsh, R. S. White, S. J. Horsefield, B. Sichler, P. Leon, and M. Recq. Constraints on rifting processes from refraction and deep tow magnetic data: The example of the Galicia continental margin (West Iberia). *Rifted Ocean-Continent Boundaries*, pages 197–217, 1995.

A. P. Singh. The deep crustal accretion beneath the Laxmi Ridge in the northestern Arabian Sea: the plume model again. *Journal of Geodynamics*, 27(4-5):609–622, 1999.

J. Skogseid and O. Eldholm. Early Cenozoic crust at the Norwegian continental margin and the conjugate Jan Mayen Ridge. *Journal of Geophysical Research*, 92:11471–11491, 1987.

W. H. F. Smith and D. T. Sandwell. Global sea floor topography from satellite altimetry and ship depth soundings. *Science*, 277:1956–1962, 1997.

P. Spudditch and J. A. Orcutt. Petrology and porosity of an oceanic site: results from waveform modeling of seismic refraction data. *Journal of Geophysical Research*, 85: 1409–1433, 1980.

R. K. Staples, R. S. White, B. Brandsdóttir, W. Menke, P. K. H. Maguire, and J. H. McBride. Faeroe-Iceland Ridge experiment 1. Crustal structure of northeastern Iceland. *Journal of Geophysical Research*, 102:7849–7866, 1997.

M. Talwani. Computation with the help of a digital computer of magnetic anomalies caused by bodies of arbitrary shape. *Geophysics*, 30(5):49–59, 1965.

M. Talwani and C. Reif. Laxmi Ridge - A continental sliver in the Arabian Sea. *Marine Geophysical Researches*, 20:259–271, 1998.

M. Talwani, C. C. Windisch, and M. G. Langseth. Reykjanes Ridge crest: a detailed geophysical study. *Journal of Geophysical Research*, 76:473–517, 1971.

M. Talwani, J. C. Worzel, and M. Landisman. Rapid gravity calculations for two-dimensional bodies with application to the Mendocino submarine fracture zone. *Journal of Geophysical Research*, 64:49–59, 1959.

M. Talwani and B. Zelt. Some recent developments in the acquisition and processing of seismic data. *Tectonophysics*, 286:123–142, 1998.

J. Thorson. Reconstruction of slant stacks: Stanford exploration project report no. 14. *Stanford University*, pages 83–91, 1978.

M. Torne, M. Fernandez, W. Wheeler, and R. Karpuz. Three-dimensional crustal structure of the Voring Margin (NE Atlantic): A combined seismic and gravity image. *Journal of Geophysical Research*, 108(B2), 2003.

S. Treitel. The complex weiner filter. *Geophysics*, 39(2):169–173, 1974.

R. Van der Voo and M. W. McElhinny. Global paleopoles; data base off to good start. *Eos, Transactions, American Geophysical Union*, 70(31):748, 1989.

D. Vandamme, V. Courtillot, J. Besse, and R. Montigny. Paleomagnatism and age-determinations of the Deccan Traps (India)- Results of a Nagpur-Bombay traverse and review of earlier work. *Review of Geophysics*, 29(2):159–190, 1991.

M. Vardy. Crustal architecture of conjugate rifted margins: The Seychelles and Laxmi Ridge margins in the NW Indian Ocean. *Masters' dissertation, NOC,S, Southampton*, 2005.

E. E. Vera, J. C. Mutter, P. Buhl, J. A. Orcutt, A. J. Harding, M. E. Kappus, R. S. Detrick, and T. M. Brocher. The structure of 0 to 0.2 My old oceanic crust at 9°N on the East Pacific Rise from expanded spread profiles. *Journal of Geophysical Research*, 95:15529–15556, 1990.

J. Verhoef, B. Collette, J. Danobeitia, H. Roeser, and W. Roest. Magnetic anomalies off West-Africa (28-38n). *Marine Geophysical Researches*, 13:81–103, 1991.

L. G. Viereck, D. Love, I. L. Gibson, J. Hertogen, L. M. Parson, and A. C. Morton. Chemical stratigraphy and petrology of the Vøring Plateau tholeiitic lavas and interlayered volcaniclastic sediments at ODP Hole 642E. *Proc. Scientific Results, ODP, Leg 104, Norwegian Sea*, pages 367–396, 1989.

D. Wang, R. Van der Voo, and D. R. Peacor. Why is the remenant magnetic intensity of Cretaceous MORB so much higher than that of mid to late Cenzoic MORB? *Geosphere*, 1:138–146, 2005.

A. B. Watts. *Isostacy and flexure of the lithosphere.* Cambridge University Press, UK, 2001.

B. Wernicke. Low angle normal faults in the Basin and Range province: Nappe tectonics in an expanding oregen. *Nature*, 291:645–648, 1981.

R. S. White. Crustal structure and magmatism of North Atlantic continental margins. *Journal of the Geological Society, London*, 149:841–854, 1992.

R. S. White and D. McKenzie. Magmatism at rift zones: the generation of volcanic continental margins and flood basalts. *Journal of Geophysical Research*, 94(B6):7685–7729, 1989.

R. S. White, D. McKenzie, and R. O'Nions. Oceanic crustal thickness from seismic measurements and rare earth inversions. *Journal of Geophysical Research*, 97:19683–19715, 1992.

R. S. White, G. D. Spence, S. R. Fowler, D. P. McKenzie, G. K. Westbrook, and A. N. Bowen. Magmatism at rifted continental margins. *Nature*, 330:439–444, 1987.

B. M. Whiting, G. D. Karner, and N. W. Driscoll. Flexural strength and stratigraphic development of the west Indian continental margin. *Journal of Geophysical Research*, 99:13791–13811, 1994.

R. B. Whitmarsh. Some aspects of plate tectonics in the Arabian Sea. *Initial reports of the deep sea drilling project, v23, Washington, D.C., U.S. Government Printing Office*, pages 527–535, 1974.

R. B. Whitmarsh, G. Manatschal, and T. A. Minshull. Evolution of magma-poor continental margins from rifting to seafloor spreading. *Nature*, 413:150–154, 2001a.

R. B. Whitmarsh, T. A. Minshull, S. M. Russell, S. M. Dean, K. E. Louden, and D. Chian. The role of syn-rift magmatism in the rift-to-drift evolution of the West Iberia continental margin: geophysical observations. *Non-Volcanic Rifting of Continental Margins: A Comparison of Evidence from Land and Sea. Geological Society, London, Special Publications*, 187:107–124, 2001b.

R. B. Whitmarsh and P. J. Wallace. The rift-to-drift development of the West Iberia nonvolcanic continental margin: A summary and review of the contribution of Ocean Drilling Program leg 173. *Proceedings of the Ocean Drilling Program, Scientific Results*, 173, 2001.

R. B. Whitmarsh, R. S. White, S. J. Horsefield, J. C. Sibuet, M. Recq, and V. Louvel. The ocean-continent boundary off the western continental margin of Iberia: Crustal structure west of Galacia Bank. *Journal of Geophysical Research*, 101(B12):28291–28314, 1996.

B. M. Wilson. *Igneous petrogenesis: A global tectonic approach.* Springer, 1989.

D. S. Wilson, S. Umino, S. Miyashita, G. D. Acton, R. Anma, S. R. Barr, A. Belghoul, J. Carlut, D. M. Christie, R. M. Coggon, K. M. Cooper, C. Cordier, L. Crispini, D. S. Rodriguez, F. Einaudi, L. Galli, Y. Gao, J. Geldmacher, L. A. Gilbert, N. W. Hayman, E. Herrero-Bervera, N. Hirano, S. Holter, S. Ingle, S. Jiang, U. Kalberkamp, M. Kerneklian, J. Koepke, C. Laverne, H. L. Lledo Vasquez, J. Maclennan, S. Morgan, N. Neo, H. J. Nichols, S. H. Park, M. K. Reichow, T. Sakuyama, T. Sano, R. Sandwell, B. Scheibner, C. E. Smith-Duque, S. A. Swift, P. Tartarotti, D. A. H. Teagle, A. A. Tikku, M. Tominaga, E. A. Veloso, T. Yamasaki, S. Yamazaki, C. Ziegler, J. C. Alt, and N. R. Banerjee. Drilling to gabbro in intact ocean crust. *Science*, 312(5776):1016–1020, 2006.

M. Wilson. Geochemical signature of oceanic and continental basalts: a key to mantle dynamics. *Journal of the Geological Society of London*, 150:977–990, 1993.

W. Wilson. Speed of sound in seawater as a function of temperature, pressure and salinity. *Journal of Acoustical Society of America*, 32:641–644, 1960.

O. Yilmaz. *Seismic data processing.* Society of Exploration Geophysicists, 1987.

C. A. Zelt. Modelling strategies and model assesment for wide-angle seismic traveltime data. *Geophysical Journal International*, 139:183–204, 1999.

C. A. Zelt and R. B. Smith. Seismic traveltime inversion for 2-d crustal velocity structure. *Geophysical Journal International*, 108:16–34, 1992.